THÈSE

En vue de l'obtention du

DOCTORAT DE L'UNIVERSITÉ DE TOULOUSE

Délivré par :

Institut National Polytechnique de Toulouse (INP Toulouse)

Discipline ou spécialité :

Signal, Image, Acoustique et Optimisation

Présentée et soutenue par :

M. ENIK SHYTERMEJA

le jeudi 14 décembre 2017

Titre :

Design and Performance of a GNSS Single-frequency Multi-constellation Vector Tracking Architecture for Urban Environments

---

Ecole doctorale :

Mathématiques, Informatique, Télécommunications de Toulouse (MITT)

Unité de recherche :

Laboratoire de Télécommunications (TELECOM-ENAC)

Directeur(s) de Thèse :

M. OLIVIER JULIEN

M. AXEL JAVIER GARCIA PENA

Rapporteurs :

M. GONZALO SECO-GRANADOS, UNIVERSIDAD AUTONOMA DE BARCELONE

M. JARI NURMI, TAMPERE UNIVERSITY

Membre(s) du jury :

M. JARI NURMI, TAMPERE UNIVERSITY, Président

M. AXEL JAVIER GARCIA PENA, ECOLE NATIONALE DE L'AVIATION CIVILE, Membre

M. CHRISTOPHE MACABIAU, ECOLE NATIONALE DE L'AVIATION CIVILE, Membre

Mme AUDREY GIREMUS, UNIVERSITE BORDEAUX 1, Membre

M. OLIVIER JULIEN, ECOLE NATIONALE DE L'AVIATION CIVILE, Membre

I do not think that there is any other quality so essential to success of any kind as the quality of perseverance.

It overcomes almost everything, even nature.

From *John D. Rockefeller*

Optimism is the faith that leads to achievement. Nothing can be done without hope and confidence.

From *Helen Keller*

Abstract

In the last decade, Global Navigation Satellites Systems (GNSS) have gained a significant position in the development of urban navigation applications and associated services. The urban environment presents several challenges to GNSS signal reception that are translated in the positioning domain into a decreased navigation solution accuracy up to the lack of an available position. Two main signal distortions are generated from the urban environment conditions.

On one hand, the reception of reflected or diffracted GNSS Line-Of-Sight (LOS) echoes in addition to the direct LOS signal generates the phenomenon known as multipath that represents the major detrimental positioning error source in urban canyons. From the receiver point of view, the multipath affects the code and carrier tracking loops. Consequently, the pseudo-range and Doppler measurements are degraded.

On the other hand, the total or partial obstruction of the GNSS LOS by the urban environment obstacles causes GNSS LOS blockage or GNSS LOS shadowing phenomena. The reception of Non-LOS (NLOS) signals introduces a bias on the pseudo-range measurements if only NLOS satellites are tracked. The LOS shadowing can also decrease the LOS signal carrier-to-noise ratio and thus making the signal more vulnerable to the multipath effect.

Finally, the resulting degraded pseudo-range and Doppler measurements cause the navigation processor to compute an inaccurate position solution or even a positioning loss in the case of few available measurements. Thus, it is evident that advanced signal processing techniques are necessary to mitigate these undesired effects in order to ensure the accuracy and availability of the position solution.

For this matter, Vector Tracking (VT) constitutes a promising approach able to cope with the urban environment-induced effects including multipath, NLOS reception and signal outages. Standard GNSS receivers use a decentralized architecture, separating the scalar code/carrier tracking task from the navigation algorithm. Whereas in vector tracking, a deep integration between the signal processing and the navigation processor exists. This thesis is particularly focused on the proposal and design of a dual constellation GPS + Galileo single frequency L1/E1 Vector Delay Frequency Lock Loop (VDFLL) architecture for the automotive usage in urban environment. From the navigation point of view, VDFLL represents a concrete application of information fusion, since all the satellite tracking channels are jointly tracked and controlled by the common navigation Extended Kalman filter (EKF).

In this configuration, the EKF-estimated navigation solution drives the code delay (VDLL part) and carrier frequency (VFLL part) Numerical Control Oscillators (NCOs) in the feedback loop. The choice of the dual-constellation single frequency vector tracking architecture ensures an increased number of observations, with the inclusion of the Galileo E1 measurements. An increased satellite in-view availability is directly translated in a higher measurement redundancy and improved position accuracy

in urban environment. This configuration also allows the conservation of the low-cost feasibility criteria of the mobile user's receiver.

Moreover, the use of single frequency L1 band signals implies the necessity of taking into account the ionospheric error effect. In fact, even after the application of the Klobuchar and Nequick ionosphere error correction models to the GPS and Galileo pseudorange measurements, respectively, a resultant ionospheric residual error appears in the received observations.

The originality of this work relies on the implementation of a dual-constellation VDFLL architecture, capable of estimating the ionosphere residuals present in the received observations and coping with the urban environment-induced effects. Within the scope of this thesis, a realistic dual-constellation GNSS signal emulator comprising the navigation module has been developed. The developed signal emulator is a powerful tool for flexible and reliable GNSS receiver testing and is designed in a modular manner to accommodate several test scenarios and an efficient switch between the scalar- and vector tracking operation modes.

This dissertation investigates the VDFLL superiority w.r.t the scalar tracking receiver in terms of positioning performance and tracking robustness for a real car trajectory in urban area in the presence of multipath and ionosphere residual error.

For this matter, several tests were conducted with the inclusion of different error sources at the GNSS signal emulator with the objective of validating the performance of the VDFLL architecture. These tests proved the VDFLL capability in assuring an accurate and stable navigation solution within the $4\ m$ error bound even during frequent satellite outages periods. Whereas, the scalar tracking receiver experiences position error jumps up to the level of $20\ m$ due to the reduced number of observations. Moreover, the VDFLL tracking robustness was noted both in the code delay and carrier frequency estimations due to the channel aiding property of the vectorized architecture. Whereas concerning the scalar tracking technique, the significant code delay estimation errors due to the LOS signal blockages are the cause of the loss-of-lock conditions that trigger the initiation of the re-acquisition process for those channels. On the contrary, a continuous signal tracking was guaranteed from the proposed VDFLL architecture.

Acknowledgements

This work was financially supported by EU FP7 Marie Curie Initial Training Network MULTI-POS (Multi-technology Positioning Professionals) under grant nr. 316528.

Several people have played an important role during this long path toward the Ph.D. thesis defense that I would like to deeply acknowledge.

First and foremost, I want to thank my thesis director Olivier Julien who always found time in his tight schedule to answer my questions, correcting my thesis chapters and provided me with interesting ideas and research tracks from his vast background in the field. I am also thankful to my thesis co-director Axel Garcia-Pena for his constant support and numerous constructive discussions that oriented me toward efficient candidate solutions. Their contribution laid the foundation of a productive and stimulating Ph.D. experience. Furthermore, the joy and enthusiasm they both had for my research work was motivational for me, even during tough times in the Ph.D. pursuit.

I gratefully acknowledge Professor Jari Nurmi and Associate Professor Gonzalo Seco-Granados for reviewing my Ph.D. thesis, providing me with interesting comments and participating as jury members for the thesis defense. I would also like to thank Dr. Audrey Giremus for attending the thesis defense and for the provision of great advices concerning the further advancement of this research. I am also thankful to Dr. Christophe Macabiau for his precious suggestions concerning the ionosphere estimation module.

My sincere thanks also goes to Dr. Manuel Toledo-Lopez, Dr. Miguel Azaola-Saenz and Henrique Dominguez, who provided me with the opportunity to join their team in GMV, Spain as an invited researcher, and who gave me their practical insights regarding the receiver design and problematics in urban environment.

Je remercie particulièrement mes collègues du laboratoire SIGNAV et EMA qui m'ont accueilli très chaleureusement au sein du labo, m'ont permis d'apprendre la langue et culture française et aussi pour leur contribution à la bonne ambiance au quotidien. C'est pour cela que je tiens à remercier Jérémy (le support continu pour le sujet de filtre de Kalman et pour les discussions de rugby), Paul (le premier accueil des nouveaux et toujours disponible à mes questions), Florian (le footballer strasbourgeois et expert de l'évolution de l'UE), Anaïs (l'agente marseillaise en action), Amani (coéquipier des heures tardives de fin thèse), Antoine (monsieur des open sources), Anne-Christine (joueuse de badminton en repos le mercredi), Carl (le supporteur de Leeds et l'anti-Barça à vie), Eugene (le Gangnam style sur Toulouse), Ikhlas (partageuse du PC de simulation), Sara (point de référence des conférences au SIGNAV), Rémi (le philosophe parisien) , Christophe (le producteur de bière artisanale), Alexandre (le chef d'unité internationale), Hélène (défenseur des droits des femmes) et Rémi (toujours jeune et avec l'esprit rockeur à vie).

Je souhaite aussi un bon courage à tous ceux qui soutiendront leur thèse dans les prochains mois: Enzo, Quentin (avec sa fatigue le matin), Jade, Johan (monsieur soirée extrême jusqu'à le lever du soleil et blaguer « raciste modérée ») et aussi les nouveaux doctorants: Capucine (mademoiselle lapins

et axolotls), Roberto (il juventino da Matera), Aurin (l'italien posé), Anne-Marie, Seif (l'expert de sécurité sociale) et Thomas (voleur de chaise).

Je tiens également à remercier mon co-bureau depuis le début et amoureux de la nourriture JB, avec qui j'ai partagé des très bons moments aussi en voyage des conférences en Etats Unis. Et puis il y a aussi tous ceux qui ont déjà fini leur thèse depuis quelques temps: Alizé (organisatrice des soirées par excellence), Ludo, Marion, Lina, Philipe, Myriam, Jimmy et Leslie. Pour finir, je souhaite remercier Cathy et Collette pour leur support dans la préparation logistique des missions.

Je ne peux pas oublier de mentionner mes amis « le trio » Giuseppe, Marco et Simon, pour les bons moments en week-ends et voyages en Europe et Etats Unis.

Finally, I would like to express my eternal gratitude to my parents and family for the education provided to me and their unconditional love and support that served as a strong source of motivation especially in the complicated moments along this journey. Last but not least, I want to acknowledge the love and assistance of my girlfriend that served as an anti-stress during this last period.

Abbreviations

AAIM	Autonomous Aircraft Integrity Monitoring
ADC	Analog to Digital Convertor
AGC	Automatic Gain Controller
AOD	Age Of Data
ARNS	Aeronautical Radio Navigation Services
BOC	Binary Offset Carrier
BPSK	Binary Phase Shift Keying
BDS	BeiDou Navigation Satellite System
BDT	BeiDou Time
C/A	Coarse/Acquisition
CAF	Cross Ambiguity Function
CBOC	Composite Binary Offset Carrier
CDDIS	Crustal Dynamics Data Information System
CDMA	Code Division Multiple Access
CIR	Channel Impulse Response
C/NAV	Commercial Navigation
CS	Commercial Service
CWI	Continuos Wave Interference
DGNSS	Differential Global Navigation Satellite System
DLL	Delay Lock Loop
DOD	Department of Defense
DOP	Dilution of Precision
DP	Dot Product
DSSS	Direct-Sequence Spread Spectrum
DVB-T	Digital Video Broadcasting Terrestrial
ECEF	Earth-Centered Earth-Fixed
EGNOS	European Geostationary Navigation Overlay Service
EKF	Extended Kalman Filter
EML	Early Minus Late
EMLP	Early Minus Late Product
ENAC	Ecole Nationale de l'Aviation Civile
ESA	European Spatial Agency
FDE	Fault Detection and Exclusion
FDMA	Frequency Division Multiple Access
FLL	Frequency Lock Loop
F/NAV	Freely Accessible Navigation
FPGA	Field-Programmable Gate Array
GAGAN	GPS Aided GEO Augmented Navigation system
GBAS	Ground Based Augmentation System
GEO	Geostationary Earth Orbit
GIVE	Grid Ionospheric Vertical Error

GNSS	Global Navigation Satellite Systems
GPS	Global Positioning System
GSA	European GNSS Agency
GSO	GeosynchronouS earth Orbit
GST	Galileo Satellite Time
ICAO	International Civil Aviation Organization
IF	Intermediate Frequency
IGS MGEX	International GNSS Service Multi-GNSS Experiment and Pilot project
I/NAV	Integrity Navigation
INS	Inertial Navigation System
IRNSS	Indian Regional Navigation Satellite System
ITU	International Telecommunication Union
KF	Kalman Filter
LBS	Location Based Services
LFSR	Linear Feedback Shift Register
LNA	Low Noise Amplifier
LOS	Line-of-Sight
MBOC	Multiplexed Binary Offset Carrier
MCS	Master Control Station
MOPS	Minimum Operational Performance Requirements
MSAS	MTSAT Satellite Augmentation System
MTSAT	Multifunctional Transport SATellites
NAVSTAR	Navigation Signal Timing and Ranging
NRZ	Non-return to zero
PDP	Power Delay Plot
PDF	Probability Distribution Function
PPS	Precise Positioning Service
PRS	Public Regulated Service
PSD	Power Spectrum Density
PVT	Position, Velocity and Time
QZSS	Quasi-Zenith Satellite System
RHCP	Right Hand Circularly Polarized
RUC	Road User Charging
SAR	Search and Rescue
SAW	Surface Acoustic Wave
SDCM	System for Differential Corrections and Monitoring
SiS	Signal-in-Space
SISA	Signal-in-Space Accuracy
SLAM	Simultaneous Localization and Mapping
SoL	Safety-of-Life
SNR	Signal-to-Noise Ratio
SPS	Standard Positioning Service
ST	Scalar Tracking
TEC	Total Electron Content
TT&C	Tracking, Telemetry and Control
UHF	Ultra-High Frequency
URA	User Range Accuracy

VHF	Very-High Frequency
VDLL	Vector Delay Lock Loop
VFLL	Vector Frequency Lock Loop
VDFLL	Vector Delay Frequency Lock Loop
VT	Vector Tracking
WAAS	Wide Area Augmentation System
WLS	Weighted Least Square
ZAOD	Zero Age Of Data

Table of Contents

List of Figures

List of Tables

1. Introduction

1.1. Background and Motivation

Global Navigation Satellites Systems (GNSS) are increasingly present in our life and represent a key player in the world economy mostly due to the expansion of the location-based services (LBS) [GSA, 2017]. In the past years, a constant evolution of the GNSS systems from the first and well-known US Global Positioning System (GPS) toward the upgrade and/or full deployment of the Russian GLONASS, European Galileo, Chinese BeiDou and the regional augmentation systems has been observed. However, the expansion of GNSS usage is not only related to the evolution of satellite constellation payload (signal modulation, data message structure, atomic clock standard etc.) but also to the development of new applications and services.

As stated in the GNSS market report in [GSA, 2017], an important part of the GNSS applications are found for the automotive usage in urban environments that are characterized by difficult signal reception conditions. Among these applications are the safety-of-life (driver assistance) and liability-critical (such as Road User Charging) services that demand very high quality of service expressed in terms of accuracy, integrity, availability and continuity. In these obstructed environments, the received signals are severely affected by the urban obstacles including buildings, lampposts and trees that attenuate their amplitudes and generate fast signals' phase oscillations.

Two main signal distortions are generated from the urban environment conditions that are multipath and LOS blockage or shadowing. Multipath is produced by the superposition of the direct LOS signal with its reflected or diffracted replicas, which significantly affect the code and carrier tracking processes. Indeed, multipath reception causes the distortion of the correlation function between the incoming code and local replica code thus, introducing errors larger than the linear region of the code/carrier discriminator functions. Consequently, the generated pseudo-range and Doppler measurements are degraded. In the worst-case scenario, the direct LOS signal can be totally blocked by the urban obstacles generating the GNSS LOS blockage phenomena. For those satellites under strong signal fading conditions, the carrier-to-noise (C/N_0) ratio can drop below the 10 dB-Hz level [Bhattacharyya, 2012] and introducing large biases on the pseudorange measurements and cycle slips for the carrier phase observations.

Another signal distortion that is not considered in this dissertation is the RF signal unintentional and intentional (jamming) interference that reduces the C/N_0 of the received GNSS signals and therefore, jeopardizing the GNSS receiver operation up to preventing the signal acquisition or causing the channel loss-of-lock.

These urban-induced effects are detrimental to the pseudorange and Doppler measurements generated by the user receiver that are further translated into a decreased position solution accuracy up to the lack of an available position estimation. In order to cope with these severe urban conditions, two distinct research axes may be identified. The first one consists on coupling the GNSS

measurements with the Inertial Navigation System (INS) data referred to as the GNSS/INS hybridization algorithms. The GNSS measurements fusion with the INS offline data assures the availability and continuity of the navigation solution even when the GNSS measurements are severely corrupted or even unavailable during satellite outage periods. The second research path, which is adopted in this dissertation, relies on the implementation of advanced GNSS signal processing techniques. Our attention is directed to the Vector Tracking (VT) technique, which is capable of dealing with the urban-induced effects such as multipath, NLOS reception and satellite outages.

Standard GNSS receivers track each satellite independently through the technique referred to as scalar tracking, whose task is to estimate the code delay, carrier frequency and phase of the incoming signals on a satellite-by-satellite basis in a sequential process through the following operations such as: correlation, discriminator, loop filtering, code/carrier NCO update up to the local replica generator block. The goal of the code/carrier loop filters is the discriminators' outputs filtering for noise reduction at the input of receiver oscillator. Furthermore, the code/carrier NCOs are responsible of converting the filtered discriminator output into a frequency correction factor that is fed back to the code replica and carrier generators. In contrast to scalar tracking, where each visible satellite channel is being tracked individually and independently, vector tracking performs a joint signal tracking of all the available satellites. Indeed, the code/carrier loop filters and NCO update blocks are removed and replaced by the navigation filter. Therefore, VT exploits the knowledge of the estimated receiver's position and velocity to control the feedback to the local signal generators of each tracking channel. The VT technique can improve the tracking of some attenuated or blocked signals due to the channel aiding property based on the navigation solution estimation. This feature clearly positions the vector tracking architectures as the leading advanced signal processing techniques in urban environments.

Different vector tracking architectures can be designed based on the code delay and/or carrier phase/frequency tracking loop modifications. The concept of vector tracking was first proposed in [Parkinson, 1996] in the form of a vectorized code tracking loop for the GPS L1 signal tracking, referred to as Vector Delay Lock Loop (VDLL). This work emphasized the VDLL tracking superiority over the scalar tracking technique in terms of code delay tracking accuracies in low C/N_0 ratios. An important part of the research study was focused on the review of possible VT configurations and on their performance analysis criterions. Indeed, most of the relevant works in this subject were concentrated into the VT performance analysis in jamming conditions or signal power drops such as in [Gustafson and Dowdle, 2003], [Won et al., 2009], [Lashley et al., 2010] and [Bevly, 2014].

This thesis is particularly focused on the proposal and detailed design of the dual constellation single frequency vector tracking architecture for the automotive usage in urban environment. The justifications regarding the choice of the dual-constellation but single-frequency vectorized architecture are herein presented:

- The dual-constellation configuration implies an increased number of received observations that is translated into a higher position estimation accuracy and availability. Recalling the channel aiding feature of the vector tracking technique and that the feedback loop to the signal generators is obtained from the positioning solution, a better position estimation is therefore projected into an increased signal tracking accuracy;
- The choice of a single frequency band architecture significantly reduces the architecture complexity and respects the low-cost requirement of the mobile user's receiver module.

Since this research work is conducted in the framework of a European-funded project, the focus is oriented to the integration of the US GPS and European Galileo systems' freely-available signals in the designed receiver architecture. Therefore, the Open Service (OS) GPS L1 C/A and Galileo E1-C (pilot) signals are considered in this Ph.D. thesis.

Among the different vector tracking configurations, in this thesis the Vector Delay Frequency Lock Loop (VDFLL) architecture is implemented, where the navigation filter is in charge of estimating both the code delay (VDLL) and the Doppler frequency change (VFLL) of each incoming signal in order to close the code and carrier feedback loops. This architecture, representing a complete deep information fusion algorithm, is selected since it enhances the vehicle dynamics tracking capability of the receiver.

Beside the urban environment-related error sources, the atmospheric disturbances introduce propagation delays to the satellite-transmitted signals. In this work, the attention was directed to the ionosphere contribution, representing the major atmosphere-induced delay in a single-frequency receiver to the code measurements after the correction of the satellite clock error. Indeed, the ionosphere acts as a dispersive medium to the GNSS signals, delaying the incoming signal code and advancing its carrier phase. Furthermore, the use of dual constellation but single frequency L1 band signals does not allow the entire correction of the ionosphere delay. As a result, an ionosphere residual is present in the GPS and Galileo pseudorange measurements after the application of the Klobuchar and NeQuick ionosphere error correction models, respectively. The ionosphere residuals can be modelled according to the civil aviation standard as a first-order Gauss Markov process having an exponentially decaying autocorrelation function and a large correlation time of 1800 seconds [ICAO, 2008].

The novelty of this dissertation relies on the implementation of a dual-constellation GPS/Galileo single frequency L1/E1 VDFLL architecture, capable of estimating the ionosphere residuals present in the received observations and coping with the urban environment-induced effects such as multipath and NLOS signal reception. The inclusion of the ionosphere residuals estimation process for the VDFLL architecture is associated with the augmentation of the position, velocity and time state vector with the ionosphere residuals per each tracked satellite. This dissertation provides the detailed mathematical formulation of the adjusted VDFLL process and measurement models in the ionosphere residuals' estimation operation mode.

Finally, this dissertation investigates the detailed performance analysis in the navigation- and channel estimation levels between the designed VDFLL architecture and the scalar tracking receiver in urban environment representative and in the presence of ionosphere residuals.

Within the scope of this thesis, a realistic dual-constellation dual-frequency GNSS signal emulator, comprising the navigation module and the vector tracking capability, has been developed. The term emulator is related to the fact that the GPS L1 C/A and Galileo E1-C signals of interest are generated at the correlator output level, which permits to skip the correlation operation characterized by a high computational load. The simulation option was selected against the use of real GNSS signals due to the testing flexibility offered by the signal emulator in terms of new tracking techniques and different navigation filter's configurations, as it is the case of the designed vectorized receiver architecture. Furthermore, the GNSS signal emulator allows the total control on the simulation parameters comprising the user motion, signal reception environment and GNSS signal's characteristics, which

permit to finely evaluate the impact on each separate and joint error sources into the navigation performance and tracking robustness.

The most sensitive part of the signal emulator concerns the urban propagation channel modelling. After a refined state-of-the-art in this domain, the wideband DLR Land Mobile Multipath Channel model (LMMC) was chosen for the generation of a representative of urban environment signal's reception conditions. However, this urban channel model was customized based on our requirements and later integrated into the signal emulator at the correlator output level.

The objectives of the Ph.D. work are detailed in the following section.

1.2. Thesis Objectives

The global objective of this dissertation is the development of advanced and innovative techniques capable of ensuring the robustness of an integrated GPS/Galileo receiver for automotive usage in urban environment. More precisely the focus is directed to the dual constellation GPS/Galileo but single frequency receiver using the Open Service GPS L1 C/A and Galileo E1-C pilot signals.

The overall Ph.D. thesis objective can be further divided into the following sub-objectives:

1. The review of the GNSS signal propagation delays and measurement errors in the urban environment:
    - ❖ Study of the ionosphere effect on the GNSS code and Doppler measurements, focusing on the Klobuchar and NeQuick correction models for the GPS and Galileo signals, respectively. The study of the ionosphere residual modelling in the civil aviation domain;
    - ❖ Analysis of the multipath and LOS blockage impact on the code and carrier tracking process and sorting the available GNSS multipath mitigation techniques at the signal processing stage.
2. The study of candidate techniques capable of increasing the receiver's robustness in urban environment. This objective includes:
    - ❖ Identification of the approaches or indicators that are able to detect and/or remove the received NLOS signals either prior the signal processing block or before being included in the navigation module:
        i. The estimated C/N_0 can represent a measurement quality indicator providing two alternatives, either to down-weight or remove the "bad" measurements at the navigation level.
    - ❖ The review of the vector tracking techniques in terms of their operation principle, possible configurations and their limits in signal-constrained environments.
3. The design and development of a dual-constellation GPS/Galileo single frequency L1/E1 vector tracking architecture for automotive usage in urban environment conditions. The attention is also directed toward the detailed description of the process and measurement model adapted to the proposed configuration;

4. Review of available urban propagation channel models, which are able to simulate realistic urban environments and applicable for the GNSS receivers. Furthermore, the urban channel model adaptation to the simulator and to the vector tracking architecture is also required;
5. The detailed performance analysis through extensive tests of the proposed vectorized architecture with respect to the scalar tracking receiver representing the benchmark.

1.3. Thesis Contributions

The main contributions of this Ph.D. thesis are listed as following:

1. Proposal and design of a dual-constellation GPS/Galileo single frequency band L1/E1 VDFLL architecture using the Open Service (OS) GPS L1 C/A and Galileo E1-C pilot signals, able to increase the receiver robustness in urban environments;
2. Development of a dual constellation GPS/Galileo GNSS signal emulator integrating the scalar tracking receiver configuration and the vector tracking capability. The implemented signal emulator is entirely configurable and designed in a modular manner comprising the following main modules: the generation of the propagation delays and measurement errors, the code/carrier signal tracking unit and the navigation processor. Moreover, an efficient switch is implemented that allows the passage from the scalar to the vector tracking operation or vice versa;
3. Customization of the selected DLR urban propagation channel model to the vector tracking update rate and the generation of the required urban scenario along with the LOS/NLOS echoes data to assure the signal emulator operation in an urban environment representative;
4. Formulation of the signal emulator correlator output according to the LOS/NLOS echoes amplitude, relative delay, phase and Doppler frequency information;
5. Adaptation of the proposed VDFLL architecture allowing the estimation process of the ionosphere residuals per tracking channel;
6. Provision of the detailed mathematical expressions for the modified state and measurement model of the VDFLL EKF filter with an emphasis on the augmentation of the process and measurement noise covariance matrixes with the ionosphere residuals-related uncertainties;
7. Proposition and implementation of a second VDFLL configuration, referred to in this dissertation as the VDFLL satellite selection operation mode, for harsh urban conditions with frequent satellite outages. This design differs from the classic VDFLL architecture of point 2 since the position estimation and NCO feedback loop is carried on by the LOS satellites only.
8. In-depth performance assessment for different test scenarios and error sources of the proposed VDFLL architecture against the scalar tracking configuration serving as benchmark, concerning both the navigation estimation and code/carrier tracking errors.

The articles published along this dissertation are listed below:

[Shytermeja et al., 2014] E. Shytermeja, A. Garcia-Pena and O. Julien, *Proposed architecture for integrity monitoring of a GNSS/MEMS system with a Fisheye camera in urban environment*, in Proceedings of International Conference on Localization and GNSS (ICL-GNSS), 2014, pp. 1–6.

[Shytermeja et al., 2016] E. Shytermeja, A. Garcia-Pena and O. Julien, *Performance Evaluation of VDFLL Architecture for a Dual Constellation L1/E1 GNSS Receiver in Challenging Environments*, in Proceedings of the 29th International Technical Meeting of The Satellite Division of the Institute of Navigation (ION GNSS+ 2016), Portland, US, Sep. 2016, pp. 404–416.

[Shytermeja et al., 2016] E. Shytermeja, A. Pena and O. Julien, *Performance Comparison of a proposed Vector Tracking architecture versus the Scalar configuration for a L1/E1 GPS/Galileo receiver*, in Proceedings of GNSS European Navigation Conference (ENC), Helsinki, Finland, May 2016.

[Shytermeja et al., 2017] E. Shytermeja, M.J. Pasnikowski, O. Julien and M.T. Lopez, *GNSS Quality of Service in Urban Environment*, Chapter 5 of Multi-Technology Positioning book, Springer International Publishing, Mar. 2017, pp. 79–105.

[Shytermeja et al., 2017] E. Shytermeja, A. Garcia-Pena and O. Julien, *Dual – constellation Vector Tracking Algorithm in Ionosphere and Multipath Conditions*, in Proceedings of International Technical Symposium on Navigation and Timing (ITSNT), Toulouse, France, Nov. 2017.

1.4. Thesis Outline

This dissertation is structured as follows.

Chapter 2 provides the description of GNSS system composition with the emphasis on the reference US GPS system and the under-development European Galileo constellation, as this research is conducted in the framework of a European-funded research project. In addition, the Open Service (OS) GNSS signals of interest are presented that are the GPS L1 C/A and Galileo E1-C pilot component. A great attention was given to the signal structure comprising the modulation scheme, the code rate and the power spectrum.

Chapter 3 synthetizes the GNSS receiver processing and is constituted of two main parts. Firstly, the measurement error sources are provided in details. The attention is directed to the description of the multipath error and the ionosphere propagation delay along with the Klobuchar (for GPS) and NeQuick (for Galileo) ionosphere correction models. Furthermore, the GNSS code and carrier measurement model along with the time correlation property of the atmospheric errors are detailed. Whereas, the second part of this chapter is dedicated to the receiver's analog and digital processing blocks. A particular attention is focalized to the description of the code (DLL) and carrier (PLL/FLL) tracking loops with an emphasis on the discriminator functions and their errors' analysis.

Chapter 4 presents the dual-constellation scalar GNSS navigation processor that represents the comparison standard with respect to the proposed vectorized architecture. The receiver's clock modelling for the dual-constellation operation mode is firstly introduced. The main part of this chapter

is dedicated to the design of two different navigation algorithms, namely the Weighted Least Square (WLS) and Extended Kalman Filter (EKF), for the dual-constellation single-frequency GPS/Galileo L1/E1 receiver. The WLS algorithm is described in details since it is employed at the initialization step only for both the scalar and vector tracking receivers. Afterwards, the EKF architecture is responsible for the navigation solution estimation. The EKF system model and the observation functions for the integration of the GNSS code pseudoranges and carrier pseudorange rate measurements are developed in details.

Chapter 5 describes the proposed vector tracking architecture to be used in signal-constrained environments. The chapter starts with the introduction of the VT architecture fundamentals in comparison to the conventional scalar tracking process and summarizes the pros and cons of the vector tracking algorithm along with a state-of-the-art of the research works in this field. In the second part, the VDFLL architecture aiming at the estimation of the ionosphere residuals is proposed. Then, the PVT state vector, augmented with the ionosphere residual errors from each tracked channel, is described. The adjustments of the process and measurement noise covariance matrixes as a result of the ionosphere residuals inclusion in the state vector are provided in the third part. This chapter concludes with the detailed formulation of the code and carrier NCO updates in the feedback loop, computed from the VDFLL EKF-estimation navigation solution.

Chapter 6 presents the developed dual-constellation GPS/Galileo emulator, incorporating the scalar and proposed vector tracking architectures. The modular implementation of the emulator's processing blocks starting from the loading of the user motion file and the tracking parameters up to the navigation modules are presented in the detailed block diagram in the first part of the chapter. Furthermore, the sliding-window C/N_0 estimation algorithm, adapted to the VDFLL and scalar tracking receiver update rate, along with the hot 1 second re-acquisition process initiated after the loss-of-lock detection in the scalar tracking architecture, are described in details. The essential part of this chapter is represented by the correlator output remodeling with the inclusion of the multipath data from the DLR urban channel model.

Chapter 7 provides the detailed performance assessment of the proposed dual-constellation single frequency VDFLL architecture in reference to the scalar tracking receiver in urban environment representative based on the results obtained from several simulation test scenarios. This performance analysis is performed in the system level, in terms of the user's navigation solution estimation accuracy in the vehicle frame and in the channel level, represented by the code delay and Doppler frequency estimation errors. The chapter first reminds the test setup by presenting the urban car trajectory and a summary of the two architectures differences regarding the tracking and navigation parameters. The first test aims at the validation of the VDFLL architecture capability in estimating the ionosphere residuals via Monte Carlo simulations. Then, the comparison is extended to the complete urban environment by adding the presence of multipath conditions and LOS blockages to the ionosphere residuals. Last but not least, the analysis is performed is severe urban conditions, characterized by a quite reduced number of observations, and including the performance assessment for the VDFLL architecture on satellite selection mode. The performance analysis is enhanced by the use of error statistics and distribution functions.

Chapter 8 draws conclusions based on the results obtained in this Ph.D. thesis and presents recommendations for research work topics that could be addressed in the future.

2. GNSS Signals Structure

Global navigation satellite systems refer to the navigation systems with global coverage capable of providing the user with a three-dimensional positioning and timing solution by radio signals ranging transmitted by orbiting satellites. The work conducted in this thesis focuses on the GNSS signal tracking and more precisely, on the advanced tracking techniques in signal-constrained environment. Therefore, the main objective of this chapter is the description of the GNSS signal structure.

In details, Section 2.1 introduces the GNSS system overview, including the space-, control- and user segment composition and a description of the individual systems.

Section 2.2 describes the GNSS signals structure with an emphasis on the GPS L1 C/A and Galileo E1 OS signals modulation and navigation data structure that will be later required in the following chapters.

Finally, the chapter conclusions will be drawn in Section 2.3.

2.1. GNSS System Overview

The fully operational GNSS systems are the Global Positioning System (GPS) developed by the USA and the Russian system GLObal Navigation Satellite System (GLONASS). Currently, there are also two navigation systems under deployment namely, the European Galileo and BeiDou developed by China.

A typical GNSS system is composed of three segments:

- the space segment
- the control segment
- the user segment

The first one (*the space segment*) is made by a constellation of satellites that transmit a signal used both as a ranging signal and as an information broadcasting signal. The *control segment* tracks and monitors each satellite, and uploads to the space segment the information to be broadcasted, e.g. its predictions of future satellite orbit parameters (ephemerides) and on-board atomic clock corrections. Finally, the *user segment* consists of all the ground receivers computing their own Position, Velocity and Time (PVT) computations from the reception of the space segment satellites' signals.

2.1.1. The Space Segment

The space segment comprises the satellites, organized collectively as a constellation, orbiting around Earth. The satellites broadcast high frequency (HF) signals in the L band towards the Earth that allow the receiver to estimate its 3-D position and time after processing the received signals. The already-deployed GNSS systems are the following:

- The US **GPS** system, declared fully operational in June of 1995, is the satellite-based navigation system developed by the U.S. Department of Defense under the NAVSTAR program launched in the late 80s [GPS.gov, 2013]. The GPS constellation currently consists of 31 healthy and operational satellites flying in Medium Earth Orbit (MEO) at an altitude of 20.200 km and located in 6 approximately circular orbital planes with a 55° inclination with respect to the equatorial axis and orbital periods of nearly half sidereal day [Kaplan and Hegarty, 2006]. The United States is committed to maintaining the availability of at least $21 + 3$ operational GPS satellites, 95% of the time. Each GPS satellite carries a cesium and/or rubidium atomic clock to provide timing information for the signals broadcasted by the satellites [GPS.gov, 2016];
- **GLONASS** is a space-based satellite navigation system with global coverage operated by the Russian Aerospace Defense Forces whose development began under the Soviet Union in 1976 and by 2010 achieved 100% coverage of the Russian territory [GLONASS, 2008]. In October 2011, the full orbital constellation of 24 satellites was restored, enabling full global coverage. The GLONASS constellation is composed of 24 satellites on three circular orbital planes at 19.100 km altitude and with a nearly 65° inclination [Navipedia-GLO, 2016];
- **Galileo** is the European global navigation satellite system that is still under deployment and its baseline design is expected to be composed of 30 satellites ($24 + 6$ spares) located on 3 MEO orbits at 23222 km altitude with a 56° inclination with respect to the equatorial axis [GSA, 2010]. Currently, the Galileo constellation is composed of 18 satellites after the last launch of 4 simultaneous satellite payloads from the Ariane 5 Launcher in November 2016. This system was designed with the principle of compatibility and interoperability with the GPS system based on the agreement signed by both parties in March 2006 [GPS.gov, 2006]. It is important to highlight the fact that Galileo will constitute the first satellite navigation system provided specifically for *civil purposes* [GSA, 2016];
- The **BeiDou** Navigation Satellite System (BDS) is the Chinese GNSS system, whose space segment in its final stage will be composed of 35 satellites, comprising 5 geostationary orbit satellites for backward compatibility with BeiDou-1, and 30 non-geostationary satellites (27 in MEO orbit and 3 in inclined geosynchronous orbit (GSO)) that will offer global coverage as well as a stronger coverage over China [Navipedia, 2016]. As a consequence, the BeiDou space segment composition totally differs from the other GNSS space segments due the inclusion of GeoSynchronous earth Orbit (GSO) or Geostationary Earth Orbit (GEO) satellites that in their initial design are intended for regional coverage. GSO orbit match the Earth rotation period on its axis while GEO can be considered as a particular case of GSO with zero inclination and zero eccentricity. All GEO satellites are orbiting at an altitude equal to 35786 km and seem fixed from the user's perspective on the Earth surface.

A summary of the four GNSS systems space segment parameters are summarized in Table 2-1.

Table 2-1. *Space segment parameters of the four GNSS constellations [GSA, 2010], [GPS.gov, 2013].*

Constellations	GPS	GALILEO	GLONASS	BeiDou
Political entity	United States	European Union	Russia	China
Orbital altitude	20 200 km (MEO)	23 222 km (MEO)	19 100 km (MEO)	21 528 km (MEO) 35 786 km (GEO GSO)
Orbit type	Circular			Circular for MEO Elliptical for GSO
Period	11 h 58 min 2 s	14 h 05 min	11 h 15 min	12 h 38 min
Number of orbital planes	6	3	3	3
Orbital Inclination	55°	56°	64.8°	55°
Number of nominal satellites	24	30	24	27 (MEO)+ 3 (GSO) + 5 (GEO)
Multiple Access	CDMA	CDMA	FDMA → CDMA*	CDMA
Center Frequencies [MHz]	L1(1575.42) L2(1227.60) L5(1176.45)	E1(1575.42) E6(1278.75) E5b (1207.14) E5a (1176.45)	L1 (1602) L2 (1246) L3 (1201)	B1 (1561.098) B1-2 (1589.742) B3(1268.52) B2(1207.14)
Datum	WGS-84	GTRF	PZ-90.11	CGCS2000
Reference time	GPS time	GST**	GLONASS time	BDT**

* GLONASS transition from FDMA toward CDMA in the third generation satellites (experimental CDMA payload in the GLONASS-M launch in June 2014) [Navipedia-GLO, 2016]
** GST = Galileo System Time
*** BDT = BeiDou System Time

The GNSS frequency plan along with the signals of interest structure description are provided in section 2.2.

2.1.2. The Control Segment

The GNSS control segment consists in a network of monitoring, master control and ground uplink stations responsible of the monitoring and reliability of the overall GNSS system. As a consequence, the control segment is composed of the following stations:

- *The monitoring or sensor stations*: typically consisting of a ground antenna, a dual-frequency receiver, dual atomic frequency standards, meteorological sensors and local workstations. They are responsible of performing several tasks, such as: navigation data demodulation, signal tracking, range and carrier measurement computation and atmospheric data collection. This data provided from the sensor station are further sent to the master control station;

- *The master control station*: provides the central command and GNSS constellation control and is in charge of: monitoring the satellite orbits along with the prediction/estimation of the satellite clock and ephemeris parameters; maintaining the satellite health status; generating the navigation messages; keeping the GNSS time and commanding satellite maneuvers especially in satellite vehicle failures [Kaplan and Hegarty, 2006];

- *The ground uplink stations:* is a globally distributed ground antenna network providing the Tracking, Telemetry & Control (TT&C) functions between the master control station and the space segment through the transmission in the S-band of the navigation data and payload control commands to each satellite in space.

2.1.3. The User Segment

This segment consists of the GNSS receiver units that are able to process the received satellite signals with the main objective of providing the PVT solution. A typical receiver is composed of three processing stages:

- *A RF front-end*: is the first stage of the signal processing chain starting from the receiver antenna that is typically not considered as part of the front-end stage. This stage includes the Low Noise Amplifier (LNA), the Intermediate Frequency (IF) down-converter, the IF band-pass filter, the Automatic Gain Control (AGC) and the quantization/sampling block. The output of this block is the discrete version of the received Signal-in-Space (SiS);

- *A signal processing unit*: in charge of signal acquisition and tracking to provide the required synchronization between the receiver-generated signal replica with the incoming GNSS signal;

- *A navigation module*: is the final processing block that is responsible for the navigation message demodulation, satellite position computation, pseudorange measurements computation, application of the appropriate corrections to the calculated measurements, and lastly computing the user's navigation solution.

The two first processing stages are described in more details in Chapter 3, while the navigation module description, without taking into account the navigation message demodulation process, is given in Chapter 4.

2.1.4. GNSS Services Description

GPS is the most known and worldwide used navigation system that provides two distinct services:

- *Standard Positioning Service (SPS)*, that is available free of charge for the civil community and represents the dominant worldwide used service [GPS.gov, 2008];

- *Precise Positioning Service (PPS)*, for authorized military and selected government users. The detailed performance levels definition concerning the military GPS service are found in [GPS.gov, 2007].

Similarly to GPS, the government-owned GLONASS and BeiDou systems also provide two levels of positioning services: open (public) and restricted (military). On the contrary, the only civilian GNSS system, referring to the European Galileo system, once fully operational will offer four high-performance worldwide services [GSA, 2016]:

- *Open Service (OS):* Open and free of charge service intended for 3-D positioning and timing;
- *Commercial Service (CS):* A service complementary to the OS by the provision of additional encrypted navigation signals and added-value services;
- *Public Regulated Service (PRS):* A service restricted to government-authorized users for sensitive applications with a high level of service continuity requirement;
- *Search and Rescue Service (SAR):* Europe's contribution to COSPAS-SARSAT, an international satellite-based search and rescue distress alert detection system.

2.2. GNSS Signal Structure

This subsection introduces the GNSS signal frequency plan with an emphasis on the signals of interest in this Ph.D. thesis, namely the GPS L1 C/A and Galileo E1C signals.

Satellite navigation signals are broadcasted in a frequency band allocated to the RNSS (Radio Navigation Satellite System). Only the GNSS signals that are intended to be used in the civil aviation domain, are broadcasted in the protected band for safety-of-life applications, referred to as the Aeronautical Radio Navigation Services (ARNS) frequency band. This frequency bands allocation is provided by International Telecommunication Union (ITU).

The GPS and Galileo signals frequency bands are illustrated in Figure 2-1. The signals of interest to this research work are allocated in the RNSS L1 band.

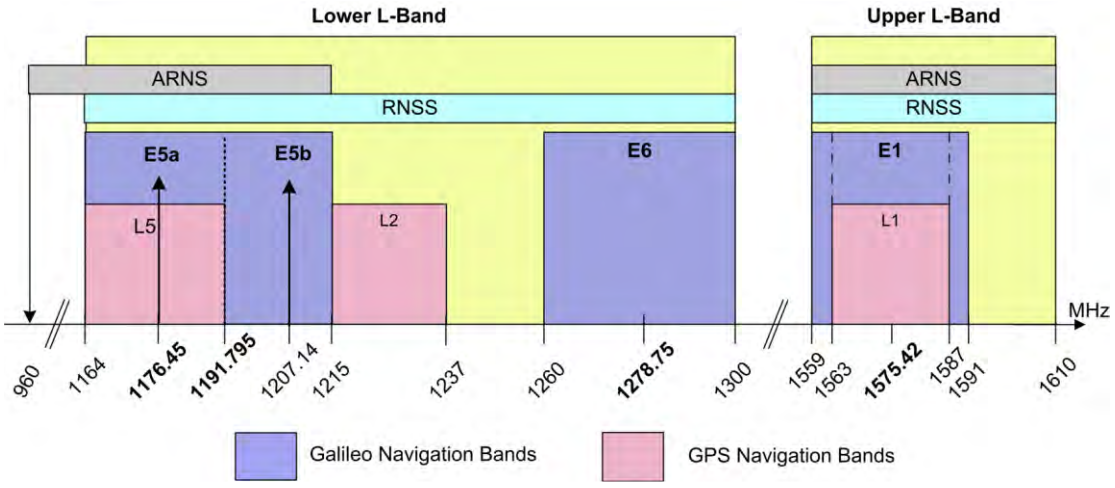

Figure 2-1. *GPS and Galileo navigation frequency plan [GSA, 2010]*.

2.2.1. Legacy GPS L1 Signal Structure

The transmitted GPS L1 C/A signals comprises three signal components, as depicted in Figure 2-2:

- The signal carrier centered at $f_{L1} = 1575.42\ MHz$ and transmitting the Binary Phase Shift Keying (BPSK) modulated signal;
- The spreading code waveform $c(t)$ referred to as the Pseudo-Random Noise (PRN) code sequence. The PRN code is constituted by a sequence of 1023 chips, repeated each $1\ ms$, finally providing a 1.023 Mchips per second rate. The PRN code is essential in the GNSS systems, since it permits the receiver to uniquely differentiate each emitting satellite and to allow the receiver to achieve synchronization with the incoming signals;
- The navigation data $d(t)$ consists of a ± 1 data stream at 50 bits per second rate.

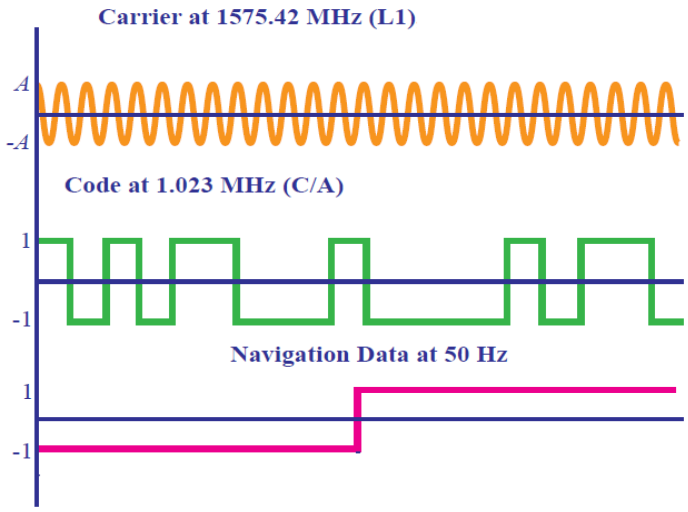

Figure 2-2. *GPS L1 C/A signal composition*.

GPS signals are currently transmitted using two PRN ranging codes:

- *the coarse/acquisition (C/A) code* that provides coarse ranging for civil applications and is also used for the acquisition of P(Y) code;
- *the precision (P) code*: a bi-phase modulated at a longer repetition period, intended for precision ranging for US military and US Department of Defense (DOD)-authorized users. The *P(Y)-code* is used whenever the anti-spoofing (AS) mode of operation is activated and encryption of the P-code is performed.

The GPS L1 signal, whose modulation scheme is given in Figure 2-3, consists of two carrier components that are in phase quadrature with each other. Each carrier component is Binary Phase Shift Keying (BPSK) modulated by a separate bit train. One bit train is the modulo-2 sum of the C/A code and the navigation data $d(t)$, while the other is the modulo-2 sum of the P(Y) code and the navigation data $d(t)$ [GPS.gov, 2013].

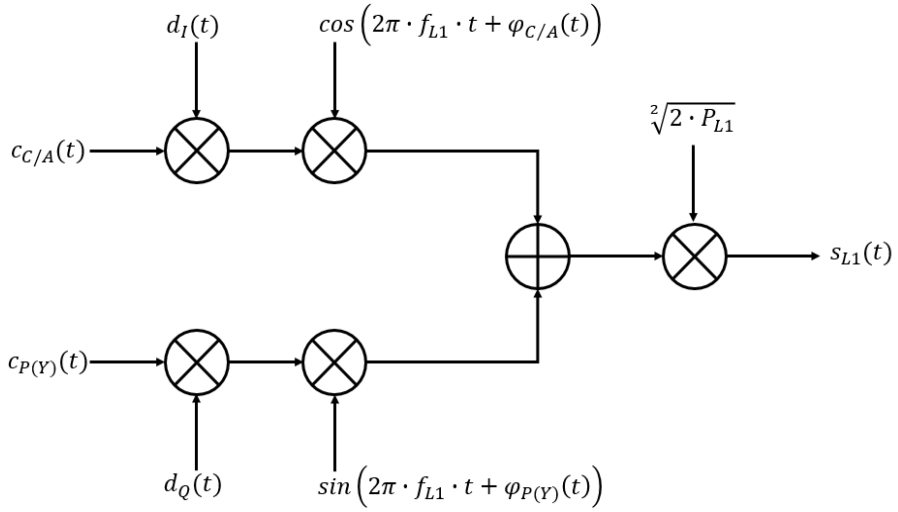

Figure 2-3. *Modulation scheme for the GPS L1 signal*.

Therefore, when neglecting the signal's Quadrature (Q) branch containing the $P(Y)$ code, the GPS L1 C/A signal can be written as:

$$s_{L1\,C/A}(t) = \sqrt[2]{2 \cdot P_{C/A}} \cdot c_{C/A}(t) \cdot d_I(t) \cdot \cos\left(2\pi \cdot f_{L1} \cdot t + \varphi_{C/A}(t)\right) \qquad (2\text{-}1)$$

Where:

- $P_{C/A} = \frac{A_{C/A}^2}{2}$ is the received GPS C/A signal power, where the symbol A denotes the signal amplitude;
- $c_{C/A}(t) = \pm 1$ represents the C/A PRN code sequence with a code chipping rate of $f_{c_{C/A}} = 1.023\ Mchips/s$;
- $d_I(t)$ represents the navigation data sequence for the In-Phase signal branch (C/A signal) at a 50 symbols/sec rate;
- f_{L1} is the L1 band carrier frequency $f_{L1} = 154 \cdot f_0 = 1575.42\ MHz$ where $f_0 = 10.23\ MHz$ is the on-board atomic clock frequency standard;
- $\varphi_{C/A}$ is the C/A time-varying carrier phase delay expressed in radians;

2.2.1.1. GPS L1 C/A Code description

The spreading code of the GPS L1 C/A signal is a pseudo-random noise sequence used to spread the signal spectrum over a wide frequency bandwidth, with respect to the bandwidth required to transmit the navigation data, accordingly to the Direct-Sequence Spread Spectrum (DSSS). The PRN code is different for each satellite and it allows the GPS L1 C/A receiver to differentiate among the different satellites transmitting at the same carrier frequency L1, based on the Code Division Multiple Access (CDMA) principle. The GPS L1 C/A PRN code of each satellite, used for satellite identification and thus, allowing the receiver to correctly differentiate among the different satellites transmitting at the same L1 carrier frequency, is a Gold code from the same Gold code family [Gold, 1967]. The choice of a Gold code is related to its good correlation property by means of autocorrelation peak isolation from the side peaks [Spilker et al., 1998]. As previously stated, each L1 C/A PRN code has a duration of $1\ ms$ at a chipping rate of $1023\ kbps$, meaning that each code has a length of $1023\ chips$ [GSA, 2010].

GPS L1 C/A PRN code is $BPSK(1)$-modulated, or pulse shaped as denoted in the communication field, which in the Navigation Satellite field means that:

- the PRN code chipping rate f_c is equal to $1 \times 1.023\ MHz$;
- $m(t)$ is a rectangular shaping waveform of one chip length, as depicted in green in Figure 2-2.

Knowing that the C/A code shaping waveform is rectangular, the repeating code sequence $c_{C/A}(t)$ can be modeled as [Gleason and Gebre-Egziabher, 2009]:

$$c_{C/A}(t) = \sum_{i=-\infty}^{+\infty} \left(\left(\sum_{k=1}^{N} c_k . rect_{T_C}\left(t - kT_C - \frac{T_C}{2}\right) \right) * \delta(t - iNT_C) \right) \quad (2\text{-}2)$$

Assuming that the C/A code is a very long code with random properties, the C/A code autocorrelation function can be approximated by a triangle function expressed as:

$$h_{NRZ}(t) = \begin{cases} 1 - \dfrac{\tau}{T_C} & if\ -T_C \le t \le T_C \\ 0 & elsewhere \end{cases} \quad (2\text{-}3)$$

The L1 C/A Power Spectral Density (PSD) can be approximated as the Fourier transform of the autocorrelation function expressed in Eq. (2-3). Therefore, the GPS C/A power spectrum density (PSD) can be approximated as:

$$G_{C/A}(f) = T_C \cdot \left(\frac{\sin\left(\frac{\pi \cdot f}{f_C}\right)}{\left(\frac{\pi \cdot f}{f_C}\right)} \right)^2 \quad (2\text{-}4)$$

The normalized code autocorrelation function and power spectrum density (PSD) of the GPS L1 C/A signal are illustrated in Figure 2-4.

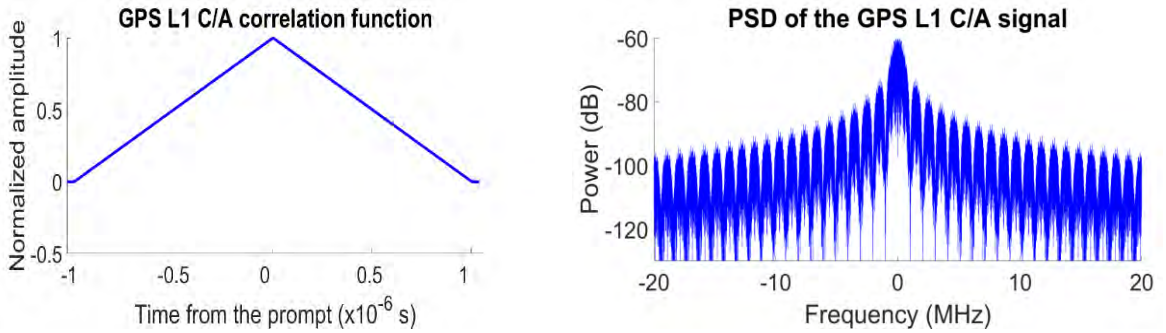

Figure 2-4. *Normalized code autocorrelation function (on the left) and normalized PSD (on the right) of the GPS L1 C/A signal [Pagot, 2016].*

2.2.1.2. GPS L1 C/A Navigation Message Structure

The navigation information message of the GPS L1 C/A signal is called the NAV message and is organized in a hierarchic structure. The NAV message is composed of super-frames where each one is constituted of 25 frames and each frame contains 1500 bits. Each frame is divided into five subframes, and each subframe consists of 10 words of 30 bits each, with the most significant bit (MSB) of the word transmitted first. At a 50 bps data transmission rate, the complete super-frame transmission requires 12.5 minutes.

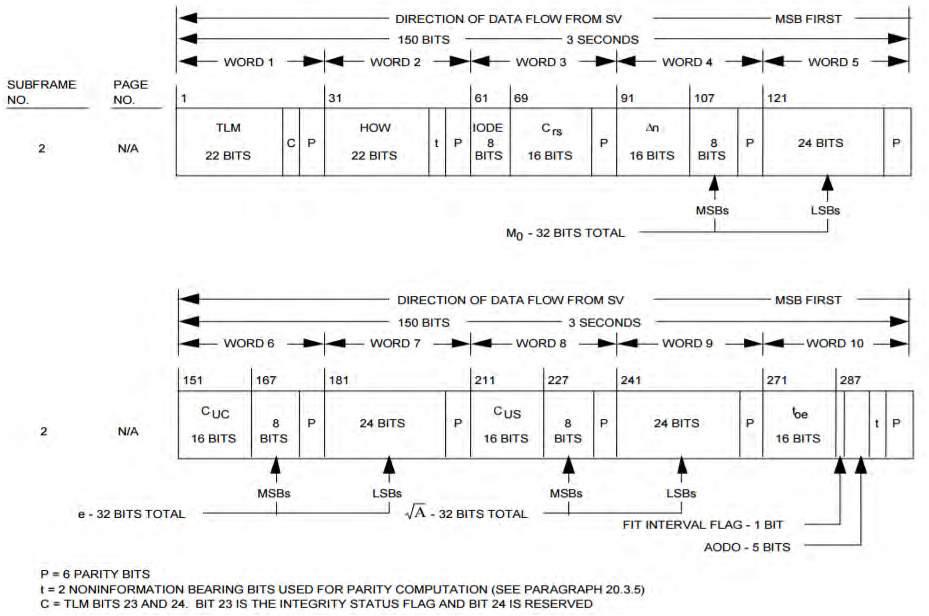

Figure 2-5. *The GPS L1 C/A navigation message structure [GPS.gov, 2013].*

The information placed in each subframe is given below [GPS.gov, 2013]:

- *Subframe 1*: includes the clock reference time t_{0c} as well as the satellite clock error parameters required for the satellite clock error correction, the ionospheric group delay T_{GD} for the ionospheric group delay error correction and the issue of the date and clock for each satellite;
- *Subframe 2 and 3*: contain the satellite ephemeris data with several hours validity, necessary for the precise satellite position and velocity computation;
- *Subframe 4*: containing the satellite almanacs, ionospheric correction terms and GPS-UTC time conversion coefficients for PRN 25 and higher;
- *Subframe 5*: includes the subframe 4 parameter for PRN 1 to 24.

2.2.2. Galileo E1 Open Service (OS) Signal Structure

Galileo E1 OS represents the first Galileo civilian signal intended for mass-market and safety-critical applications, which is the equivalent GPS L1 C/A signal for the Galileo system. Galileo E1 signals are broadcast on the same L1 center frequency as the GPS L1 signal and thus, enabling the use of the same antenna, front-end and receiver technology to simultaneously process the GPS L1 C/A & Galileo E1 signals.

2.2.2.1. Galileo E1 OS Code description

Within the scope of GPS & Galileo compatibility and interoperability and to reduce the mutual interference between the GPS L1 and Galileo E1 signals modulated over the same carrier frequency, the Galileo E1 signal spectrum is modified with respect to the GPS L1 C/A signal spectrum by introducing a sub-carrier element. The introduction of a subcarrier element is named in the Navigation Satellite field as the modification of the signal modulation or of the PRN code modulation. For Galileo E1 OS, the family of subcarriers being introduced is known as Binary Offset Carrier (BOC) modulation

and consists of two parameters: the sub-carrier frequency and spreading code rate. The implemented BOC modulation is denoted as $BOC(m,n)$ where the two integer parameters m and n represent:

- m: sub-carrier frequency in multiples of $1.023\ MHz$;
- n: code chipping rate in multiples of $1.023\ Mcps$ (Mchips per second).

In fact, both Galileo E1 OS and the modernized GPS L1C signals implement the Multiplexed BOC (MBOC)$(6,1,1/11)$ modulation, resulting from multiplexing the wideband BOC$(6,1)$ signal with the narrowband BOC$(1,1)$ signal, where $1/11$ of the power is allocated to the high frequency component [GSA, 2010]. The actual Galileo E1 OS signal implements a specific MBOC modulation, referred to as Composite BOC (CBOC)$(6,1,1/11)$, which adds or subtracts the BOC$(6,1)$ spreading symbols with the BOC$(1,1)$ [Avila-Rodriguez et al., 2006]. The Galileo E1 OS CBOC signal generation for both the data $E1-B$ and pilot $E1-C$ channels is illustrated in Figure 2-6.

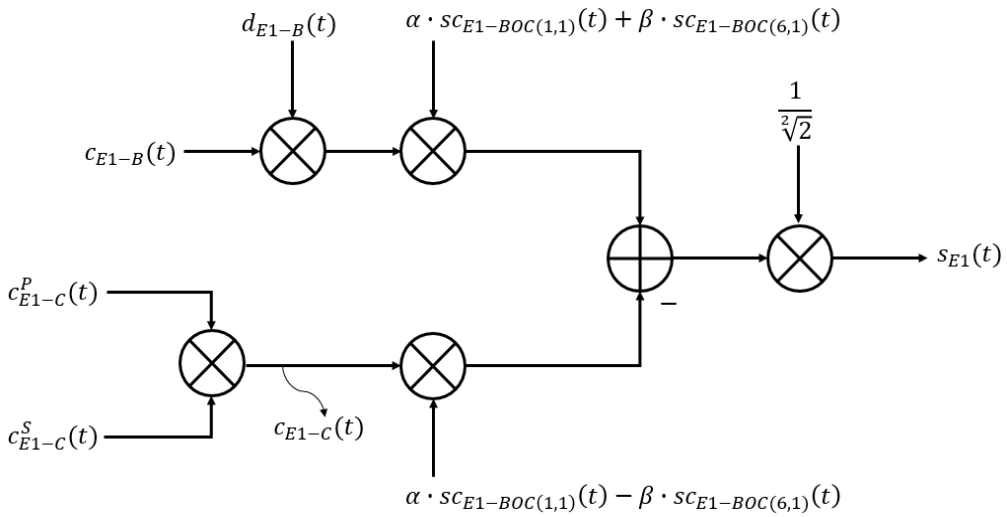

$\alpha = \sqrt[2]{\frac{10}{11}}$ and $\beta = \sqrt[2]{\frac{1}{11}}$.

Figure 2-6. *Modulation scheme for the Galileo E1 OS signal*.

Therefore, the E1 OS CBOC signal is generated according to Eq. (2-5):

$$\begin{aligned} s_{E1\,OS}(t) = \frac{1}{\sqrt[2]{2}} \cdot [&c_{E1-B}(t) \cdot d_{E1-B}(t) \cdot CBOC(6,1,1/11,'+') \\ &- c^P_{E1-C}(t) \cdot c^S_{E1-C}(t) \cdot CBOC(6,1,1/11,'-')] \\ &\cdot \cos\left(2\pi \cdot f_{L1} \cdot t + \varphi_{E1-OS}(t)\right) \end{aligned} \qquad (2\text{-}5)$$

- Where, Galileo E1 OS sub-carriers for the E1-B data and E1-C pilot channels, are respectively defined as:

E1-B data: $$CBOC(6,1,1/11,'+') = \sqrt[2]{\frac{10}{11}} sc_{BOC(1,1)}(t) + \sqrt[2]{\frac{1}{11}} sc_{BOC(6,1)}(t)$$

E1-C pilot: $$CBOC(6,1,1/11,'-') = \sqrt[2]{\frac{10}{11}} sc_{BOC(1,1)}(t) - \sqrt[2]{\frac{1}{11}} sc_{BOC(6,1)}(t) \qquad (2\text{-}6)$$

with BOC sub-carrier given by: $sc_{BOC(X,1)} = sign\left(\sin\left(2\pi \cdot R_{s,X} \cdot t\right)\right)$ for $R_{s,X} = X \cdot 1.023 \cdot 10^{-6}$ chips/s;

- $c_{E1-B}(t)$ and $c_{E1-C}^{P}(t)$ are the code spreading sequences carried by the data and pilot E1 OS components, respectively. Both these code sequences have a length of 4092 chips and a chipping rate equal to 1.023 Mega-chips per second (Mcps);
- $d_{E1-B}(t)$ represents the I/NAV navigation message modulating the data component at 250 symbols per second (sps);
- $c_{E1-C}^{S}(t)$ denotes the secondary code on the pilot component, having a length of 25 chips and a rate of 250 chips per second;
- $\varphi_{E1-OS}(t)$ is the E1 carrier phase offset.

For the E1C (pilot) and E1B (data) components, the $CBOC(6,1,1/11)$ autocorrelation function can be expressed by means of $BOC(1,1)$ and $BOC(6,1)$ autocorrelation and cross-correlation functions combination as [Julien et al., 2006]:

$$R_{CBOC(6,1,1/11,'+/-')}(\tau) = \frac{10}{11}\cdot R_{BOC(1,1)}(\tau) + \frac{1}{11}\cdot R_{BOC(6,1)}(\tau) \pm 2\cdot\frac{\sqrt[2]{10}}{11}\cdot R_{BOC(1,1)/BOC(6,1)}(\tau) \quad (2\text{-}7)$$

where the $\pm$ sign for the cross-correlation term refers to the E1-B (data) and E1-C (pilot) channels, respectively.

In this thesis, only the Galileo E1C or pilot component that employs the $(CBOC(6,1,1/11\,,-)$ modulation, will be treated as it is known that it provides better tracking performance [Paonni et al., 2010]. Figure 2-7 illustrates the normalized PSD and autocorrelation function of the Galileo E1-C signal for finite PRN code sequences.

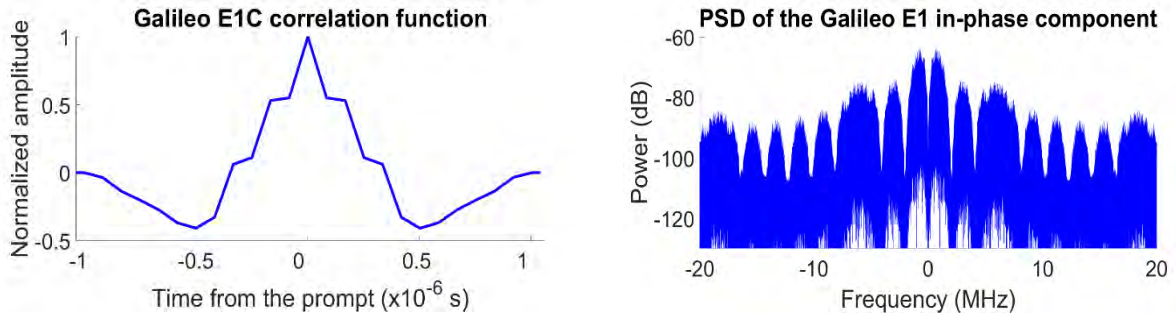

Figure 2-7. *Normalized code autocorrelation function (on the left) and normalized PSD (on the right) of the Galileo E1-C signal [Pagot, 2016].*

2.2.2.2. Galileo E1-B Navigation Message Structure

The Galileo signal data channels transmit three different message types according to the Galileo services, such as: the freely available navigation (F/NAV) message for the OS, the integrity navigation message (I/NAV) corresponding to the OS and Safety-of-Life (SoL) services and lastly, the commercial navigation (C/NAV) message associated to the Commercial Service (CS), as provided in Table 2-2:

Table 2-2. *Galileo navigation message types* [GSA, 2010].

Message Type	Service	Signal Component
F/NAV	OS	E5a-I
I/NAV	OS/SoL	E1-B and E5b-I
C/NAV	CS	E6-B

The I/NAV message, carried by the E1-B OS signal and shown in blue in Table 2-2, consists of one frame that is divided into subframes, where each subframe is also divided into 15 pages, as illustrated in Figure 2-8.

T_0 (GST_0 sync.) (s)	E1-B Content						E1-B Page	E1B Sub frame ID
0	Spare Word (2/2)	Res	SAR	Spare	CRC	Res	Odd	N-1
1	Word 2 (1/2)						Even	N
2	Word 2 (2/2)	Res	SAR	Spare	CRC	Res	Odd	N
3	Word 4 (1/2)						Even	N
4	Word 4 (2/2)	Res	SAR	Spare	CRC	Res	Odd	N
5	Word 6 (1/2)						Even	N

Figure 2-8. *Galileo E1-B subframe structure [GSA, 2010].*

As it can be observed, the pages are transmitted in two parts. The first part is denoted “even”, illustrated in red, while the second part is denoted “odd”, depicted in blue. The data field is composed of a word of 128 bits (112 bits in the even page + 16 bits in the odd page), as described in details in [GSA, 2010].

2.2.3. Summary of the Signals of Interest

Table 2-3 aims at providing an overview of the GPS and Galileo signals of interest in terms of modulation scheme, occupied band, code and data rate. The other GPS and Galileo signals are not described because they will not be used in this thesis.

Table 2-3. *Space segment parameters of the signals of interest.*

Constellations	**GPS**	**GALILEO**	
Signal Band	L1	E1	
Signal	L1 C/A	E1-B	E1-C
Carrier frequency (MHz)	1575.420		
Bandwidth (MHz)	24.552		
Polarization	Right Hand Circular Polarized (RHCP)		
Modulation scheme	$BPSK(1)$	$CBOC(6,1,1/11,+)$	$CBOC(6,1,1/11,-)$

Navigation data	ON	ON	OFF
Navigation Data (sps^*)	50	250	Pilot
Spectral occupation – main lobes (MHz)	2.046	4.092	4.092
Spreading code rate $(Mcps^*)$	1.023		
Primary code length $(chip)$	1023	4092	4092
Primary code duration (ms)	1	4	4
Secondary code length	No	No	25
* sps = symbols per second * Mcps = Mega chips per second			

2.3. Conclusions

In this chapter, a general overview of the GNSS systems and signals was presented. This chapter started with the description of the GNSS system composition for both the fully operational and under-deployment GNSS systems. Among all GNSS constellations, the focus is directed toward two of them, namely the United State GPS constellation and the European Galileo constellation, as this work is performed in the framework of a European-funded research project.

The attention was directed to the signal structure comprising the modulation scheme, code rate, spectrum properties of the two signals of interest being the GPS L1 C/A and Galileo E1-C (pilot) signals that are later considered in the signal processing and navigation algorithm sections.

3. GNSS Receiver Processing

This chapter aims at providing a clear description of the GNSS receiver structure and more particularly its typical signal processing stage beginning from the GNSS SiS reception by the receiver's antenna, up to the measurement generation stage. This chapter is composed of two main sub-sections such as: the GNSS measurement errors and the GNSS receiver architecture.

A division between the signal propagation delays and the measurement errors affecting the tracking loops is envisaged. First of all, the main sources causing the GNSS signal propagation delays including the satellite and receiver clock delays, the atmosphere-induced delays (comprising the ionosphere and troposphere contributions) are discussed in section 3.1. In this section, the focus is directed to the description of the Klobuchar and NeQuick correction models, respectively for the GPS L1 and Galileo E1 signals, along with the formulation of the ionosphere residual variances.

Then, section 3.2 describes in details the major error sources affecting the code/carrier tracking loops, with an emphasis on multipath and receiver thermal noise. Furthermore, the oscillator phase and frequency PSDs based on the Allan variance model are also herein defined. The correlation in-time property of ionosphere and troposphere residual errors are summarized in section 3.3.

Section 3.4.1 briefly describes the receiver's analog section also known as the RF front-end. The main part of this chapter is dedicated to the digital receiver's processing stage in section 3.5, comprising the generation of the correlator outputs, the acquisition stage and finalizing with the code and carrier tracking loops. The focus is directed to the analysis of the code and carrier tracking process, aiming at the formulation of the code delay, carrier frequency/phase errors variance in the presence of thermal noise since they are later employed in the measurement covariance matrix inside the navigation algorithm.

Finally, the chapter conclusions will be drawn in section 3.6.

3.1. GNSS Signal Propagation Delays

This section details the main sources introducing delays to the GNSS Signal-in-Space (SiS) along with the description of the models employed to estimate and further mitigate these induced delays.

3.1.1. Satellite Clock Delay

GNSS signal transmission time from each satellite is directly controlled by the atomic clocks on board of the space vehicle. Even though atomic clocks are used for their high frequency stability, clock error deviations between the satellite time and the GPS reference time drift slowly. The Master Control Station (MCS) on ground thus models the onboard clock deviation with respect to the GPS reference time using a quadratic polynomial in time, whose coefficients are transmitted to the user through the navigation message. The satellite clock correction model for each satellite in view i is provided as follows [Grewal et al., 2007] and [Kaplan and Hegarty, 2006]:

$$\varepsilon_{sv,i} = a_{f_0,i} + a_{f_1,i} \cdot \left(t_{sv,i} - t_{0c}\right) + a_{f_2,i} \cdot \left(t_{sv,i} - t_{0c}\right)^2 + \delta t_R \qquad (3\text{-}1)$$

where:

- $a_{f_0,i}$ denotes the clock bias for the i^{th} satellite vehicle in units of $[s]$;
- $a_{f_1,i}$ denotes the clock drift for the i^{th} satellite vehicle in units of $[s/s]$;
- $a_{f_2,i}$ denotes the clock frequency drift (aging) for the i^{th} satellite vehicle in units of $[s/s^2]$;
- $t_{sv,i}$ is the current time epoch of the i^{th} satellite vehicle expressed in $[s]$;
- t_{oc} is the clock data reference time broadcasted in the navigation message and expressed also in $[s]$;
- δt_R is a small relativistic clock error caused by the orbital eccentricity in units of $[s]$.

The above-described polynomial model is valid for a time interval of $4 - 6$ hours [Grewal et al., 2007]. The residual satellite clock error (after correction) thus depends on the satellite clock stability, the control segment network and the corrections latency. Therefore, the residual satellite clock error decreases with more stable atomic clocks on board of the space vehicles and with improved models computed by the control segment. The residual satellite clock error results in a ranging error that typically vary from 0.3 to 4 m depending on the type of the satellite and the age of the broadcasted data. More precisely, the residual clock error slowly degrades over time until the next upload. At zero age of data (ZOAD), clock errors for a typical satellite are on the order of 0.8m [Kaplan and Hegarty, 2006]. The nominal 1-sigma (1σ) clock error over AOD is in the level of 1.1 m, based on the data presented in [Taylor and Barnes, 2005] and [Dieter et al., 2003].

3.1.2. Satellite Ephemeris Error

In fact, this term is not a part of the propagation time delay but appears in the pseudorange error budget, which will be provided at the end of this section. However since in the literature, the satellite clock and ephemeris errors are jointly represented as a single term, a brief description will be provided in this sub-section.

The satellite ephemeris delay results from the mismatch between the satellite actual position and its predicted position from the satellites ephemeris broadcasted in the navigation message. The satellite ephemeris are generated using curve fitting of the control's segment best prediction of each satellite position at the time of upload. The ephemeris error is therefore caused by the satellite orbit prediction error and exhibits typical magnitudes of $1 \div 6\ m$. The effective pseudorange and carrier-phase errors due to the satellite ephemeris errors are obtained by projecting the satellite position error vector onto the satellite-to-user line-of-sight (LOS) vectors. The effective pseudorange or carrier-phase error due to ephemeris prediction errors is on the order of $0.8\ m\ (1\sigma)$ [Kaplan and Hegarty, 2006].

User Range Accuracy (URA) for GPS system and Signal-in-Space Accuracy (SISA) for Galileo, are a statistical indicator of the GNSS ranging accuracy due to satellite clock and ephemeris errors. In other words, assuming that these errors are modelled as zero mean Gaussian random variables, the standard deviation of these errors are assumed represented by the URA or SISA parameter that are broadcasted in the navigation message. The integrity performance requirement, in [GSA, 2010], specifies a SISA value, for both nominal and degraded mode of $\sigma_{sv/eph} = 0.85\ m$.

3.1.3. Ionospheric Propagation Delay

The ionosphere is a dispersive medium located approximately from 70 to 1000 km above the Earth surface and is composed of free ions and electrons that directly influence the GNSS signal propagation. The ionosphere layer has an opposite effect on the code (pseudorange) and carrier phase measurements, resulting in a group delay of the code measurement (Δ_c) and a phase advance (Δ_Φ) of the same magnitude but opposite sign as given in Eq. (3-2). The ionosphere-induced propagation delay, is a function of the time of the day, satellite elevation, user position, season, solar activity and scintillations [Kaplan and Hegarty, 2006]. This extra path delay on the code pseudorange (Δ_c) and carrier phase measurement (Δ_Φ) can be modeled by:

$$\Delta_c = -\Delta_\Phi \approx \frac{40.3 \times TEC}{f^2} \qquad (3\text{-}2)$$

where:

- f is the signal carrier frequency in $[Hz]$;
- The total electron content (TEC) is the electron density along the path length expressed in units of TEC units (TECU) where $1\ TECU = 10^{16}\ electrons/m^2$;

In order to model the dependence of the ionospheric delay with the satellite elevation, it is also possible to approximate the ionospheric delay using:

$$\varepsilon_{iono}(t) \approx -F_{pp} \cdot \frac{40.3 \times TEC}{f^2} \qquad (3\text{-}3)$$

where F_{pp} denotes the obliquity factor, also referred to as the mapping function, that is strictly dependent on the satellite elevation angle and the height of the maximum electron density.

Different models are employed to estimate the ionospheric delays and further mitigate the ionospheric-induced errors such as:

- *Single-frequency GPS receivers:* use the Klobuchar model for the ionospheric delay estimation, whose parameters are transmitted in the navigation message [Klobuchar, 1987]. The Klobuchar model removes about 50 % of the ionospheric delay error at the mid-latitudes [Kaplan and Hegarty, 2006].
    - A more efficient technique performing the ionospheric error correction is the International GPS Service that publishes a global TEC map for all the users around the world. The IGS model, possible only in post processing, requires the users to calculate the ionospheric delay from their own TEC. This model is proven to reduce at least 80 % of the ionospheric error;
- *Single-frequency Galileo receivers*: use the NeQuick ionospheric model, provided through the Galileo navigation message, represents a tridimensional and time-dependent ionospheric electron density model, which provides the electron density along any ray path as a function of the position and time [Di Giovanni and Radicella, 1990];
- *Dual-frequency iono-free combination*: exploiting the frequency-dependent characteristic of the ionospheric delay. Therefore, the first order ionospheric delay can be totally removed by combining measurements on two different frequencies from the same satellite.

3.1.3.1. Single-frequency GPS Ionosphere error correction

Most single-frequency GPS receivers use the Klobuchar model to correct the ionospheric delay that uses the α and β parameters, transmitted in the navigation message, to compute the ionospheric delay's amplitude and period.

The standard deviation of the ionospheric residual error $\sigma_{iono,L1}$ for the single-frequency GPS L1 signal is computed as follows [Klobuchar, 1987] [RTCA, 2006]:

$$\sigma_{iono,L1} = F \cdot \tau_{iono-vert,L1} \tag{3-4}$$

where:

- F is the mapping function that scales the ionospheric delay estimated for signals arriving at the zenith to the other elevation angles θ:

$$F = 1.0 + 16 \cdot \left(0.53 - \frac{\theta}{\pi}\right)^3 \tag{3-5}$$

- $\tau_{iono-vert,L1}$ is the minimum standard deviation of ionospheric vertical error in $[m]$ and related to the receiver's geomagnetic latitude φ_m by the following expression:

$$\tau_{iono-vert,L1} = \begin{cases} 9\ m = 0 & \leq [\varphi_m] \leq 20 \\ 4.5\ m = 20 \leq [\varphi_m] \leq 55 \\ 6\ m = 55 \leq [\varphi_m] \end{cases} \tag{3-6}$$

Thus, the standard deviation of the ionospheric residual error $\sigma_{iono,L1}$ is given by:

$$\sigma_{iono,L1} = \begin{cases} F \cdot 9 & 0 \leq [\varphi_m] \leq 20 \\ F \cdot 4.5 & 20 \leq [\varphi_m] \leq 55 \\ F \cdot 6 & 55 \leq [\varphi_m] \end{cases} \tag{3-7}$$

3.1.3.2. Single-frequency Galileo Ionosphere error correction

Galileo single-frequency receivers are capable of counteracting with the errors induced by the ionospheric propagation delay using the Galileo single-frequency NeQuick model, which is a tridimensional and time-dependent ionospheric electron density model that provides the electron density along any ray path as a function of the position and time [European Commission, 2016]. This technique consists in deriving real-time ionospheric delay predictions based on the Effective Ionization level A_z, determined as specified in the Galileo OS SIS ICD [GSA, 2010]:

$$A_z = a_{i0} + a_{i1} \cdot MODIP + a_{i2} \cdot MODIP^2 \tag{3-8}$$

where:

- (a_{i0}, a_{i1}, a_{i2}) are the effective ionization level 1st, 2nd and 3rd parameters, respectively, broadcasted in the Galileo navigation message;
- $MODIP$ is a table grid expressed in degrees that defines five ionospheric disturbance flags for the Region 1 to 5 according to the geomagnetic field, as shown:

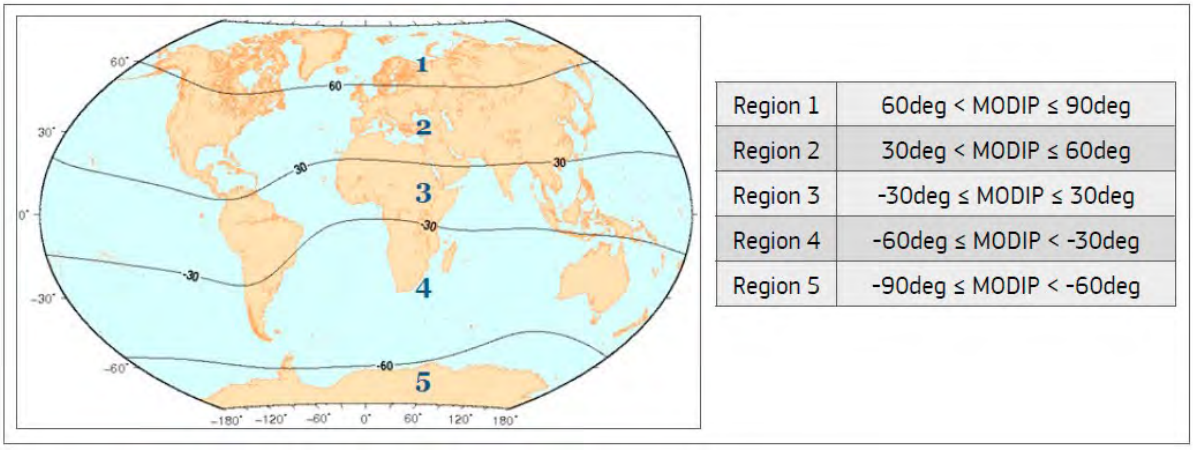

Region 1	60deg < MODIP ≤ 90deg
Region 2	30deg < MODIP ≤ 60deg
Region 3	-30deg ≤ MODIP ≤ 30deg
Region 4	-60deg ≤ MODIP < -30deg
Region 5	-90deg ≤ MODIP < -60deg

Figure 3-1. *MODIP regions associated to the table grid [European Commission, 2016].*

The receiver then calculates the integrated Slant Total Electron Content along the path using the *NeQuick* model and converts it to the slant delay as follows [European Commission, 2016]:

$$d_{Igr} = \frac{40.3}{f^2} \cdot \int N \cdot dl = \frac{40.3}{f^2} \cdot 10^4 \cdot STEC \; [m] \tag{3-9}$$

where:

- d_{Igr} is the ionospheric group delay expressed in $[m]$;
- f is the E1 OS carrier frequency in $[Hz]$;
- N is the electron density in $[electrons/m^3]$;
- $STEC$ is the Slant Total Electron Content in $[electrons/m^2]$;

In this work, instead of estimating the data series of the ionospheric delay d_{Igr}, a simplified NeQuick model is implemented, which consists in approximating the STEC value as the Vertical TEC (VTEC) scaled by the mapping function F of Eq. (3-5) as follows:

$$STEC_{NeQuick} \approx F \cdot VTEC \tag{3-10}$$

where VTEC presents daily variations, depending on the solar cycle phase, with the maximum peak during day time and the minimum at night. The Galileo test receiver requirements specify that the ionosphere residual error standard deviation of the single-frequency receiver must not exceed the first-order delay of $20\ TEC$ units STEC, or the $30\ \%$ of the delay magnitude, whichever is larger as stated in [Salos, 2012]:

$$\sigma_{iono-E1} = \begin{cases} \frac{40.3}{f^2} \cdot 10^4 \cdot 0.3 \cdot F \cdot VTEC & if\ STEC = F \cdot VTEC \geq 66.7 \\ \frac{40.3}{f^2} \cdot 10^4 \cdot 20 & if\ STEC = F \cdot VTEC < 66.7 \end{cases} \tag{3-11}$$

In order to compute the ionospheric residual error, the VTEC position grid from the IGS VTEC database is converted into geomagnetic latitude using Klobuchar conversion formula.

3.1.3.3. Dual-frequency iono-free combination

This approach exploits the frequency-dependent characteristic of the ionospheric delay and consists on combining the code measurements from two different frequencies to build a iono-free pseudorange measurement as:

$$\rho_{iono-free} = c_1 \cdot \rho_1 + c_2 \cdot \rho_2 \quad (3\text{-}12)$$

Where:

- $\rho_{iono-free}$ is the iono-free pseudorange measurement;
- ρ_1, ρ_2 are the pseudorange measurements at the frequency band 1 and 2, respectively;
- c_1, c_2 are the combination coefficients, computed as:

$$c_1 = \frac{f_1^2}{f_1^2 - f_2^2}$$
$$c_2 = \frac{f_2^2}{f_2^2 - f_1^2} \quad (3\text{-}13)$$

where f_1, f_2 denote the carrier frequency of the frequency band 1 and 2, respectively.

The dual-frequency combination totally removes the first order ionospheric delay but leaving the high order terms that have an insignificant effect on the code/phase measurements compared to the other error sources. However in this research work, the dual-frequency iono-free combination is not implemented since this work aims at the development of the dual-constellation single-frequency vector tracking receiver.

3.1.4. Tropospheric Propagation Delay

The troposphere is the lower part of the atmosphere, extended up to 70 km over the Earth's surface, and is a non-dispersive medium for frequencies up to 15 GHz. The tropospheric delay is a function of the tropospheric refractive index, which is dependent upon the local temperature, pressure, and relative humidity [Kaplan and Hegarty, 2006].

The tropospheric delay is modelled as having a wet component and a dry component. The wet component, arising from water-vapor content variation, is difficult to be modelled but accounts for approximately 10% of the tropospheric delay. The dry component is relatively well modeled and accounts for approximately 90% of the tropospheric delay [Farrell, 1998]. A tropospheric model employed for the tropospheric code delay correction is specified for the civil aviation GNSS receivers. The standard deviation of the tropospheric residual error is defined as the product of the vertical error standard deviation $\sigma_{tropo,v}$ and the mapping function F_{tropo} that depends on the satellite's elevation angle θ, as follows [ICAO, 2006] and [EUROCAE, 2010]:

$$\sigma_{tropo} = F_{tropo} \cdot \sigma_{tropo,v} \quad (3\text{-}14)$$

Where:

$$F_{tropo} = \begin{cases} \dfrac{1.001}{\sqrt[2]{0.002001 + \sin^2\theta}} & for\ \theta \geq 4^\circ \\ \dfrac{1.001}{\sqrt[2]{0.002001 + \sin^2\theta}} \cdot (1 + 0.015 \cdot (4 - \theta)^2)\ for\ 2^\circ \leq \theta < 4^\circ \end{cases} \quad (3\text{-}15)$$

with $\sigma_{tropo,v} = 0.12\ m$.

3.2. Sources of Errors Affecting the GNSS Receiver Synchronization Capability

After detailing the atmospheric effect on the signal propagation delay, the attention is now directed to the GNSS measurement errors that can significantly degrade the signal tracking performance. Indeed, the impact of the atmospheric sources on the signal propagation time do not seriously affect the tracking loops behavior except for the occurrence of very high ionospheric or tropospheric activity. The main errors' sources that affect the GNSS receiver synchronization capability are the following:

- Multipath,
- Receiver noise and dynamics,
- Signal interference.

3.2.1. Multipath Error

Multipath is an environment-dependent phenomenon defined as the reception of reflected and/or diffracted replicas of the desired LOS GNSS signal due to the presence of obstacles encountered in the receiver surroundings. On the receiver side, signals interference is observed between the direct path or LOS signal that corresponds to the true geometric satellite-receiver distance and the reflected/diffracted echoes. Since the path traveled by a reflection is always longer than the direct path, multipath arrivals are delayed with respect to the direct path. Multipath errors vary significantly in magnitude depending on the environment within which the receiver is located, satellite elevation angle, receiver signal processing, antenna gain pattern, and signal characteristics [Kaplan and Hegarty, 2006]. In fact, the nature of the reflective source has a great influence on the multipath amplitude, delay and phase. Multipath represents the major pseudorange error source in urban environment that if not properly de-weighted or mitigated, are further projected in the position estimation domain.
Beside the phenomenon of reflection and diffraction, the direct signal path is also subject to the shadowing effect. Indeed, shadowing represents the excess attenuation of the direct path, typically introduced when the direct path propagates through foliage or a structure. The shadowing of the direct path and multipath have combined effects on the relative amplitudes of direct path and the multipath echoes. In some cases, shadowing of the direct path may be so severe that the receiver can only track the multipath echoes, referred to as *Non Line-of-Sight (NLOS) signal* reception. The error introduced by multipath echoes depends upon their delays, but also their power and carrier phase relative to the one of the direct path [Parkinson, 1996]. The received carrier phase of the multipath-affected signal has also a direct influence on the degree and character of the distortion.

When no multipath is present, the received noiseless waveform at the antenna input is described in analytical form by:

$$s(t) = a_0 \cdot x(t - \tau_0) \cdot e^{-j\varphi_0} \qquad (3\text{-}16)$$

where:

- $x(t)$ is the complex envelope of the transmitted signal;
- τ_0 is the satellite-receiver signal propagation time;
- φ_0 is the received signal phase in $[rad]$.

Then, a simple model for the complex envelope of a received signal with multipath, neglecting the noise and interference contributions, at the antenna input is provided as follows:

$$r(t) = a_0 \cdot x(t - \tau_0) \cdot e^{-j\varphi_0} + \sum_{n=1}^{N} a_n \cdot x(t - \tau_n) \cdot e^{-j\varphi_n} \quad (3\text{-}17)$$

where:

- N denotes the total number of received multipath echoes;
- (a_0, τ_0, φ_0) denotes the amplitude, propagation delay and phase of the received direct path;
- (a_n, τ_n, φ_n) denotes the amplitude, propagation delay and phase of the received multipath echoes;

The expression in Eq. (3-17) can be rewritten using the parameters relating the multipath echoes to the direct path as:

$$r(t) = a_0 \cdot \left[x(t - \tau_0) \cdot e^{-j\tilde{\varphi}_0} + \sum_{n=1}^{N} \tilde{a}_n \cdot e^{-j\tilde{\varphi}_n} \cdot x(t - \tau_0 - \tilde{\tau}_n) \right] \quad (3\text{-}18)$$

where:

- $\tilde{a}_n = a_n / a_0$ is the multipath-to-direct ratio (MDR) of the amplitudes;
- $\tilde{\tau}_n = \tau_n - \tau_0$ is the excess delay of the multipath echoes;
- $\tilde{\varphi}_n$ is the phase of each multipath echo.

In the GNSS context, multipath has a great effect on the signal's code and carrier tracking accuracies, which will be detailed in the following section.

3.2.2. Receiver Noise

3.2.2.1. Thermal Noise

The thermal noise is present at the receiver front-end and perturbs the code and carrier tracking process, causing pseudorange and pseudorange rate errors. It is assumed to be modelled by a zero-mean white Gaussian distribution with the PSD computed as:

$$N_0 = k_B \cdot T_{sys} \quad (3\text{-}19)$$

where:

- $k_B = -228.6\ dBW/K/Hz$ is the Boltzmann constant;
- T_{sys} is the system noise temperature defined through the Friis formula and depending on the front-end architecture, in specifics the filters and Low Noise Amplifier (LNA).

For a typical receiver, it is common to assume that the noise PSD $N_0 = -201.5\ dBW/Hz$ [Julien, 2006].

3.2.2.2. Oscillator Phase Noise Model

This error originates from the deviation of receiver oscillator from its nominal frequency and is modelled for both the satellite and receiver clock. The satellite's oscillator error results in a timing

error δt_{s_Osc} w.r.t to the GPS time. In a similar manner at the receiver level, the receiver's oscillator noise impacts the local replica generation, resulting in a timing error δt_{Rx_Osc} that cause errors on the code and phase measurements during the tracking process. The oscillator phase error has a greater impact on the carrier phase tracking compared to the code tracking process, due to the shorter carrier wavelength w.r.t the code chip length [Parkinson, 1996].

The satellite clock modelling can be realized by two distinct approaches. The first technique consists in modelling the satellite clock error through the three parameters $(a_{f_0}, a_{f_1}, a_{f_2})$, reflecting the clock bias, drift and aging, which are sent by each satellite in-view i in the ephemeris data, as presented in Eq. (3-1). However, this modelling provides a very stable satellite clock error that does not affect the code/carrier tracking loops [Julien et al., 2004]. Therefore, a second approach that models the satellite oscillator phase noise has been proposed in the literature [Grewal et al., 2007], [Parkinson, 1996]. This method, generating the oscillator phase noise based on a system of differential equations, is proposed in [Winkel, 2003] and is valid for both the satellite and receiver clock error modelling.

The receiver oscillator noise can be modelled as consisting of two state models such as the phase and frequency error terms. The frequency error state is modeled as a random walk process coming after integrating a white noise term. Whereas, the phase error state is modeled as the integral of the frequency error after adding another white noise term (independent from the white noise of the frequency error) [Grewal et al., 2007].

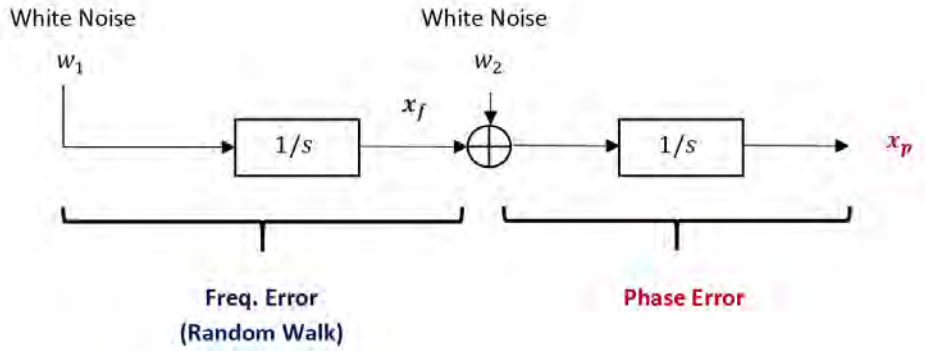

Figure 3-2. *The receiver oscillator error model comprising the clock frequency x_f and phase x_p components.*

The oscillator noise model in the continuous time domain, given in Figure 3-2, is described by the following equation [Winkel, 2003]:

$$\dot{X} = \frac{d}{dt}\begin{bmatrix} x_p \\ x_f \end{bmatrix} = \begin{bmatrix} 0 & 1 \\ 0 & 0 \end{bmatrix} \cdot \begin{bmatrix} x_p \\ x_f \end{bmatrix} + \begin{bmatrix} \sqrt[2]{h_0/2} \cdot w_1 \\ \pi \cdot \sqrt[2]{2h_{-2}} \cdot w_2 \end{bmatrix} \qquad (3\text{-}20)$$

Where:

- x_f and x_p denote the oscillator frequency and phase errors, respectively;
- h_{-2}, h_0 represent the random walk ($h_{-2}\ in\ [Hz]$) and the white noise frequency term ($h_0\ in\ [s]$) of the oscillator frequency error.
- w_1 and w_2 are independent zero-mean white noise processes with variance 1.

With the inclusion of the flicker noise contribution ($w_{fl} \leftrightarrow h_{-1}$), the resulting time error is represented through the Allan variance that denotes the root mean square (RMS) of the oscillator

time error between two consecutive samples separated by τ time interval and is given by [Winkel, 2003]:

$$\sigma^2_{Allan}(\tau) = \frac{h_0}{2 \cdot \tau} + 2 \cdot \ln(2) \cdot h_{-1} + \frac{2 \cdot \pi^2}{3} \cdot \tau \cdot h_{-2} \qquad (3\text{-}21)$$

Thus, the system of equations in Eq. (3-20) is now augmented with the flicker term relation as [Winkel, 2003]:

$$\dot{X} = \frac{d}{dt}\begin{bmatrix} x_p \\ x_f \\ x_3 \\ x_{fl} \end{bmatrix} = \begin{bmatrix} 0 & 1 & 0 & 0 \\ 0 & 0 & 0 & 0 \\ 0 & 0 & 0 & 1 \\ 0 & 0 & -\frac{\omega_0^2}{\sqrt[2]{3}} & -\sqrt{\frac{2}{\sqrt[2]{3}}}\omega_0 \end{bmatrix}\begin{bmatrix} x_p \\ x_f \\ x_3 \\ x_{fl} \end{bmatrix} + \begin{bmatrix} w_p \cdot \sqrt[2]{h_0/2} \\ w_f \cdot \pi \cdot \sqrt[2]{2h_{-2}} \\ 0 \\ w_{fl} \cdot \frac{2}{\sqrt[2]{3}} \cdot \sqrt[2]{\pi \cdot h_{-1} \cdot \omega_0} \end{bmatrix} \qquad (3\text{-}22)$$

where:

- $\omega_0 = 2\pi \cdot f_0$ is the oscillator nominal frequency in $[rad]$;
- w_{fl} denotes the flicker Gaussian noise process that is independent to the other noise terms and has variance 1;
- x_3 is an added term reflecting the flicker frequency noise.

With the inclusion of the flicker noise component x_{fl}, the oscillator time fluctuation is expressed by the sum of $x_p + x_3$, where x_p describes the white and random walk frequency noise and x_3 represents the flicker noise component. Therefore, the oscillator phase and frequency noise PSDs are obtained after applying the discretization of the continuous time model in Eq. (3-22).

The (h_0, h_1, h_2) values for five different oscillators are summarized in Table 3-1.

Table 3-1. *Allan variance parameters for different oscillator types [Winkel, 2003]*

		Oscillator Parameters		
		$\boldsymbol{h_0(s)}$	$\boldsymbol{h_{-1}}$	$\boldsymbol{h_{-2}(Hz)}$
Receiver	**Quartz**	$2e^{-19}$	$7e^{-21}$	$2e^{-20}$
	TCXO*	$1e^{-21}$	$1e^{-20}$	$2e^{-20}$
	OCXO**	$8e^{-20}$	$2e^{-21}$	$4e^{-23}$
Satellite	**Rubidium**	$2e^{-20}$	$7e^{-24}$	$1e^{-29}$
	Cesium	$1e^{-19}$	$1e^{-25}$	$2e^{-23}$
* TCXO = Temperature Controlled Crystal Oscillator ** OCXO = Oven Controlled Crystal Oscillator				

From the parameters given in Table 3-1, it can be easily observed the long-term stability of the Rubidium and Cesium oscillator types, which provides longer validity of the oscillator timing error modeling states in the navigation message [Kaplan and Hegarty, 2006]. Therefore, these two oscillator types are employed by the GNSS satellites. It can be noticed that the satellite oscillator-induced phase error exhibits a slowly variation in time, thus having a minimal impact on the error budget. Therefore, it can be stated that the tracking process is mostly affected by the low-cost receiver oscillator error.

As a consequence, the receiver phase error is driven by the receiver oscillator error. The TCXO oscillator exhibits higher short-term stability (integration shorter than a few tens of milliseconds) with respect to the Quartz and OCXO receiver-used oscillators. This is the main reason why in this thesis, the TCXO oscillator noise model will be implemented in the receiver algorithm.

A reference to the above described oscillator noise model will be later made in the Kalman filter description in Chapter 4.

3.2.3. Receiver Dynamics

The sudden and fast changes of the receiver's dynamics impact both the code and carrier tracking loops, resulting in changes of the code delay, carrier phase and frequency parameters. Indeed, the high receiver dynamics can significantly degrade the tracking performance up to the loss-of-lock occurrence.

3.2.4. Interferences

GNSS signal interferences affect the received signal spectrum and as a consequence, will impact the tracking process since these interferences are not filtered out at the front-end stage. However, in this thesis the interference effect on the tracking loops is not taken into account.

3.3. Correlation of the Measurement Errors

3.3.1. GNSS Code and Carrier Measurement Model

The nominal code pseudorange measurement ρ, after the inclusion of the propagation delays and measurement errors that were provided above, computed by the receiver for a given satellite i at epoch k is modelled as follows:

$$\rho^{(i)}(k) = R^{(i)}(k) + c \cdot \left(b_{Rx} - b_s^{(i)}\right) + \varepsilon_{sat/eph}^{(i)}(k) + \varepsilon_{iono}^{(i)}(k) + \varepsilon_{tropo}^{(i)}(k) + \varepsilon_{mult}^{(i)}(k) + \varepsilon_n^{(i)}(k) \text{ [m]} \quad (3\text{-}23)$$

where:

- ρ is the code pseudorange measurement in $[m]$;
- R is the satellite to receiver geometrical (Euclidian) distance in $[m]$;
- b_{Rx}, b_s are the user's receiver and satellite clock biases, respectively, expressed in $[s]$;
- $\varepsilon_{sat/eph}$ denote the ephemeris and satellite clock errors in $[m]$;
- ε_{iono} and ε_{tropo} denote the residual ionosphere and troposphere errors in $[m]$;
- ε_{mult} is the delay induced by the multipath effect$[m]$;
- ε_n represents the receiver's thermal noise $[m]$;

As it can observed, the receiver's dynamics and the interference contributions are not present in the pseudorange measurement in Eq. (3-23) since these two error sources cannot be directly represented in the measurement domain. In fact, these two errors majorly impact the code/carrier signal tracking performance and therefore, their effects can be better quantified in the tracking domain.

Whereas, the general carrier pseudorange rate measurement $\dot{\rho}$ computed by the receiver for a given satellite i at epoch k, after neglecting the slowly-varying satellite clock and ephemeris error, is given by:

$$\begin{aligned}\dot{\rho}^{(i)}(k) = &\left(\dot{x}_s^{(i)}(k) - \dot{x}(k)\right)\cdot a_x^{(i)}(k) + \left(\dot{y}_s^{(i)}(k) - \dot{y}(k)\right)\cdot a_y^{(i)}(k) + \left(\dot{z}_s^{(i)}(k) - \dot{z}(k)\right)\cdot a_z^{(i)} \\ &+c\cdot \dot{b}_{Rx}(k) + \dot{\varepsilon}_{iono}^{(i)}(k) + \dot{\varepsilon}_{tropo}^{(i)}(k) + \dot{\varepsilon}_{mult}^{(i)}(k) + \dot{\varepsilon}_n^{(i)} \left[\frac{m}{s}\right]\end{aligned} \quad (3\text{-}24)$$

Where:

- $(\dot{x}_s^{(i)}, \dot{y}_s^{(i)}, \dot{z}_s^{(i)})(k)$ and $(\dot{x}, \dot{y}, \dot{z})(k)$ represent the i^{th} satellite and user's velocities vectors in the ECEF reference frame, respectively, expressed in $[m/s]$;
- $a_x^{(i)} = \frac{\left(x_s^{(i)} - x\right)}{\sqrt[2]{\left(x_s^{(i)} - x\right)^2 + \left(y_s^{(i)} - y\right)^2 + \left(z_s^{(i)} - z\right)^2}}$ denotes the LOS projection along the X-axis. A similar computation is done for the other coordinates.
- $\dot{b}_{Rx}$ is the receiver's clock drift, expressed as the clock bias time derivative in $[m/s]$;
- $\dot{\varepsilon}_{iono}, \dot{\varepsilon}_{tropo}$ denote the time-correlated errors induced by the ionospheric and tropospheric delay rate errors in $[m/s]$;
- $\dot{\varepsilon}_{mult}$ denotes the error induced by the multipath effect on the carrier frequency in $[m/s]$;
- $\dot{\varepsilon}_n$ denotes the receiver's thermal noise effect on the carrier measurement in $[m/s]$;

Since in this dissertation the urban multipath and noise contributions are added at correlator output, the herein adopted pseudorange and pseudorange rate measurements are then expressed as:

$$\begin{aligned}\rho^{(i)}(k) &= R^{(i)}(k) + c\cdot\left(b_u - b_s^{(i)}\right) + \varepsilon_{sat/eph}^{(i)}(k) + \varepsilon_{iono}^{(i)}(k) + \varepsilon_{tropo}^{(i)}(k)\ [\mathrm{m}] \\ \dot{\rho}^{(i)}(k) &= \left(\dot{x}_s^{(i)}(k) - \dot{x}(k)\right)\cdot a_x^{(i)}(k) + \left(\dot{y}_s^{(i)}(k) - \dot{y}(k)\right)\cdot a_y^{(i)}(k) + \left(\dot{z}_s^{(i)}(k) - \dot{z}(k)\right)\cdot a_z^{(i)} \\ &\quad +c\cdot \dot{b}_{Rx}(k) + \dot{\varepsilon}_{iono}^{(i)}(k) + \dot{\varepsilon}_{tropo}^{(i)}(k)\left[\frac{m}{s}\right]\end{aligned} \quad (3\text{-}25)$$

The pseudorange errors caused by each independent source are modelled by zero-mean normal distributions, overbounding the real error distribution as:

$$\varepsilon_X \sim N(0, \sigma_X^2) \quad (3\text{-}26)$$

where X represents the error's source type including, the satellite/ephemeris (sat/eph), ionosphere $(iono)$, troposphere $(tropo)$, multipath $(mult)$ and noise $(noise)$ contributions.

In the GNSS literature, the User Equivalent Range Error (UERE) reflects the error budget of the pseudorange measurements that is based on the computation of the different error contributions presented above. Assuming that all these error contribution are independent from each other, the UERE variance for each satellite i is computed as:

$$\sigma^{2}{}_{UERE}^{(i)} = \sigma^{2}{}_{sat/eph}^{(i)} + \sigma^{2}{}_{iono}^{(i)} + \sigma^{2}{}_{tropo}^{(i)} + \sigma^{2}{}_{mult}^{(i)} + \sigma^{2}{}_{n}^{(i)}\ [m^2] \quad (3\text{-}27)$$

The sigma UERE relation in Eq. (3-27) is further fed to the measurement covariance matrix, concerning the pseudorange measurements, of the Weighted Least Square (WLS) navigation algorithm.

3.3.2. Description of the First Order Gauss-Markov process

Several measurement errors that were described above are correlated in time and usually modelled as a first order Gauss-Markov (GM) process, having an exponentially decaying autocorrelation function, as standardized in [ICAO, 2008]. The first-order Gauss-Markov stationary process is widely used in this thesis for the modelling of the measurements' errors and biases, with the later that will be estimated in the proposed solution. A first-order GM process is expressed in continuous time as follows:

$$\dot{b} = -\frac{1}{\tau} \cdot b + w_b \qquad (3\text{-}28)$$

Where:

- b is the GM random process with zero mean and variance σ_b^2;
- τ is the error correlation time;
- w_b is the process driven noise with zero mean and variance $\sigma_{w_b}^2$.

The discrete time model of the GM random process is expressed as follows:

$$b_k = e^{-\frac{\Delta T}{\tau}} \cdot b_{k-1} + w_k \qquad (3\text{-}29)$$

Where:

- b_k is the process value at the k^{th} epoch;
- τ is the GM process correlation time in seconds;
- ΔT is the sampling period in seconds;
- w_k is the value of the process driven noise at the k^{th} epoch.

In discrete time, the process driven noise variance $\sigma_{w_k}^2$ is deduced from the global GM process using the following relation:

$$\sigma_{w_k}^2 = \sigma_{b_k}^2 \cdot \left(1 - e^{-\frac{2 \cdot \Delta T}{\tau}}\right) \qquad (3\text{-}30)$$

The main parameters that are required for the full description of the GM process are the correlation time τ and the process driven noise variance $\sigma_{w_k}^2$.

3.3.3. Correlation Time of the Measurement Errors

This part presents the correlation time values for the nominal measurement error terms.

3.3.3.1. Ephemeris and Satellite Clock Error Correlation Time

Ephemeris (orbital parameters) errors and the ranging errors due to the satellite oscillator deviation from its nominal frequency vary slowly in time and are re-initialized every hour though the control segment updates [ICAO, 2009]. Therefore, the correlation time of the GM process describing the measurement error due to the ephemeris and satellite clock inaccuracies is set to $\tau_{sv/eph} = 3600\ s$ according to the GPS and Galileo Minimum Operational Performance Requirements (MOPS), presented in [ICAO, 2009] and [EUROCAE, 2010].

3.3.3.2. Ionospheric Error Correlation Time

Ionospheric errors are modelled according to the Klobuchar and NeQuick correction models with their own residual errors, respectively employed for the GPS and Galileo signals. According to the only available civil aviation standards [ICAO, 2009] and [EUROCAE, 2010], the ionospheric residual error has a correlation time set for both GPS and Galileo signals to $\tau_{iono} = 1800\ s$.

3.3.3.3. Tropospheric Error Correlation Time

Similarly to the ionospheric errors, the correlation time of the tropospheric errors is chosen accordingly to the [ICAO, 2009] standard to $\tau_{tropo} = 1800\ s$.

3.3.3.4. Multipath Error Correlation Time

The multipath error model, standardized for the civil aviation domain [ICAO, 2006], is not applicable to the urban environment GNSS use. For this purpose, a channel model that is designed for GNSS users in urban road scenario, has been employed to generate the LOS and multipath echoes. Further details concerning the generation of the urban propagation channel are found in Chapter 6.

3.3.4. Summary

Table 3-2 summarizes the propagation delays and measurement errors modelling, comprising the errors' characteristics in terms of standard deviation and temporal correlation, affecting the GPS L1 and Galileo E1 code and Doppler measurements. Further details concerning the ionosphere residual rate impact on the pseudorange rate error along with its model derived from the code measurement are detailed in the proposed solution in Chapter 5.

Table 3-2. *GNSS measurement errors modelling.*

Measurement	Error	Model	Standard deviation	Correlation time
Pseudorange	**Ephemeris + Satellite clock (URA for GPS SISA for Galileo)**	Gauss Markov	$\sigma_{sv/eph} = 0.85\ m$	$\tau_{sv/eph} = 3600\ s$
	Ionosphere	Gauss Markov	Klobuchar model (GPS) $\sigma_{iono,L1} = F \cdot \tau_{iono-vert,L1}$	$\tau_{iono} = 1800\ s$
			NeQuick model (Galileo) $\sigma_{iono-E1} = VTEC \cdot \tau_{iono-vert,E1}$	
	Troposphere	Gauss Markov	$\sigma_{tropo} = F_{tropo} \cdot \sigma_{tropo,v}$	$\tau_{tropo} = 1800\ s$
	Receiver Thermal Noise	Gaussian $\sigma_{n,L1/E1}\ (DLL)$		
	Multipath	Urban Channel model (Chapter 5)		
Pseudorange rate	**Ephemeris + Satellite clock**	Negligible		
	Ionosphere	Gaussian	Derivation of the Iono. Residual error (Chapter 5)	N/A
	Troposphere	Gaussian	Derivation of the Troposphere error	N/A
	Receiver Thermal Noise	Gaussian		
	Multipath	Urban Channel model (Chapter 6)		
N/A – Not Applicable				

3.4. Analog Signal Processing

This section will first present the general architecture of the GNSS receiver and later describing the analog front-end.

3.4.1. GNSS Receiver Architecture

The overall goal of any GNSS navigation receiver is the computation of the user's navigation solution based on the parallel processing of the received signals from the different GNSS satellites in-view. Indeed, GNSS receivers rely on accurate synchronization between their local time and the satellites time scale in order to generate distance (pseudorange estimation) and velocity (Doppler frequency estimation) measurements [Dovis and Mulassano, 2009]. The high level block diagram representation of a generic GNSS receiver architecture is illustrated in Figure 3-3. In this configuration, the receiver's macro blocks are:

- *The analog RF front-end*: represents the first stage of the signal processing chain starting from the receiver antenna (radiating element) output, which is not typically considered as part of the front-end stage. This includes the Low Noise Amplifier (LNA), the Intermediate Frequency (IF) down-converter, the IF band-pass filter, the frequency synthesizer, the receiver oscillator and the quantization/sampling stage. The output of this block is the discrete version of the received Signal-in-Space (SiS);

- *The digital processing stage*: is a process performed in parallel for each signal of interest and is in charge of the signal acquisition and synchronization, with the later achieved through the code/carrier tracking process. The receiver performs the correlation operation between the received signal and the receiver-generated local replica in order to extract the GNSS signal information. Then, the signal acquisition is initiated with the objective of detecting the signal presence and also roughly estimating the code delay (τ) and Doppler frequency (f_D). Furthermore, this coarse estimation of the code delay and Doppler frequency is refined through the code/carrier tracking loops. The switch mechanism, illustrated in Figure 3-3, highlights the passage through the acquisition block (switch in point S_1) either only in the initialization step (satellite appearance) or when a loss-of-lock event occurs. This means that for the other measurement epochs, the code/carrier tracking process can operate directly after the correlation block (switch in point S_2). When the code and carrier synchronization is achieved, the receiver is capable of demodulating the navigation message samples. The digital stage design is dependent on the characteristics of the signal of interest (such modulation, expected dynamics, etc.) and the targeted application (aircraft, vehicle, pedestrian);

- *The measurement processing*: is the final processing block that performs the following tasks:

    - *The data demodulation, frame synchronization and parity decoding*: are performed in this order for the GPS signals with the objective of resolving the sign ambiguity and validating the legitimacy of the Handover word (HOW) of the navigation message that contains the Z-count, which contains the message time reference [Parkinson, 1996]. Only after these steps are performed, the demodulation of the other words can initiate and their data, including the satellite position and clock correction terms, the satellite health, ionosphere correction coefficients etc. can be stored;

    - *The measurement generation* is achieved in two consecutive steps:

        - *The generation of the raw pseudorange and pseudorange rate measurements*: is achieved by using the code phase and carrier frequency estimation errors obtained from the code and carrier tracking loops, respectively. Indeed, the transit time measurement for each satellite is

extracted from the code phase offset and thus, providing the raw pseudorange measurement. Similarly, the raw carrier Doppler (pseudorange rate) measurement can be extracted from the carrier phase/frequency tracking loop by means of a carrier accumulator [Kaplan and Hegarty, 2006];

- *Correction of the pseudorange and pseudorange rate measurements*: of the raw measurements, obtained from the code/carrier tracking loops, is achieved by applying the ionosphere and satellite clock/ephemerides corrections from the navigation message data after demodulation;

- *PVT solution computation*: by feeding the corrected measurements to the navigation module that computes the user's navigation solution using different approaches such as the Least Square (LS), Weighted Least Square (WLS) or Kalman filter (KF) estimators.

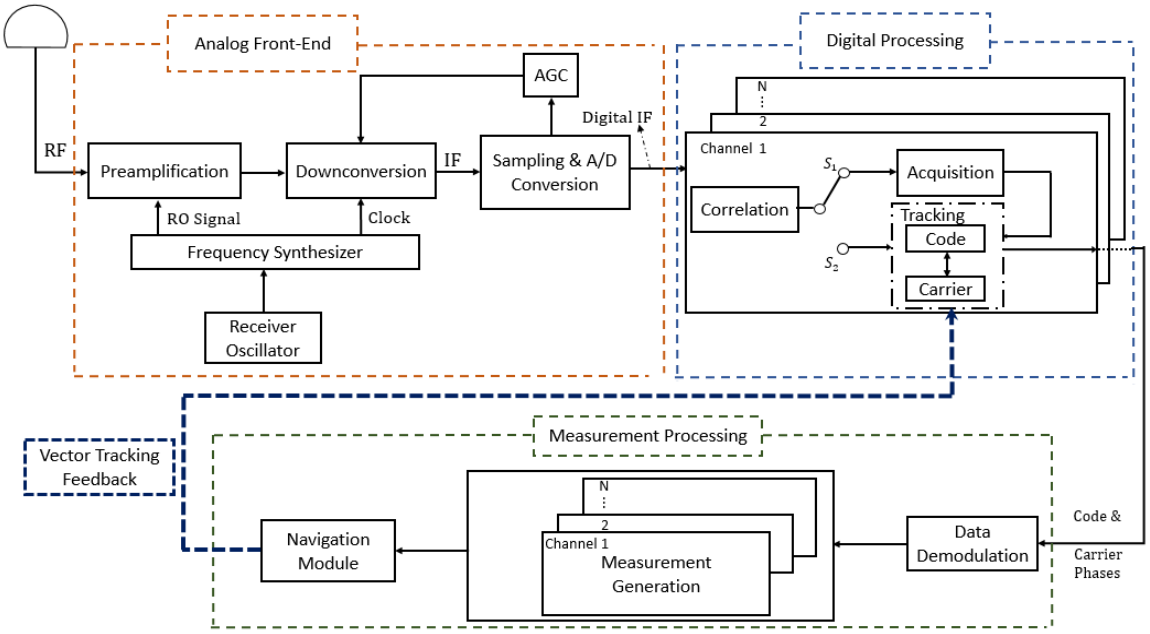

Figure 3-3. *The high level block diagram representation of a generic GNSS receiver architecture*.

When observing the receiver block diagram in Figure 3-3, the Vector Tracking feedback loop in dashed blue line can be easily noted. Contrary to the conventional or scalar tracking architecture, where the signal and measurement processing are totally separated blocks, vector tracking controls the tracking's loop feedback based on the navigation solution estimation. The detailed description of the vector tracking algorithm is provided in Chapter 5.

3.4.2. Description of the Analog Front-End

Constituting the first stage of the signal processing chain, the analog signal processing is responsible for the filtering and downconversion of the received RF signal. This block consists of filters, a Low Noise Amplifier (LNA), a frequency synthesizer, signal downconversion and conversion to baseband, mixers, local oscillators and an Automatic Gain Control (AGC) [Parkinson, 1996]. The final block in the front-end path is the Analog-to-Digital Converter (ADC) that is in charge of converting the IF or baseband analog signal into digital samples [Borre et al., 2007].

3.4.2.1. Antenna

Even though the receiver's antenna (radiating element) is not per se part of the receiver front-end, its short description will be given here since it represents the first component in the signal reception path. The fundamental antenna parameters that characterize its performance are the frequency selectivity, antenna gain and polarization [Parkinson, 1996].

Concerning the first parameter, it must be noted that the GNSS antenna is designed to accept GNSS signals from one of the three possible bands such as L1, L2 and L5. However for certain applications, multi-frequency band antennas may be used.

The user's GNSS antenna has the same electric field orientation as the GNSS signals polarization that are right-hand circularly polarized (RHCP). This design is quite effective for multipath mitigation since the signal reflected off obstacles exhibits a change of polarization [Borre et al., 2007]. The parameters reflecting the isolation between the gain for RHCP and LHCP signals are referred to as the axial ratio. The antenna gain pattern has a significant impact on the received signal quality and the performance of the consequent digital processing stage. Most GNSS receivers employ quasi-omnidirectional antenna having approximately the same gain towards all directions, which is preferable for applications for which the orientation of the antenna can vary greatly. More directive antennas are however preferable when the antenna orientation is known a priori (for instance in civil aviation or for a car). The antenna gain typically varies as a function of the satellite elevation angle with a typical gain at zenith of $+4.5\ dB$ that decreases by up to $10\ dB$ at an 5° elevation angle [Misra, P., 2001].

3.4.2.2. Analog front-end

As previously stated, the objectives of the receiver front-end are fourfold:

- the amplification of the signal of interest;
- the down-conversion to Intermediate Frequency (IF) or baseband;
- the signal filtering in order to remove the interference contribution and thus, only select the signal of interest;
- the digitization of the filtered signal;

The functional block diagram elements of the analog front-end, depicted in Figure 3-4, will be described in details.

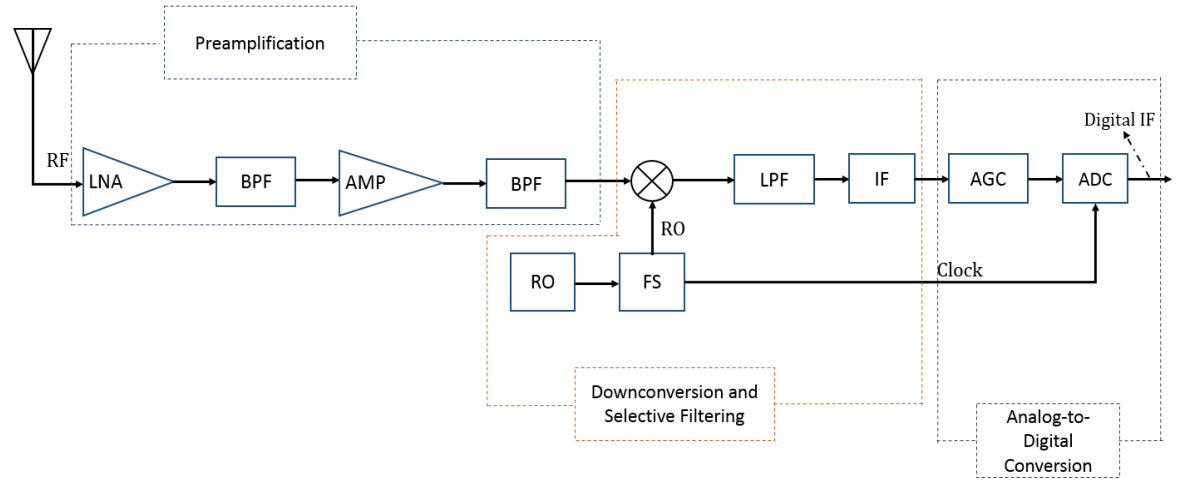

RF – Radio Frequency signal
BPF – Band Pass Filter
AMP – Amplifier
RO – Receiver Oscillator
FS – Frequency Synthesizer
RO – Local Oscillator signal
LPF – Low Pass Filter
IF – Intermediate Frequency Filter
AGC – Automated Gain Control
A/D – Analog-to-Digital conversion

Figure 3-4. *The functional block diagram of the analog front-end processing*.

3.4.2.2.1. Preamplification

This block achieves burn-out protection from peak signal power possibly induced from the high power incoming signal, the LNA and several stages of low selectivity bandpass filtering, as illustrated in Figure 3-4.

3.4.2.2.1.1. Low Noise Amplifier (LNA)

The GNSS signal power at the antenna output is very low to a level of $-158.5\ dBW$ and can be easily buried under the noise level [Kaplan and Hegarty, 2006]. Therefore, the antenna is connected to a low noise amplifier (LNA) that is designed with the objective of amplifying the received low-power signal without significantly degrading its signal-to-noise ratio and therefore, minimizing the additional noise created by the amplifier. The LNA is the main component setting the equivalent noise figure of the front-end according to the Friis formula [Parkinson, 1996]. It is thus of great importance to have a LNA with a high gain and a low noise figure.

3.4.2.2.1.2. Bandpass Filters (BPF)

The analog front-end includes several bandpass filters in different processing stages, aiming at the provision of additional frequency selectivity and interference rejection. The BPF eliminates the high-power signal components, narrows the signal bandwidth through rejecting the out-of-band noise and frequencies generated by the amplifiers and mixer [Bhattacharyya, 2012]. These filters prevent the saturation by strong out-of-band signals and remove any unwanted signal generated by that electronic component. At the RF stage, the BPF are generally not very selective due to the high carrier frequency of the useful signal [Grewal et al., 2007].

3.4.2.2.1.3. Amplifier (AMP)

After the LNA, it is possible to further amplify the signal if required. The total amplification shall ensure that the signal power has an acceptable level for the analog-to-digital conversion. Normally this task is not achieved by a single amplifier but through cascaded multistage amplifiers.

3.4.2.2.2. Mixing and Intermediate Frequency (IF) sampling

The GNSS signal downconversion from the L band to a suitable IF frequency is performed to ease the digital processing in the following stages. It is accomplished by mixing the incoming signal with a local signal replica generated by the reference oscillator (RO) and frequency synthesizer (FS), as shown in Figure 3-4.

3.4.2.2.2.1. Frequency Synthesizer (FS)

The frequency synthesizer is an electronic circuit that generates frequency ranges from a single reference oscillator. The widely used frequency standard in GNSS receivers is the indirect digital (PLL) synthesizers including integer-N and fractional-N. In specifics, the multipliers are replaced with Phase Lock Loops (PLL) that employ a Voltage Control Oscillator (VCO) and high-speed dividers [Parkinson, 1996]. The reason behind this configuration, is related to the lack of capability of the receiver oscillator to generate by its own the desired local oscillator frequency.

3.4.2.2.2.2. Receiver Oscillator (RO)

The resulting IF signal is obtained from the difference between the signal- and local oscillator frequencies. The received noisy signal from each satellite i ($r_i(t)$) in the time-domain is represented as follows:

$$r_i(t) = A_i \cdot d_i(t-\tau_i) \cdot c_i(t-\tau_i) \cdot \cos\left[2\pi \cdot f_L \cdot t + \varphi_{0,i}(t)\right] + n(t) \qquad (3\text{-}31)$$

where:

- A_i denotes the signal amplitude;
- $d_i(t-\tau_i)$ denotes the navigation data;
- $c_i(t-\tau_i)$ is the PRN code signal;
- τ_i is the signal transit time from satellite i to the user's receiver;
- $\varphi_{0,i}(t)$ is the time-dependent initial phase of the received signal, including the Doppler frequency contribution;
- f_L represents the signal's carrier frequency in the L band;
- $n(t)$ represents the additive noise.

By denoting the receiver oscillator signal by $r_{RO}(t) = 2 \cdot \cos(2\pi \cdot f_{RO} \cdot t)$, the output of the signal mixing consists of upper and lower sideband components having the same power and expressed by:

$$\begin{aligned} r_i(t) \cdot r_{RO}(t) = {} & A_i \cdot d_i(t-\tau_i) \cdot c_i(t-\tau_i) \cdot \cos\left[2\pi \cdot f_L \cdot t + \varphi_{0,i}(t)\right] \\ & \cdot \left\{\cos\left[2\pi \cdot \left(f_L + f_{RO}\right) \cdot t + \varphi_{0,i}(t)\right] + \cos\left[2\pi \cdot \left(f_L - f_{RO}\right) \cdot t + \varphi_{0,i}(t)\right]\right\} + n(t) \end{aligned} \qquad (3\text{-}32)$$

For the further processing stages, only the lower sideband is desired and therefore, the upper sideband signal $\left(\cos\left[2\pi \cdot \left(f_L + f_{RO}\right) \cdot t + \varphi_{0,i}(t)\right]\right)$ is eliminated via the band-pass filter (BPF), as illustrated in Figure 3-4. The mixing operation generates harmonics that shall be removed through the use of bandpass filters at IF.

In addition, these filters are also responsible for the out-of-band interference and image noise rejection [Parkinson, 1996]. Since now the signal is downconverted in IF, these filters can be much more selective and capable to reject efficient out-of-band interference.

3.4.2.2.3. Analog-to-Digital Conversion (ADC)

The ADC constitutes the final step of the GNSS receiver analog front-end processing. Its objectives are the analog signal sampling, the signal's amplitude quantization and the signal digitization.

3.4.2.2.3.1. Sampling

The receiver's sampling frequency is determined by the IF frequency and front-end bandwidth. The sampling rate, as described by the Nyquist theory, shall be at least twice the signal bandwidth. The widely-used sampling techniques in modern GNSS receivers is referred to as the baseband sampling [Parkinson, 1996]. In this technique, a baseband conversion process precedes the sampling that is achieved by mixing the IF signal with two LOs signals, one of which is 90° shifted with respect to the other (in quadrature). It is preferable to employ an anti-aliasing LPF to eliminate the aliases present in the sampled signal's spectrum after the sampling process.

3.4.2.2.3.2. Quantization

The signal is later fed to the ADC block for the quantization and digitization process.

The quantization consists of dividing the signal input dynamic range into $2^{N_{bit}}$ output intervals where N_{bit} is the number of quantization bits. Most low-cost receivers use 1 quantization bit to digitize the samples for which only the signal transition information is extracted. Therefore, the quantization output indicates two levels for the positive and/or negative samples. This configuration does not require the use of the Automated Gain Control (AGC) [Grewal et al., 2007]. However, the 1-bit quantization exhibits two main disadvantages: firstly, the introduction of $1.96\ dB$ loss in the signal-to-noise (SNR) ratio and secondly, increased susceptibility to interfering and jamming signals [Parkinson, 1996]. Typical high-end receivers use from 1.5- to 3-bit sample quantization, with three to eight output level ranges. In the literature, it is mentioned that military receivers using more than 3 bits for the quantization are less likely to saturate the ADC [Grewal et al., 2007]. The quantization error, described as the difference between the analog input to the ADC and the digitized output levels, decreases with the increase of the front-end bandwidth and number of quantization bits [Gleason and Gebre-Egziabher, 2009].

3.4.2.2.3.3. Automated Gain Controller (AGC)

Multibit quantization receivers require the use of an AGC system to provide an appropriate dynamic range, interference signal rejection and quantization level control. In other words, the main goal of an AGC is keeping the ADC input level constant and matching with the ADC dynamic range. The AGC system block diagram, implemented in a feed-back configuration, is illustrated in Figure 3-5.

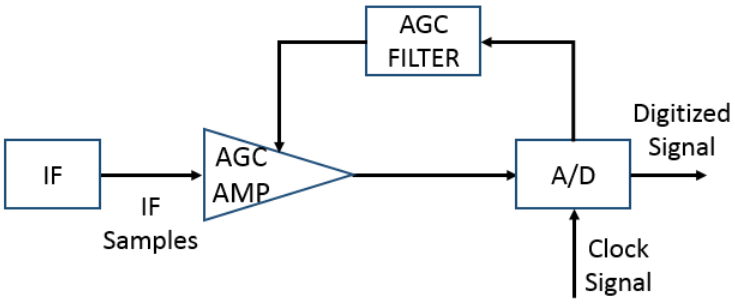

Figure 3-5. *The high level block diagram representation of the AGC block*.

3.4.2.2.4. Signal expression at the Front-end output

The signal at the output of the RF front-end $\tilde{r}(t)$ can be expressed as a function of the impulse response of the RF front-end $h_{RF}(t)$ through the convolution operation $(*)$ as:

$$\tilde{r}(t) = h_{RF}(t) * r_i(t) \tag{3-33}$$

The signal received from satellite i at the output of the Analog front-end $r_i[n]$ after the filtering operation can be modeled as:

$$\tilde{r}_i[n] = A_i \cdot d_i(nT_s - \tau_i) \cdot c_i(nT_s - \tau_i) \cdot \cos\left[2\pi \cdot f_{IF} \cdot nT_s + \varphi_{0,i}(nT_s)\right] + n(nT_s) \tag{3-34}$$

where $f_s = 1/\,T_s$ is the sampling frequency in hertz.

3.5. Digital Signal Processing

The digital signal processing initiates after the sampling and discretization process at the end of the analog front-end. Herein, the digitized signal will be split and fed to multiple channel processing blocks, corresponding to each tracked signal. Following the GNSS receiver architecture illustrated in Figure 3-3, the digital signal processing blocks conducts three main operations, the correlation, the acquisition, the code/carrier tracking. In fact, the signal acquisition is performed only at the satellite first appearance and on the code/carrier tracking loss-of-lock occurrence. The correlation process represents a fundamental operation and is defined in section 3.5.1. The acquisition principle is introduced in 3.5.2 whereas the detailed description of the code and carrier tracking loops, constituting an important part of this Ph.D. thesis, are given in 3.5.3. This section concludes with the pseudorange and pseudorange rate measurement generation that will later be fed to the navigation module. It must be pointed out that the data demodulation process is not tackled since it falls out of this work scope.

3.5.1. Correlation

The correlation process is the basic operation performed in the digital signal processing part and depends on the GNSS signal properties, especially the spreading code characteristics. In order to extract the information form the GNSS signal that is buried in the noise level, the receiver performs the correlation operation between the incoming signal and two local replicas generated by the receiver's Numerical Control Oscillator (NCO), with a 90° shift between them. The local replicas, including a copy of the signal PRN code and carrier frequency, in the discrete-time domain defined for the interval $[T_0 + (k-1) \cdot T_s, T_0 + k \cdot T_s]$ are given by:

$$\begin{aligned} r_{NCO\_I}[T_s - \hat{\tau}] &= c(T_s - \hat{\tau}) \cdot \cos\left[2\pi \cdot (f_{IF} + \hat{f}_D) \cdot T_s\right] \\ r_{NCO\_Q}[T_s - \hat{\tau}] &= c(T_s - \hat{\tau}) \cdot \sin\left[2\pi \cdot (f_{IF} + \hat{f}_D) \cdot T_s\right] \end{aligned} \tag{3-35}$$

Where:

- $\hat{\tau}$ is the delay of the local PRN code replica in seconds;
- $\hat{f}_D$ is the replica's Doppler frequency expressed in hertz;
- T_s is the correlation (integration) interval in seconds.

Inside the short correlation interval, the Doppler frequency does not vary much and this entails that the received filtered signal phase may be written as a function of the initial phases as:

$$\begin{aligned}\widehat{\varphi}(k \cdot T_{int}) &= \widehat{\varphi}_0 + 2\pi \cdot \hat{f}_D \cdot T_s \\ \varphi(k \cdot T_{int}) &= \varphi_0 + 2\pi \cdot f_D \cdot T_s\end{aligned} \tag{3-36}$$

where:

- $(\varphi_0, \widehat{\varphi}_0)$ denotes the filtered received signal- and local replica phase at the beginning of the correlation interval, respectively;
- $(f_D, \hat{f}_D)$ denotes the Doppler frequency of the filtered received signal and local replica, respectively;

The correlation operation is computed over an integration interval that is one or a multiple of the PRN code period. Even though the actual correlation operation is performed in the discrete-time domain, for simplicity purpose the signal correlation here is presented in continuous-time. The resulting correlation function R for the in-phase signal branch can be expressed as:

$$\begin{aligned}\tilde{R}\left(\varepsilon_\tau, \varepsilon_{f_d}, \varepsilon_\varphi\right) &= \frac{1}{T_{int}} \int_0^{T_s} r_{NCO\_I}(t - \hat{\tau}) \cdot \tilde{r}(t) dt \\ &= \frac{1}{T_{int}} \int_0^{T_s} c(t - \hat{\tau}) \cos\left(2\pi \cdot (f_{IF} + \hat{f}_D) \cdot t + \hat{\varphi}_0\right) \cdot \tilde{r}(t)\, dt\end{aligned} \tag{3-37}$$

where:

- $\tilde{R}$ is the correlation of the local replica with the filtered incoming signal;

Assuming a constant code and carrier Doppler evolution during the coherent integration and also considering that the correlation is performed within one data bit, the in-phase correlator output affected by thermal noise can be simplified to [Julien, 2006]:

$$\begin{aligned}I\left(\varepsilon_\tau, \varepsilon_{f_d}, \varepsilon_\varphi\right)(t) &= \frac{A \cdot d}{2 \cdot T_s} \int_0^{T_s} c(t - \tau) \cdot c(t - \hat{\tau}) dt \cdot \int_0^{T_s} \cos\left(2\pi \cdot \varepsilon_{f_D} \cdot t + \varepsilon_{\varphi_0}\right) dt + n_I(t) \\ &= \frac{A \cdot d}{2 \cdot T_s} \cdot \tilde{R}_c(t - \hat{\tau}) \cdot \frac{1}{2\pi \cdot \varepsilon_{f_D}} \cdot \sin\left(2\pi \cdot \varepsilon_{f_D} \cdot t + \varepsilon_{\varphi_0}\right)\Big|_0^{T_s} + n_I(t) \\ &= \frac{A}{2} \cdot d \cdot \tilde{R}_c(\varepsilon_\tau) \cdot \cos\left(\varepsilon_{\varphi_0} + \pi \cdot \varepsilon_{f_D} \cdot t\right) \cdot \mathrm{sinc}\left(\pi \cdot \varepsilon_{f_D} \cdot t\right) + n_I(t)\end{aligned} \tag{3-38}$$

where:

- $\tilde{R}_c(\varepsilon_\tau)$ is the correlation function between the two spreading codes of the local replica and the filtered received signal;
- $\varepsilon_\tau = \tau - \hat{\tau}$ denotes the code delay error in seconds;
- $\varepsilon_{f_D} = f_D - \hat{f}_D$ denotes the Doppler frequency error expressed in Hertz;
- $\varepsilon_{\varphi_0} = \varphi_0 - \hat{\varphi}_0$ denotes the carrier phase error at the beginning of the integration interval in radians;

Performing the same procedure for the quadrature-phase (Q) correlator output, the final I and Q signal's correlator outputs are summarized below:

$$I(\varepsilon_\tau, \varepsilon_{f_d}, \varepsilon_\varphi)(t) = \frac{A}{2} \cdot d \cdot \widetilde{R}_c(\varepsilon_\tau) \cdot \cos\left(\varepsilon_{\varphi_0} + \pi \cdot \varepsilon_{f_D} \cdot t\right) \cdot \mathrm{sinc}\left(\pi \cdot \varepsilon_{f_D} \cdot t\right) + n_I(t)$$
$$Q(\varepsilon_\tau, \varepsilon_{f_d}, \varepsilon_\varphi)(t) = \frac{A}{2} \cdot d \cdot \widetilde{R}_c(\varepsilon_\tau) \cdot \sin\left(\varepsilon_{\varphi_0} + \pi \cdot \varepsilon_{f_D} \cdot t\right) \cdot \mathrm{sinc}\left(\pi \cdot \varepsilon_{f_D} \cdot t\right) + n_Q(t) \quad (3\text{-}39)$$

where $n_I(t)$ and $n_Q(t)$ represent the noise at the in-phase and quadrature correlator outputs, respectively, that are modelled as independent terms following a centered Gaussian distribution with zero mean and variance given by:

$$\sigma_{n_I}^2 = \sigma_{n_Q}^2 = \frac{N_0}{4 \cdot T_{int}} \quad (3\text{-}40)$$

where N_0 represents the noise power spectral density (PSD) depending on the system noise temperature and expressed in dB/W/Hz.

The In-phase and Quadrature correlator outputs, expressed in discrete time for the k^{th} integration interval defined in Eq. (3-35), are given by:

$$I(k) = \frac{A}{2} \cdot d(k) \cdot \widetilde{R}_c\left(\varepsilon_\tau(k)\right) \cdot \cos\left(\varepsilon_{\varphi_0}(k) + \pi \cdot \varepsilon_{f_D}(k) \cdot T_{int}\right) \cdot \mathrm{sinc}\left(\pi \cdot \varepsilon_{f_D}(k) \cdot T_{int}\right) + n_I(k)$$
$$Q(k) = \frac{A}{2} \cdot d(k) \cdot \widetilde{R}_c\left(\varepsilon_\tau(k)\right) \cdot \sin\left(\varepsilon_{\varphi_0}(k) + \pi \cdot \varepsilon_{f_D}(k) \cdot T_{int}\right) \cdot \mathrm{sinc}\left(\pi \cdot \varepsilon_{f_D}(k) \cdot T_{int}\right) + n_Q(k) \quad (3\text{-}41)$$

3.5.2. Acquisition

The acquisition process aims at detecting the presence of the GNSS signals of interest. This acquisition process is based on the correlation operation, described in the previous section, between a set of local replicas and the GNSS signal of interest. The signal is declared present when the acquisition detector crosses the predefined threshold, which is computed based on the probability of false alarm (P_{fa}). As a consequence, the acquisition algorithm not only allows the detection of the signal but also provides a rough estimate of the code delay and Doppler frequency pair (τ, f_D). The estimation of the pair (τ, f_D) can thus be seen as a two-dimensional search in the code delay and frequency domain, based on the evaluation of the *Cross Ambiguity Function (CAF)*.

The search space covers the full two-dimension uncertainty in the code phase delay and Doppler frequency offset [Dovis and Mulassano, 2009]. For this purpose, the acquisition grid is formed by discretizing the 2D search space in N_τ number of code delay bins and N_{f_D} number of Doppler frequency bins [Kaplan and Hegarty, 2006]. The acquisition grid of size $N_\tau \cdot N_{f_D}$ is illustrated in Figure 3-6. The combination of one code delay bin and one Doppler frequency bin represents a cell that is denoted by the estimated pair $(\hat{\tau}_m, \hat{f}_{D_p})$ where $\hat{\tau}_m$ and $\hat{f}_{D_p}$ are the cell central values for the code bin number $m = 1 \div N_\tau$ and frequency bin number $p = 1 \div N_{f_D}$. The CAF function $\left(R_{CAF}(m \cdot \Delta\tau, p \cdot \Delta f_D)\right)$ is defined as the correlation between the incoming signal and a locally-generated replica with variable code delay and Doppler shift, given by:

$$R_{CAF}(m \cdot \Delta\tau, p \cdot \Delta f_D) = \int_0^{T_s} c(t - m \cdot \Delta\tau) \cos(2\pi \cdot (f_{IF} + p \cdot \Delta f_D) \cdot t + \varphi_0) \cdot \tilde{r}(t)\, dt \quad (3\text{-}42)$$

where:

- $\tilde{r}$ is the incoming signal after the IF sampling, front-end filtering and digitizing process;

- c is the generated code replica with a certain delay bin value $m \cdot \Delta\tau$ in chips;
- The cosine terms denotes the In-Phase generated carrier frequency term with a Doppler offset set to $p \cdot \Delta f_D$ where Δf_D is the Doppler frequency bin size;
- N denotes the length of the accumulation interval.

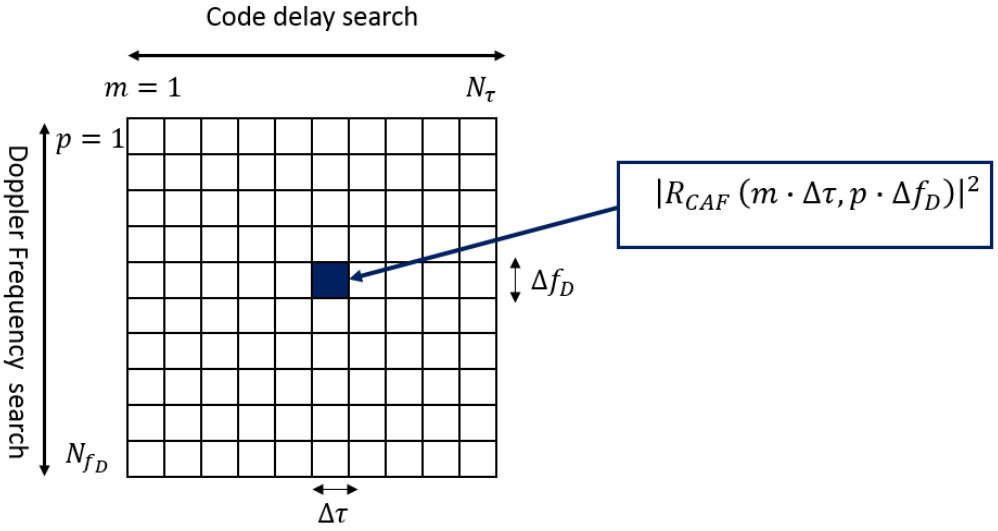

Figure 3-6. *The estimation of the code delay and Doppler frequency pair in the acquisition grid.*

In order to remove the CAF function sensitivity from the data bit sign and incoming signal phase, the $(\hat{\tau}_i, \hat{f}_{D_k})$ pair is estimated on the squared CAF envelope $\left(\left|R_{CAF}(i \cdot \Delta\tau, k \cdot \Delta f_D)\right|^2\right)$. During the signal acquisition process, the search for the correlation peak is accomplished by comparing the signal-plus-noise power at each grid cell with a threshold that is set based on the noise floor [Parkinson, 1996]. A typical signal acquisition detector is given by:

$$T = \sum_{k=0}^{K} \left(I^2(k) + Q^2(k)\right) \qquad (3\text{-}43)$$

where K denotes the number of non-coherent summations.

In most GPS L1 C/A receivers, the typical size for the code delay bin is set to half of a chip, which is compliant with the code tracking requirement. It must be noted that shorter delay step may be used but with the cost of significantly increasing the acquisition time and computation burden of the acquisition algorithm due to the increase of the search space. On the other hand, the Doppler frequency bin width (Δf_D) is typically determined by the coherent integration time T_{int} as $\Delta f_D = {}^{2}/_{(3 \cdot T_{int})}$ [Kaplan and Hegarty, 2006].

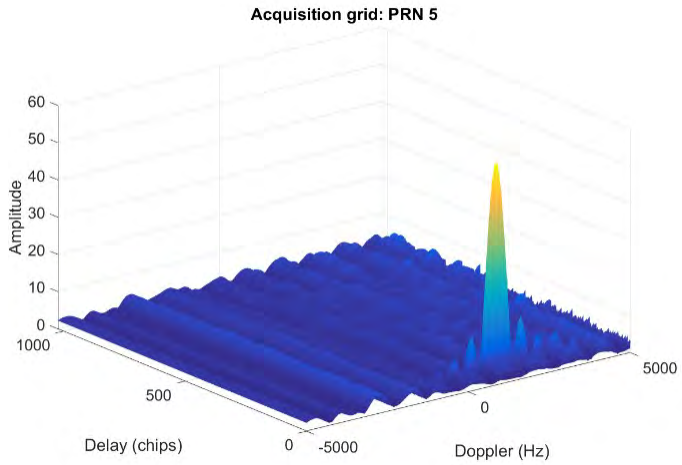

Figure 3-7. *Example of the Cross Ambiguity Function (CAF) in the acquisition grid for the acquired PRN 5 signal.*

Figure 3-7 illustrates an example of the Cross Ambiguity Function (CAF) in the acquisition grid for a GPS L1 C/A signal. In this case, the GPS PRN5 signal is successfully acquired since the signal power is over the defined threshold. It must be highlighted the fact that the acquisition process is the longest and with the highest computation charge among all the GNSS signal processing stages. Different search-space algorithms are used for the estimation of the code delay and Doppler frequency pair through the acquisition grid, as described in [Parkinson, 1996], [Kaplan and Hegarty, 2006]. When the acquisition process is finished, then the receiver can further continue the tracking procedure of the received signal.

3.5.3. Scalar Tracking

The scalar tracking process is conducted in a channelized structure for all the satellites in view, whose presence was detected in the acquisition stage. The objective of the tracking process is to refine the coarse estimations of the code delay and Doppler frequency provided by the acquisition block and to precisely follow the signal properties change over time [Borre et al., 2007]. Similar to the acquisition process, tracking is based on the correlation. The high-level block diagram representation of the scalar tracking architecture is illustrated in Figure 3-8.

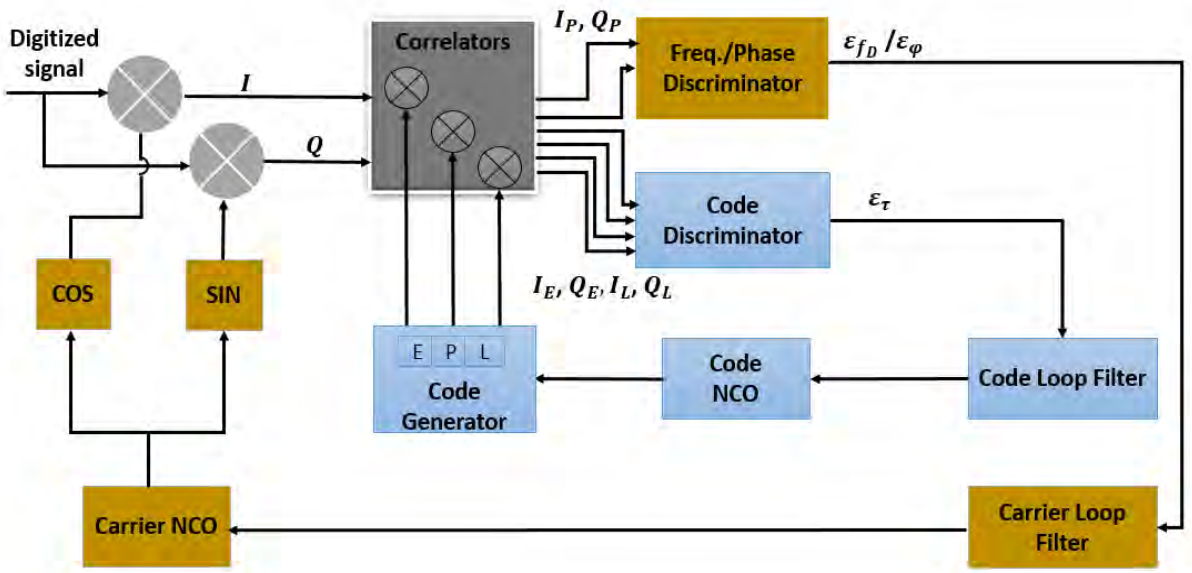

Figure 3-8. *High-level block diagram representation of the conventional tracking architecture.*

The tracking stage, employed for each satellite in view, includes two sub-modules:

- *Code tracking*, responsible for continuously tracking the code phase offset (ε_τ) between the incoming signal's code and the local replica, generally using a closed feedback loop referred to as the Delay Lock Loop (DLL). In this loop, at least three local code replicas, referred to as the early, prompt and late replica, are generated and correlated with the incoming signal.

- *Carrier tracking,* in charge of estimating the residual Doppler shift (ε_{f_D}) and the carrier phase offset (ε_φ). The carrier tracking module that compensates the residual Doppler shift (ε_{f_D}), is called a Frequency Lock Loop (FLL) while the carrier tracking loop that compensates the carrier phase error is referred to as the Phase Lock Loops (PLL) [Borre et al., 2007]. It must be pointed out that for certain applications, an FLL-aided PLL loop may be also used.

The conventional scalar tracking architecture, whose block diagram representation is given in Figure 3-8, includes the following main modules:

- *Correlators*: refers to the block that accumulates the three correlator output pairs resulting from the combination of the in-phase and quadrature signal components with the three delayed code spreading sequences that are generated from the code generator;

- *Code/carrier discriminators*: process the correlators' outputs to provide measurable quantities of the code delay- and carrier frequency/phase errors. Different discriminator functions may be employed to measure the incoming signal parameters change over time;

- *Low-pass filters*: main goal is to filter the discriminators' outputs for noise reduction at the input of the local oscillator;

- *Numerical Control Oscillator (NCO)*: converts the filtered discriminator output into a correction factor that is fed back to the code replica and carrier generators, which in its turn are used to generate the local replicas for the next epoch.

Note that the association of the low-pass filters and the NCO provides the so-called equivalent loop filter. The equivalent filter's response to the user's dynamics is strictly dependent on the filter's loop order and its equivalent noise bandwidth. In details, higher noise bandwidth implies faster loop response time (and thus better response to high magnitude user's dynamics) but with the drawback of dealing with noisier results due to the shorter integration time. In terms of the filter's loop order consideration, the higher the loop filter, the better the filter capability to follow the high order user's dynamics is [Kaplan and Hegarty, 2006]. Therefore, the following remarks can be made concerning the loop filter's order:

- 1st order filters are sensitive to the velocity stress;
- 2nd order filters are sensitive to the acceleration stress;
- 3rd order filters are sensitive to the jerk stress.

It is important to point out that the 1st and 2nd order loop filters are employed both in aided and unaided carrier tracking loops and they are stable at all noise bandwidths. On the other side, the 3rd order filter is used in unaided carrier tracking loops only and remains stable for noise bandwidth $B_n \leq 18\ Hz$ [Kaplan and Hegarty, 2006]. Keen readers may find detailed description of the loop filters in [Parkinson, 1996], [Kaplan and Hegarty, 2006] and [Betz, 2002].

The scalar tracking is continuously run for each satellite-user channel in order to precisely estimate the code delay and carrier frequency/phase evolution in time [Borre et al., 2007]. When the channel loss of lock condition occurs, the acquisition stage should be performed for that particular satellite in order to generate a new rough estimation of the signals' code delay and carrier frequency. Once the new rough estimate is obtained, the tracking process can restart for that particular satellite.

In the GNSS receiver, the code delay and carrier frequency/phase lock loops are jointly used. However, for a better understanding of the tracking loops, the carrier and code tracking loops are separately analyzed in details in the following sub-sections.

3.5.3.1. Carrier Phase Tracking (PLL)

The carrier phase tracking is accomplished by the phase lock loop (PLL), designed to keep the carrier phase alignment between the incoming signal and its local replica. The general structure of the PLL is similar to the frequency lock loop (FLL) one and is provided in Figure 3-9. The objectives of the phase tracking loop are:

- The computation of a phase reference for the detection of the GNSS modulated data signal;
- The provision of precise Doppler measurements by using the phase rate information;
- The generation of carrier phase measurements required for high-accuracy applications;
- The provision of the integrated Doppler rate aiding for the code tracking loop.

The dashed code tracking block is not an integral part of the carrier tracking loop.

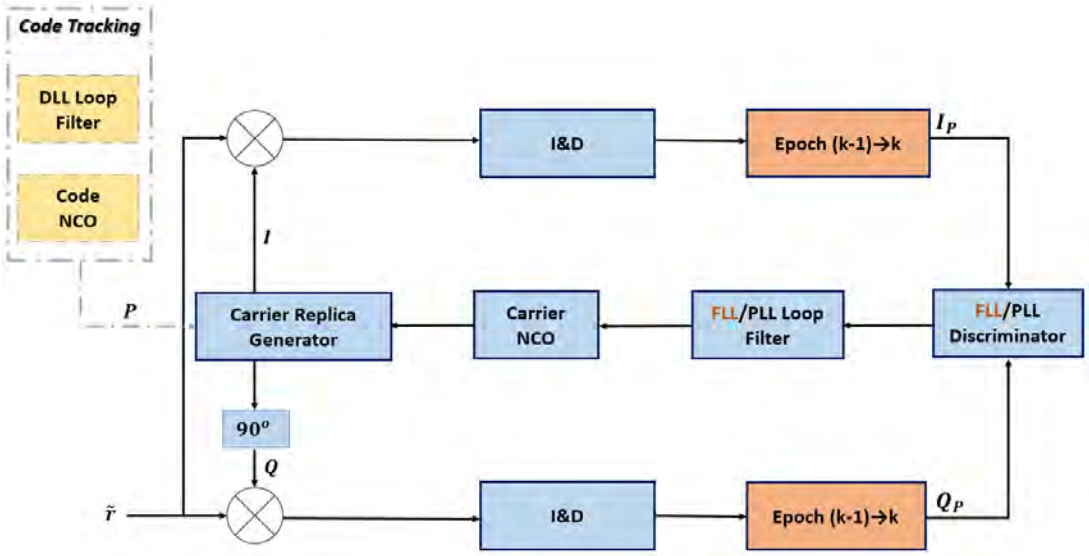

Figure 3-9. *The generic tracking loop representation including both the FLL and PLL loops.*

The received filtered signal $\tilde{r}$ is split into two branches, shifted by 90° among them. In one branch, the signal is multiplied by the In-phase local carrier, and the other by the quadrature phase local carrier. In order to achieve these tasks, the PLL employs a phase discriminator to assess the resultant phase estimation error $\left(\varepsilon_{\varphi}(k)\right)$ between the incoming signal phase and the replica phase, using the in-phase and quadrature prompt correlation values IP and QP. Further, the PLL filter filters the noise estimation and afterwards, the carrier NCO transforms the estimated phase error into a frequency variation that modifies the NCO nominal frequency for the successive epoch.

3.5.3.1.1. Carrier Phase Discriminators

The choice of the phase discriminator depends on the signal structure and on the presence of the navigation data. Therefore, the presence of the navigation data limits the upper limit of the integration time to the navigation data bit duration, which is $20\ ms$ and $4\ ms$ for the GPS L1 and Galileo E1 OS data channels, respectively. Moreover, the phase discriminator must be insensitive to the half cycle jumps (180° phase shift) due to the polarity switch at the bit transition [Julien, 2006]. The main phase discriminators used for the data channels are the following [Parkinson, 1996]:

- Dot-Product (DP) or the generic Costas discriminator:

$$D_{DP}\left(\varepsilon_{\varphi,k}\right) = QP_k \cdot IP_k \tag{3-44}$$

- Arctangent (Atan) discriminator:

$$D_{Atan}\left(\varepsilon_{\varphi,k}\right) = \operatorname{atan}\left(\frac{QP_k}{IP_k}\right) \tag{3-45}$$

For a pilot (data-less) channel, two main discriminators can be used:

- The coherent discriminator [Hegarty and Van Dierendonck, 1999]:

$$D_{coh}\left(\varepsilon_{\varphi,k}\right) = QP_k \tag{3-46}$$

- The Extended arctangent (Atan2) phase discriminator [Macabiau et al., 2003]:

$$D_{Atan2}\left(\varepsilon_{\varphi,k}\right) = \operatorname{atan2}\left(\frac{QP_k}{IP_k}\right) \tag{3-47}$$

3.5.3.1.2. PLL Error Analysis

The PLL performance is affected by the following error sources:

- the thermal noise;
- multipath;
- the dynamic stress error;
- the receiver oscillator frequency noise;
- the oscillator vibration;
- signal interference;

Taking into consideration that all the error sources provided above are independent from each-other, the carrier phase tracking error variance can be computed as:

$$\sigma_{PLL}^2 = \sigma_{th}^2 + \sigma_{mult}^2 + \sigma_{dyn}^2 + \sigma_{osc}^2 + \sigma_{vib}^2 + \sigma_{inter}^2 \quad (3\text{-}48)$$

3.5.3.1.2.1. Thermal noise

Assuming that the RF front-end filter is modeled by a filter with a unity gain within $\pm B_f/2$ Hz and null elsewhere, the variance of the carrier phase tracking error due to the thermal noise for the non-coherent atan PLL and coherent discriminators are given in m^2 by [Kaplan and Hegarty, 2006]:

$$\sigma_{PLL,atan}^2 = \left(\frac{c}{2\pi \cdot f_{carr}}\right)^2 \cdot \frac{B_{PLL}}{C/N_0 \left(\int_{-B_f/2}^{+B_f/2} S(f)df\right)} \left(1 + \frac{1}{2 \cdot T_{int} \cdot C/N_0 \left(\int_{-B_f/2}^{+B_f/2} S(f)\, df\right)}\right) [m^2] \quad (3\text{-}49)$$

$$\sigma_{PLL,coh}^2 = \left(\frac{c}{2\pi \cdot f_{carr}}\right)^2 \cdot \frac{B_{PLL}}{C/N_0 \left(\int_{-B_f/2}^{+B_f/2} S(f)df\right)} [m^2] \quad (3\text{-}50)$$

where

- C/N_0 is the carrier to noise ratio in hertz;
- T_{int} is the coherent integration time in second;
- S is the power spectral density of the signal at the receiver antenna output (which depends on the modulation type), normalized to unit area over infinite bandwidth;
- f_{carr} is the carrier frequency set to $1.57542\ GHz$ for the L1/E1 band;
- B_{PLL} is the carrier phase loop noise bandwidth in hertz.

From the PLL error variance model given above, it can be noticed that the PLL performance is dependent upon the following parameters:

- *The integration time* T_{int}: A high integration time decreases the PLL thermal noise variance but fails to track high user dynamics resulting to a possible loss of lock condition;
- *The equivalent loop bandwidth* B_{PLL}: A narrow loop bandwidth decreases the PLL thermal noise variance but may lead to a loss of lock for high dynamics;
- *The chosen PLL discriminator*.

3.5.3.1.2.2. Multipath

In strong multipath conditions or when tracking NLOS signals only, the PLL input phase error is significantly increased and thus passing the phase discriminator stability region. In this case, the phase

estimation turns into opposite sign and therefore, causing the phase discriminator to undergo a cycle slip. Under this condition, the phase lock is lost and the signal's re-acquisition process is started.

3.5.3.1.2.3. Dynamic Stress Error

The PLL is very sensitive toward the user's dynamics due to the short L1/E1 wavelength. Furthermore, a sudden variation of the user's dynamics leads to an increase of the phase error estimation that may pass the phase discriminator linear region. Therefore, the dynamic stress error impact on the phase estimation may be decreased when using high order PLLs, which are capable of following the different user dynamics evolution. Most GNSS receivers use third order PLLs to account for any kind of signal dynamics orders. In specific, the third-order loop is sensitive to the jerk error and therefore, can track the phase change with constant frequency acceleration. The dynamic stress error is expressed by [Bastide, 2004]:

$$\theta_{e,\varepsilon_\varphi} = 2\pi \cdot \frac{T_{int}^3}{K_3} \cdot \frac{d\varphi^3}{dt^3} \; [rad] \qquad (3\text{-}51)$$

where:

- K_3 is the 3rd order coefficient of the discrete PLL [Stephens and Thomas, 1995];
- $\frac{d\varphi^3}{dt^3}$ denotes the third order carrier phase estimation in $\left(\frac{cycle^3}{s^3}\right)$.

3.5.3.1.2.4. Oscillator Frequency Noise

The oscillator frequency noise, also referred to as the Allan deviation noise, is the result of the oscillator central frequency instability that introduces a phase jitter to the phase of the local replica. The phase error induced from the oscillator frequency noise depends from the receiver oscillator type (related to the Allan variance parameters h_{-2}, h_{-1} and h_0) and the PLL loop bandwidth B_{PLL}, for which a higher loop bandwidth induces a better modelling of the oscillator frequency noise [Irsigler and Eissfeller, 2003].

3.5.3.1.2.5. Oscillator Vibration

Similarly to the oscillator frequency noise, the oscillator vibration impact on the phase estimation is dependent upon the oscillator type and PLL bandwidth. Indeed, the higher the PLL loop bandwidth, the lower the phase error caused by the oscillator vibration.

3.5.3.1.2.6. Signal Interference

The signal interference represents an important error source for the phase estimation, implying high phase errors that pass the discriminator linear region and thus, leading to loss of locks and/or cycle slips. In this dissertation, the only interference source that is considered is in fact the multipath reception conditions.

3.5.3.1.3. PLL Tracking Error Threshold

The conservative mechanism to assess the PLL tracking threshold is to find the lowest C/N_0 that creates a carrier phase estimation error that exceeds the PLL discriminator linearity region in a statistically non-negligible way. The linearity region of the pilot PLL discriminators is $\pi/2$ and it is $\pi/4$ for the data discriminators, as stated in [Kaplan and Hegarty, 2006]:

$$3\sigma_{PLL} = 3\sigma_{j,PLL} + \theta_{e,\varepsilon_\varphi} \leq \frac{\pi}{2} \quad \text{for pilot channel}$$
$$3\sigma_{PLL} = 3\sigma_{j,PLL} + \theta_{e,\varepsilon_\varphi} \leq \frac{\pi}{4} \quad \text{for data channel} \qquad (3\text{-}52)$$

where:

- $\sigma_{j,PLL} = \sqrt[2]{\sigma^2_{PLL,th} + \sigma^2_{PLL,osc-vib} + \sigma^2_{PLL,osc-f}}$ denotes the 1-sigma phase jitter due to the thermal noise ($\sigma_{PLL,th}$), oscillator vibration ($\sigma_{PLL,osc-vib}$) and oscillator frequency ($\sigma_{PLL,osc-f}$) errors;
- $\theta_{e,\varepsilon_\varphi}$ is the dynamic stress error in the PLL tracking loop, defined in Eq. (3-51).

3.5.3.2. Carrier Frequency Tracking (FLL)

The Frequency Lock Loop (FLL) aims at tracking the Doppler-shifted carrier frequency of the incoming GNSS signal that includes mainly the satellite-to-user receiver motion and the user clock drift. The simplified block diagram representation of the carrier tracking structure is shown in Figure 3-9.

The FLL is a feedback loop similar to the PLL with the exception that it relies on a discriminator that estimates the frequency error between the Doppler frequency of the incoming signal and its local replica. The frequency discriminators measure the carrier phase change over two consecutive time epochs. It thus uses correlator outputs of two consecutive epochs ($k-1 \rightarrow k$) to compute the discriminator, illustrated by the two orange blocks in Figure 3-9. Therefore, the frequency tracking operation can be seen as the differential carrier phase tracking [Parkinson, 1996]. In most GNSS receivers, both the frequency and phase lock loops (FLL and PLL) are used for the carrier tracking but in different stages. First, the FLL loop is employed due to the higher pull-in range and since the FLL discriminators are less sensitive to high dynamics. When the FLL achieves to pull the NCO frequency into the PLL range, the PLL is activated with the objective of locking the incoming signal carrier phase [Groves, 2013].

3.5.3.2.1. Carrier Frequency Discriminators

The carrier frequency discriminator extracts the Doppler frequency error by operating on the In-Phase and Quadrature Prompt pair (IP, QP) of two consecutive epochs, as illustrated via the orange block in Figure 3-9. The commonly used normalized FLL discriminators are:

- Cross-Product (CP) discriminator:

$$D_{CP}(\varepsilon_{f_D,k}) = \frac{IP_{k-1} \cdot QP_k - IP_k \cdot QP_{k-1}}{IP_{k-1} \cdot QP_k + IP_k \cdot QP_{k-1}} \qquad (3\text{-}53)$$

- Decision-directed cross-product (DDCP) discriminator:

$$D_{DDCP}(\varepsilon_{f_D,k}) = \frac{(IP_{k-1} \cdot QP_k - IP_k \cdot QP_{k-1}) \cdot \text{sign}(IP_{k-1} \cdot IP_k + QP_{k-1} \cdot QP_k)}{IP_{k-1} \cdot QP_k + IP_k \cdot QP_{k-1}} \qquad (3\text{-}54)$$

- Differential Arctangent (Atan) discriminator:

$$D_{Atan}(\varepsilon_{f_D,k}) = \tan^{-1}\left(\frac{QP_k}{IP_k}\right) - \tan^{-1}\left(\frac{QP_{k-1}}{IP_{k-1}}\right) \qquad (3\text{-}55)$$

- Four-Quadrant Arctangent (Atan2) discriminator [Curran, 2010]:

$$D_{Atan2}(\varepsilon_{f_D,k}) = \tan 2^{-1}\left(\frac{IP_{k-1}\cdot QP_k - IP_k\cdot QP_{k-1}}{IP_{k-1}\cdot IP_k + QP_{k-1}\cdot QP_k}\right) \quad (3\text{-}56)$$

Figure 3-10 compares the frequency error outputs of the Cross Product (CP) discriminator in blue and the Atan2 discriminator in red, assuming no noise in the IP and QP correlator outputs and a $10\ ms$ correlation duration.

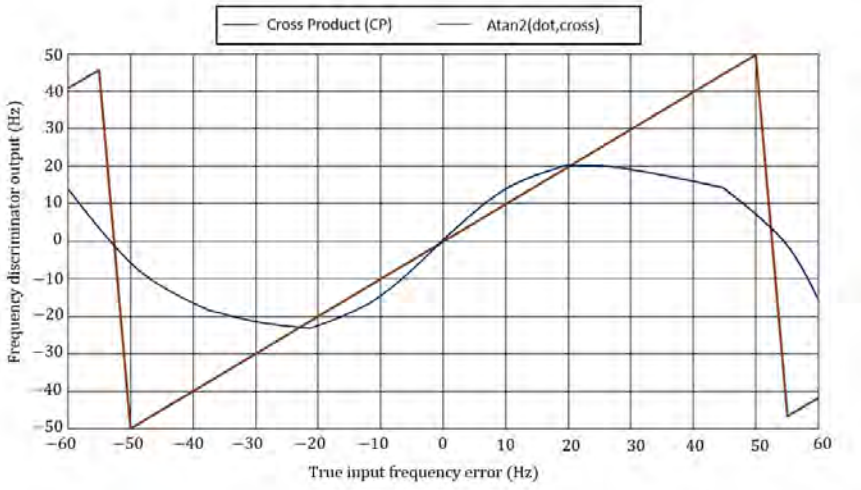

Figure 3-10. *Comparison of the frequency lock loop discriminators.*

The cross-product (CP) and four-quadrant (Atan2) discriminators are sensitive to data bit sign changes and therefore, the prompt samples for the in-phase and quadrature branches shall be collected within the same data period if these discriminators are used.

On the other side, the decision-directed cross-product (DDCP) and the differential arctangent (Atan) discriminators are insensitive to the phase reversals in the data bit transition boundaries [Parkinson, 1996]. References [Kaplan and Hegarty, 2006] and [Parkinson, 1996] summarize the main characteristics of the frequency discriminators. It is shown that the cross-product discriminator is optimal in low SNR conditions, being preferable to be employed in urban environments.

3.5.3.2.2. FLL Error Analysis

The FLL tracking performance is mainly affected by the following error sources:

- the thermal noise;
- multipath;
- the dynamic stress error;
- signal interference.

Taking into consideration that all the error sources provided above are independent from each-other, the carrier frequency tracking error variance can be computed as:

$$\sigma^2_{FLL} = \sigma^2_{th} + \sigma^2_{mult} + \sigma^2_{dyn} + \sigma^2_{inter} \quad (3\text{-}57)$$

The multipath and signal interference effects on the carrier frequency tracking induce the frequency error to exceed the frequency discriminator pull-in range up to the frequency loss-of-lock occurrence. Moreover, the reference oscillator vibration and oscillator frequency noise (also called Allan

deviation–induced frequency jitter) are small-order effects on the FLL and are considered negligible [Kaplan and Hegarty, 2006].

The rule of thumb for the FLL tracking threshold is that the maximum expected carrier frequency estimation error must not exceed one-fourth the frequency discriminator pull-in range, stated in [Kaplan and Hegarty, 2006] as:

$$3\sigma_{FLL} = 3\sigma_{FLL,th} + \theta_{e,\varepsilon_{f_D}} \leq \frac{1}{4 \cdot T_{FLL}} \quad (3\text{-}58)$$

where:

- $\sigma_{FLL,th}$ denotes the 1-sigma thermal noise frequency jitter;
- $\theta_{e,\varepsilon_{f_D}}$ is the dynamic stress error in the FLL tracking loop;
- T_{FLL} is the FLL loop period.

The FLL error variance due to the thermal noise is given by:

$$\sigma_{FLL}^2 = \left(\frac{c}{2\pi \cdot f_{carr}}\right)^2 \cdot \frac{4 \cdot F \cdot B_{FLL}}{T_{int}^2 \cdot {C}/{N_0}} \cdot \left[1 + \frac{1}{{C}/{N_0} \cdot T_{int}}\right] \quad (3\text{-}59)$$

Where $F = 1$ at high C/N_0 reception conditions and $F = 2$ near the threshold that is computed as $1/4 \cdot T_I$.

3.5.3.3. Code Delay Tracking

The code delay tracking process is directly initiated after the incoming signal's detection achieved in the acquisition stage. Its main objective is to maintain the alignment between the local replica's PRN code and the received signal spreading code by refining the code delay measurement that is later used to steer the code NCO. This code delay error measurement is later used to compute the pseudorange observation.

The code tracking is performed by means of a DLL loop that is a feedback loop capable of steering the local PRN code delay based on the estimation of the code delay error ε_τ. The general structure of the DLL loop is illustrated in Figure 3-11.

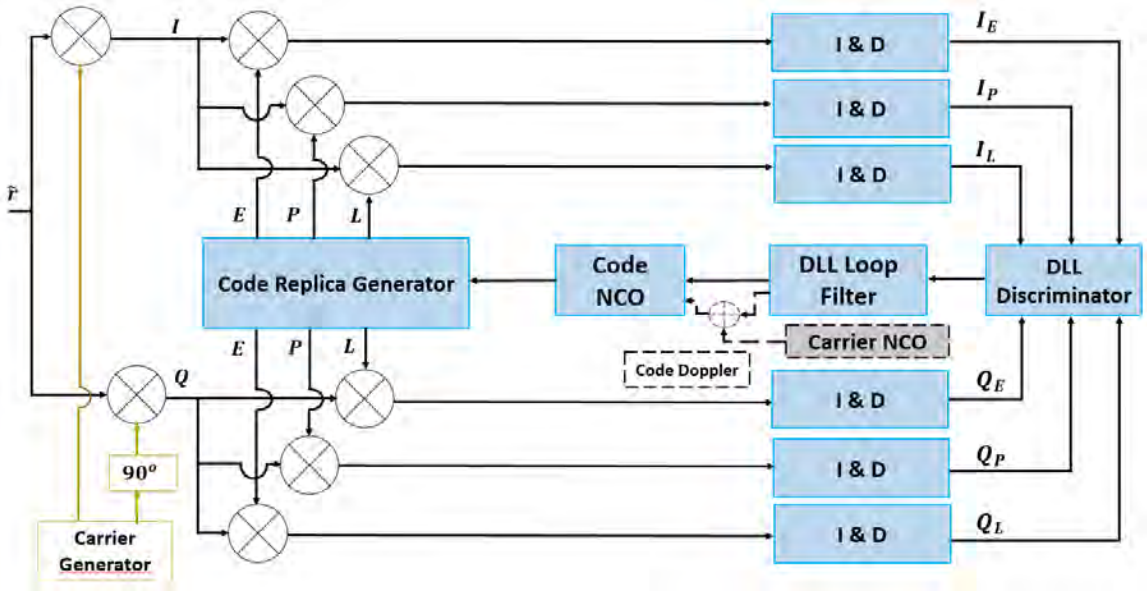

Figure 3-11. *Generic code tracking (DLL) loop.*

The in-phase and quadrature signal replica components, which are 90° shifted w.r.t each other and obtained from the carrier generator that is not an integral part of the DLL loop, are multiplied by three delayed spreading code replicas (Early, Prompt and Late). The prompt PRN code replica (P) is the local PRN code generated synchronously with the incoming PRN code according to the receiver, the early PRN code replica (E) is advanced by $(d_c \cdot T_c)/2$ w.r.t the prompt PRN code and the late code replica (L) is delayed by $(d_c \cdot T_c)/2$ compared to the prompt PRN code, where d_c denotes the correlator spacing and is expressed as the time delay between the Early and Late code replicas in unit of chips.

The correlation between each local replica with the in-phase and quadrature signal samples generates one correlator pair. Finally, three correlator pairs are obtained at the end of this operation, expressed by:

$$
\begin{aligned}
IE_k &= \frac{A}{2} \cdot d_k \cdot R_c\left(\varepsilon_{\tau,k} + \frac{d_c \cdot T_c}{2}\right) \cdot \cos(\varepsilon_{\varphi,k}) \cdot \operatorname{sinc}(\pi \cdot \varepsilon_{f_{D,k}} \cdot t) + n_{IE,k} \\
IP_k &= \frac{A}{2} \cdot d_k \cdot R_c(\varepsilon_{\tau,k}) \cdot \cos(\varepsilon_{\varphi,k}) \cdot \operatorname{sinc}(\pi \cdot \varepsilon_{f_{D,k}} \cdot t) + n_{IP,k} \\
IL_k &= \frac{A}{2} \cdot d_k \cdot R_c\left(\varepsilon_{\tau,k} - \frac{d_c \cdot T_c}{2}\right) \cdot \cos(\varepsilon_{\varphi,k}) \cdot \operatorname{sinc}(\pi \cdot \varepsilon_{f_{D,k}} \cdot t) + n_{IL,k} \\
QE_k &= \frac{A}{2} \cdot d_k \cdot R_c\left(\varepsilon_{\tau,k} + \frac{d_c \cdot T_c}{2}\right) \cdot \sin(\varepsilon_{\varphi,k}) \cdot \operatorname{sinc}(\pi \cdot \varepsilon_{f_{D,k}} \cdot t) + n_{QE,k} \\
QP_k &= \frac{A}{2} \cdot d_k \cdot R_c(\varepsilon_{\tau,k}) \cdot \sin(\varepsilon_{\varphi,k}) \cdot \operatorname{sinc}(\pi \cdot \varepsilon_{f_{D,k}} \cdot t) + n_{QP,k} \\
QL_k &= \frac{A}{2} \cdot d_k \cdot R_c\left(\varepsilon_{\tau,k} - \frac{d_c \cdot T_c}{2}\right) \cdot \sin(\varepsilon_{\varphi,k}) \cdot \operatorname{sinc}(\pi \cdot \varepsilon_{f_{D,k}} \cdot t) + n_{QL,k}
\end{aligned}
\qquad (3\text{-}60)
$$

where:

- $(\varepsilon_{\tau,k}, \varepsilon_{\varphi,k}, \varepsilon_{f_{D,k}})$ denotes the code delay, carrier phase and frequency estimation errors at epoch k, expressed as the difference between the true (unknown) and the locally-estimated terms;
- $d_c \cdot T_c$ refers to the E-L chip spacing with d_c representing the fraction of chip spacing and T_c denotes the code chip period;

- n_{xy} represents the noise term at the correlator output (where x – in-phase (I) or quadrature (Q) and y – early (I), prompt (P) or late (L) code delays) that are correlated and following a centered Gaussian distribution with zero mean and variance $\sigma^2_{n_{xy}}$ given in Appendix A.1.

3.5.3.3.1. Code delay discriminators

The code delay information of the incoming signal is in fact contained in the correlation function peak. However, the search of the correlation peak maximum is not an effective approach [Dovis and Mulassano, 2009]. Instead, a null-searching technique is employed by the GNSS receivers, based on a discriminator function that is null (zero) when the local code is synchronized to the incoming PRN code. The code discriminator output as a function of the code delay error, known as the *S-curve*, is mathematically given by:

$$S(\varepsilon_\tau) = R_c\left(\varepsilon_\tau + \frac{d_c \cdot T_c}{2}\right) - R_c\left(\varepsilon_\tau - \frac{d_c \cdot T_c}{2}\right) \quad (3\text{-}61)$$

In Figure 3-12, the top plot depicts the Early (blue), the Prompt (green) and the Late (red) local code replicas for the normalized and unfiltered BPSK correlation function for a correlator spacing of $C_s = 1$ chip, whereas, the S-curve generated from their difference is illustrated below.

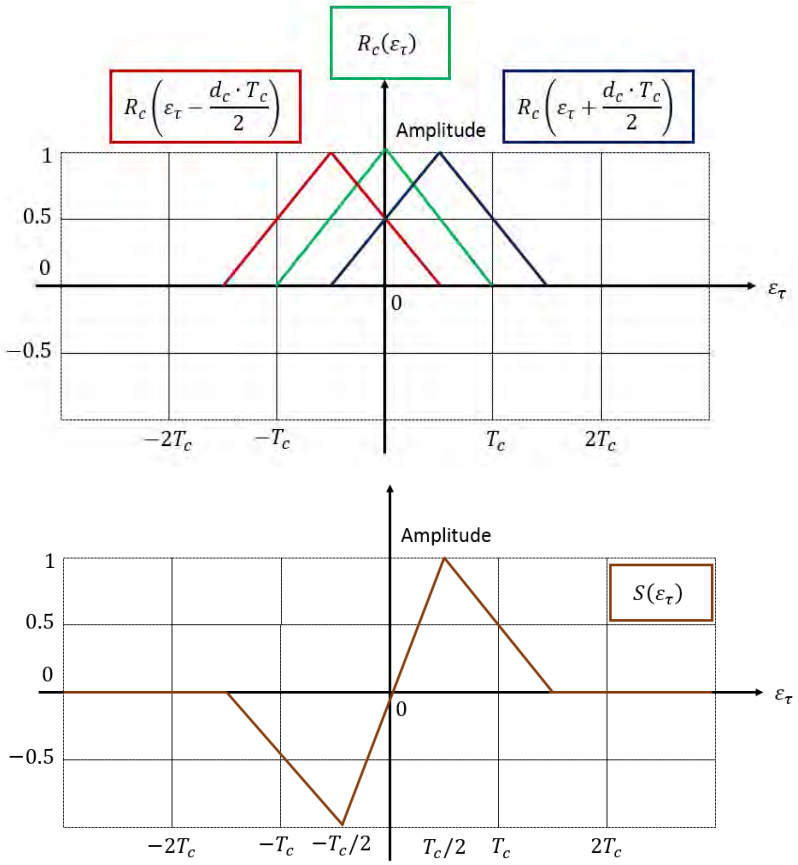

Figure 3-12. *The S-curve for the normalized BPSK correlation function with $T_c = 1$ chip.*

The DLL aims at tracking the zero-crossing of the discriminator function in the linear region around the code delay error ε_τ equal to zero, which in Figure 3-12 is the region $\left[-{}^{d_c \cdot T_c}/_2; {}^{d_c \cdot T_c}/_2\right]$.

In fact, the discriminator output can thus be seen as proportional to the true code delay error. It can therefore be used to command the NCO in charge of generating the prompt local code according to:

$$\hat{\tau}_{k+1} = \hat{\tau}_k - \frac{S_k}{\gamma} \quad (3\text{-}62)$$

where γ is the slope of the S-curve that depends on the choice of the code discriminator. As a consequence, a zero-crossing of the S-curve represents the code tracking locked point.

The most common discriminators, employed in GNSS receiver, are the non-coherent *Early Minus Late Power (EMLP)* and the *Dot Product (DP)* discriminators. These two discriminators are considered as non-coherent since they do not need carrier phase estimation to provide a relevant output, and therefore are insensitive to the PLL tracking behavior. This is translated into a higher tracking robustness. These two discriminators are defined by:

$$D_{EMLP}(\varepsilon_{\tau,k}) = \left(IE_k^2 + QE_k^2\right) - \left(IL_k^2 + QL_k^2\right) \quad (3\text{-}63)$$

$$D_{DP}(\varepsilon_{\tau,k}) = (IE_K - IL_K) \cdot IP_k + (QE_K - QL_K) \cdot QP_k \quad (3\text{-}64)$$

From Eq. (3-64), it can be easily noted that three complex correlators are needed for the DLL loop using the EMLP discriminator, whereas only two are required for the DP discriminator. The linear tracking region of the code discriminators is dependent upon the signal's correlation function shape. In fact, for a correct functioning of the discriminator function, the chip spacing must be selected so that the early and late correlator outputs are always evaluated at the correlation function main peak. For this, the EMLP and DP discriminators require a correlator spacing set less than 1 chip and 0.5 chip for the GPS L1 BPSK and Galileo BOC signals, respectively.

In order to remove the amplitude sensitivity of the code discriminators, normalization factors shall be applied to have a direct access to the code tracking error. The two most used normalization models for the EMLP and DP code discriminators are the following [Dierendonck et al., 1992]:

$$N_{EMLP,k} = \left(IE_k^2 + QE_k^2\right) + \left(IL_k^2 + QL_k^2\right) \quad (3\text{-}65)$$

$$N_{DP,k} = (IE_k + IL_k) \cdot IP_k + (QE_k + QL_k) \cdot QP_k \quad (3\text{-}66)$$

By applying the normalization factors of Eq. (3-65) and (3-66) to the two code discriminators expressions in Eq. (3-63) and (3-64), respectively, the normalized EMLP and DP discriminator functions are obtained [Julien, 2006]:

$$D_{EMLP_{norm},k} = \frac{(2 - \alpha \cdot d_c \cdot T_c) \cdot D_{EMLP,k}}{2\alpha \cdot N_{EMLP}} \quad (3\text{-}67)$$

$$D_{DP_{norm},k} = \frac{(2 - \alpha \cdot d_c \cdot T_c) \cdot D_{DP,k}}{2\alpha \cdot N_{DP}} \quad (3\text{-}68)$$

where:

- α corresponds to the absolute value of the slope of the autocorrelation function main peak that is $\alpha = 1$ for GPS L1 BPSK (1) signal and $\alpha = 3$ for Galileo E1 OS;
- T_c is the code chip period in second/chip;

- d_c refers to the Early – Later code replica chip spacing. Example: d_c is set to $0.5\ chip$ for GPS L1 BPSK (1) signal and d_c is set to $0.2\ chips$ for Galileo E1 OS.

3.5.3.3.2. DLL error analysis

The main error sources affecting the DLL tracking performance are the following:

- the thermal noise;
- multipath;
- the dynamic stress error;
- signal interference;

Taking into consideration that all the error sources provided above are independent from each-other, the code delay tracking error variance can be computed as:

$$\sigma_{DLL}^2 = \sigma_{th}^2 + \sigma_{mult}^2 + \sigma_{dyn}^2 + \sigma_{inter}^2 \qquad (3\text{-}69)$$

The receiver's oscillator noise and vibration, described in the carrier phase/frequency tracking loops, do not constitute an important voice in the code delay error budget and thus will not be presented [Ward and Fuchser, 2013].

3.5.3.3.2.1. Thermal Noise

It is important to understand that since the two above described code discriminators use differently the correlator outputs, they might be affected in a different manner by the errors' sources. This is in fact the case for the impact of thermal noise.

Taking into account only the thermal error and assuming a perfect normalization, no frequency error after the carrier wipe-off process, an ideal RF front-end filter with unity gain within $\pm B_f/2\ (Hz)$ and null elsewhere and a small code delay error, the non-coherent DLL EMLP tracking error variance due to the thermal noise is given by [Betz and Kolodziejski, 2000]:

$$\sigma_{EMLP,k}^2 = \left(\frac{c}{f_{code}}\right)^2 \cdot \frac{B_{DLL} \cdot \int_{-B_f/2}^{+B_f/2} S(f) sin^2(\pi f \cdot d_c \cdot T_c) df}{(2\pi)^2 \cdot C/N_0 \left(\int_{-B_f/2}^{+B_f/2} S(f) sin(\pi f \cdot d_c \cdot T_c) df\right)^2} \cdot \left(1 + \frac{\int_{-B_f/2}^{+B_f/2} S(f) sin^2(\pi f \cdot d_c \cdot T_c) df}{T_{int} \cdot C/N_0 \left(\int_{-B_f/2}^{+B_f/2} S(f) cos(\pi f \cdot d_c \cdot T_c) df\right)^2}\right) [m^2] \qquad (3\text{-}70)$$

Where:

- B_{DLL} is the code loop noise bandwidth in (Hz);
- $S(f)$ is the power spectral density of the signal at the receiver's antenna output that depends upon the modulation type and is normalized to unit area over infinite bandwidth;
- B_f is the double-sided font-end bandwidth in (Hz);
- $T_c = 1/f_{code}$ is the code chip period where f_{code} is the code chipping rate;
- d_c is the Early – Later code correlator spacing in (chips);
- C/N_0 is the carrier to noise ratio in (Hz);
- T_{int} is the integration time in second.

Assuming an infinite front-end bandwidth B_f, the EMLP closed-loop error variance can be approximated by [Julien et al., 2004]:

$$\sigma^2_{EMLP,k} = \left(\frac{c}{f_{code}}\right)^2 \cdot \frac{B_{DLL} \cdot d_c \cdot T_c}{2\alpha \cdot C/N_0} \cdot \left(1 + \frac{2}{(2 - \alpha \cdot d_c \cdot T_c) \cdot C/N_0 \cdot T_{int}}\right)[m^2] \quad (3\text{-}71)$$

Where α is the slope of the code autocorrelation function around the main peak, as already presented in Eq. (3-67) and (3-68), and points out the sensitivity of the DLL tracking error variance from the signal's modulation type.

In the same way and in same conditions, the DLL tracking error variance can be estimated for a DP discriminator as [Julien, 2006]:

$$\sigma^2_{DP,k} = \left(\frac{c}{f_{code}}\right)^2 \cdot \frac{B_{DLL} \cdot \int_{-B_f/2}^{+B_f/2} S(f) sin^2(\pi f \cdot d_c \cdot T_c) df}{(2\pi)^2 \cdot C/N_0 \left(\int_{-B_f/2}^{+B_f/2} S(f) sin(\pi f \cdot d_c \cdot T_c) df\right)^2} \cdot \left(1 + \frac{1}{T_{int} \cdot C/N_0 \left(\int_{-B_f/2}^{+B_f/2} S(f) df\right)^2}\right)[m^2] \quad (3\text{-}72)$$

Whereas, its approximation for an infinite front-end bandwidth B_f, is given by [Julien, 2006]:

$$\sigma^2_{DP,k} = \left(\frac{c}{f_{code}}\right)^2 \cdot \frac{B_{DLL} \cdot d_c \cdot T_c}{2\alpha \cdot C/N_0} \cdot \left(1 + \frac{1}{C/N_0 \cdot T_{int}}\right)[m^2] \quad (3\text{-}73)$$

Therefore, the code tracking loop performance is a function of the following parameters:

- *The correlator spacing*: the code tracking error is smaller for narrower correlator spacing;
- *The equivalent loop bandwidth*: primarily determined by the loop filter, it is chosen accordingly to the receiver dynamics. The narrower the loop bandwidth, the greater the noise resistance, but the longer it takes to respond to the user dynamics. Typically, for moderate receiver dynamics (such as vehicles), code tracking loop bandwidths on the order of 1 Hz are used when aided by the carrier tracking [Grewal et al., 2007];
- *The coherent integration time* T_{int}: the code tracking error squaring losses are inversely proportional to the integration time. Nevertheless, a long coherent integration time implies that the tracked parameters have a low update rate and the signal conditions may vary during that period;
- *The correlation function shape*: Eq. (3-71) and Eq. (3-73) show that Galileo E1 OS tracking error is lower w.r.t the GPS L1 one due to the three-times sharper autocorrelation function around the main peak of the Galileo spreading code.

3.5.3.3.2.2. Multipath

From the code tracking perspective, multipath reflections shifts the correlation peak and significantly distorts the correlation function between the received LOS signal and the locally-generated receiver's replica. When compared to the thermal noise impact on the code delay estimation accuracy, it can be

said that multipath represents the major tracking error source. The multipath-induced errors on the code delay estimation, if not properly mitigated, are reflected in the pseudorange observations and later projected into large position errors.

The S-curves for the EMLP and DP code discriminators for an unfiltered GPS L1 C/A signal under normal and multipath reception condition are depicted in Figure 3-13.

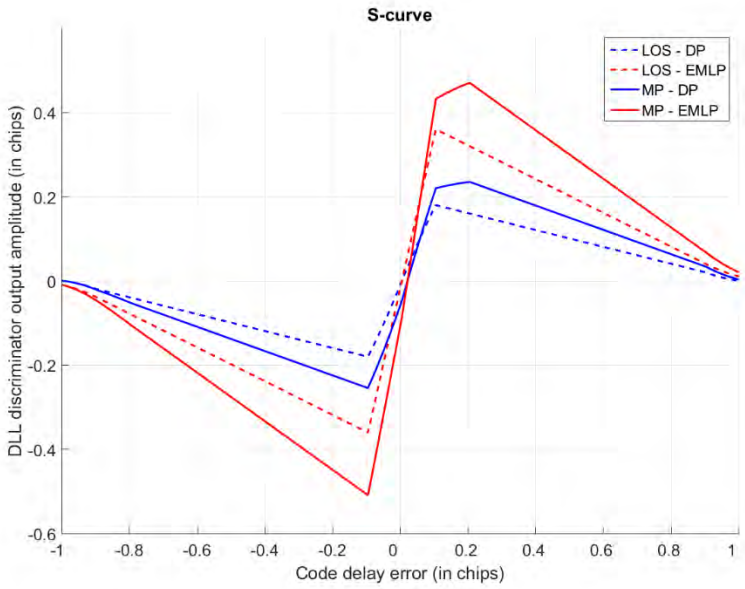

Figure 3-13. *Illustration of the S-curves for an unfiltered GPS L1 C/A signal in the absence of noise and in the presence of multipath.*

The S-curves in Figure 3-13, are presented for the EMLP and DP code discriminators with a chip spacing of $d_c = 0.2$ chip. In dashed blue is the Dot Product (DP) discriminator for the line-of-sight (LOS) signal reception, while the DP discriminator for a multipath-affected signal (MP) is given by the continuous blue line. The EMLP discriminator curves for the LOS and multipath signal are illustrated in dashed and continuous red lines, respectively. The EMLP and DP S-curves, illustrated in continuous red and blue lines, respectively, have biased estimation errors due to the tracking of a multipath-affected incoming signal that may result in a possible false lock at $+0.2\ chip$. It must be pointed out that the multipath-affected code delay discriminator curves are obtained by overlapping the S-curves of the ideal "LOS" signal and of its delayed echo.

Multipath impact on the code delay estimation depends on the correlator spacing and the DLL equivalent loop bandwidth. Indeed, a narrower correlator spacing and a larger code loop bandwidth result in a lower susceptibility of the code tracking loop w.r.t multipath. Therefore, the Galileo E1 OS signal offers a better resistance to the multipath error when comparing to the GPS L1 BPSK(1) signal due its narrower correlator spacing.

From the literature, multipath mitigation techniques can be separated in two classes:

- ***Spatial processing techniques***: employing antenna design in combination with signal propagation geometry characteristics to isolate the LOS signal [Grewal et al., 2007]. The following solutions fall in this category:

- *Antenna location analysis*: locating the less multipath-likely reception position or placing the antenna at ground level to minimize the possibility of having multipath delays coincident with the direct path delay;
- *Use of choke rings antennas*: that are big size, high cost ground plane antennas attenuating ground-reflected multipath signals. These antennas are used for multipath mitigation in airport GBAS stations;
- *Directive antenna arrays*: forming a high-gain pattern in the LOS direction and attenuating the signals coming from the other directions;
- *Long-term signal observation*: analysis of the satellite motion effect on multipath geometry through long observations. It is an effective method for differential GNSS stations;

➢ ***Time-domain processing techniques****:* referred to the multipath mitigation techniques operating at the GNSS receiver processing stage. This class groups the majority of GNSS multipath mitigation techniques and based on the level of intervention in the processing chain, the following sub-categories can be distinguished:

- *Techniques at the signal processing stage*: discriminating the LOS signal from the multipath echoes at the correlation level;
- *Techniques at the position level*: aiming at detection and further excluding biased measurement at the PVT level;
- *Advanced signal processing techniques*: employing the Vector Tracking (VT) technique that performs joint channel tracking and positioning solution via Kalman Filter estimation module.

The scope of this thesis is in fact driven toward the implementation of a dual constellation and single frequency GPS/Galileo L1/E1 VT algorithm capable of mitigation satellite outages and multipath induced errors. Further details of the proposed technique are given in Chapter 5.

3.5.3.3.2.3. Dynamic Stress Error

The previous analysis and remarks concerning the signal dynamics on the PLL loop, are still valid for the code delay tracking (DLL). Thus, the higher the DLL loop order is, the lower the dynamic stress error impact on the code tracking performance will be and therefore, a higher tracking robustness is achieved. However, most GNSS receivers use a PLL/FLL-aided DLL configuration that permits the absorption of the signal's dynamics from the carrier tracking loop and thus, the code DLL loop is responsible for tracking only the dynamic residuals. Therefore, the dynamic stress error impact on the 1st order DLL loop is provided by:

$$\theta_{e,\varepsilon_\tau} = \frac{T_{int}}{K_1} \cdot \frac{dR}{dt} \; [chip] \qquad (3\text{-}74)$$

where:

- K_1 is the 1st order coefficient of the discrete DLL [Stephens and Thomas, 1995];
- $\frac{dR}{dt}$ denotes the first order code delay estimation in $\left(\frac{chip}{s}\right)$.

3.5.3.3.3. DLL Tracking Error Threshold

When neglecting the influence of multipath and signal interference, the dominant code delay error sources are the thermal noise and the dynamic stress error. The conservative rule for the DLL tracking threshold is that the 3-sigma code error jitter due to the error sources given above, must not exceed the discriminator's linear region (half of the code discriminator region) as stated in [Kaplan and Hegarty, 2006]. Thus, the code tracking threshold for the two signals of interest is expressed as:

$$3\sigma_{DLL} = 3\sigma_{DLL,th} + \theta_{e,\varepsilon_\tau} \leq \frac{d_c}{2} \tag{3-75}$$

where:

- $\sigma_{DLL,th}$ denotes the 1-sigma phase jitter due to the thermal noise provided in Eq. (3-71) and (3-73);
- $\theta_{e,\varepsilon_\tau}$ is the dynamic stress error affecting the DLL tracking loop, defined in Eq. (3-74).

3.5.3.4. Lock detection and C/N_0 estimation

The lock detector objective is to assess whether the incoming signal is correctly being tracked in the channel level [Kaplan and Hegarty, 2006]. The phase lock is detected using the normalized estimate of the cosine of twice the carrier phase $\left(C_{2\varphi_k}\right)$. Whereas for the code delay lock loop (DLL), the tracking is not pursued when the carrier-to-noise rate estimation is low. Thus, the phase lock quality indicator is computed from the Prompt correlator outputs and estimated as follows [Parkinson, 1996]:

$$C_{2\varphi_k}(k) = \frac{NBD_k}{NBP_k} \tag{3-76}$$

where the narrowband power difference at the k^{th} epoch is provided from the In-Phase and Quadrature Prompt (IP, QP) correlator outputs as:

$$NBD_k = \left(\sum_{i=1}^{M} IP_i\right)_k^2 - \left(\sum_{i=1}^{M} QP_i\right)_k^2 \tag{3-77}$$

where M denotes the number of coherent integrations.

Whereas, the narrowband signal plus noise power is given by:

$$NBP_k = \left(\sum_{i=1}^{M} IP_i\right)_k^2 + \left(\sum_{i=1}^{M} QP_i\right)_k^2 \tag{3-78}$$

Afterwards, the receiver checks the estimated phase lock test value against pre-defined thresholds, whose value is strictly dependent on the application type and the accuracy/availability trade-off. The phase lock can be detected when:

$$C_{2\varphi_k} \geq 0.4 \tag{3-79}$$

The carrier-to-noise ratio per tracking channel is estimated using the signal-plus-noise power ratio measured in different noise bandwidths. Therefore, the wideband power computed over M correlation intervals of 1 ms length can be expressed as:

$$WBP_k = \left(\sum_{i=1}^{M} \left(IP_i^2 + QP_i^2 \right) \right)_k^2 \quad (3\text{-}80)$$

Therefore, the normalized power is defined as [Dierendonck et al., 1992]:

$$NP_k = \frac{NBP(k)}{WBP(k)} \quad (3\text{-}81)$$

The estimated mean of the normalized power, representing the code lock detector, is given by [Parkinson, 1996]:

$$\mu_{NP} = \frac{1}{K} \cdot \sum_{k=1}^{K} NP_k \quad (3\text{-}82)$$

where $K = 50$ represents the number of non-coherent integrations averaged over 1 second interval.

Finally, the estimated carrier-to-noise ratio is computed as:

$$C/N_{0_{est}} = 10\log_{10} \cdot \left(\frac{1}{T} \cdot \frac{\mu_{NP} - 1}{M - \mu_{NP}} \right) \quad (3\text{-}83)$$

for which T is the non-coherent integration time.

3.6. Conclusions

In this chapter, the GNSS receiver processing has been presented in details. A conceptual division in two main parts was envisaged in this chapter: the measurements errors description from section 3.1 to 3.4.1 and the detailed scalar receiver synchronization in the remaining sections.

Concerning the measurement errors, a separation has been made between the error sources affecting the signal propagation delay and those that impact the tracking loops performance. Among all the possible propagation delay sources provided in section 3.1, the attention was directed to the ionosphere contribution, representing the major atmosphere-induced delay to the code measurement after the correction/estimation of the satellite and receiver clock errors. Therefore, the ionosphere residual error variance models for the GPS and Galileo signals, respectively, were provided in 3.1.3. Whereas, the measurement errors affecting the code/carrier synchronization, with the emphasis on the receiver noise and multipath, were described in section 3.2. In fact, the oscillator phase noise model with the inclusion of the phase and frequency noise PSDs formulation, based on the Allan variance parameters, will be latter referred to in the receiver's clock error modelling in the following chapter. The correlation in-time characteristic of the ionosphere residual error, modelled as a first order GM process, along with a summary of the measurement error was given in section 3.3.

The second part of the chapter starts with the overall picture of the GNSS receiver provided through the block diagram representation. The receiver's analog section was presented in section 3.4.1 where its main components were described such as: the RF front-end, the ADC and the receiver's oscillator. Whereas, in 3.5 the receiver's digital block was detailed. The generation of the three correlator output pairs was introduced in 3.5.1, required for the incoming signals code delay and Doppler frequency search performed in the acquisition step (3.5.2). A particular attention was directed toward the description of the code (DLL) and carrier (PLL/FLL) tracking loops in 3.5.3 with an emphasis on the

discriminator functions and the errors analysis aiming at the provision of the DLL/FLL/PLL error variances. Last but not least, the C/N_0 estimation for the scalar tracking receiver was provided in the end of this chapter.

4. Scalar Receiver Navigation Processor

This chapter aims at providing a clear description of the GNSS scalar dual-constellation receiver structure and more particularly its measurement processing and navigation solution computation.

This chapter starts with the provision of the raw pseudorange and pseudorange rate measurements' model, including the atmospheric propagation delays and tracking errors' contribution, for the dual-constellation receiver in section 4.1. Then, section 4.2 describes in details the corrected measurement generation process with an emphasis on the appearance of the ionosphere residuals and residuals rates in the pseudorange and pseudorange rate measurements, respectively, after the application of the ionosphere correction models.

Section 4.3 introduces the two navigation algorithms namely, the Weighted Least Square (WLS) and the Extended Kalman Filter (EKF) adopted in this thesis to estimate the user's navigation solution in the presence of the ionosphere residuals. The former technique is initially used to provide the first user's position estimation and afterwards, a switch toward the EKF algorithm is applied in the implemented scalar receiver configuration. In details, the state transition and measurement model of the EKF technique are both provided in details in section 4.3.2.

Finally, the chapter conclusions will be drawn in 4.4.

4.1. Raw Measurement Model

Recalling the expression in Eq. (3-23), the pseudorange measurement ρ for a given satellite i at epoch k, is modelled as follows:

$$\rho^{(i)}(k) = \left(\tau^{(i)}(k) + \Delta t^{(i)}_{Rx-sat}(k)\right) \cdot c + \varepsilon^{(i)}_{tot}(k) + \varepsilon^{(i)}_{n}(k)\ [m] \qquad (4\text{-}1)$$

where:

- τ is the true signal propagation time from the satellite to the receiver on ground, expressed in $[s]$;
- $\Delta t^{(i)}_{Rx-sat}$ represents the error between the receiver (Rx) and the i^{th} satellite clock time, expressed in $[s]$;
- c denotes the speed of light in $[m/s]$;
- $\varepsilon^{(i)}_{tot}$ denotes the propagation delays from Eq. (3-23) that are grouped in one term, expressed in $[m]$;
- $\varepsilon^{(i)}_{n}$ represents the synchronization errors due to receiver noise, multipath and interference in $[m]$.

According to the relation in Eq. (4-1) and since this thesis focuses on the dual-constellation GPS/Galileo receiver, it is thus required to present the propagation delays for both GPS and Galileo constellations as:

$$\begin{aligned}\rho_{GPS}^{(i)}(k) &= \left(\tau_{GPS}^{(i)} + \Delta t_{Rx-sat,GPS}^{(i)}\right)(k)\cdot c + \varepsilon_{tot,GPS}^{(i)}(k) + \varepsilon_{n,GPS}^{(i)}(k)\\ \rho_{Gal}^{(i)}(k) &= \left(\tau_{Gal}^{(i)} + \Delta t_{Rx-sat,Gal}^{(i)}\right)(k)\cdot c + \varepsilon_{tot,Gal}^{(i)}(k) + \varepsilon_{n,Gal}^{(i)}(k)\end{aligned} \quad (4\text{-}2)$$

It is of great interest to further develop the clock error term $\Delta t_{Rx-sat}^{(i)}$ as following:

$$\begin{aligned}\Delta t_{Rx-sat,GPS}^{(i)}(k) &= \Delta t_{Rx-GPS}(k) - \Delta t_{sat,GPS}^{(i)}(k)\\ &= \left(t_{Rx}(k) - t_{GPS}(k)\right) - \left(t_{sat,GPS}^{(i)}(k) - t_{GPS}(k)\right)\end{aligned} \quad (4\text{-}3)$$

where:

- t_{Rx} is the receiver time corresponding to epoch k of the receiver's clock in $[s]$;
- $t_{sat,GPS}^{(i)}$ is the i^{th} satellite clock time according to the satellite clock in $[s]$;
- t_{GPS} represents the GPS system time, computed by the GPS Master Control Station on ground as the weighted average of each GPS satellite time measurement, expressed also in $[s]$;

Performing the same steps for the clock term concerning the i^{th} Galileo satellite, the following expression can be written:

$$\begin{aligned}\Delta t_{Rx-sat,Gal}^{(i)}(k) &= \Delta t_{Rx-Gal}(k) - \Delta t_{sat,Gal}^{(i)}(k)\\ &= \left(t_{Rx}(k) - t_{Gal}(k)\right) - \left(t_{sat,Gal}^{(i)}(k) - t_{Gal}(k)\right)\end{aligned} \quad (4\text{-}4)$$

with $t_{sat,Gal}^{(i)}$ and t_{Gal} representing the i^{th} Galileo satellite clock time and the Galileo system time, respectively, expressed in $[s]$.

Focusing on the first term of Eq. (4-4), denoting the receiver's clock error w.r.t the Galileo system time, the following modifications can be applied:

$$\begin{aligned}\Delta t_{Rx-Gal}(k) &= t_{Rx}(k) - t_{Gal}(k)\\ &= \left(t_{Rx}(k) - t_{GPS}(k)\right) + \left(t_{GPS}(k) - t_{Gal}(k)\right)\\ &= \Delta t_{Rx-GPS}(k) + \Delta t_{GPS/Gal}(k)\end{aligned} \quad (4\text{-}5)$$

where $\Delta t_{GPS/Gal}$ is the inter-constellation clock offset, which in this thesis is considered as provided in a very reliable way by the Galileo navigation message. It is thus neglected from the propagation delay computation.

In other words, the receiver's clock error w.r.t Galileo time (t_{Gal}) can be approximated to the receiver's clock error w.r.t the GPS system time as:

$$\begin{aligned}\Delta t_{Rx-Gal}(k) &= \Delta t_{Rx-GPS}(k) + \Delta t_{GPS/Gal}(k)\\ &\approx \Delta t_{Rx-GPS}(k)\end{aligned} \quad (4\text{-}6)$$

According to the expression in Eq. (4-6) and within the hypothesis of omitting the inter-constellation clock term, it may be stated that only one receiver clock bias is present in the pseudorange measurements for both the GPS and Galileo constellations.

Based on the relations provided in Eq. (4-1) and (4-6), the code propagation delay for the i^{th} GPS satellite at epoch k, is provided by:

$$\begin{aligned}\rho_{GPS}^{(i)}(k) &= \left(\tau_{GPS}^{(i)}(k) + \Delta t_{Rx-sat,GPS}^{(i)}(k)\right)\cdot c + \varepsilon_{tot,GPS}^{(i)}(k) + \varepsilon_{n,GPS}^{(i)}(k) \\ &= \left[\tau_{GPS}^{(i)}(k) + \left(\Delta t_{Rx-GPS}(k) - \Delta t_{sat,GPS}^{(i)}(k)\right)\right]\cdot c + \varepsilon_{tot,GPS}^{(i)}(k) + \varepsilon_{n,GPS}^{(i)}(k) \\ &= c\cdot\tau_{GPS}^{(i)}(k) + c\cdot\Delta t_{Rx-GPS}(k) - c\cdot\Delta t_{sat,GPS}^{(i)}(k) + \varepsilon_{tot,GPS}^{(i)}(k) + \varepsilon_{n,GPS}^{(i)}(k) \\ &= d_{GPS}^{(i)}(k) + b_{Rx-GPS}(k) - b_{s,GPS}^{(i)}(k) + \varepsilon_{tot,GPS}^{(i)}(k) + \varepsilon_{n,GPS}^{(i)}(k)\ [m]\end{aligned} \qquad (4\text{-}7)$$

where the newly introduced terms for each epoch k denote:

- $d_{GPS/Gal}^{(i)} = \sqrt[2]{\left(x_{s,GPS/Gal}^{(i)}(k) - x_u(k)\right)^2 + \left(y_{s,GPS/Gal}^{(i)}(k) - y_u(k)\right)^2 + \left(z_{s,GPS/Gal}^{(i)}(k) - z_u(k)\right)^2}$ is the true geometrical distance between the i^{th} GPS/Galileo satellite and the receiver for which:
  - $\left(x_{s,GPS/Gal}^{(i)}, y_{s,GPS/Gal}^{(i)}, z_{s,GPS/Gal}^{(i)}\right)$ denotes the i^{th} GPS/Galileo satellite position at transmit time, computed from the broadcast ephemeris file and expressed in the ECEF frame;
  - $\left(x_u^{(i)}, y_u^{(i)}, z_u^{(i)}\right)$ denotes the user's position at receive time, obtained from the user's trajectory file and expressed in the ECEF frame;
- b_{Rx-GPS} is the receiver's clock bias expressed in meter;
- $b_{s,GPS}^{(i)}$ is the i^{th} GPS satellite clock error expressed in meter;

The same relation also holds for the code propagation delay of the Galileo satellites, expressed as:

$$\rho_{Gal}^{(i)}(k) = d_{Gal}^{(i)}(k) + b_{Rx-GPS}(k) - b_{s,Gal}^{(i)}(k) + \varepsilon_{tot,Gal}^{(i)}(k) + \varepsilon_{n,GPS}(k)\ [m] \qquad (4\text{-}8)$$

where the common receiver's clock bias term (b_{Rx-GPS}) between the two pseudorange measurements is illustrated in green.

For simplicity of notation, the receiver's clock bias is substituted by $b_{Rx-GPS} = b_{Rx}$.

In order to clearly observe the atmosphere-induced delays, the GPS and Galileo propagation delays can be written as:

$$\begin{aligned}\rho_{GPS}^{(i)}(k) &= d_{GPS}^{(i)}(k) + b_{Rx}(k) - b_{s,GPS}^{(i)}(k) + \varepsilon_{iono,GPS}^{(i)}(k) + \varepsilon_{tropo,Gal}^{(i)}(k) + \varepsilon_{n,GPS}^{(i)}(k)[m] \\ \rho_{Gal}^{(i)}(k) &= d_{Gal}^{(i)}(k) + b_{Rx}(k) - b_{s,Gal}^{(i)}(k) + \varepsilon_{iono,Gal}^{(i)}(k) + \varepsilon_{tropo,Gal}^{(i)}(k) + \varepsilon_{n,Gal}^{(i)}(k)\ [m]\end{aligned} \qquad (4\text{-}9)$$

where:

- $\varepsilon_{iono,GPS}^{(i)}$ and $\varepsilon_{iono,Gal}^{(i)}$ represent the ionosphere propagation delay contributions on the GPS and Galileo pseudorange measurements, respectively, expressed in $[m]$.

- $\varepsilon_{tropo,GPS}^{(i)}$ and $\varepsilon_{tropo,Gal}^{(i)}$ represent the troposphere propagation delay contributions on the GPS and Galileo pseudorange measurements, respectively, expressed in $[m]$.

A similar relation can be written for the carrier's phase delay with the difference that the carrier phase measurement experiences a phase advance due to the ionosphere delay given by:

$$\begin{aligned}\varphi_{GPS}^{(i)}(k) &= d_{GPS}^{(i)}(k) + b_{Rx}(k) - b_{s,GPS}^{(i)}(k) - \varepsilon_{iono,GPS}^{(i)}(k) + N_{GPS}^{(i)}(k) + \varepsilon_{tropo,GPS}^{(i)}(k) + \varepsilon_{n,p,GPS}^{(i)}\ [rad]\\ \varphi_{Gal}^{(i)}(k) &= d_{GPS}^{(i)}(k) + b_{Rx}(k) - b_{s,Gal}^{(i)}(k) - \varepsilon_{iono,Gal}^{(i)}(k) + N_{Gal}^{(i)}(k) + \varepsilon_{tropo,Gal}^{(i)}(k) + \varepsilon_{n,p,Gal}^{(i)}\ [rad]\end{aligned} \quad (4\text{-}10)$$

Where:

- $N_{GPS}^{(i)}$ and $N_{Gal}^{(i)}$ represent the carrier phase ambiguities for the GPS and Galileo carrier phase measurement, respectively, expressed in radian;
- $\varepsilon_{n,p,GPS}^{(i)}$ and $\varepsilon_{n,p,Gal}^{(i)}$ denote the phase synchronization errors due to receiver noise, multipath and interference in radian;

Neglecting the contribution of the slowly varying satellite clock error and troposphere delay, the pseudorange rate measurements (in m/s) for the i^{th} GPS and Galileo satellites is expressed as follows:

$$\begin{aligned}\dot{\rho}_{GPS/Gal}^{(i)}(k) = &\left(\dot{x}_{s,GPS/Gal}^{(i)}(k) - \dot{x}_u(k)\right)\cdot a_{x,GPS/Gal}^{(i)}(k) + \left(\dot{y}_{s,GPS/Gal}^{(i)}(k) - \dot{y}_u(k)\right)\cdot a_{y,GPS/Gal}^{(i)}(k)\\ &+ \left(\dot{z}_{s,GPS/Gal}^{(i)}(k) - \dot{z}_u(k)\right)\cdot a_{z,GPS/Gal}^{(i)} + \dot{b}_{Rx}(k) + \dot{\varepsilon}_{iono,GPS/Gal}^{(i)}(k) + \dot{\varepsilon}_{n,GPS/Gal}^{(i)}(k)\end{aligned} \quad (4\text{-}11)$$

Where:

- $a_{l,GPS/Gal}^{(i)}$ denote the LOS projections along the three ECEF axes $(l = x, y, z)$ that are computed as:

$$\begin{aligned}a_{x,GPS/Gal}^{(i)} &= \frac{\left(x_s^{(i)}(k) - x_u(k)\right)}{\sqrt[2]{\left(x_s^{(i)}(k) - x_u(k)\right)^2 + \left(y_s^{(i)}(k) - y_u(k)\right)^2 + \left(z_s^{(i)}(k) - z_u(k)\right)^2}}\\ a_{y,GPS/Gal}^{(i)} &= \frac{\left(y_s^{(i)}(k) - y_u(k)\right)}{\sqrt[2]{\left(x_s^{(i)}(k) - x_u(k)\right)^2 + \left(y_s^{(i)}(k) - y_u(k)\right)^2 + \left(z_s^{(i)}(k) - z_u(k)\right)^2}}\\ a_{z,GPS/Gal}^{(i)} &= \frac{\left(z_s^{(i)}(k) - z_u(k)\right)}{\sqrt[2]{\left(x_s^{(i)}(k) - x_u(k)\right)^2 + \left(y_s^{(i)}(k) - y_u(k)\right)^2 + \left(z_s^{(i)}(k) - z_u(k)\right)^2}}\end{aligned} \quad (4\text{-}12)$$

- $\left(\dot{x}_s^{(i)}, \dot{y}_s^{(i)}, \dot{z}_s^{(i)}\right)(k)$ and $(\dot{x}_u, \dot{y}_u, \dot{z}_u)(k)$ represent the i^{th} satellite and user's velocities, respectively, expressed in the ECEF reference frame in $\left[\frac{m}{s}\right]$;
- $\dot{b}_{Rx}$ is the receiver's clock drift common for both the GPS and Galileo Doppler measurements expressed in $\left[\frac{m}{s}\right]$;
- $\dot{\varepsilon}_{iono,GPS/Gal}^{(i)}$ denotes the ionosphere delay rate appearing in the GPS and Galileo pseudorange rate measurements, respectively, also expressed in $\left[\frac{m}{s}\right]$;
- $\dot{\varepsilon}_{n,GPS/Gal}^{(i)}(k)$ represents the synchronization errors due to receiver noise, multipath and interference affecting the GPS/Galileo pseudorange rate measurements.

When developing the phase measurement difference between two consecutive epochs $(k-1 \rightarrow k)$, the ionosphere delay rate term $\left(\dot{\varepsilon}^{(i)}_{iono,GPS|Gal}\right)$ emerges and is expressed as:

$$\dot{\varepsilon}^{(i)}_{iono,GPS/Gal} = \frac{\varepsilon^{(i)}_{iono,GPS/Gal}(k-1) - \varepsilon^{(i)}_{iono,GPS/Gal}(k)}{T} \; [m/s] \tag{4-13}$$

Finally, the code and phase propagation delays presented in Eq. (4-9) and (4-10), are further used to initialize the code/carrier tracking loops as follows:

$$\begin{aligned} \tau^{(i)}_{0,GPS|Gal}(k) &= \frac{\rho^{(i)}_{GPS/Gal}(k)}{c} \; [s] \\ \varphi^{(i)}_{0,GPS|Gal}(k) &= \varphi^{(i)}_{GPS/Gal} \; [rad] \\ f_{D}{}^{(i)}_{0,GPS|Gal}(k) &= \frac{\left(\varphi^{(i)}_{GPS/Gal}(k) - \varphi^{(i)}_{GPS/Gal}(k-1)\right)}{2\pi \cdot T} \; [Hz] \end{aligned} \tag{4-14}$$

where the triplet $\left(\tau^{(i)}_{0,GPS|Gal}, \varphi^{(i)}_{0,GPS|Gal}, f_{D}{}^{(i)}_{0,GPS|Gal}\right)$ represents the true code delay, carrier phase and Doppler frequency for the i^{th} GPS and Galileo tracking channel.

4.2. Corrected Measurement Model

After the application of the Klobuchar and NeQuick ionosphere error correction models to the GPS and Galileo pseudorange measurements, respectively, a resultant ionosphere residual appears in the received observations. The same happens after the application of the tropospheric and satellite clock correction models. Therefore, the corrected pseudorange and pseudorange rate measurement models for both GPS and Galileo satellites remain the same as in the above section, but with the appearance of residuals for the ionosphere, troposphere and satellite clock terms.

Therefore, the corrected GPS and Galileo pseudorange measurements can be written as:

$$\begin{aligned} \rho^{(i)}_{GPS,corr}(k) &= d^{(i)}_{GPS}(k) + b_{Rx}(k) - b^{(i)}_{s,GPS}(k) + b^{(i)}_{iono,GPS}(k) + b^{(i)}_{tropo,Gal}(k) + \varepsilon^{(i)}_{n,GPS}(k) [m] \\ \rho^{(i)}_{Gal,corr}(k) &= d^{(i)}_{Gal}(k) + b_{Rx}(k) - b^{(i)}_{s,Gal}(k) + b^{(i)}_{iono,Gal}(k) + b^{(i)}_{tropo,Gal}(k) + \varepsilon^{(i)}_{n,Gal}(k) \; [m] \end{aligned} \tag{4-15}$$

where:

- $b^{(i)}_{iono,GPS/Gal}$ denote the GPS and Galileo ionosphere residuals affecting the i^{th} satellite after the application of the Klobuchar and NeQuick ionosphere correction models, respectively, expressed in $\left[\frac{m}{s}\right]$;
- $b^{(i)}_{tropo,GPS/Gal}$ denote the GPS and Galileo troposphere residuals affecting the i^{th} satellite after the application of the troposphere correction model, respectively, expressed in $\left[\frac{m}{s}\right]$.

A similar relation can be written for the corrected GPS and Galileo pseudorange rate measurements as follows:

$$\begin{aligned} \dot{\rho}^{(i)}_{GPS/Gal,corr}(k) = &\left(\dot{x}^{(i)}_{s,GPS/Gal}(k) - \dot{x}_u(k)\right) \cdot a^{(i)}_{x,GPS/Gal}(k) + \left(\dot{y}^{(i)}_{s,GPS/Gal}(k) - \dot{y}_u(k)\right) \cdot a^{(i)}_{y,GPS/Gal}(k) \\ &+ \left(\dot{z}^{(i)}_{s,GPS/Gal}(k) - \dot{z}_u(k)\right) \cdot a^{(i)}_{z,GPS/Gal} + \dot{b}_{Rx}(k) + \dot{b}^{(i)}_{iono,GPS/Gal}(k) + \dot{\varepsilon}^{(i)}_{n,GPS/Gal}(k) \end{aligned} \tag{4-16}$$

where $\dot{b}_{iono,GPS/Gal}^{(i)}(k)$ represents the ionosphere residual rate affecting the i^{th} pseudorange rate measurement for the GPS and Galileo constellations, expressed as:

$$\dot{b}_{iono,GPS|Gal}^{(i)}(k) = \frac{b_{iono,GPS/Gal}^{(i)}(k-1) - b_{iono,GPS/Gal}^{(i)}(k)}{T} \quad [m/s] \tag{4-17}$$

Finally, the corrected pseudorange and pseudorange measurements from the $i = 1 \div N$ GPS L1/ Galileo E1 tracking channels, respectively provided in Eq. (4-15) and Eq.(4-16), are included in the measurement vector $\boldsymbol{z_k}$ as input to the scalar navigation filter provided by:

$$\boldsymbol{z_{k,scalar}} = \left[\left(\rho_{corr}^{(1)}\ \rho_{corr}^{(2)}\ \cdots \rho_{corr}^{(N)}\right) \vdots \left(\dot{\rho}_{corr}^{(1)}\ \dot{\rho}_{corr}^{(2)}\ \cdots \dot{\rho}_{corr}^{(N)}\right)(k)\right]_{2N\times 1} \tag{4-18}$$

4.3. Navigation processor

This section discusses the navigation solution estimation techniques implemented in the scalar tracking receiver and that are also used at the initialization step of the vector tracking algorithm, beginning with the description of the Weighted Least Square (WLS) technique and later with the discrete Extended Kalman Filter (EKF) navigation solution. Both techniques use as input the pseudorange and pseudorange rate measurements, obtained from the code and carrier tracking blocks, respectively, to estimate the user's position and velocity 3-D vectors along with the clock bias and drift terms.

In this work, the Position and Velocity (PV) state vector is considered since it is appropriate for automotive kinematic applications that are characterized by moderate dynamics. Even though a dual constellation receiver is implemented in this thesis, in section 4.1 was shown that a single receiver clock bias is present in the pseudorange measurements for both the GPS and Galileo constellations.

Based on these considerations, the absolute PVT state vector that is common for both the WLS and EKF navigation algorithms can be given in vector format as:

$$\boldsymbol{X} = \begin{bmatrix} x \\ \dot{x} \\ y \\ \dot{y} \\ z \\ \dot{z} \\ b_{Rx} \\ \dot{b}_{Rx} \end{bmatrix}_{8\times 1} \tag{4-19}$$

where:

- $[x, y, z]^T$ represents the 3-D user's position expressed in the ECEF frame in $[m]$;
- $[\dot{x}, \dot{y}, \dot{z}]^T$ represents the 3-D user's velocity expressed in the ECEF frame in $[m/s]$;
- $[b_{Rx}, \dot{b}_{Rx}]^T$ denote the user's clock bias in $[m]$ and drift in $\left[\frac{m}{s}\right]$, respectively.

For high dynamics GNSS applications, the augmentation of the state vector with the three acceleration states along each ECEF axis and the use of higher carrier tracking loop orders are strongly suggested. In this dissertation, the pseudorange and pseudorange rate measurements, required for the PV

navigation solution, come from the filtered DLL and 3rd order PLL outputs, respectively. Recalling the observations' expressions in Eq. (4-15) and (4-16), two direct links can be observed between:

- The code delay measurement from the DLL block ↔ user's position and clock bias (x, y, z, b_{Rx});
- The Doppler frequency measurement from the PLL block ↔ user's velocity and clock drift $(\dot{x}, \dot{y}, \dot{z}, \dot{b}_{Rx})$;

4.3.1. Weighted Least Square (WLS) solution

Both the pseudorange and pseudorange rate observations, coming from N tracked satellites, are each modeled as nonlinear equations involving one set of four unknowns. Obviously, at least four pseudorange and pseudorange rate measurement pairs from four satellites are required to solve the equations for the eight total unknowns. A simple approach to solving these equations is to linearize them about an approximate user position and solve them iteratively, until the change in the estimate is sufficiently small [Parkinson, 1996]. The idea is to start with a rough estimate of the user PV and clock terms and further, refine the estimation in successive iterations to best fit the incoming measurements. Let $\boldsymbol{x}_0 = (x_0, y_0, z_0)$, $\boldsymbol{v}_0 = (\dot{x}_0, \dot{y}_0, \dot{z}_0)$ and $\boldsymbol{b}_0 = (b_0, \dot{b}_0)$ be the initial guesses of the user's position, velocity and clock bias/drift terms, respectively. The corresponding pseudorange and pseudorange rate approximations for each satellite i, based on the initial estimates $\boldsymbol{x}_0$, $\boldsymbol{v}_0$ and $\boldsymbol{b}_0$ can be written as [Misra, P., 2001]:

$$
\begin{aligned}
\rho_0^{(i)} &= \left|\boldsymbol{x_s^{(i)}} - \boldsymbol{x_0}\right| + b_0 + \varepsilon_n^{(i)} \\
&= \sqrt[2]{\left(x_s^{(i)} - x_0\right)^2 + \left(y_s^{(i)} - y_0\right)^2 + \left(z_s^{(i)} - z_0\right)^2} + b_0 + \varepsilon_n^{(i)} \\
\delta\dot{\rho}^{(i)} &= (\boldsymbol{v_s^{(i)}} - \boldsymbol{v_0}) \cdot \boldsymbol{a_0^{(i)}} + c \cdot (\dot{b} - \dot{b}_0) + \dot{\varepsilon}_n^{(i)} \\
&= \left(\dot{x}_s^{(i)} - \dot{x}_0\right) \cdot \frac{\left(x_s^{(i)} - x_0\right)}{\sqrt[2]{\left(x_s^{(i)} - x_0 - \delta x\right)^2 + \left(y_s^{(i)} - y_0 - \delta y\right)^2 + \left(z_s^{(i)} - z_0 - \delta z\right)^2}} \\
&+ \left(\dot{y}_s^{(i)} - \dot{y}_0\right) \cdot \frac{\left(y_s^{(i)} - y_0\right)}{\sqrt[2]{\left(x_s^{(i)} - x_0 - \delta x\right)^2 + \left(y_s^{(i)} - y_0 - \delta y\right)^2 + \left(z_s^{(i)} - z_0 - \delta z\right)^2}} \\
&+ \left(\dot{z}_s^{(i)} - \dot{z}_0\right) \cdot \frac{\left(z_s^{(i)} - z_0\right)}{\sqrt[2]{\left(x_s^{(i)} - x_0 - \delta x\right)^2 + \left(y_s^{(i)} - y_0 - \delta y\right)^2 + \left(z_s^{(i)} - z_0 - \delta z\right)^2}} \\
&+ c \cdot \left(\dot{b} - \dot{b}_0\right) + \dot{\varepsilon}_n^{(i)}
\end{aligned}
\qquad (4\text{-}20)
$$

The true states are linked to their initial guesses through the following relations:

$$
\begin{aligned}
\boldsymbol{x} &= \boldsymbol{x}_0 + \delta\boldsymbol{x} \\
b &= b_0 + \delta b \\
\boldsymbol{v} &= \boldsymbol{v}_0 + \delta\boldsymbol{v} \\
\dot{b} &= \dot{b}_0 + \delta\dot{b}
\end{aligned}
\qquad (4\text{-}21)
$$

where:

- $\delta\boldsymbol{x}$ and $\delta\boldsymbol{v}$ are the 3-D position and velocity corrections along the three axes, respectively, which are applied to the initial estimates;

- $\boldsymbol{x_s^{(i)}} = [x_s^{(i)}, y_s^{(i)}, z_s^{(i)}]^T$ and $\boldsymbol{v_s^{(i)}} = [\dot{x}_s^{(i)}, \dot{y}_s^{(i)}, \dot{z}_s^{(i)}]^T$ represent the 3-D i[th] satellite position and velocity vectors in the ECEF frame;
- $\boldsymbol{a_{i,0}}$ are the direction cosines (LOS projection) from the estimated receiver location to the satellite;
- δb and $\delta \dot{b}$ denote the clock bias and drift corrections, respectively.;
- $\varepsilon_n^{(i)}$ and $\dot{\varepsilon}_n^{(i)}$ denote the receiver's noise effect on the pseudorange and pseudorange rate measurements, respectively.

The Least Square (LS)-based techniques solve the navigation solution around the state vector correction term. In this work, this is achieved by developing a system of linear equations for each locked satellite to determine the unknown terms $\delta \boldsymbol{x}$, δb, $\delta \boldsymbol{v}$ and $\delta \dot{b}$ given by:

$$
\begin{aligned}
\delta\rho^{(i)} &= \left|\boldsymbol{x_s^{(i)}} - \boldsymbol{x_0} - \delta\boldsymbol{x}\right| + (b_0 + \delta b) + \varepsilon_n^{(i)} \\
&= \sqrt[2]{\left(x_s^{(i)} - x_0 - \delta x\right)^2 + \left(y_s^{(i)} - y_0 - \delta y\right)^2 + \left(z_s^{(i)} - z_0 - \delta z\right)^2} + (b_0 + \delta b) + \varepsilon_n^{(i)} \\
\delta\dot{\rho}^{(i)} &= \left|\boldsymbol{v_s^{(i)}} - \boldsymbol{v_0} - \delta\boldsymbol{v}\right| \cdot \boldsymbol{a_i} + (\dot{b}_0 + \delta\dot{b}) + \dot{\varepsilon}_n^{(i)} \\
&= \left(\dot{x}_s^{(i)} - \dot{x}_0 - \delta\dot{x}\right) \cdot \frac{\left(x_s^{(i)} - x_0 - \delta x\right)}{\sqrt[2]{\left(x_s^{(i)} - x_0 - \delta x\right)^2 + \left(y_s^{(i)} - y_0 - \delta y\right)^2 + \left(z_s^{(i)} - z_0 - \delta z\right)^2}} \\
&+ \left(\dot{y}_s^{(i)} - \dot{y}_0 - \delta\dot{y}\right) \cdot \frac{\left(y_s^{(i)} - y_0 - \delta y\right)}{\sqrt[2]{\left(x_s^{(i)} - x_0 - \delta x\right)^2 + \left(y_s^{(i)} - y_0 - \delta y\right)^2 + \left(z_s^{(i)} - z_0 - \delta z\right)^2}} \\
&+ \left(\dot{z}_s^{(i)} - \dot{z}_0 - \delta\dot{z}\right) \cdot \frac{\left(z_s^{(i)} - z_0 - \delta z\right)}{\sqrt[2]{\left(x_s^{(i)} - x_0 - \delta x\right)^2 + \left(y_s^{(i)} - y_0 - \delta y\right)^2 + \left(z_s^{(i)} - z_0 - \delta z\right)^2}} \\
&+ \left(\dot{b}_0 + \delta\dot{b}\right) + \dot{\varepsilon}_n^{(i)}
\end{aligned}
\qquad (4\text{-}22)
$$

By applying the 1[st] order Taylor series approximation on the estimated distance, the following expression is obtained:

$$
\begin{aligned}
\left|\boldsymbol{x_{s,i}} - \boldsymbol{x_0} - \delta\boldsymbol{x}\right| &\approx \sqrt[2]{\left(x_s^{(i)} - x_0\right)^2 + \left(y_s^{(i)} - y_0\right)^2 + \left(z_s^{(i)} - z_0\right)^2} \\
&\quad - \frac{\left(x_s^{(i)} - x_0\right) \cdot \delta x + \left(y_s^{(i)} - y_0\right) \cdot \delta y + \left(z_s^{(i)} - z_0\right) \cdot \delta z}{\sqrt[2]{\left(x_s^{(i)} - x_0\right)^2 + \left(x_s^{(i)} - y_0\right)^2 + \left(x_s^{(i)} - z_0\right)^2}} \\
&= \left|\boldsymbol{x_s^{(i)}} - \boldsymbol{x_0}\right| - \frac{\left(\boldsymbol{x_s^{(i)}} - \boldsymbol{x_0}\right)}{\left|\boldsymbol{x_s^{(i)}} - \boldsymbol{x_0}\right|} \cdot \delta\boldsymbol{x} \\
&= \left|\boldsymbol{x_s^{(i)}} - \boldsymbol{x_0}\right| - \boldsymbol{a_0^{(i)}} \cdot \delta\boldsymbol{x}
\end{aligned}
\qquad (4\text{-}23)
$$

where $\boldsymbol{a_0^{(i)}}$ are the direction cosines or LOS projections from the initial receiver location (denoted as 0) to the satellite i, computed along the three ECEF axes as:

$$a_{0,x}^{(i)} = \frac{\left(x_s^{(i)} - x_0\right)}{\sqrt[2]{\left(x_s^{(i)} - x_0\right)^2 + \left(y_s^{(i)} - y_0\right)^2 + \left(z_s^{(i)} - z_0\right)^2}}$$

$$a_{0,y}^{(i)} = \frac{\left(y_s^{(i)} - y_0\right)}{\sqrt[2]{\left(x_s^{(i)} - x_0\right)^2 + \left(y_s^{(i)} - y_0\right)^2 + \left(z_s^{(i)} - z_0\right)^2}} \qquad (4\text{-}24)$$

$$a_{0,z}^{(i)} = \frac{\left(z_s^{(i)} - z_0\right)}{\sqrt[2]{\left(x_s^{(i)} - x_0\right)^2 + \left(y_s^{(i)} - y_0\right)^2 + \left(z_s^{(i)} - z_0\right)^2}}$$

A similar approximation holds also for the pseudorange rate observation.

All the linearized measurements are combined into a single vector $\delta \boldsymbol{z}$, whose first N entries are code discriminator outputs and the later terms are the carrier frequency discriminator outputs obtained for the N satellites, given as:

$$\delta \boldsymbol{z} = \left[\delta\rho^{(1)}\ \delta\rho^{(2)} \cdots \delta\rho^{(N)}, \delta\dot{\rho}^{(1)}\ \delta\dot{\rho}^{(2)} \cdots \delta\dot{\rho}^{(N)}\right]^T_{2N\times 1} \qquad (4\text{-}25)$$

The new set of $2N$ linear equations that need to be solved are written as follows:

$$\delta \boldsymbol{z} = \boldsymbol{H} \cdot \delta \boldsymbol{X} + \boldsymbol{\varepsilon} \qquad (4\text{-}26)$$

Or,

$$\delta \boldsymbol{z}_{2N\times 1} = \boldsymbol{H}_{\boldsymbol{2N\times 8}} \cdot \begin{bmatrix} \delta x \\ \delta \dot{x} \\ \delta y \\ \delta \dot{y} \\ \delta z \\ \delta \dot{x} \\ \delta b \\ \delta \dot{b} \end{bmatrix}_{8\times 1} + \begin{bmatrix} \varepsilon_{\delta\rho}^{(1)} \\ \varepsilon_{\delta\rho}^{(2)} \\ \vdots \\ \varepsilon_{\delta\rho}^{(N)} \\ \varepsilon_{\delta\dot{\rho}}^{(1)} \\ \varepsilon_{\delta\dot{\rho}}^{(2)} \\ \vdots \\ \varepsilon_{\delta\dot{\rho}}^{(N)} \end{bmatrix}_{2N\times 1} \qquad (4\text{-}27)$$

$\delta\rho$

where $\boldsymbol{H}_{\boldsymbol{2N\times 8}}$ is referred to as the geometric matrix relating the measurement differences to the user delta state estimations, defined as:

$$\delta \boldsymbol{X} = [\delta x \quad \delta \dot{x} \quad \delta y \quad \delta \dot{y} \quad \delta z \quad \delta \dot{z} \quad c \cdot \delta b \quad c \cdot \delta \dot{b}]_{8\times 1}$$

$$\boldsymbol{H}_{2N\times 8} = \begin{bmatrix} -a_{0,x}^{(1)} & 0 & -a_{0,y}^{(1)} & 0 & -a_{0,z}^{(1)} & 0 & 1 & 0 \\ -a_{0,x}^{(2)} & 0 & -a_{0,y}^{(2)} & 0 & -a_{0,z}^{(2)} & 0 & 1 & 0 \\ \vdots & \vdots & \vdots & \vdots & \vdots & \vdots & \vdots & \vdots \\ -a_{0,x}^{(N)} & 0 & -a_{0,y}^{(N)} & 0 & -a_{0,z}^{(N)} & 0 & 1 & 0 \\ 0 & -a_{0,x}^{(1)} & 0 & -a_{0,y}^{(1)} & 0 & -a_{0,z}^{(1)} & 0 & 1 \\ 0 & -a_{0,x}^{(2)} & 0 & -a_{0,y}^{(2)} & 0 & -a_{0,z}^{(2)} & 0 & 1 \\ \vdots & \vdots & \vdots & \vdots & \vdots & \vdots & \vdots & \vdots \\ 0 & -a_{0,x}^{(N)} & 0 & -a_{0,y}^{(N)} & 0 & -a_{0,z}^{(N)} & 0 & 1 \end{bmatrix}_{2N\times 8} \quad \begin{matrix} \\ \\ \\ \\ \dot{\delta\rho} \\ \\ \\ \\ \end{matrix} \qquad (4\text{-}28)$$

where $a_{0,l}^{(i)}$ are the LOS projections from the initial user location (subscript 0) to the satellite ($i = 1 \div N$) along each ECEF axis $l = x, y, z$, already presented in Eq. (4-24). The state vector $\delta\boldsymbol{X}$ is given above the observation matrix $\boldsymbol{H}$ in order to facilitate the understanding of the corresponding pairs between the two. The first N rows of the observation matrix denote the partial derivatives of the pseudorange measurements differences (shown in red) w.r.t the vector states, whereas, the partial derivatives of the pseudorange rate measurements differences (shown in blue) are included in the later N rows.

The measurement errors $\boldsymbol{\varepsilon}$, presented in section 3.1 and 3.2**,** are modelled as Gaussian-distributed with zero mean and covariance matrix R, given by:

$$E(\boldsymbol{\varepsilon}) = 0$$
$$cov(\boldsymbol{\varepsilon}) = E(\boldsymbol{\varepsilon} \cdot \boldsymbol{\varepsilon}^T) = \boldsymbol{R} \cdot \boldsymbol{I_{2N\times 2N}} \qquad (4\text{-}29)$$

where $\boldsymbol{I_{2N\times 2N}}$ is the $(2N \times 2N)$ identity matrix.

The WLS technique removes the implicit assumption of equal quality among all the measurements by applying different weighting coefficients appropriately to each measurement residual. Therefore, the measurement covariance matrix R results in the following diagonal matrix:

$$\boldsymbol{R} = \text{diag}\left[\sigma^{2}{}_{\delta\rho}^{(i)}, \cdots, \sigma^{2}{}_{\delta\rho}^{(N)}, \sigma^{2}{}_{\delta\dot{\rho}}^{(i)}, \cdots, \sigma^{2}{}_{\delta\dot{\rho}}^{(N)}\right]_{2N\times 2N} \qquad (4\text{-}30)$$

The first N entries refer to the pseudorange measurements variance, which in the receiver configuration designed in this thesis encompass two independent contributions such as the thermal noise influence and the ionosphere residuals presence in the received code measurements after correction, computed as:

$$\sigma^{2}{}_{\delta\rho}^{(i)} = \left(\frac{c}{f_{code}}\right)^2 \cdot \sigma^{2}{}_{DLL}^{(i)} + \sigma^{2}{}_{iono}^{(i)} \; [m^2] \qquad (4\text{-}31)$$

where:

- $\sigma^{2}{}_{DLL}^{(i)}$ is the close-loop code delay error variance due to the thermal noise, which depends on the code discriminator type, DLL integration time and bandwidth and is computed in Eq. (3-71) and (3-73);
- $\sigma^{2}{}_{iono}^{(i)}$ denotes the ionosphere residual variance that is computed from the Klobuchar (GPS L1 C/A channels) and NeQuick (Galileo E1 OS channels) described in Eq. (3-7) and (3-11), respectively;

- $f_{code} = 1.023 \cdot 10^6 chip/s$ is the L1/E1 code chipping rate.

Regarding the pseudorange rate measurements, the thermal noise is the major error source since the ionosphere residuals vary slowly in time. Therefore, the closed-loop FLL/PLL error variance model reflects the pseudorange rate error variance budget as follows:

$$\boldsymbol{R}_{(N\div 2N)\times(N\div 2N)} = \left(\frac{c}{f_{carr}}\right)^2 \cdot \mathrm{diag}\left[{\sigma^2}_{PLL/FLL}^{(1)}, \cdots, {\sigma^2}_{PLL/FLL}^{(N)}\right]_{(N\div 2N)\times(N\div 2N)} \quad (4\text{-}32)$$

where:

- ${\sigma^2}_{PLL/FLL}^{(i)}$ denotes the closed-loop carrier phase/frequency error variance due to the thermal noise, computed in Eq. (3-49) and (3-50);
- $f_{carr} = 1.57542 \cdot 10^9 Hz$ is the L1/E1 carrier frequency.

The WLS estimate is the one that minimizes the sum of the squared residuals (derived in Appendix B.1), given by:

$$\delta \boldsymbol{x} = \left(\boldsymbol{H^T R^{-1} H}\right)^{-1} \boldsymbol{H^T R^{-1}} \cdot \delta \boldsymbol{z}, \quad (4\text{-}33)$$

and its covariance matrix (described in details in Appendix B.2) is computed as:

$$cov\{\delta \boldsymbol{X}\} = (\boldsymbol{H^T \cdot R^{-1} \cdot H})^{-1} \quad (4\text{-}34)$$

Eq. (4-33) and (4-34) show that the user's PVT estimation depends upon two factors such as: the variance of the ranges and pseudorange rate errors, enclosed in the measurement covariance matrix ($\boldsymbol{R}$) and on the user-satellite geometry defined by the observation matrix ($\boldsymbol{H}$). The user-satellite geometry contribution on the navigation solution accuracy is characterized from the Dilution of Precision (DOP) parameters, presented in [Kaplan and Hegarty, 2006]. The state vector estimate quality for a single epoch is described by the root mean square (RMS) errors as:

$$\begin{aligned} RMS_{position} &= \sqrt[2]{\left(\sigma_{\delta x}^2 + \sigma_{\delta y}^2 + \sigma_{\delta z}^2\right)} \\ RMS_{position+clock\_bias} &= \sqrt[2]{\left(\sigma_{\delta x}^2 + \sigma_{\delta y}^2 + \sigma_{\delta z}^2 + \sigma_{c\cdot\delta b}^2\right)} \\ RMS_{velocity} &= \sqrt[2]{\left(\sigma_{\delta \dot{x}}^2 + \sigma_{\delta \dot{y}}^2 + \sigma_{\delta \dot{z}}^2\right)} \\ RMS_{velocity+clock\_drift} &= \sqrt[2]{\left(\sigma_{\delta \dot{x}}^2 + \sigma_{\delta \dot{y}}^2 + \sigma_{\delta \dot{z}}^2 + \sigma_{c\cdot\delta \dot{b}}^2\right)} \end{aligned} \quad (4\text{-}35)$$

The new, improved estimates of the user position, velocity, clock bias and clock drift are computed as:

$$\begin{aligned} \hat{\boldsymbol{x}} &= \boldsymbol{x_0} + \delta \boldsymbol{x} \\ \hat{\boldsymbol{v}} &= \boldsymbol{v_0} + \delta \boldsymbol{v} \\ \hat{b}_{Rx} &= b_0 + \delta b \\ \hat{\dot{b}}_{Rx} &= \dot{b}_0 + \delta \dot{b} \end{aligned} \quad (4\text{-}36)$$

Or in vector format:

$$\boldsymbol{X} = \boldsymbol{X_0} + \boldsymbol{\delta X} \tag{4-37}$$

The weighted least square solution is iterated recursively until the change in the state vector estimation is sufficiently small ($< 10^{-3}$) [Parkinson, 1996].

4.3.2. The Extended Kalman Filter (EKF) estimation

The WLS solution that was described above is a snapshot position estimation technique, using the pseudorange and pseudorange rate measurements of the current epoch and an initial estimate of the state vector, to provide user's PVT solution at that same instant. The Kalman filter is a Bayesian estimation technique, firstly presented in [Kalman, 1960], which incorporates the measurements from the past epochs to obtain a more accurate navigation solution. The Kalman filter strength relies on the use of the dynamic model that together with the measurement model enable the provision of an optimal navigation estimation [Groves, 2013]. Similarly to the LS estimators, the core elements of the Kalman filter are the state and measurement vectors. However in the KF estimators, an error covariance matrix is associated to the state vector, representing the uncertainties in the state estimates and the degree of correlation between the states estimated and their errors. A Kalman filter is a recursive estimator of the system states of a linear stochastic system and includes two distinct models, such as:

- *The system model*, referred to as the time-propagation model that describes the variation in time of the state vector $\boldsymbol{X}$ and its corresponding covariance matrix $\boldsymbol{P}$, which describes the uncertainty of the state estimation. In other words, the system model reflects the user's dynamics variation;
- *The measurement model,* describing the measurement vector, expressed as a function of the state vector, in the absence of noise.

A Kalman filter that addresses the problem of estimating the state of a discrete-time controlled process that is governed by *non-linear* stochastic relations is referred to as an *extended Kalman filter* or EKF [Kaplan and Hegarty, 2006]. In the discrete EKF, the measurements are included in discrete time epochs and their models are linearized about the current state estimation. Herein, the state transition and observation models are non-linear functions of the state vector, given by:

$$\begin{aligned} \boldsymbol{X_k} &= f(\boldsymbol{X_{k-1}}, \boldsymbol{u_{k-1}}) + \boldsymbol{w_k} \\ \boldsymbol{z_k} &= h(\boldsymbol{X_k}) + \boldsymbol{v_k} \end{aligned} \tag{4-38}$$

where:

- $\boldsymbol{X_{k-1}}$, $\boldsymbol{X_k}$ denote the state vector comprising the user's absolute position, velocity and clock terms propagated in two consecutive time epochs $(k-1) \rightarrow k$;
- $\boldsymbol{z_k}$ is the measurement vector;
- $\boldsymbol{w_k}$ and $\boldsymbol{v_k}$ are the process and observation noise vectors, which are both assumed to follow a Gaussian distribution with zero mean and covariance matrixes denoted as $\boldsymbol{Q_k}$ and $\boldsymbol{R_k}$, respectively;
- $\boldsymbol{u_{k-1}}$ is the input control vector from the previous epoch $k-1$;
- f is the non-linear state function relating the state at the previous time step $k-1$ to the state at the current time step k;

- h is the non-linear measurement function relating the state vector $\boldsymbol{X_k}$ to the measurement vector $\boldsymbol{z_k}$;

In what follows, the notation $\boldsymbol{X_{m|n}}$ represents the estimate of $\boldsymbol{X}$ at the epoch m given measurements from epoch n up to the current epoch m, where $n \leq m$. The same consideration holds also for the other vector and matrix terms.

In this thesis, the selection criteria of the EKF algorithm is related to its capability to resolve the non-linearity issues for the navigation system. The detailed flowchart of the EKF estimation process is illustrated in Figure 4-1, where it can be noticed that the EKF estimation equations fall in two categories:

- *State prediction (time update)* equations, performing the propagation in time of the state vector $\boldsymbol{X_{k|k-1}}$ and its covariance matrix $\boldsymbol{P_{k|k-1}}$ from the previous time epoch $(k-1)$ to the current one k;
- *Measurement update (correction)* equations, refining the *a priori* state vector and covariance matrix estimations $(\boldsymbol{X_{k|k-1}}, \boldsymbol{P_{k|k-1}})$ by feeding the current epoch measurements $(\boldsymbol{z_{input}})$ into the filter and thus, obtaining the improved *a posteriori* estimates $(\boldsymbol{X_{k|k}}, \boldsymbol{P_{k|k}})$.

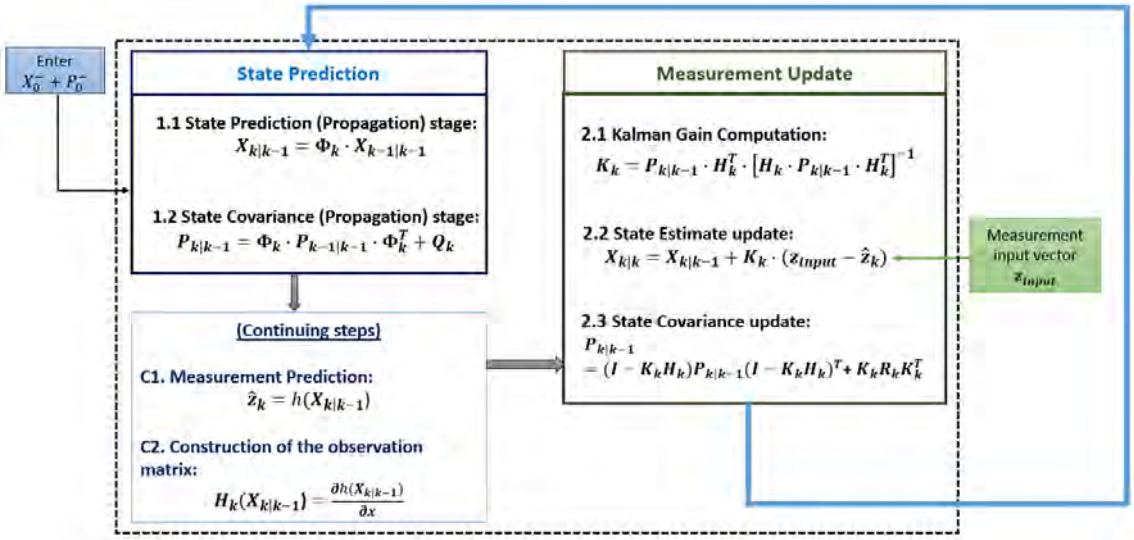

Figure 4-1. *The complete flowchart of the EKF recursive operation.*

In Figure 4-1, the state prediction and measurement update blocks are depicted by the blue and green blocks, respectively, whereas the feedback loop is illustrated via the blue line. The EKF estimation requires the initialization of the state vector and its error covariance matrix at step 0, shown in the light blue block. The state update is performed by incorporating the measurement input vector (light green block) in the process.

4.3.2.1. EKF State Space description

4.3.2.1.1. EKF State continuous-time model

The continuous-time EKF state model is given by:

$$\frac{d}{dt}\boldsymbol{X}(t) = \boldsymbol{F}(t)\cdot\boldsymbol{X}(t) + \boldsymbol{B}(t)\cdot\boldsymbol{w}(t)$$

$$\frac{d}{dt}\begin{bmatrix} x \\ \dot{x} \\ y \\ \dot{y} \\ z \\ \dot{z} \\ b_{Rx} \\ \dot{b}_{Rx} \end{bmatrix}_{8\times1} = \begin{bmatrix} A_{2\times2} & 0_{2\times2} & 0_{2\times2} & 0_{2\times2} \\ 0_{2\times2} & A_{2\times2} & 0_{2\times2} & 0_{2\times2} \\ 0_{2\times2} & 0_{2\times2} & A_{2\times2} & 0_{2\times2} \\ 0_{2\times2} & 0_{2\times2} & 0_{2\times2} & A_{2\times2} \end{bmatrix} \cdot \begin{bmatrix} x \\ \dot{x} \\ y \\ \dot{y} \\ z \\ \dot{z} \\ b_{Rx} \\ \dot{b}_{Rx} \end{bmatrix}_{8\times1} + \begin{bmatrix} 0 & 0 & 0 & 0 & 0 \\ 1 & 0 & 0 & 0 & 0 \\ 0 & 0 & 0 & 0 & 0 \\ 0 & 1 & 0 & 0 & 0 \\ 0 & 0 & 0 & 0 & 0 \\ 0 & 0 & 1 & 0 & 0 \\ 0 & 0 & 0 & 1 & 0 \\ 0 & 0 & 0 & 0 & 1 \end{bmatrix}_{8\times5} \cdot \begin{bmatrix} w_{\dot{x}} \\ w_{\dot{y}} \\ w_{\dot{z}} \\ w_b \\ w_d \end{bmatrix} \quad (4\text{-}39)$$

where:

- $\boldsymbol{X}$ is the state vector having as entries the user's position $[x\ y\ z]$, velocity $[\dot{x}\ \dot{y}\ \dot{z}]$ and user's clock bias and drift terms $[b_{Rx}\ \dot{b}_{Rx}]$, expressed in unit of $[m]$ and $\left[\frac{m}{s}\right]$, respectively;
- $\frac{d}{dt}\boldsymbol{X}$ denotes the time derivation operation applied to the state vector;
- $\boldsymbol{F}$ represents the state transition matrix describing the user's platform and receiver's clock dynamics;
- $\boldsymbol{B}$ represents the colored noise transition matrix;
- $\boldsymbol{w}$ is the process noise vector representing the uncertainties affecting the system model, coming from the user's dynamics and the receiver oscillator;
- $A_{2\times2} = \begin{bmatrix} 0 & 1 \\ 0 & 0 \end{bmatrix}$ represent the position/velocity and clock biases/drift state transition sub-matrixes.

Concerning the process noise vector $\boldsymbol{w}$, the five tuning factors of its continuous-time covariance matrix $\boldsymbol{Q}$ associated with the noise affecting the states**,** are grouped into two main categories**:**

- *User's dynamics sensitive*: reflecting the uncertainty concerning the vehicle dynamics and including the velocity error variance terms along the three ECEF axes $(\sigma_{\dot{x}}^2, \sigma_{\dot{y}}^2, \sigma_{\dot{y}}^2)$ that are projected in the position domain through the state transition sub-matrix $A_{2\times2}$;
- *Receiver's oscillator noise PSD*: including the oscillator's phase noise PSDs affecting the receiver clock biases denoted as σ_b^2 and the oscillator's frequency noise variance σ_d^2 related to the user's clock drift. Both these PSD values depend on the Allan variance parameters (h_0, h_{-1} and h_{-2}).

4.3.2.1.2. EKF State discrete-time model

The discretization of the state vector estimation is obtained by applying the expectation operator E on the state-space model of Eq. (4-39), yielding:

$$E\left(\frac{d}{dt}\boldsymbol{X}(t)\right) = \frac{d}{dt}\left(\widehat{\boldsymbol{X}}(t)\right) = \boldsymbol{F}(t)\cdot\widehat{\boldsymbol{X}}(t) \tag{4-40}$$

Solving the differential equation above provides the state vector estimation at time t as a function of the state vector at time $t-\tau$ as [Groves, 2013]:

$$\widehat{\boldsymbol{X}}(t) = \exp\left(\int_{t-\tau}^{t}\boldsymbol{F}(t)dt\right)\cdot\widehat{\boldsymbol{X}}(t-\tau) \tag{4-41}$$

When performing this step, the state transition matrix $\boldsymbol{F}$ is fixed in time and thus, the discrete state transition matrix $\boldsymbol{\Phi}_k$ is then computed as:

$$\boldsymbol{\Phi}_k \approx \exp(\boldsymbol{F}\cdot\Delta T) \tag{4-42}$$

Where $\Delta T = t_{k-1} - t_k$ is the time step between two successive epochs. The matrix exponential is calculated as the Taylor's power-series expansion of the continuous-time transition matrix $\boldsymbol{F}$ as:

$$\boldsymbol{\Phi}_k = \sum_{n=0}^{+\infty}\frac{\boldsymbol{F}_k^n\cdot\Delta T^n}{n!} = I + \boldsymbol{F}\cdot\Delta T + \frac{1}{2}\cdot\boldsymbol{F^2}\cdot\Delta T^2 + \frac{1}{6}\cdot\boldsymbol{F^3}\cdot\Delta T^3 + \cdots \tag{4-43}$$

Since the EKF navigation filter adopted in this thesis has a short propagation time ΔT, explained in the following chapter, the power-series expansion is truncated in the first-order solution. Thus, the discrete transition matrix is given by:

$$\boldsymbol{\Phi}_k = I + \boldsymbol{F}\cdot\Delta T \tag{4-44}$$

Substituting Eq. (4-44) into the continuous state transition matrix of Eq. (4-39), the final discrete state transition matrix is the following:

$$\boldsymbol{\Phi}_k = \begin{bmatrix} A_{d,2\times2} & 0_{2\times2} & 0_{2\times2} & 0_{2\times2} \\ 0_{2\times2} & A_{d,2\times2} & 0_{2\times2} & 0_{2\times2} \\ 0_{2\times2} & 0_{2\times2} & A_{d,2\times2} & 0_{2\times2} \\ 0_{2\times2} & 0_{2\times2} & 0_{2\times2} & A_{d,2\times2} \end{bmatrix} \tag{4-45}$$

where $\boldsymbol{A}_{d,2\times2} = \begin{bmatrix} 1 & \Delta T \\ 0 & 1 \end{bmatrix}$.

As assumed in [Brown and Hwang, 1996], the matrix $E[w(\varepsilon)\cdot w^T(\epsilon)]$ is a Dirac delta functions matrix known from the continuous model. Therefore, the solution of the differential equation shown in Eq. (4-39) in discrete time at the successive time epoch t_k, can be written as:

$$X(t_k) = \boldsymbol{\Phi}(t_k, t_{k-1})\cdot\boldsymbol{X}(t_k) + \int_{t_{k-1}}^{t_k}\boldsymbol{\Phi}(t_k,\tau)\cdot\boldsymbol{w}(\tau)\cdot d\tau \tag{4-46}$$

where the discrete white process noise sequence is represented by the integral relation $\boldsymbol{w}(k) = \int_{t_{k-1}}^{t_k}\boldsymbol{\Phi}(t_k,\tau)\cdot\boldsymbol{w}(\tau)\cdot d\tau$, whose covariance matrix is given as:

$$\begin{aligned}\boldsymbol{Q}_k &= E\left[\boldsymbol{w}_k \cdot \boldsymbol{w}_k^T\right] \\ &= \int_{t_{k-1}}^{t_k} \boldsymbol{\Phi}(t_k,\tau) \cdot \boldsymbol{Q}(\tau) \cdot \boldsymbol{\Phi}^T(t_k,\tau) \cdot d\tau\end{aligned} \quad (4\text{-}47)$$

where $\boldsymbol{Q}$ is the continuous-time process noise covariance matrix. In the following equations, the discrete process noise covariance matrix will be computed separately for the user's dynamics and oscillator's tuning factors according to the relation in Eq. (4-47).

Therefore, the process noise discretization for the position and velocity states along the X axis is computed as:

$$\begin{aligned}\boldsymbol{Q}_{x,k} &= \int_{t_{k-1}}^{t_k} \boldsymbol{A}_{d,2\times2}(t_k,\tau) \cdot \boldsymbol{Q}_{\mathbf{2\times2}}(\tau) \cdot \boldsymbol{A}_{d,2\times2}^T(t_k,\tau) \cdot d\tau \\ &= \int_{t_{k-1}}^{t_k} \begin{bmatrix}1 & \Delta T\\ 0 & 1\end{bmatrix} \cdot \begin{bmatrix}0 & 0\\ 0 & \sigma_{\dot{x}}^2\end{bmatrix} \cdot \begin{bmatrix}1 & 0\\ \Delta T & 1\end{bmatrix} \cdot d\tau \\ &= \sigma_{\dot{x}}^2 \cdot \begin{bmatrix}\Delta T^3/_3 & \Delta T^2/_2\\ \Delta T^2/_2 & \Delta T\end{bmatrix}\end{aligned} \quad (4\text{-}48)$$

where $\boldsymbol{A}_{d,2\times2} = \begin{bmatrix}1 & \Delta T\\ 0 & 1\end{bmatrix}$ is the discrete representation of the continuous time state transition sub-matrix, given in Eq. (4-45).

Similarly, the same logic is applied to obtain the discrete time process noise covariance matrixes for the Y- and Z- axis user's position projections, as follows:

$$\boldsymbol{Q}_{y,k} = \sigma_{\dot{y}}^2 \cdot \begin{bmatrix}\Delta T^3/_3 & \Delta T^2/_2\\ \Delta T^2/_2 & \Delta T\end{bmatrix} \quad (4\text{-}49)$$

and,

$$\boldsymbol{Q}_{z,k} = \sigma_{\dot{z}}^2 \cdot \begin{bmatrix}\Delta T^3/_3 & \Delta T^2/_2\\ \Delta T^2/_2 & \Delta T\end{bmatrix} \quad (4\text{-}50)$$

where $(\sigma_{\dot{x}}^2, \sigma_{\dot{y}}^2, \sigma_{\dot{z}}^2)$ are the velocities noise error variance along the three ECEF axes.

Applying the discretization process of Eq. (4-48) to the user's clock covariance states, the following relation is obtained:

$$\begin{aligned}\boldsymbol{Q}_{clk,k} &= \int_{t_{k-1}}^{t_k} \boldsymbol{A}_{d,2\times2}(t_k,\tau) \cdot \boldsymbol{Q}_{\boldsymbol{clk,2\times2}}(\tau) \cdot \boldsymbol{A}_{d,2\times2}^T(t_k,\tau) \cdot d\tau \\ &= \int_{t_{k-1}}^{t_k} \begin{bmatrix}1 & \Delta T\\ 0 & 1\end{bmatrix} \cdot \begin{bmatrix}\sigma_b^2 & 0\\ 0 & \sigma_d^2\end{bmatrix} \cdot \begin{bmatrix}1 & 0\\ \Delta T & 1\end{bmatrix} \cdot d\tau \\ &= \begin{bmatrix}\sigma_b^2 \cdot \Delta T + \sigma_d^2 \cdot \Delta T^3/_3 & \sigma_d^2 \cdot \Delta T^2/_2\\ \sigma_d^2 \cdot \Delta T^2/_2 & \sigma_d^2 \cdot \Delta T\end{bmatrix}\end{aligned} \quad (4\text{-}51)$$

However, an alternative receiver's clock process noise covariance matrix is used in this thesis. The discrete receiver's clock process noise covariance matrix is modelled based on the Allan variance parameters (including also the flicker noise term h_{-1}) from Table 3-1, given by:

$$\boldsymbol{Q_{clk,k}} = \begin{bmatrix} \sigma^2_{b,discr} & \sigma^2_{b-d,discr} \\ \sigma^2_{b-d,discr} & \sigma^2_{d,discr} \end{bmatrix} \quad (4\text{-}52)$$

where:

- The discrete-time oscillator's phase PSD is computed as [Brown and Hwang, 1996]:

$$\sigma^2_{b,discr} = \frac{h_0}{2} \cdot \Delta T + 2 \cdot h_{-1} \cdot \Delta T^2 + \frac{2}{3} \cdot \pi^2 \cdot h_{-2} \cdot \Delta T^3 \quad (4\text{-}53)$$

- $\sigma^2_{b-d,discr} = h_{-1} \cdot \Delta T + \pi^2 \cdot h_{-2} \cdot \Delta T^2$ denotes the receiver's oscillator frequency PSD influence on the clock bias;
- The discrete-time oscillator's frequency noise variance $\sigma^2_{d,disc}$ related to the receiver's clock drift component is expressed as:

$$\sigma^2_{d,discr} = \frac{h_0}{2 \cdot \Delta T} + 4 \cdot h_{-1} + \frac{8}{3} \cdot \pi^2 \cdot h_{-2} \cdot \Delta T^2 \quad (4\text{-}54)$$

Combining the expressions in Eq. (4-48), (4-49), (4-50) and (4-52), the final discrete process noise covariance matrix is written as:

$$\boldsymbol{Q}_k = \mathrm{diag}\left[\boldsymbol{Q}_{x,k}, \boldsymbol{Q}_{y,k}, \boldsymbol{Q}_{z,k}, \boldsymbol{Q}_{clk,k}\right]_{8\times 8} \quad (4\text{-}55)$$

4.3.2.2. EKF Observation model

4.3.2.2.1. Non-linear Measurements model

The general non-linear relation between the state and the measurement vector which is required for an EKF is the following one:

$$\boldsymbol{z_k} = h(\boldsymbol{X_k}) + \boldsymbol{v_k} \quad (4\text{-}56)$$

where:

- h is the *non-linear* function relating the measurement $\boldsymbol{z_k}$ to the state $\boldsymbol{X_k}$;
- $\boldsymbol{v_k}$ is *the measurement noise vector* that is modelled as a zero-mean uncorrelated Gaussian noise process and independent to the process noise w_k.

For GNSS positioning in open sky conditions, this model matches (under some simplifications) the relationship between the pseudorange and pseudorange rate measurements and the user PVT solution. The measurement model customization for GNSS positioning in open sky conditions is done next.

For the scalar tracking receiver, the measurement vector $\boldsymbol{z_k}$ includes the pseudoranges $\rho^{(i)}$ and Doppler measurements $\dot{\rho}^{(i)}$, output from the code/carrier tracking process for the $i = 1 \div N$ GPS L1/ Galileo E1 tracking channels after applying the ionosphere correction models, presented in Eq. (4-18):

$$\boldsymbol{z_k} = \left[\left(\rho^{(1)}_{corr}\ \rho^{(2)}_{corr}\ \cdots \rho^{(N)}_{corr}\right) \vdots \left(\dot{\rho}^{(1)}_{corr}\ \dot{\rho}^{(2)}_{corr}\ \cdots \dot{\rho}^{(N)}_{corr}\right)(k)\right]_{2N\times 1} \quad (4\text{-}57)$$

The mathematical model of GNSS code pseudorange measurements provided by the receiver for a given satellite i (from the GPS $(N1)$ and Galileo $(N2)$ satellites in-view) at epoch k to be integrated within the EKF architecture can be written as:

$$\rho_{corr}^{(i)} = \begin{cases} |\boldsymbol{r_i}(k) - \boldsymbol{r_u}(k)| + \boldsymbol{X_k}(7) + b_{iono,GPS}^{(i)}(k) + \varepsilon_{n,GPS}^{(i)}(k), & 0 < i \leq N1 \\ |\boldsymbol{r_i}(k) - \boldsymbol{r_u}(k)| + \boldsymbol{X_k}(7) + b_{iono,Gal}^{(i)}(k) + \varepsilon_{n,Gal}^{(i)}(k), & N1 < i \leq N \end{cases} \quad (4\text{-}58)$$

where:

- $|\boldsymbol{r_i}(k) - \boldsymbol{r_u}(k)| = \sqrt[2]{\left(x_s^{(i)}(k) - \boldsymbol{X_k}(1)\right)^2 + \left(y_s^{(i)}(k) - \boldsymbol{X_k}(3)\right)^2 + \left(z_s^{(i)}(k) - \boldsymbol{X_k}(5)\right)^2}$ is the satellite-to-user geometric distance at the current epoch k where $\left(x_s^{(i)}, y_s^{(i)}, z_s^{(i)}\right)(k)$ and $\left(\boldsymbol{X_k}(1), \boldsymbol{X_k}(3), \boldsymbol{X_k}(5)\right)$ represent the i^{th} satellite and user's coordinates in the ECEF reference frame, respectively;
- $\boldsymbol{X_k}(7)$ denotes the receiver's clock bias state w.r.t the GPS time;
- $b_{iono,GPS}^{(i)}(k)$ and $b_{iono,Gal}^{(i)}(k)$ represent the ionosphere residuals appearing at the GPS and Galileo code measurements after the application of the ionosphere correction models, respectively;
- $\varepsilon_{n,GPS/Gal}^{(i)}(k)$ represents the error due to the receiver's thermal noise, assumed to be white, centered Gaussian-distributed;

Therefore, the observation function $\left(h_1^{(i)}\right)$ relating the pseudorange measurements to the state vector includes the following terms for the receiver configuration in this thesis:

$$h_1^{(i)}(\boldsymbol{X_k}) = |\boldsymbol{r_i}(k) - \boldsymbol{r_u}(k)| + b_{Rx}(k) + b_{iono,GPS|Gal}^{(i)}(k) + \varepsilon_n^{(i)}(k) \quad (4\text{-}59)$$

Whereas, the remaining N-entries of the measurement vector $\boldsymbol{z_k}$, constituted by the Doppler measurements from both the GPS and Galileo satellites, are related to the state vector through the observation function $\left(h_2^{(i)}\right)$:

$$\begin{aligned} h_2^{(i)}(\boldsymbol{X_k}) = &\left(\dot{x}_s^{(i)}(k) - \boldsymbol{X_k}(2)\right) \cdot a_x^{(i)}(k) + \left(\dot{y}_s^{(i)}(k) - \boldsymbol{X_k}(4)\right) \cdot a_y^{(i)}(k) \\ &+ \left(\dot{z}_s^{(i)}(k) - \boldsymbol{X_k}(6)\right) \cdot a_z^{(i)} + \boldsymbol{X_k}(8) + \dot{b}_{iono,GPS|Gal}^{(i)}(k) + \dot{\varepsilon}_{n,GPS/Gal}^{(i)}(k) \end{aligned} \quad (4\text{-}60)$$

Where:

- The LOS projections along the three ECEF axes ($l = x, y, z$) are computed as:

$$\begin{aligned} a_x^{(i)} &= \frac{\left(x_s^{(i)}(k) - \boldsymbol{X_k}(1)\right)}{\sqrt[2]{\left(x_s^{(i)}(k) - \boldsymbol{X_k}(1)\right)^2 + \left(y_s^{(i)}(k) - \boldsymbol{X_k}(3)\right)^2 + \left(z_s^{(i)}(k) - \boldsymbol{X_k}(5)\right)^2}} \\ a_y^{(i)} &= \frac{\left(y_s^{(i)}(k) - \boldsymbol{X_k}(3)\right)}{\sqrt[2]{\left(x_s^{(i)}(k) - \boldsymbol{X_k}(1)\right)^2 + \left(y_s^{(i)}(k) - \boldsymbol{X_k}(3)\right)^2 + \left(z_s^{(i)}(k) - \boldsymbol{X_k}(5)\right)^2}} \\ a_z^{(i)} &= \frac{\left(z_s^{(i)}(k) - \boldsymbol{X_k}(5)\right)}{\sqrt[2]{\left(x_s^{(i)}(k) - \boldsymbol{X_k}(1)\right)^2 + \left(y_s^{(i)}(k) - \boldsymbol{X_k}(3)\right)^2 + \left(z_s^{(i)}(k) - \boldsymbol{X_k}(5)\right)^2}} \end{aligned} \quad (4\text{-}61)$$

- $\left(\dot{x}_s^{(i)}, \dot{y}_s^{(i)}, \dot{z}_s^{(i)}\right)(k)$ and $\left(\boldsymbol{X_k}(2), \boldsymbol{X_k}(4), \boldsymbol{X_k}(6)\right)(k)$ represent the i^{th} satellite and user's velocities from the state vector, respectively, expressed in the ECEF reference frame;
- $\dot{b}_{iono,GPS|Gal}^{(i)}$ denotes the ionosphere residual rate appearing in the GPS and Galileo pseudorange rate measurements, respectively, defined in Eq. (4-17);

- $\boldsymbol{X_k}(8)$ is the receiver's clock drift state common for both the GPS and Galileo Doppler measurements;
- $\dot{\varepsilon}^{(i)}_{n,GPS/Gal}(k)$ denotes the receiver's thermal noise effect on the GPS and Galileo pseudorange rate measurements.

The measurement noise vector $\boldsymbol{v_k} = [\varepsilon_n^{(1)}, \cdots, \varepsilon_n^{(N)}, \dot{\varepsilon}_n^{(1)}, \cdots, \dot{\varepsilon}_n^{(N)}]^T$, including the noise terms affecting the pseudorange and pseudorange rate measurements, is modelled as a zero-mean uncorrelated Gaussian noise process and independent to the process noise w_k, given by:

$$\begin{aligned} E[\boldsymbol{v_k}] &= 0 \\ E[\boldsymbol{v_k} \cdot \boldsymbol{w_l^T}] &= 0 \\ E[\boldsymbol{v_k} \cdot \boldsymbol{v_l^T}] &= \boldsymbol{R}_k \cdot \delta_{kl}, \qquad \text{for all } k \text{ and } l \end{aligned} \tag{4-62}$$

where δ_{kl} denotes the Kronecker's delta and $\boldsymbol{R}_k$ represents the *measurement noise covariance matrix*.

The measurement covariance matrix R of the uncorrelated code and Doppler measurements is the same one used for the WLS technique, which was provided in Eq. (4-30) - (4-32).

4.3.2.2.2. Linearization of the EKF Observations

Following the EKF estimation flowchart of Figure 4-1, the successive step after the state propagation is the computation of the Kalman gain in Step 2.1. For this matter, the measurement prediction $\boldsymbol{z}_k$ and observation matrix H_k shall be calculated.

The predicted measurement vector $\hat{\boldsymbol{z}}_k$ is computed by applying the non-linear observation functions (h_1 and h_2) from Eq. (4-59) and (4-60), relating the pseudorange and pseudorange rate measurements, respectively, with the state vector prediction $\boldsymbol{X}_{k|k-1}$. The predicted measurement vector consists of two entries per channel, in specifics the predicted pseudorange $\hat{\rho}_k^{(i)}$ and pseudorange rates $\hat{\dot{\rho}}_k^{(i)}$ for each satellite $i = 1 \div N$:

$$\hat{\boldsymbol{z}}_k = \left[(\hat{\rho}_k^{(1)} \ \hat{\rho}_k^{(2)} \ \cdots \ \hat{\rho}_k^{(N)}) \vdots (\hat{\dot{\rho}}_k^{(1)} \ \hat{\dot{\rho}}_k^{(2)} \ \cdots \ \hat{\dot{\rho}}_k^{(N)}) \right]_{2N \times 1} \tag{4-63}$$

In the Cartesian ECEF-frame, the predicted satellite-user ranges $\hat{R}_k^{(i)}$ per each tracked satellite $i = 1 \div N$ are furtherly computed as:

$$\hat{R}_k^{(i)} = \sqrt[2]{\left(x_s^{(i)}(k) - \boldsymbol{X}_{k|k-1}(1)\right)^2 + \left(y_s^{(i)}(k) - \boldsymbol{X}_{k|k-1}(3)\right)^2 + \left(z_s^{(i)}(k) - \boldsymbol{X}_{k|k-1}(5)\right)^2} \tag{4-64}$$

where $\left(\boldsymbol{X}_{k|k-1}(1), \boldsymbol{X}_{k|k-1}(3), \boldsymbol{X}_{k|k-1}(5)\right)$ represents the predicted user's position vector.

The predicted pseudorange measurements are obtained by adding to the predicted ranges the predicted user's clock bias term $\boldsymbol{X}_{k|k-1}(7)$:

$$\hat{\rho}_k^{(i)} = \hat{R}_k^{(i)} + \boldsymbol{X}_{k|k-1}(7) \tag{4-65}$$

Similarly, the predicted pseudorange rate $\hat{\dot{\rho}}_k^{(i)}$ can be computed as:

$$\begin{aligned}\hat{\rho}_k^{(i)} &= \left(\dot{x}_s^{(i)}(k) - \boldsymbol{X}_{k|k-1}(2)\right)\cdot \hat{a}_x^{(i)}(k) + \left(\dot{y}_s^{(i)}(k) - \boldsymbol{X}_{k|k-1}(4)\right)\cdot \hat{a}_y^{(i)}(k) \\ &+ \left(\dot{z}_s^{(i)}(k) - \boldsymbol{X}_{k|k-1}(6)\right)\cdot \hat{a}_z^{(i)}(k) + \boldsymbol{X}_{k|k-1}(8)\end{aligned} \quad (4\text{-}66)$$

where:

- $\left(x_s^{(i)}(k), y_s^{(i)}(k), z_s^{(i)}(k)\right)$ and $\left(\dot{x}_s^{(i)}(k), \dot{y}_s^{(i)}(k), \dot{z}_s^{(i)}(k)\right)$ denote the 3D position and velocity vectors, respectively, of the i^{th} satellite that are obtained from the ephemerides data and expressed in Cartesian coordinates;
- $\left(\boldsymbol{X}_{k|k-1}(1), \boldsymbol{X}_{k|k-1}(3), \boldsymbol{X}_{k|k-1}(5)\right)$ and $\left(\boldsymbol{X}_{k|k-1}(2), \boldsymbol{X}_{k|k-1}(4), \boldsymbol{X}_{k|k-1}(6)\right)$ refer to the predicted user's absolute position and velocity vectors along the X, Y and Z axes, respectively;
- $\boldsymbol{X}_{k|k-1}(7)$ denotes the user's clock predicted bias expressed in $[m]$;
- $\boldsymbol{X}_{k|k-1}(8)$ is the predicted user's clock drift in $\left[\frac{m}{s}\right]$;
- while the LOS unit vectors from the i^{th} satellite to the predicted user position $\left(\boldsymbol{X}_{k|k-1}(1), \boldsymbol{X}_{k|k-1}(3), \boldsymbol{X}_{k|k-1}(5)\right)$ are computed as follows for each ECEF axes:

$$\hat{a}_x^{(i)} = \frac{\left(x_s^{(i)} - \boldsymbol{X}_{k|k-1}(1)\right)}{\hat{R}_k^{(i)}}$$

$$\hat{a}_y^{(i)} = \frac{\left(y_s^{(i)} - \boldsymbol{X}_{k|k-1}(3)\right)}{\hat{R}_k^{(i)}} \quad (4\text{-}67)$$

$$\hat{a}_z^{(i)} = \frac{\left(z_s^{(i)} - \boldsymbol{X}_{k|k-1}(5)\right)}{\hat{R}_k^{(i)}}$$

From the pseudorange rate expression given in Eq. (4-66), let us denote by $\hat{V}_k^{(i)}$ the predicted relative satellite-to-receiver velocity vector without taking into account the clock drift component given by:

$$\begin{aligned}\hat{V}_k^{(i)} &= \left(\dot{x}_{s,i}(k) - \boldsymbol{X}_{k|k-1}(2)\right)\cdot \hat{a}_x^{(i)}(k) + \left(\dot{y}_{s,i}(k) - \boldsymbol{X}_{k|k-1}(4)\right)\cdot \hat{a}_y^{(i)}(k) \\ &+ \left(\dot{z}_{s,i}(k) - \boldsymbol{X}_{k|k-1}(6)\right)\cdot \hat{a}_z^{(i)}(k)\end{aligned} \quad (4\text{-}68)$$

4.3.2.2.3. EKF Observation matrix $\boldsymbol{H}_k$

The predicted measurements, incorporated in the predicted measurement vector $\hat{\boldsymbol{z}}_k$, are communicated to the main EKF filter as a function of the predicted state vector $\boldsymbol{X}_{k|k-1}$ through the observation (design) matrix $\mathbf{H}_k$ that includes the partial derivatives of the observations w.r.t the predicted states as:

$$\boldsymbol{H}_k(\boldsymbol{X}_{k|k-1}) = \frac{\partial \hat{\boldsymbol{z}}_k}{\partial \boldsymbol{X}_{k|k-1}} \quad (4\text{-}69)$$

Let us first compute the first N rows of the design matrix $\boldsymbol{H}_k$, relating the predicted pseudorange measurements $\hat{\rho}_k^{(i)}$ to the predicted user states using the $h_1$function from Eq. (4-59), for the $N1$ GPS and $N2$ Galileo satellites:

$$\begin{bmatrix} \frac{\partial h_1(\hat{\rho}_k^{(i=1\div N1)}|\boldsymbol{X}_{k|k-1})}{\partial \boldsymbol{X}_{k|k-1}(1)} & \cdots & \frac{\partial h_1(\hat{\rho}_k^{(i=1\div N1)}|\boldsymbol{X}_{k|k-1})}{\partial \boldsymbol{X}_{k|k-1}(8)} \end{bmatrix} = \begin{bmatrix} -\hat{a}_{x,GPS}^{(i)} & 0 & -\hat{a}_{y,GPS}^{(i)} & 0 & -\hat{a}_{z,GPS}^{(i)} & 0 & 1 & 0 \end{bmatrix}$$
$$\begin{bmatrix} \frac{\partial h_1(\hat{\rho}_k^{(i=1\div N2)}|\boldsymbol{X}_{k|k-1})}{\partial \boldsymbol{X}_{k|k-1}(1)} & \cdots & \frac{\partial h_1(\hat{\rho}_k^{(i=1\div N2)}|\boldsymbol{X}_{k|k-1})}{\partial \boldsymbol{X}_{k|k-1}(8)} \end{bmatrix} = \begin{bmatrix} -\hat{a}_{x,Gal}^{(i)} & 0 & -\hat{a}_{y,Gal}^{(i)} & 0 & -\hat{a}_{z,Gal}^{(i)} & 0 & 1 & 0 \end{bmatrix} \quad (4\text{-}70)$$

The remaining $(N \div 2N)$ rows of the design matrix $\boldsymbol{H}_k$ include the partial derivatives of the predicted pseudorange rates measurements $\hat{\rho}_k^{(i)}$ w.r.t the predicted state vector $\boldsymbol{X}_{k|k-1}$. The partial derivatives are computed separately for the position and velocity terms of the predicted state vector. The pseudorange rate partial derivative w.r.t the predicted state position along the X-axis $\left(v_x^{(i)}\right)$ can be written according to the Eq. (4-60) as:

$$\begin{aligned} v_x^{(i)}(k) &= \frac{\partial h_2\left(\hat{\rho}_k^{(i=1\div N)}|\boldsymbol{X}_{k|k-1}\right)}{\partial \boldsymbol{X}_{k|k-1}(1)} \\ &= \left(x_s^{(i)}(k) - \boldsymbol{X}_{k|k-1}(1)\right) \cdot \frac{\hat{V}_k^{(i)}}{\hat{R}_k^{(i)^2}} - \frac{\left(\dot{x}_s^{(i)}(k) - \boldsymbol{X}_{k|k-1}(2)\right)}{\hat{R}_k^{(i)}} \end{aligned} \quad (4\text{-}71)$$

Similary, the pseudorange rate partial derivatives w.r.t to the predicted user's position along the Y- and Z-axes are given by the h_2 function defined in Eq. (4-60):

$$\begin{aligned} v_y^{(i)}(k) &= \frac{\partial h_2\left(\hat{\rho}_k^{(i=1\div N)}|\boldsymbol{X}_{k|k-1}\right)}{\partial \boldsymbol{X}_{k|k-1}(3)} \\ &= \left(y_s^{(i)}(k) - \boldsymbol{X}_{k|k-1}(3)\right) \cdot \frac{\hat{V}_k^{(i)}}{\hat{R}_k^{(i)^2}} - \frac{\left(\dot{y}_s^{(i)}(k) - \boldsymbol{X}_{k|k-1}(4)\right)}{\hat{R}_k^{(i)}} \end{aligned} \quad (4\text{-}72)$$

$$\begin{aligned} v_z^{(i)}(k) &= \frac{\partial h_2\left(\hat{\rho}_k^{(i=1\div N)}|\boldsymbol{X}_{k|k-1}\right)}{\partial \boldsymbol{X}_{k|k-1}(5)} \\ &= \left(z_s^{(i)}(k) - \boldsymbol{X}_{k|k-1}(5)\right) \cdot \frac{\hat{V}_k^{(i)}}{\hat{R}_k^{(i)^2}} - \frac{\left(\dot{z}_s^{(i)}(k) - \boldsymbol{X}_{k|k-1}(6)\right)}{\hat{R}_k^{(i)}} \end{aligned} \quad (4\text{-}73)$$

On the other side, the design matrix $\boldsymbol{H}_k$ elements corresponding to the partial derivatives of the predicted pseudorange rates measurements $\hat{\rho}_k^{(i)}$ w.r.t the velocity terms of the predicted state vector $\boldsymbol{X}_{k|k-1}$,are denoted as $(v_{\dot{x}}^{(i)}, v_{\dot{y}}^{(i)}, v_{\dot{z}}^{(i)})$ and given by:

$$\begin{aligned} v_{\dot{x}}^{(i)}(k) &= \frac{\partial h_2\left(\hat{\rho}_k^{(i=1\div N)}|\boldsymbol{X}_{k|k-1}\right)}{\partial \boldsymbol{X}_{k|k-1}(2)} = -\frac{\left(x_s^{(i)} - \boldsymbol{X}_{k|k-1}(1)\right)}{\hat{R}_k^{(i)}} = -\hat{a}_x^{(i)} \\ v_{\dot{y}}^{(i)}(k) &= \frac{\partial h_2\left(\hat{\rho}_k^{(i=1\div N)}|\boldsymbol{X}_{k|k-1}\right)}{\partial \boldsymbol{X}_{k|k-1}(4)} = -\frac{\left(y_s^{(i)} - \boldsymbol{X}_{k|k-1}(3)\right)}{\hat{R}_k^{(i)}} = -\hat{a}_y^{(i)} \\ v_{\dot{z}}^{(i)}(k) &= \frac{\partial h_2\left(\hat{\rho}_k^{(i=1\div N)}|\boldsymbol{X}_{k|k-1}\right)}{\partial \boldsymbol{X}_{k|k-1}(6)} = -\frac{\left(z_s^{(i)} - \boldsymbol{X}_{k|k-1}(5)\right)}{\hat{R}_k^{(i)}} = -\hat{a}_z^{(i)} \end{aligned} \quad (4\text{-}74)$$

and the partial derivative of the pseudorange rate prediction w.r.t to the clock drift term of the state vector ($v_{\dot{b}}^{(i)}$) is computed as:

$$v_{\dot{b}}^{(i)}(k) = \frac{\partial h\left(\hat{\rho}_k^{(i=1\div N)} \middle| \boldsymbol{X}_{k|k-1}\right)}{\partial \boldsymbol{X}_{k|k-1}(8)} = 1 \tag{4-75}$$

Finally, the dual-constellation observation matrix is constructed by combining the partial derivatives terms concerning the pseudorange and pseudorange rate measurements for the $N1$ GPS and $N2$ Galileo locked satellites, given in Eq. (4-70) - (4-75):

$$\boldsymbol{X_{GPS/Gal}} = [x \quad \dot{x} \quad y \quad \dot{y} \quad z \quad \dot{z} \quad b_{Rx} \quad \dot{b}_{Rx}]_{8\times 1}^{T}$$

$$\boldsymbol{H_{2N\times 8}} = \begin{matrix} \rho_{GPS} \\ \\ \\ \rho_{Gal} \\ \\ \\ \dot{\rho}_{GPS} \\ \\ \\ \dot{\rho}_{Gal} \\ \\ \end{matrix} \begin{bmatrix} -\hat{a}_{x,GPS}^{(1)} & 0 & -\hat{a}_{y,GPS}^{(1)} & 0 & -\hat{a}_{z,GPS}^{(1)} & 0 & 1 & 0 \\ -\hat{a}_{x,GPS}^{(2)} & 0 & -\hat{a}_{y,GPS}^{(2)} & 0 & -\hat{a}_{z,GPS}^{(2)} & 0 & 1 & 0 \\ \vdots & \vdots & \vdots & \vdots & \vdots & \vdots & \vdots & \vdots \\ -\hat{a}_{x,GPS}^{(N1)} & 0 & -\hat{a}_{y,GPS}^{(N1)} & 0 & -\hat{a}_{z,GPS}^{(N1)} & 0 & 1 & 0 \\ -\hat{a}_{x,Gal}^{(1)} & 0 & -\hat{a}_{y,Gal}^{(1)} & 0 & -\hat{a}_{z,Gal}^{(1)} & 0 & 1 & 0 \\ -\hat{a}_{x,Gal}^{(2)} & 0 & -\hat{a}_{y,Gal}^{(2)} & 0 & -\hat{a}_{z,Gal}^{(2)} & 0 & 1 & 0 \\ \vdots & \vdots & \vdots & \vdots & \vdots & \vdots & \vdots & \vdots \\ -\hat{a}_{x,Gal}^{(N2)} & 0 & -\hat{a}_{y,Gal}^{(N2)} & 0 & -\hat{a}_{z,Gal}^{(N2)} & 0 & 1 & 0 \\ v_{x,GPS}^{(1)} & -\hat{a}_{x,GPS}^{(1)} & v_{y,GPS}^{(1)} & -\hat{a}_{y,GPS}^{(1)} & v_{z,GPS}^{(1)} & -\hat{a}_{z,GPS}^{(1)} & 0 & 1 \\ v_{x,GPS}^{(2)} & -\hat{a}_{x,GPS}^{(2)} & v_{y,GPS}^{(2)} & -\hat{a}_{y,GPS}^{(2)} & v_{z,GPS}^{(2)} & -\hat{a}_{z,GPS}^{(2)} & 0 & 1 \\ \vdots & \vdots & \vdots & \vdots & \vdots & \vdots & \vdots & \vdots \\ v_{x,GPS}^{(N1)} & -\hat{a}_{x,GPS}^{(N1)} & v_{y,GPS}^{(N1)} & -\hat{a}_{y,GPS}^{(N1)} & v_{z,GPS}^{(N1)} & -\hat{a}_{z,GPS}^{(N1)} & 0 & 1 \\ v_{x,Gal}^{(1)} & -\hat{a}_{x,Gal}^{(1)} & v_{y,Gal}^{(1)} & -\hat{a}_{y,Gal}^{(1)} & v_{z,Gal}^{(1)} & -\hat{a}_{z,Gal}^{(1)} & 0 & 1 \\ v_{x,Gal}^{(2)} & -\hat{a}_{x,Gal}^{(2)} & v_{y,Gal}^{(2)} & -\hat{a}_{y,Gal}^{(2)} & v_{z,Gal}^{(2)} & -\hat{a}_{z,Gal}^{(2)} & 0 & 1 \\ \vdots & \vdots & \vdots & \vdots & \vdots & \vdots & \vdots & \vdots \\ v_{x,Gal}^{(N2)} & -\hat{a}_{x,Gal}^{(N2)} & v_{y,Gal}^{(N2)} & -\hat{a}_{y,Gal}^{(N2)} & v_{z,Gal}^{(N2)} & -\hat{a}_{z,Gal}^{(N2)} & 0 & 1 \end{bmatrix} \tag{4-76}$$

4.3.2.3. EKF Computation steps

The first stage of the EKF estimation, referred to as the "state prediction" in Figure 4-1, corresponds to the forward time projection of the state vector $\boldsymbol{X}_{k|k-1}$ and state covariance matrix $\boldsymbol{P}_{k|k-1}$ prior to the measurement inclusion, is performed in two steps:

1. ***State prediction:***

$$\boldsymbol{X}_{k|k-1} = \boldsymbol{\Phi}_k \cdot \boldsymbol{X}_{k-1|k-1} \tag{4-77}$$

2. ***State matrix covariance prediction:***

$$\boldsymbol{P}_{k|k-1} = \boldsymbol{\Phi}_k \cdot \boldsymbol{P}_{k-1|k-1} \cdot \boldsymbol{\Phi}_k^T + \boldsymbol{Q}_k \tag{4-78}$$

The Kalman gain matrix $\boldsymbol{K}_k$ can be thought of as a blending factor having as a main objective the minimization of the *a posteriori* state vector and its error covariance matrix. In other words, it reflects the convergence speed of the EKF filter and is computed as:

$$\boldsymbol{K}_k = \boldsymbol{P}_{k|k-1} \cdot \boldsymbol{H}_k^T \cdot \left[\boldsymbol{H}_k \cdot \boldsymbol{P}_{k|k-1} \cdot \boldsymbol{H}_k^T + \boldsymbol{R}_k\right]^{-1} \tag{4-79}$$

The state vector estimate update $\boldsymbol{X}_{k|k}$ is obtained using the following expression:

$$\boldsymbol{X}_{k|k} = \boldsymbol{X}_{k|k-1} + \boldsymbol{K}_k \cdot (\boldsymbol{z}_{input} - \hat{\boldsymbol{z}}_k) = x_k^- + K_k \cdot \delta z_k \quad (4\text{-}80)$$

Where $\boldsymbol{z}_{input}$ is the measurement input vector comprising the pseudorange and pseudorange rate measurements output from the DLL and PLL tracking loops, respectively.

The final step of the EKF estimation workflow is the state vector error covariance matrix update, given by:

$$\boldsymbol{P}_{k|k} = (\boldsymbol{I} - \boldsymbol{K}_k \cdot \boldsymbol{H}_k) \cdot \boldsymbol{P}_{k|k-1} \quad (4\text{-}81)$$

In the implemented EKF navigation filter in this work, a different representation of the state covariance update is employed for stability reason [Groves, 2013]:

$$\boldsymbol{P}_{k|k} = (\boldsymbol{I} - \boldsymbol{K}_k \cdot \boldsymbol{H}_k) \cdot \boldsymbol{P}_{k|k-1} \cdot (\boldsymbol{I} - \boldsymbol{K}_k \cdot \boldsymbol{H}_k)^T + \boldsymbol{K}_k \cdot \boldsymbol{R}_k \cdot \boldsymbol{K}_k^T \quad (4\text{-}82)$$

4.4. Conclusions

In this chapter, the dual-constellation scalar GNSS navigation processor has been presented. This chapter starts with the receiver's clock modelling for the dual-constellation operation mode. In section 4.1 it was proved that, within the hypothesis of omitting the inter-constellation clock term, only one receiver's clock bias term can characterize both the GPS and Galileo measurements. This result indeed simplifies the navigation solution due to the reduction of the number of states that need to be estimated.

Section 4.2 introduced the corrected measurements' generation model, concerning both the pseudorange and pseudorange rate observations. The emphasis was directed to the observations' equations after the application of the ionosphere Klobuchar (for GPS L1 C/A) and NeQuick (for the Galileo E1 OS) correction models. In fact, the ionosphere residuals and residuals rate appear into the code and Doppler measurements, respectively, obtained after the code/carrier tracking process.

The central part of this chapter is dedicated to the design of two distinct navigation algorithms in section 4.3, namely the Weighted Least Square (WLS) and Extended Kalman Filter (EKF), for the dual-constellation single-frequency GPS/Galileo L1/E1 receiver. First, the WLS technique is described in details since it is used at the navigation initialization step for both the scalar and vector tracking receiver. Afterwards, the EKF technique is chosen to provide the user's navigation solution estimation. The EKF system model, reflecting the user's dynamics variation through the absolute Position, Velocity and Time (PVT) state vector and its error covariance matrix representation has been entirely described. Moreover, the measurement model that relates the incoming pseudoranges and pseudorange rate observations from the DLL and 3rd PLL tracking loops (after the ionosphere delay correction) to the state vector is detailed.

In the following chapter, an advanced tracking loop architecture referred to as vector tracking for the dual-constellation receiver is tackled.

5. Proposed Dual-Constellation Vector Tracking Architecture

In the previous chapters, the conventional GNSS receiver processing both in the tracking and positioning domain was detailed. In this chapter, the dual-constellation single frequency vector tracking receiver for the automotive usage is proposed and investigated.

In section 5.1, the urban environment-induced effects on the tracking process and the positioning performance are detailed. In these environments, multipath and GNSS signal blockage are often encountered and introduce severe distortions of the correlation function up to satellite's loss of lock condition. As a consequence, a position error increase is observed due to the limited number of error-affected measurements fed to the EKF navigation filter.

For this purpose, the attention is directed toward the vector tracking (VT) concept able to cope with the severe urban conditions and referred to as an advanced tracking technique that jointly performs the tracking and navigation tasks. An overall picture of the VT architecture and its main differences with respect to scalar tracking are given in section 5.2. Previous conducted works on the vector tracking subject are summarized in the second part of section 5.2.

In section 5.3, the proposed dual constellation GPS/Galileo single frequency L1/E1 vector tracking architecture implemented for the automotive usage in urban environment is analyzed in details. This technique significantly improves the positioning accuracy compared to the single constellation receiver due to the increased number of observations through the inclusion of the Galileo pseudorange and Doppler measurements into the navigation module. Moreover, the joint code delay and Doppler carrier frequency tracking for all the satellites in-view performed by the common navigation filter ensures better receiver's dynamics estimation. This approach is also capable of estimating the ionosphere residual errors that appear after the application of the ionosphere correction models. The detailed flowchart of the vector tracking algorithm and the relation between the state vector and observation model is also exposed. Last but not least, the vectorized NCO feedback to the code/carrier tracking loops along with the measurements' model are detailed.

The chapter conclusions are provided in Section 5.4.

5.1. Problematic in Urban Environment

Since this research work aims at the automotive usage of the GNSS receiver in urban environment, the urban environment-induced effects on the tracking and positioning performance shall be first described.

The urban environment presents several challenges to GNSS signal reception and its posteriori processing, severely degrading the positioning accuracy. The main problems arising from the urban environment conditions, are the following:

- *Multipath*: defined as the reception of reflected or diffracted GNSS LOS echoes (from the ground, buildings, foliage, lampposts, etc.) in addition to the direct LOS signal;
- *Attenuation or blockage of the GNSS LOS signal*: is a phenomenon arising due to the partial or total obstruction of the GNSS LOS from the urban environment characteristics;
- *Interference:* occurring due to the presence of a wide class of interfering signals, falling within the GNSS frequency bands. The dominant source of interference is related to the reception of continuous wave interference (CWI) signals, generated from Ultra-High Frequency (UHF) and Very-High Frequency (VHF) TV transmitters, Digital Video Broadcasting Terrestrial (DVB-T) system and so on.

The consequences of the above mentioned urban environment error sources either on the received signal or at the receiver correlator output w.r.t. the ideal reception of a GNSS signal are the following [Shytermeja et al., 2014]:

- *Distortion of the receiver's correlation function*: between the received multipath-contaminated signal and the receiver's locally generated replica. In the GNSS context, the multipath reception leads to a degradation of the incoming signal's code and carrier estimations accuracy up to a loss of lock of the code and carrier tracking loops. Consequently, the pseudoranges and Doppler measurements fed to the navigation filter are deteriorated;
- *Only Non-LOS (NLOS) signals reception*: occurs when the direct LOS GNSS signal is blocked and thus, only reflected signals are received. A bias on the pseudo-range and Doppler measurements is introduced if only NLOS signals are tracked. This bias can be very important as it is representative of the extra-path travelled by the NLOS signal compared to the theoretical LOS signal. The LOS shadowing can also decrease the LOS signal C/N_0 and thus makes the signal more vulnerable to the multipath effect;

Finally, the resulting degraded measurements cause the navigation processor to compute an inaccurate position solution or even to be unable to compute one in the case of only few available measurements. For the receiver's scalar tracking configuration in the presence of weak signals or significant signal power drops, frequent loss-of-locks of the affected satellite occur. Therefore, the signal re-acquisition process should be initiated for the loss-of-lock satellites and during this period, their measurements are not fed to the navigation processor due to their lack of accuracy.

Thus, it is evident that advanced signal processing techniques are necessary to mitigate these undesired effects in order to ensure the accuracy and availability of the position solution. A promising approach for reducing the effect of multipath interference and NLOS reception is vector tracking (VT), first introduced in Chapter 7 of [Parkinson, 1996], where the signal tracking and navigation estimation tasks are accomplished by the central navigation filter.

5.2. Vector Tracking Introduction

5.2.1. Vector Tracking fundamentals

Vector tracking algorithms constitute an advanced GNSS signal processing method, having the ability to function at lower carrier-to-noise power (C/N_0) ratios and in higher user's dynamics than traditional GNSS receivers [Petovello and Lachapelle, 2006]. Contrary to the conventional or scalar tracking architecture, where each visible satellite channel is being tracked individually and independently, vector tracking performs a joint signal tracking of all the available satellites. It exploits the knowledge of the estimated receiver's position and velocity to control the tracking loops' feedback. The comparison between the scalar tracking and vector tracking architectures is illustrated in Figure 5-1.

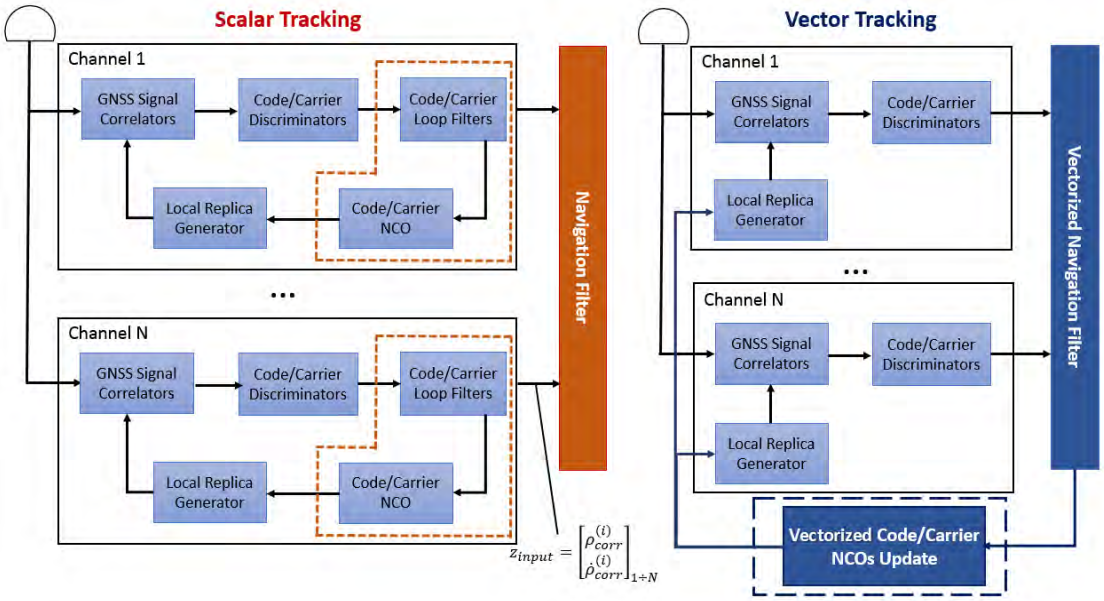

Figure 5-1. *The high-level representation of:* ***a)*** *Conventional or scalar tracking and* ***b)*** *vector tracking architectures.*

Concerning the scalar tracking architecture Figure 5-1 a), the digital down-converted signal samples are passed to each parallel tracking channel from $1 \div N$. The signal's correlator pairs, resulting from the multiplication of the in-phase and quadrature signal components with the three delayed code spreading sequences that are generated from the code generator (detailed in section 3.5.3), are later passed to the code and phase (or frequency) discriminators and their respective loop filters. The main objective of the code/carrier loop filters is the discriminators' outputs filtering for noise reduction at the input of the receiver's oscillator. Furthermore, the code/carrier NCOs are responsible of converting the filtered discriminator output into a frequency correction factor that is fed back to the code replica and carrier generators, which in turn are used to generate the local code/carrier replicas for the next epoch.

The tracking process for typical receivers, when considering both GPS L1 C/A signal and Galileo E1 OS pilot signals, is performed iteratively every correlation epoch, or approximately every $20\ ms$. For the

scalar tracking receiver implemented in this thesis and analyzed in section 4.3, the channels' pseudorange (code) and pseudorange rate (Doppler frequency) measurements are incorporated at $1\ Hz$ rate into the navigation filter to estimate the user's position, velocity and time parameters. The clear benefits of scalar tracking are their implementation simplicity and robustness linked to the channel-independent processing that does not allow the errors to spread to other tracking channels. However, on the downside, the fact that the signals are inherently related via the receiver's position and velocity is entirely ignored [Petovello and Lachapelle, 2006].

For the vector tracking architecture, depicted in Figure 5-1 b), the code and carrier tracking loops of all the satellites in-view are coupled through the navigation solution computed by the central navigation filter. The individual code/carrier loop filters and NCOs, illustrated by the dashed red line in the left figure, are eliminated and are effectively replaced by the vectorized code/carrier update block in blue. In fact, when the EKF estimates the receiver's position, the feedback to the local signal generators is obtained from the predicted ranges and range rates for each satellite in-view. The vector tracking technique exploits the coupling between the receiver's dynamics and the dynamics observed by the tracking loops. The primary advantages of vector tracking are the channel noise reduction that decreases the possibility of entering the non-linear discriminator regions and the tracking performance improvement in constrained environments, which are characterized by the low C/N_0 reception conditions [Seco-Granados et al., 2012]. In contrast to the scalar tracking technique, vector tracking can also continue its operation during momentary blockage of one or several satellites without the necessity of performing the signal re-acquisition when the satellite reappears [Petovello and Lachapelle, 2006]. The main drawback is the channel-fault coupling where the errors of certain channels can predominate the good channel estimations due to their close relation via the estimated navigation solution. Moreover, scalar tracking algorithms are needed for the vector tracking process initialization since a good initial position estimation is required for vector tracking architectures.

The above described vector tracking advantages and disadvantages are summarized in Table 5-1.

Table 5-1. *Vector tracking performance characteristics.*

VDFLL Performance Characteristics	
Advantages	***Disadvantages***
➢ Tracking improvement in *weak-signal* and *jamming* environments; ➢ Better user's dynamics tracking due to: o Channels' coupling and accumulative signal power. ➢ Higher robustness to momentary satellite outages or blockages; ➢ No *signal re-acquisition* process is performed when the signals reappear; ➢ Feasibility to *ultra-tight* GNSS/INS integration.	➢ *Initialization* from scalar tracking is a necessary requirement; ➢ Channel *fault coupling*; ➢ Increased receiver's design *complexity*; ➢ Not feasible for "of-the-shelf" GNSS receivers due to the lack of access of their correlator and discriminators outputs;

Vector tracking can be extended to the ultra-tight (deep) coupling by augmenting its architecture in Figure 5-1 b) with an inertial measurement system (INS) and by replacing the navigation filter with an integrated GNSS/INS filter [Abbott and Lillo, 2003].

In the ultra-tight coupling architecture, the data provided from the INS are used to assist the tracking loops since the relative user-satellite motion can be predicted based on the INS measurements.

5.2.2. Vector Tracking state-of-the-art

Concerning the code and carrier tracking loop modifications, the following possible vector tracking (VT) architectures are envisaged:

- *Vector Delay Locked Loop (VDLL)*: tracking only the PRN code delay evolution in a vectorized manner through the navigation filter, while the carrier tracking task is still handled via conventional scalar tracking approach independently for each satellite channel;
- *Vector Frequency Locked Loop (VFLL)*: where the incoming signals' Doppler frequency change is estimated by the EKF navigation filter, whereas the code tracking is achieved separately per each channel in the scalar tracking configuration;
- *Vector Phase Locked Loop (VPLL)*: where the incoming signals' phase is estimated by the EKF navigation filter, whereas the code tracking is achieved separately per each channel in the scalar tracking configuration;
- *Vector Delay and Frequency Locked Loop (VDFLL)*: represents a combination of VDLL and VFLL, where both the code delay and carrier frequency tracking tasks are realized by the common navigation filter.

However from the four described VT configurations, the VPLL represents by far the most challenging one. This is due to the fact that the estimated user's position is not sufficiently accurate to predict the carrier phase ambiguity, related to the impact of the propagation delays and other possible biases. Moreover, this configuration is more sensitive to the satellites' momentary outages since the signal phase recovery is more difficult due to the integer phase ambiguity issue. Therefore, the VPLL technique is not suggested for urban environments where low C/N_0 ratios are encountered since the carrier frequencies and code delays can be better tracked in these conditions w.r.t the carrier phases [Bevly, 2014].

The first vector tracking architecture, implemented in the form of the VDLL, was presented in [Parkinson, 1996] where also the main advantages of vector tracking were listed. This work highlights the VDLL superiority over scalar tracking loops in terms of code delay estimation accuracy for the GPS L1 signal. The vector tracking ability in improving the code tracking in the presence of jamming is provided in [Gustafson and Dowdle, 2003] and [Won et al., 2009].

The GPS L1 signal tracking robustness of the Vector Delay Frequency Lock Loop (VDFLL) under weak signal conditions is demonstrated in [Pany et al., 2005]. [Lashley, 2009] presents two different configurations of the VDFLL filter, using the position state and pseudorange state formulation, to show that the information sharing between the channels is an important vector tracking's performance benefit. In addition, the work in [Lashley et al., 2010] provides the comparison between the centralized and de-coupled VDFLL architectures in dense foliage, showing a $5\ dB$ performance gain of the later at high C/N_0 (more than $40\ dB$). Moreover, the VDFLL capability of continuously maintaining the L1 code/carrier tracking during simulated signal outages is shown in [Sousa and Nunes, 2014]. An interesting proposal of a simplified vector tracking integrity algorithm applied to an aircraft landing trajectory is found in [Bhattacharyya, 2012].

The vector tracking extension toward the deep GPS/INS integration has been investigated by several authors, including [Jovancevic et al., 2004], [Abbott and Lillo, 2003] and [Soloviev et al., 2004]. Each of these research works use cascaded vector tracking approaches, associating a local filter per each tracking channel. In this case, each channel has an associated Kalman filter in charge of estimating the channel errors, allowing the order reduction of the navigation filter state vector and also, enabling the channel errors inclusion in the navigation filter at a lower rate. A comparison between the different state vectors and measurement models for the cascaded vector tracking technique is performed in [Petovello and Lachapelle, 2006], whereas the importance of the correct local filter tuning is shown in [Falco et al., 2014].

5.3. The dual-constellation single-band VDFLL L1/E1 architecture

In this work, a dual constellation GPS + Galileo single frequency L1/E1 VDFLL architecture is proposed and implemented for the automotive usage in urban environment. The reason behind this choice is threefold:

- Firstly, the inclusion of the Galileo satellites measurements in the tracking and navigation module can significantly improve the availability of a navigation solution in urban canyons and heavily shadowed areas: an increased number of satellites in-view is directly translated in a higher measurement redundancy and improved position accuracy;
- Secondly, the implementation of the VDFLL tracking architecture, where the navigation filter estimates the code delay (VDLL) and the Doppler frequency change (VFLL) of each incoming signal in order to close the code and carrier feedback loops, enhances the vehicle dynamics tracking capability of the receiver;
- Thirdly, the dual-constellation single frequency vector tracking architecture ensures an increased number of observations while at the same time reducing the architecture complexity (w.r.t the dual frequency receiver) and conserving the low-cost feasibility criteria of the mobile user's receiver.

In this thesis, the non-coherent dual-constellation single frequency L1/E1 VDFLL tracking is implemented, whose architecture is illustrated in Figure 5-2.

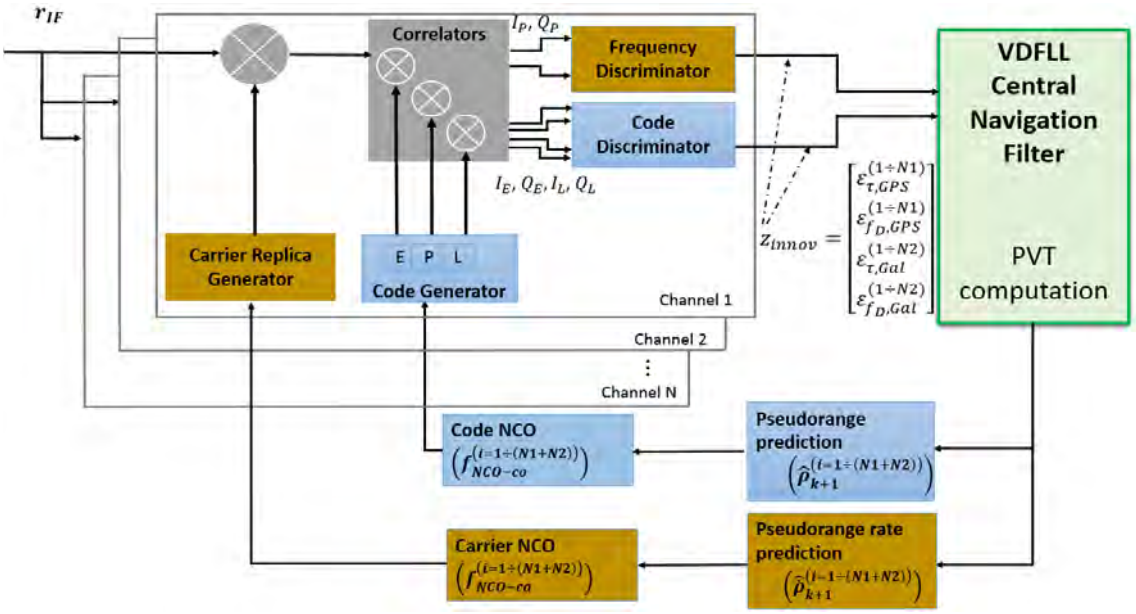

Figure 5-2. *The non-coherent L1/E1 VDFLL architecture.*

As can be observed in Figure 5-2, the central navigation filter accepts the code $\left(\varepsilon_{\tau}^{(i)}\right)$ and carrier $(\varepsilon_{f_D}^{(i)})$ discriminator outputs for each GPS $(i = 1 \div N1)$ and Galileo $(i = 1 \div N2)$ tracked channels as its input vector. Contrary to the scalar tracking counterpart, where the code and carrier NCO corrections are generated locally per each channel, in the vectorized architecture the code and carrier NCO update is achieved by projecting the predicted navigation solution in the pseudorange and pseudorange rate domains. From the navigation point of view, VDFLL represents a concrete application of information fusion, since all the tracking channels NCOs are controlled by the same navigation solution filter.

5.3.1. VDFLL State Space Model

The use of dual constellation but single frequency L1 band signals does not allow the entire correction of the ionosphere delay. As previously stated in Chapter 4, after the application of the Klobuchar or Nequick ionosphere error correction models to the GPS and Galileo pseudorange measurements, a resultant ionosphere residual error appears in the received observations. This section provides the VDFLL state model adaptation within the objective of estimating the ionosphere residuals affecting the incoming measurements.

5.3.1.1. Ionosphere Residual's state model

The ionosphere residual is correlated in time and can be modelled as a first order Gauss-Markov (GM) process, having an exponentially decaying autocorrelation function, as standardized in [ICAO, 2008]. The first-order Gauss-Markov stationary process is expressed in continuous time as follows:

$$\frac{d[b_{iono}(t)]}{dt} = -\frac{1}{\tau} \cdot b_{iono}(t) + w_{iono}(t) \qquad (5\text{-}1)$$

Where:

- b_{iono} is the ionosphere error GM random process with zero mean and variance $\sigma_{b_{iono}}^2$,which is computed using the Klobuchar (GPS L1 C/A) and NeQuick (Galileo E1 OS) correction model parameters, according the relation provided in Eq. (3-7) and (3-11);

- τ is the ionosphere error correlation time that is set to $1800\ s$ in [ICAO, 2008] and [EUROCAE, 2010];
- w_{iono} is the process driven white noise with zero mean and variance $\sigma^2_{w_{iono}}$.

The discrete time model of the ionosphere residual GM random process is expressed as follows:

$$b_{iono,k} = e^{-\frac{T_s}{\tau}} \cdot b_{iono,k-1} + w_{iono,k}\ [m] \tag{5-2}$$

where:

- $b_{iono,k}$ is the ionosphere residual at the current k^{th} epoch, expressed in $[m]$;
- τ is the GM process correlation time expressed in $[m]$;
- T_s is the sampling period expressed in $[s]$;
- $w_{iono,k}$ is the value of the process driven white noise at the k^{th} epoch.

In discrete time, the process driven noise variance $\sigma^2_{w_{b_{iono,k}}}$ is deduced from the global GM process using the following relation:

$$\sigma^2_{w_{b_{iono,k}}} = \sigma^2_{b_{iono,k}} \cdot \left(1 - e^{-\frac{2 \cdot T_s}{\tau}}\right) \tag{5-3}$$

The main parameters that are required for the full description of the GM process are the correlation time τ and the process driven noise variance $\sigma^2_{w_{b_{iono,k}}}$.

Since this work is focused on the proposal and implementation of the VDFLL algorithm, the ionosphere residual error impact on the pseudorange rate measurement and its mathematical formulation is of great interest. The effect of the ionosphere residual in the pseudorange rate measurement can be deduced through differencing the ionosphere residual error between two consecutive epochs:

$$\dot{b}_{iono,k} = \frac{b_{iono,k} - b_{iono,k-1}}{t_k - t_{k-1}} = \frac{b_{iono,k} - b_{iono,k-1}}{T_s} \quad \left[\frac{m}{s}\right] \tag{5-4}$$

Applying the discrete ionosphere residual model of Eq. (5-2) for the current epoch k and previous epoch $k-1$, the ionosphere residual rate (m/s) is expressed as:

$$\begin{aligned}
\dot{b}_{iono,k} &= \frac{e^{-\frac{T_s}{\tau}} \cdot b_{iono,k-1} + w_{iono,k} - e^{-\frac{T_s}{\tau}} \cdot b_{iono,k-2} + w_{iono,k-1}}{T_s} \\
&= \frac{e^{-\frac{T_s}{\tau}} \cdot \left(b_{iono,k-1} - b_{iono,k-2}\right) + \left(w_{iono,k} - w_{iono,k-1}\right)}{T_s} \\
&= \frac{e^{-\frac{T_s}{\tau}} \cdot \left(b_{iono,k-1} - b_{iono,k-2}\right)}{T_s} + \frac{1}{T_s} \cdot \left(w_{iono,k} - w_{iono,k-1}\right) \\
&= e^{-\frac{T_s}{\tau}} \cdot \dot{b}_{iono,k-1} + \frac{1}{T_s} \cdot \left(w_{iono,k} - w_{iono,k-1}\right)
\end{aligned} \tag{5-5}$$

The ionosphere residual rate variance is derived as:

$$\sigma^2_{\dot{w}_{b_{iono,k}}} = \frac{var(w_k - w_{k-1})}{T_s^2} = \frac{\sigma^2_{w_{b_{iono,k}}} + \sigma^2_{w_{b_{iono,k-1}}} - 2cov(w_{iono,k}, w_{iono,k-1})}{T_s^2} \tag{5-6}$$

When visualizing the cross-correlation between the two noise sequences, nearly zero correlation was observed. Thus neglecting the cross-covariance term, the ionosphere residual rate process driven variance $\sigma^2_{w_{\dot{b}_{iono,k}}}$ is computed as:

$$\sigma^2_{w_{\dot{b}_{iono,k}}} = \frac{2 \cdot \sigma^2_{w_{b_{iono,k}}}}{T_S^2} = \frac{2 \cdot \sigma^2_{b_{iono},k} \cdot \left(1 - e^{-\frac{2 \cdot T_S}{\tau}}\right)}{T_S^2} \tag{5-7}$$

5.3.1.2. VDFLL augmented-State model

In the proposed VDFLL architecture, the absolute PVT state vector of scalar tracking navigation module of Eq. (4-19) is augmented with the ionosphere error residuals affecting the pseudorange measurements at each epoch k and is expressed as follows:

$$\boldsymbol{X_{VDFLL,k}} = \boldsymbol{X}_k = \begin{bmatrix} X_{PVT} \\ b^{(1)}_{iono-GPS,k} \\ b^{(2)}_{iono-GPS,k} \\ \vdots \\ b^{(N1)}_{iono-GPS,k} \\ b^{(1)}_{iono-Gal,k} \\ b^{(2)}_{iono-Gal,k} \\ \vdots \\ b^{(N2)}_{iono-Gal,k} \end{bmatrix}_{\{8+(N1+N2)\}\times 1} \tag{5-8}$$

where:

- $X_{PVT} = [x, \dot{x}, y, \dot{y}, z, \dot{z}, b_{Rx}, \dot{b}_{Rx}]^T_{8\times 1}$ is the absolute PVT state vector employed in the scalar tracking EKF navigation module and given in Eq. (4-19);
- $b^{(i)}_{iono-GPS|Gal,k}$ denote the ionosphere residual errors in $[m]$ affecting the pseudorange measurements from the N1 GPS and N2 Galileo tracking channels, respectively.

The ionosphere residual exhibits a certain observability due to its long correlation time with respect to the other error sources. Since the derivative of a 1st order Gauss-Markov process is a white noise when referring to the statistical theory, the EKF filter is not capable of observing and later estimating the ionosphere residual rate error effect on the Doppler measurements. In order to cope with this issue, the measurement covariance matrix terms related to the Doppler measurements are increased by the ionosphere residual rate process driven variance $\sigma^2_{w_{\dot{b}_{iono,k}}}$ of Eq. (5-7).

Following the mathematical derivation of the discrete state transition matrix, detailed in the previous chapter, the VDFLL state transition matrix accounting for the ionosphere residual errors is formulated as:

$$\boldsymbol{\Phi_{VDFLL,k}} = \boldsymbol{\Phi_k} = \begin{bmatrix} \boldsymbol{\Phi}_{8\times 8} & 0 & \cdots & 0 \\ 0 & e^{-\frac{T_S}{\tau}(1)} & 0 & 0 \\ \vdots & 0 & \ddots & 0 \\ 0 & 0 & 0 & e^{-\frac{T_S}{\tau}(N)} \end{bmatrix}_{(8+N)\times(8+N)} \tag{5-9}$$

where:

- $\boldsymbol{\Phi}_{8\times8}$ is the discrete PVT state transition matrix detailed in Eq. (4-45);
- $e^{-\frac{T_S}{\tau}}$ is the exponential decaying coefficient of the ionosphere residual error for each satellite channel from $i = 1 \div N$.

The discrete process noise vector w_k is modelled as a Gaussian noise vector with zero mean and discrete covariance matrix $\boldsymbol{Q}_k$. In addition to the two process noise sources namely, the user's dynamic and the receiver's clock noises, presented in the previous chapter, the ionosphere residual process driven noise terms should be added to the noise vector, given as:

$$\boldsymbol{w_{VDFLL,k}} = \boldsymbol{w}_k = \begin{bmatrix} w_{PVT} \\ w_{iono-GPS,k}^{(1)} \\ w_{iono-GPS,k}^{(2)} \\ \vdots \\ w_{iono-GPS,k}^{(N1)} \\ w_{iono-Gal,k}^{(1)} \\ w_{iono-Gal,k}^{(2)} \\ \vdots \\ w_{iono-Gal,k}^{(N2)} \end{bmatrix}_{\{8+(N1+N2)\}\times1} \tag{5-10}$$

where:

- $w_{PVT} = [w_{\dot{x}}, w_{\dot{y}}, w_{\dot{z}}, w_b, w_d]_{5\times1}^T$ is the process noise sub-vector comprising the user's dynamics $[w_{\dot{x}}, w_{\dot{y}}, w_{\dot{z}}]_{3\times1}^T$ and the oscillator's $[w_b, w_d]_{2\times1}^T$ noise terms, detailed in Eq. (4-39);
- $w_{iono-GPS/Gal,k}^{(i)}$ represent the ionosphere residual error process noise terms affecting the pseudorange measurements from the N1 GPS and N2 Galileo tracking channels, respectively.

As a consequence, the process noise covariance matrix $\boldsymbol{Q}_k$ should take into consideration the ionospheric disturbance present on the received signal and is expressed as follows:

$$\boldsymbol{Q_{VDFLL,k}} = \boldsymbol{Q_k} = \begin{bmatrix} \boldsymbol{Q}_{8\times8} & 0 & \cdots & 0 \\ 0 & \sigma^2_{w_{b_{iono,k}}}{}^{(1)} & 0 & 0 \\ \vdots & 0 & \ddots & 0 \\ 0 & 0 & \dots & \sigma^2_{w_{b_{iono,k}}}{}^{(N)} \end{bmatrix}_{(8+N)\times(8+N)} \tag{5-11}$$

where:

- $\boldsymbol{Q}_{8\times8}$ is the discrete process noise covariance matrix comprising the user's dynamics and receiver's oscillator errors presented in Eq. (4-55);
- $\sigma^2_{w_{b_{iono,k}}}{}^{(i)}$ is the ionospheric error driven process noise for each satellite channel from $i = 1 \div N$.

5.3.2. VDFLL Observation Model

Since the VDFLL architecture performs the joint code delay and carrier frequency tracking via the EKF navigation filter, the measurement vector $\boldsymbol{z_k}$ is identical to the one presented for the scalar tracking receiver in Eq. (4-57), containing the pseudoranges $\rho^{(i)}$ and Doppler measurements $\dot{\rho}^{(i)}$, output from the code/carrier tracking process for the $i = 1 \div N$ GPS L1/ Galileo E1 tracking channels:

$$\boldsymbol{z_k} = \left[(\rho^{(1)}\ \rho^{(2)}\ \cdots \rho^{(N)}) : (\dot{\rho}^{(1)}\ \dot{\rho}^{(2)}\ \cdots \dot{\rho}^{(N)})(k)\right]_{2N\times 1} \tag{5-12}$$

Including the ionosphere residual error impact, the GNSS pseudorange measurements of a given satellite i (from the GPS ($N1$) and Galileo ($N2$) satellites in-view) at epoch k are rewritten as:

$$\rho^{(i)}(k) = \begin{cases} |\boldsymbol{r_i}(k) - \boldsymbol{r_u}(k)| + b_{Rx}(k) + b^{(i)}_{iono-GPS}(k) + \varepsilon^{(i)}_{n_{\rho,GPS}}(k), & 0 < i \le N1 \\ |\boldsymbol{r_i}(k) - \boldsymbol{r_u}(k)| + b_{Rx}(k) + b^{(i)}_{iono-Gal}(k) + \varepsilon^{(i)}_{n_{\rho,Gal}}(k) & N1 < i \le N \end{cases} \tag{5-13}$$

where:

- $|\boldsymbol{r_i}(k) - \boldsymbol{r_u}(k)| = \sqrt[2]{\left(x_s^{(i)}(k) - x(k)\right)^2 + \left(y_s^{(i)}(k) - y(k)\right)^2 + \left(z_s^{(i)}(k) - z(k)\right)^2}$ is the satellite-to-user geometric distance at the current epoch k where $(x_s^{(i)}, y_s^{(i)}, z_s^{(i)})(k)$ and $(x, y, z)(k)$ represent the i^{th} satellite and user's coordinates in the ECEF reference frame, respectively;
- $b_{Rx}(k)$ denotes the receiver's clock bias expressed in $[m]$;
- $b^{(i)}_{iono-GPS/Gal}(k)$ denote the ionosphere residual error affecting the GPS and Galileo i^{th} pseudorange measurements, respectively, expressed in $[m]$;
- $\varepsilon^{(i)}_{n_{\rho,GPS/Gal}}(k)$ is the pseudorange thermal noise assumed to be white, centered Gaussian-distributed.

The pseudorange rate measurements, constituting the remaining N-entries of the measurement vector $\boldsymbol{z_k}$, are given by:

$$\begin{aligned} \dot{\rho}^{(i)}(k) = &\left(\dot{x}_s^{(i)}(k) - \dot{x}(k)\right) \cdot a_x^{(i)}(k) + \left(\dot{y}_s^{(i)}(k) - \dot{y}(k)\right) \cdot a_y^{(i)}(k) \\ &+ \left(\dot{z}_s^{(i)}(k) - \dot{z}(k)\right) \cdot a_z^{(i)}(k) + \dot{b}_{Rx}(k) + \dot{b}^{(i)}_{iono}(k) + \dot{\varepsilon}_{n_{\dot{\rho}}}^{(i)}(k) \end{aligned} \tag{5-14}$$

Where:

- The $\left(a_x^{(i)}, a_y^{(i)}, a_z^{(i)}\right)$ are the LOS projections along the three ECEF axes, given in Eq. (4-61);
- $(\dot{x}_s^{(i)}, \dot{y}_s^{(i)}, \dot{z}_s^{(i)})(k)$ and $(\dot{x}, \dot{y}, \dot{z})(k)$ represent the i^{th} satellite and user's velocities in the ECEF reference frame, respectively;
- $\dot{b}_{Rx}(k)$ is the receiver's clock drift expressed in $\left[\frac{m}{s}\right]$;
- $\dot{b}^{(i)}_{iono}(k) = \frac{b^{(i)}_{iono}(k) - b^{(i)}_{iono}(k-1)}{T_s}$ is the ionosphere residual rate error in $\left[\frac{m}{s}\right]$, expressed as the ionosphere residual error change between two consecutive epochs ;
- $\dot{\varepsilon}_{n_{\dot{\rho}}}^{(i)}$ is the Doppler measurement thermal noise assumed to be white, centered Gaussian-distributed.

The measurement noise vector v_k is modelled as a zero-mean Gaussian noise process with measurement covariance matrix $\boldsymbol{R}_k$, expressed as:

$$\boldsymbol{R}_k = \text{diag}\left[\sigma^2{}^{(1)}_{\delta\rho_{VDFLL}}, \cdots, \sigma^2{}^{(N)}_{\delta\rho_{VDFLL}}, \sigma^2{}^{(1)}_{\delta\dot{\rho}_{VDFLL}}, \cdots \sigma^2{}^{(N)}_{\delta\dot{\rho}_{VDFLL}}\right]_{2N\times 2N}(k) \qquad (5\text{-}15)$$

In the proposed vectorized architecture, a first-order Early Minus Late Power (EMLP) discriminator has been chosen for both the GPS L1 BPSK and Galileo E1 channels. Since in the proposed vector tracking implementation, the NCO update loop is closed after the position/velocity estimation update has been performed by the navigation filter, the open-loop code tracking error variances per each tracking channel shall be fed to the measurement covariance matrix R. The code discriminator tracking error variance in presence of thermal noise and in the open-loop configuration, for both GPS L1 and Galileo E1 channels is computed in Appendix C.1 and expressed by:

$$\sigma^2{}^{(i)}_{\delta\rho_{VDFLL}}(k) = \left(\frac{c}{f_{code}}\right)^2 \cdot \frac{d \cdot T_c}{2 \cdot \alpha \cdot {C}/{N_0}^{(i)}_{est} \cdot T_{int}}\,[m^2] \qquad (5\text{-}16)$$

where:

- $\left(\frac{c}{f_{code}}\right)$ is the $s^2 \rightarrow m^2$ conversion coefficient where $c \approx 2{,}999 \cdot 10^8 m/s$ is the speed of light and $f_{code} = 1.023 \cdot 10^6 chip/s$ is the L1/E1 code chipping rate;
- α corresponds to the absolute value of the slope of the autocorrelation function main peak that is $\alpha = 1$ for GPS L1 BPSK (1) signal and $\alpha = 3$ for Galileo E1 OS;
- T_c is the code chip period in second/chip;
- d_c refers to the Early – Late code replica chip spacing that is set to $d_c = 0.5\ chip$ for GPS L1 BPSK (1) signal and $d_c = 0.2\ chip$ chips for Galileo E1 OS;
- ${C}/{N_0}^{(i)}_{est}$ refers to the estimated carrier-to-noise ratio expressed in absolute value;
- T_{int} is the code integration time in $[s]$.

The open-loop code error variance herein adopted incorporates the multipath error variance due to its large value. A similar model of the code discriminator error variance is used in [Nunes and Sousa, 2014].

The frequency discriminator performs the Doppler frequency tracking of the incoming signal that is dominated by the satellite-to-receiver motion and the user clock drift. Herein, a cross- product (CP) discriminator is employed for the carrier frequency error estimation for both the GPS and Galileo channels. The carrier frequency tracking error variance, whose mathematical formulation is derived in Appendix C.2, is given by:

$$\sigma^2{}^{(i)}_{\delta\dot{\rho}_{VDFLL}}(k) = \left(\frac{c}{f_{carr}}\right)^2 \cdot \left[\frac{1}{\pi^2 \cdot {C}/{N_0} \cdot T^3} \cdot \left(1 + \frac{1}{T \cdot {C}/{N_0}}\right)\right]\left[\frac{m^2}{s^2}\right] \qquad (5\text{-}17)$$

where $f_{carr} = 1.57542 \cdot 10^9\ Hz$ is the L1 carrier frequency and T_{FLL} is the carrier frequency update time in $[s]$.

Recalling that the designed VDFLL algorithm does not estimate the ionosphere residual rate error due to its Gaussian property, its effect on the Doppler measurement is taken into consideration by inflating

the frequency error variance of Eq. (5-17) by the ionosphere residual rate driven noise variance $\sigma^2_{w,\dot{I}_k}{}^{(i)}$ as follows:

$$\sigma^{2}{}^{(i)}_{\delta\dot{\rho}_{VDFLL}}(k) = \left(\frac{c}{f_{carr}}\right)^2 \cdot \left[\frac{1}{\pi^2 \cdot C/_{N_0} \cdot T^3} \cdot \left(1 + \frac{1}{T \cdot C/_{N_0}}\right)\right] + \sigma^2_{w_{\dot{b}_{iono,k}}}{}^{(i)} \left[\frac{m^2}{s^2}\right] \qquad (5\text{-}18)$$

Taking into account the relations in Eq. (5-17) and (5-18), the measurement noise covariance matrix has in the main diagonal the following entries:

$$\boldsymbol{R}_k = \begin{cases} \sigma^{2}{}^{(i)}_{\delta\rho_{VDFLL}}(k) & for\ 1 \le i \le N \\ \sigma^{2}{}^{(i)}_{\delta\dot{\rho}_{VDFLL}}(k) & for\ 1 \le i \le N \end{cases} \qquad (5\text{-}19)$$

where $N = N1 + N2$ denotes the GPS and Galileo tracked satellites.

5.3.3. VDFLL Measurement Prediction

Similarly to the EKF measurement model of the scalar tracking receiver, detailed in Chapter 4, the predicted measurement vector $\hat{\boldsymbol{z}}_k$ is computed by applying the non-linear observation function h on the state vector prediction $\boldsymbol{X}_{k|k-1}$ and includes the predicted pseudorange $\hat{\rho}_k^{(i)}$ and pseudorange rates $\hat{\dot{\rho}}_k^{(i)}$ for each satellite in-view $i = 1 \div N$:

$$\hat{\boldsymbol{z}}_k = \left[\left(\hat{\rho}_k^{(1)}\ \hat{\rho}_k^{(2)}\ \cdots\ \hat{\rho}_k^{(N)}\right) \vdots \left(\hat{\dot{\rho}}_k^{(1)}\ \hat{\dot{\rho}}_k^{(2)}\ \cdots\ \hat{\dot{\rho}}_k^{(N)}\right)\right]_{2N\times 1} \qquad (5\text{-}20)$$

The only difference w.r.t the previous model of Eq. (4-65) consists on the addition of the predicted ionosphere residuals errors $\hat{b}_{iono,k}^{(i)}$ to the predicted ranges and user's clock bias terms as:

$$\hat{\rho}_k^{(i)} = \hat{R}_k^{(i)} + \boldsymbol{X}_{k|k-1}(7) + \boldsymbol{X}_{k|k-1}(8+i) \qquad \text{for}\ \ 1 < i \le N \qquad (5\text{-}21)$$

where:

- $\hat{R}_k^{(i)}$ denotes the predicted *i*th satellite-user range $[m]$;
- $\boldsymbol{X}_{k|k-1}(7)$ denotes the user's clock bias predictions expressed in $[m]$;
- $\boldsymbol{X}_{k|k-1}(8+i) = \hat{b}_{iono,k}^{(i)}$ refers to the predicted ionosphere residual error in the $8+i$ element of the predicted state vector $\boldsymbol{X}_{k|k-1}$ after the eight PVT states.

Whereas, the predicted pseudorange rate $\hat{\dot{\rho}}_k^{(i)}$ is identical to the formulation already provided in Eq. (4-66):

$$\begin{aligned} \hat{\dot{\rho}}_k^{(i)} = &\left(\dot{x}_s^{(i)}(k) - \boldsymbol{X}_{k|k-1}(2)\right) \cdot \hat{a}_x^{(i)}(k) + \left(\dot{y}_s^{(i)}(k) - \boldsymbol{X}_{k|k-1}(4)\right) \cdot \hat{a}_y^{(i)}(k) \\ &+ \left(\dot{z}_s^{(i)}(k) - \boldsymbol{X}_{k|k-1}(6)\right) \cdot \hat{a}_z^{(i)}(k) + \boldsymbol{X}_{k|k-1}(8) \end{aligned} \qquad (5\text{-}22)$$

Following the mathematical derivation of the discrete state transition matrix, detailed in the previous chapter, the VDFLL observation matrix accounting for the ionosphere residual errors is formulated as:

$$\boldsymbol{H}_{\boldsymbol{VDFLL,k}} = \boldsymbol{H}_{\boldsymbol{k}} = \begin{bmatrix} \boldsymbol{H}_{\rho^{(1)},1\times 8} & 1^{(1)} & \cdots & 0 \\ \boldsymbol{H}_{\rho^{(i)},1\times 8} & 0 & \ddots & 0 \\ \boldsymbol{H}_{\rho^{(N)},1\times 8} & 0 & \ldots & 1^{(N)} \\ \boldsymbol{H}_{\dot{\rho}^{(1)},1\times 8} & 0 & \cdots & 0 \\ \boldsymbol{H}_{\dot{\rho}^{(i)},1\times 8} & 0 & \ddots & 0 \\ \boldsymbol{H}_{\dot{\rho}^{(N)},1\times 8} & 0 & \cdots & 0 \end{bmatrix}_{(2N)\times(8+N)} \tag{5-23}$$

where:

- $\boldsymbol{H}_{\rho^{(i)},1\times 8}$ is the observation matrix row containing the partial derivatives of the predicted pseudorange measurements $\hat{\rho}_k^{(i)}$ w.r.t the 8 predicted user PVT states, computed as follows for the N GPS/Galileo satellites by using the h_1 function from Eq. (4-59):

$$\left[\frac{\partial h_1\left(\hat{\rho}_k^{(i=1\div N)}|\boldsymbol{X}_{k|k-1}\right)}{\partial \boldsymbol{X}_{k|k-1}(1\div 8)}\right] = \left[-\hat{a}_x^{(i)}\ 0\ -\hat{a}_y^{(i)}\ 0\ -\hat{a}_z^{(i)}\ 0\ 1\ 0\right] \tag{5-24}$$

  and $1^{(i)}$ is the predicted pseudorange measurement derivative w.r.t the ionosphere residual error that is one at the $(8+i)^{th}$ index of the measurement matrix row for the tracked i^{th} satellite;
- $\boldsymbol{H}_{\dot{\rho}^{(1)},1\times 8}$ is the observation matrix row containing the partial derivatives of the predicted pseudorange rate measurements $\hat{\rho}_k^{(i)}$ w.r.t the 8 predicted PVT user states, for the N GPS and Galileo tracked satellites expressed by the h_2 function from Eq. (4-60):

$$\left[\frac{\partial h\left(\hat{\rho}_k^{(i=1\div N)}|\boldsymbol{X}_{k|k-1}\right)}{\partial \boldsymbol{X}_{k|k-1}(1\div 8)}\right] = \left[v_x^{(i)} - \hat{a}_x^{(i)}\ v_y^{(i)}\ -\hat{a}_y^{(i)}\ v_z^{(i)}\ -\hat{a}_z^{(i)}\ 0\ 1\right] \tag{5-25}$$

where: $(v_x^{(i)}, v_y^{(i)}, v_z^{(i)})$ and $(-a_x^{(i)}, -a_y^{(i)}, -a_z^{(i)})$ are the predicted pseudorange rate derivatives w.r.t the position and velocity states, respectively, computed in Eq. (4-71) to (4-75).

5.3.4. VDFLL Measurement Innovation vector

The proposed dual constellation VDFLL algorithm operates at a $50\ Hz$ update rate matching with the scalar code/carrier tracking update frequency. The code delay and frequency carrier estimation process are achieved per channel basis as in the scalar configuration, however in the designed vectorized architecture, the code and frequency discriminator outputs will be directly fed to the EKF navigation filter as its measurement innovation vector, as shown in Figure 5-2. This is valid under the assumption that the code delay and carrier frequency errors fall into their discriminator's linear region and since the EKF-computed code and carrier NCO feedback loops to each satellite channel are performed at the code and carrier accumulation (50 Hz) rate.

The measurement innovation vector $\boldsymbol{z}_{innov,k}$ at epoch k includes the pseudorange and pseudorange rate errors $\varepsilon_{code/carr}$ for each tracking channel $i = 1 \div N$ that are computed from the code and carrier discriminator functions using the following expression:

$$\begin{aligned}\boldsymbol{z}_{innov,k} &= \boldsymbol{z}_k - \hat{\boldsymbol{z}}_k \\ &= \left(h(\boldsymbol{X}_{k|k-1}) + \varepsilon_{code/carr}\right) - h(\boldsymbol{X}_{k|k-1}) \\ &= \left[\left(\frac{c}{f_{code}}\right)\cdot\left(\varepsilon_{\tau,GPS}^{(i=1\div N1)}\ \varepsilon_{\tau,Gal}^{(i=(N1+1)\div N)}\right) : \left(\frac{c}{f_{carr}}\right)\cdot\left(\varepsilon_{f_D,GPS}^{(i=1\div N1)}\ \varepsilon_{f_D,Gal}^{(i=(N1+1)\div N)}\right)(k)\right]_{2N\times 1}\end{aligned} \quad (5\text{-}26)$$

Where the first N terms for the GPS $N1$ and Galileo $(N1+1)\div N$ channels, related to the pseudorange errors, are expressed in $[m]$ and computed from the code discriminator outputs ε_τ , while the remaining N entries of the measurement innovation vector denote the pseudorange rate errors in $[m/s]$ obtained from the frequency discriminators.

It must be reminded that the code and carrier discriminator errors comprise the ionosphere residual and residual rates, respectively, that will be formulated in the following section.

5.3.5. VDFLL Feedback Loop: Code and Carrier NCO update

The code and carrier NCO updates for the successive time epoch $k+1$ is performed per each tracked channel i based on the state vector prediction $\boldsymbol{X}_{k+1|k}$ from Eq. (4-77), following the flowchart depicted in Figure 5-3.

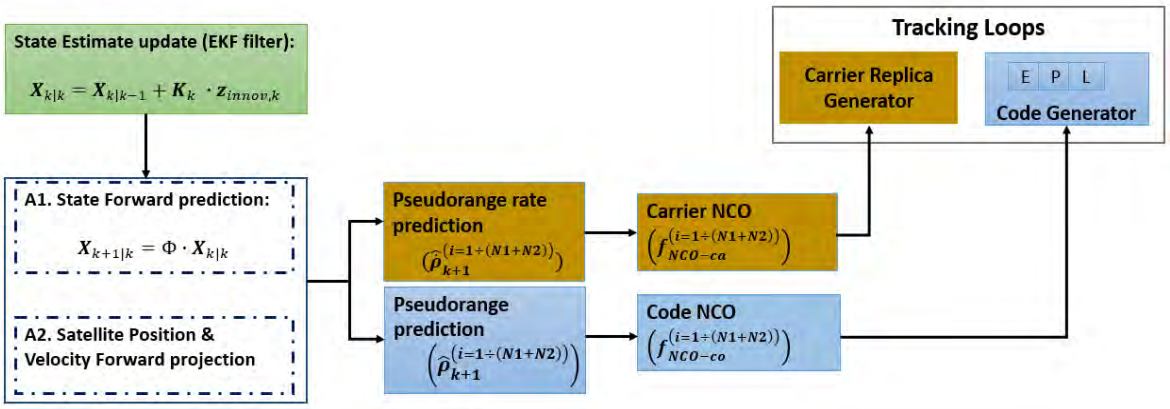

Figure 5-3. *The L1/E1 VDFLL feedback loop workflow.*

The VDFLL feedback loop is driven from the navigation filter state vector estimation at the current epoch k, which represents the final stage of the measurement update process shown in the green block of Figure 5-3 and computed based on the relations of Eq. (4-79) - (4-82):

$$\boldsymbol{X}_{k|k} = \boldsymbol{X}_{k|k-1} + \boldsymbol{K}_k \cdot \boldsymbol{z}_{innov,k} \quad (5\text{-}27)$$

where $\boldsymbol{K}_k$ is the EKF filter's Kalman gain matrix calculated in Eq. (4-79).

The estimation of the code/carrier NCOs from the VDFLL filter for the consequent time epoch requires the forward projection of the state vector and of the satellite's position and velocity from epoch $k \rightarrow k+1$, as illustrated in the A.1 and A.2 blocks above. The former is achieved by projecting the EKF-estimated state vector $\boldsymbol{X}_{k|k}$ through the state transition matrix $\boldsymbol{\Phi}_{k+1}$:

$$\boldsymbol{X}_{k+1|k} = \boldsymbol{\Phi}_{k+1} \cdot \boldsymbol{X}_{k|k} \quad (5\text{-}28)$$

whereas the satellite position and velocity for the successive epoch is estimated by shifting the current time by the VDFLL update period $T_s = 0.02\ s$.

The pseudorange rate prediction for the consequent epoch is computed as:

$$\begin{aligned}\hat{\rho}_{k+1}^{(i)} = &\left(\dot{x}_s^{(i)}(k+1) - \boldsymbol{X}_{k+1|k}(2)\right)\cdot \hat{a}_x^{(i)}(k+1) + \left(\dot{y}_s^{(i)}(k+1) - \boldsymbol{X}_{k+1|k}(4)\right)\cdot \hat{a}_y^{(i)}(k) \\ &+ \left(\dot{z}_s^{(i)}(k+1) - \boldsymbol{X}_{k+1|k}(6)\right)\cdot \hat{a}_z^{(i)}(k+1) + \boldsymbol{X}_{k+1|k}(8)\end{aligned} \quad (5\text{-}29)$$

For this purpose, the LOS projections along the three ECEF axes should be recomputed by taking into account the forward projections of the state position $\left(\boldsymbol{X}_{k+1|k}(1), \boldsymbol{X}_{k+1|k}(3), \boldsymbol{X}_{k+1|k}(5)\right)$ and satellite position $\left(x_{s,i}(k+1), y_{s,i}(k+1), z_{s,i}(k+1)\right)$ vectors, according to Eq. (4-67).

The Doppler frequency correction $\delta\hat{f}_{D,k+1}^{(i)}$ per each tracking channel i, closing the feedback loop to the carrier NCO update, is computed by projecting the predicted user's velocities and clock drift states in the pseudorange rate domain as:

$$f_{NCO-ca,k+1}^{(i)} = \delta\hat{f}_{D,k+1}^{(i)} = \left(\frac{f_{carr}}{c}\right)\cdot \hat{\rho}_{k+1}^{(i)}(Hz) \quad (5\text{-}30)$$

where $f_{NCO-ca,k+1}^{(i)}$ represents the carrier NCO command that will generate the carrier local replica for the successive epoch.

On the other hand, the relative code NCO update for each satellite channel i is computed for the next tracking epoch as the change rate of two consecutive pseudorange measurement predictions, denoted as $\hat{\rho}_k^{(i)}$ and $\hat{\rho}_{k+1}^{(i)}$, respectively given by:

$$\Delta f_{NCO-co,k+1}^{(i)} = \left(\frac{f_{code}}{c\cdot T_{EKF}}\right)\cdot\left(\hat{\rho}_{k+1}^{(i)} - \hat{\rho}_k^{(i)}\right)\ \left(\frac{chip}{s}\right) \quad (5\text{-}31)$$

where T_{EKF} is the EKF update period set to the code and carrier accumulation period.

Therefore, the code NCO frequency can be expressed by the addition of the relative code NCO to the nominal chipping frequency f_{code}, expressed as:

$$f_{NCO-co,k+1}^{(i)} = f_{code} + \Delta f_{NCO-co,k+1}^{(i)}\ \left(\frac{chip}{s}\right) \quad (5\text{-}32)$$

In contrast to the scalar receiver architecture, where the tracking and measurement processing blocks are clearly separated (see Figure 3-3), in vector tracking these two processes are closely related by the navigation filter. In addition, the proposed vector tracking algorithm, which is analyzed in details in Chapter 5, operates at the code/carrier discriminator output level. Since in this architecture there is no direct access to the observations, a different measurement representation model w.r.t the scalar receiver one is required.

5.3.6. VDFLL Corrected Measurements

The propagation delay model, already presented for the scalar tracking architecture in section 4.1, is also valid for the VDFLL architecture. The differences between the scalar and vector tracking techniques lie on the code and Doppler measurements generation model.

In fact, the pseudorange measurements at the current epoch k for the i^{th} GPS and Galileo satellite, is computed by the VDFLL algorithm at the measurement prediction stage as:

$$\rho^{(i)}_{VDFLL-est,GPS|Gal}(k) = \widehat{R}^{(i)}_k + \hat{b}_{Rx}(k) + \hat{b}^{(i)}_{iono,GPS/Gal}(k) \quad [m] \tag{5-33}$$

where:

- $\widehat{R}^{(i)}_k$ is the predicted i^{th} satellite-user range expressed in $[m]$ and computed in Eq. (4-65);
- $\hat{b}_{Rx}$ denotes the predicted user's clock bias or $\boldsymbol{X}_{k|k-1}(7)$ expressed in $[m]$ and computed at the state vector propagation stage;
- $\hat{b}^{(i)}_{iono,GPS/Gal}$ represents the predicted ionosphere residual of the i^{th} satellite in $[m]$, calculated according to Eq. (5-2).

Contrary to the scalar tracking technique, where the pseudorange rate measurement is obtained from the carrier phase change in two consecutive epochs, the VDFLL technique provides a direct access to the Doppler measurement from the velocity and clock drift states. Therefore, the VDFLL-predicted pseudorange rate measurement for the i^{th} satellite is computed as in Eq. (5-22):

$$\begin{aligned}\dot{\rho}^{(i)}_{VDFLL-est,GPS|Gal}(k) = &\left(\dot{x}^{(i)}_s(k) - \boldsymbol{X}_{k|k-1}(2)\right)\cdot \hat{a}^{(i)}_x(k) + \left(\dot{y}^{(i)}_s(k) - \boldsymbol{X}_{k|k-1}(4)\right)\cdot \hat{a}^{(i)}_y(k) \\ &+ \left(\dot{z}^{(i)}_s(k) - \boldsymbol{X}_{k|k-1}(6)\right)\cdot \hat{a}^{(i)}_z(k) + \hat{\hat{b}}_{Rx}(k) \quad \left[\frac{m}{s}\right]\end{aligned} \tag{5-34}$$

where:

- $\left(\dot{x}^{(i)}_s, y^{(i)}_s, \dot{z}^{(i)}_s\right)$ and $\left(\boldsymbol{X}_{k|k-1}(2), \boldsymbol{X}_{k|k-1}(4), \boldsymbol{X}_{k|k-1}(6)\right)$ denote the i^{th} satellite and predicted user's velocity vectors, respectively, in the ECEF frame and expressed in $\left[\frac{m}{s}\right]$;
- $\left(\hat{a}^{(i)}_x, \hat{a}^{(i)}_y, \hat{a}^{(i)}_z\right)$ are the predicted LOS projections computed using the relation in Eq. (4-67);
- $\hat{\hat{b}}_{Rx}$ is the VDFLL-predicted user's clock drift or $\boldsymbol{X}_{k|k-1}(8)$ in $\left[\frac{m}{s}\right]$.

5.4. Conclusions

The aim of this chapter was the presentation of the proposed vector tracking architecture to be used in signal-constrained environment. First, a general overview of the urban environment-induced effects such as multipath reception, GNSS LOS signal obstruction and signal interferences, on the channel tracking and positioning performance was introduced in Section 5.1. These error sources significantly affect the code and carrier tracking accuracies up to loss-of-lock conditions that are further translated into a deteriorated navigation solution performance.

Section 5.2 introduced the vector tracking (VT) principle of operation and its general block diagram representation in comparison to the conventional tracking receiver. Vector tracking represents an advanced tracking algorithm, efficient in low carrier-to-noise signal environments, which abolishes the independent channel tracking processes but instead controlling the code and carrier tracking feedback loops via the EKF-estimated user's PVT solution. Moreover, the main pros and cons of the vector tracking mechanism were summarized in Table 5-1.

The central part of this chapter was dedicated to the description of the proposed dual-constellation GPS/Galileo single-frequency L1/E1 VDFLL algorithm, capable of ensuring a high positioning performance and code/carrier tracking in harsh urban conditions due to the increased number of

observations fed to the EKF filter and the inter-channel coupling through the feedback loop. In other words, the VDFLL algorithm represents a GNSS-based information fusion system since all the tracking channels NCO commands are controlled by the same navigation solution EKF filter. Section 5.3 provided in details the VDFLL EKF estimation flowchart, including the state space and measurement model description. In this chapter, a VDFLL architecture aiming at the estimation of the ionosphere residuals was proposed. Therefore, the classic eight PVT state vector was augmented with the ionosphere residual errors from each tracked channel, modelled as a first order Gauss-Markov (GM) correlated in time. Accordingly, the process noise covariance matrix Q_k was adapted to incorporate the ionosphere residual process driven noise terms, detailed in Section 5.3.1.

The ionosphere residual rate error, expressed as the derivative in time of the ionosphere residual error, is a white noise process and there cannot be included in the EKF state vector. This required the inflation of the measurement covariance matrix R_k, related to the Doppler measurements entries, with the ionosphere residual rate error variances, given in details in Section 5.3.3.

In the proposed vector tracking algorithm, the code and frequency discriminator outputs were directly included into the EKF navigation filter as its measurement innovation vector. Finally, the code and carrier NCO updates for the successive iteration were computed starting from the EKF-updated navigation solution that is “forward projected” in time through the discrete state transition matrix, which is described in Section 5.3.5.

The next chapter deals with the presentation of the developed GNSS signal emulator, comprising the dual-constellation scalar and vector configurations along with the wideband multipath generator description.

6. The GNSS Signal Emulator Development

The previous chapters presented in specifics the dual-constellation single frequency scalar and vector tracking receiver architectures under study in this thesis. The main objective of this chapter is the detailed presentation of the developed GNSS signal emulator incorporating the two receiver's tracking and navigation architectures. Our choice toward the signal emulator, simulating the GNSS signals at the correlator output, with respect to the real data use is justified by the testing flexibility of different receiver configurations and also by the control of the simulation parameters and user dynamics.

The GNSS signal emulator architecture, including the scalar and VDFLL modules, is provided in details in section 6.1. Furthermore the sliding-window C/N_0 estimation process, proposed and implemented for the two scalar and vector tracking architectures related to their $50\ Hz$ update rate, is also presented in this section. Last but not least, the description of the hot re-acquisition algorithm initiated after the loss-of-lock occurrence for the scalar tracking technique, is also herein provided. The central part of this chapter is the mathematical model presentation concerning the integration of urban multipath channel data in the signal emulator's correlator output level, detailed in section 6.2. The description of DLR urban channel model and the urban scenario parameters along with the customization of this multipath model to our receivers' architectures are also presented. Section 6.3 provides a summary of the main implementation differences of the scalar and vector tracking navigation modules, with an emphasis on their process noise and measurement covariance matrixes.

The chapter conclusion are provided in section 6.4.

6.1. The GNSS Signal Emulator architecture

Within the scope of this Ph.D. thesis, a realistic dual-constellation dual-frequency GNSS signal emulator comprising the navigation module has been upgraded to include the vector tracking capability. The term emulator comes from the fact that the generation of the received GNSS signals is made at the correlator output level. This means that the receiver antenna, RF front-end block and the correlator blocks are directly simulated by generating the correlation function output from the mathematical model of Eq. (6-1), taking into account the effect of all sorts of error sources. As a consequence, the most time-consuming task of a real GNSS receiver that is the correlation operation is skipped. The three correlator pairs used by the tracking loops for each signal are generated based on the following model:

$$
\begin{aligned}
IE_k &= \frac{A}{2} \cdot d_k \cdot R_c\left(\varepsilon_{\tau,k} + \frac{d_c \cdot T_c}{2}\right) \cdot \cos\left(\varepsilon_{\varphi,k}\right) \cdot \operatorname{sinc}\left(\pi \cdot \varepsilon_{f_{D,k}} \cdot t\right) + n_{IE,k} \\
IP_k &= \frac{A}{2} \cdot d_k \cdot R_c\left(\varepsilon_{\tau,k}\right) \cdot \cos\left(\varepsilon_{\varphi,k}\right) \cdot \operatorname{sinc}\left(\pi \cdot \varepsilon_{f_{D,k}} \cdot t\right) + n_{IP,k} \\
IL_k &= \frac{A}{2} \cdot d_k \cdot R_c\left(\varepsilon_{\tau,k} - \frac{d_c \cdot T_c}{2}\right) \cdot \cos\left(\varepsilon_{\varphi,k}\right) \cdot \operatorname{sinc}\left(\pi \cdot \varepsilon_{f_{D,k}} \cdot t\right) + n_{IL,k} \\
QE_k &= \frac{A}{2} \cdot d_k \cdot R_c\left(\varepsilon_{\tau,k} + \frac{d_c \cdot T_c}{2}\right) \cdot \sin\left(\varepsilon_{\varphi,k}\right) \cdot \operatorname{sinc}\left(\pi \cdot \varepsilon_{f_{D,k}} \cdot t\right) + n_{QE,k} \\
QP_k &= \frac{A}{2} \cdot d_k \cdot R_c\left(\varepsilon_{\tau,k}\right) \cdot \sin\left(\varepsilon_{\varphi,k}\right) \cdot \operatorname{sinc}\left(\pi \cdot \varepsilon_{f_{D,k}} \cdot t\right) + n_{QP,k} \\
QL_k &= \frac{A}{2} \cdot d_k \cdot R_c\left(\varepsilon_{\tau,k} - \frac{d_c \cdot T_c}{2}\right) \cdot \sin\left(\varepsilon_{\varphi,k}\right) \cdot \operatorname{sinc}\left(\pi \cdot \varepsilon_{f_{D,k}} \cdot t\right) + n_{QL,k}
\end{aligned}
\tag{6-1}
$$

where:

- $(\varepsilon_{\tau,k}, \varepsilon_{\varphi,k}, \varepsilon_{f_{D,k}})$ denotes the code delay, carrier phase and frequency estimation errors at epoch k, expressed as the difference between the true (unknown) and the locally-estimated terms;
- $d_c \cdot T_c$ refers to the E-L chip spacing with d_c representing the fraction of chip spacing and T_c denotes the code chip period;
- n_{xy} represents the noise term added at the correlator output (where x – in-phase (I) or quadrature (Q) and y – early (I), prompt (P) or late (L) code delays) that are correlated and following a centered Gaussian distribution with zero mean and variance $\sigma^2_{n_{xy}}$ provided in Appendix A.2.

All the processing blocks from the GNSS signals' correlation function output generation, passing through the channels' tracking module and up to the different navigation algorithms are all designed in a modular manner. In doing so, the emulator structure is easily modified according to the test scenarios and user motion and can be efficiently switched between the scalar- and vector tracking operation modes. The developed signal emulator is a powerful tool for flexible and reliable GNSS receiver testing, offering the following key features:

- Generation of the GPS L1/L5 and Galileo E1 OS/E1C/E5a&E5b data and pilot signal correlation functions outputs;
- Import of the satellite ephemeris and almanac files for the satellites' orbits generation;
- Simulation of static and dynamic satellite signals parameters of up to the complete GPS and Galileo constellations;
- Atmospheric (ionosphere + troposphere) effects modelling on the satellite-user propagation channel;
- Generation of an urban representative multipath environment with the amplitude, delay, phase and Doppler frequency for each LOS and signal echo;
- Inclusion of signal interference sources and temporary signal outages in order to test the tracking and navigation solution performance degradation;
- Static and moving receiver trajectory (from a real stored car trajectory).

In this thesis, the focus is directed to the use of dual-constellation GPS and Galileo in the L1 band. The complete design flow of the proposed dual-constellation single-frequency GNSS signal emulator,

comprising the scalar and vector tracking operation model along with their respective navigation filters, is given in Figure 6-1.

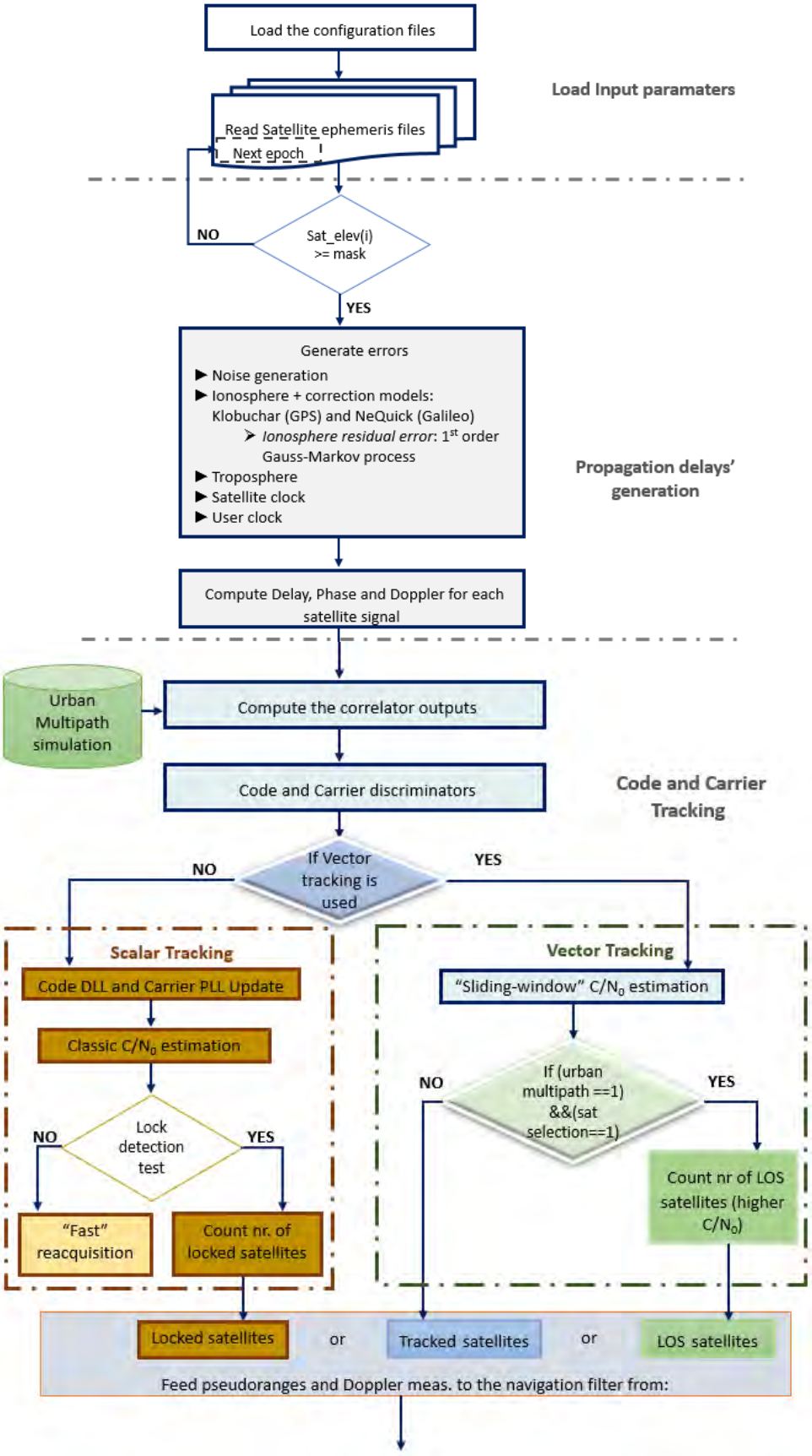
Load the configuration files
Load Input paramaters
Read Satellite ephemeris files
Next epoch
NO
Sat_elev(i) >= mask
YES
Generate errors
Noise generation
Ionosphere + correction models: Klobuchar (GPS) and NeQuick (Galileo)
Ionosphere residual error: 1st order Gauss-Markov process
Troposphere
Satellite clock
User clock
Propagation delays' generation
Compute Delay, Phase and Doppler for each satellite signal
Urban Multipath simulation
Compute the correlator outputs
Code and Carrier discriminators
Code and Carrier Tracking
If Vector tracking is used
NO
YES
Scalar Tracking
Code DLL and Carrier PLL Update
Classic C/N0 estimation
Lock detection test
NO
YES
"Fast" reacquisition
Count nr. of locked satellites
Vector Tracking
"Sliding-window" C/N0 estimation
If (urban multipath ==1) &&(sat selection==1)
NO
YES
Count nr of LOS satellites (higher C/N0)
Locked satellites
or
Tracked satellites
or
LOS satellites
Feed pseudoranges and Doppler meas. to the navigation filter from:

(1/2)

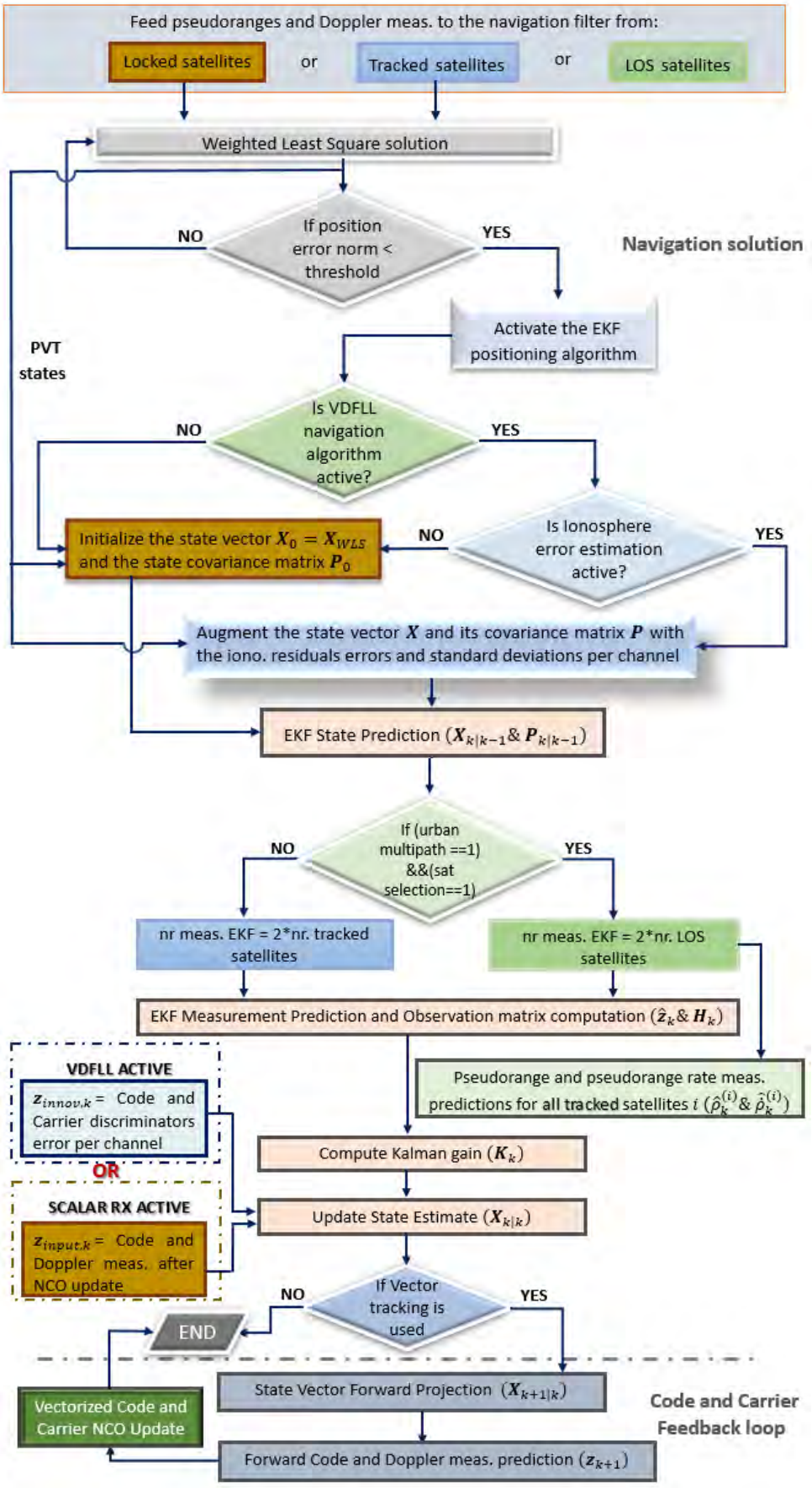
Feed pseudoranges and Doppler meas. to the navigation filter from:
Locked satellites
or
Tracked satellites
or
LOS satellites
Weighted Least Square solution
If position error norm < threshold
NO
YES
Navigation solution
Activate the EKF positioning algorithm
PVT states
Is VDFLL navigation algorithm active?
NO
YES
Initialize the state vector $X_0 = X_{WLS}$ and the state covariance matrix P_0
Is Ionosphere error estimation active?
NO
YES
Augment the state vector X and its covariance matrix P with the iono. residuals errors and standard deviations per channel
EKF State Prediction ($X_{k|k-1}$ & $P_{k|k-1}$)
If (urban multipath ==1) &&(sat selection==1)
NO
YES
nr meas. EKF = 2*nr. tracked satellites
nr meas. EKF = 2*nr. LOS satellites
EKF Measurement Prediction and Observation matrix computation ($\hat{z}_k$ & H_k)
VDFLL ACTIVE
$z_{innov,k}$ = Code and Carrier discriminators error per channel
OR
SCALAR RX ACTIVE
$z_{input,k}$ = Code and Doppler meas. after NCO update
Pseudorange and pseudorange rate meas. predictions for all tracked satellites i ($\hat{\rho}_k^{(i)}$ & $\hat{\dot{\rho}}_k^{(i)}$)
Compute Kalman gain (K_k)
Update State Estimate ($X_{k|k}$)
If Vector tracking is used
NO
YES
END
State Vector Forward Projection ($X_{k+1|k}$)
Vectorized Code and Carrier NCO Update
Forward Code and Doppler meas. prediction (z_{k+1})
Code and Carrier Feedback loop

where:

- k refers to the current GNSS epoch;
- i denotes the GPS and/or Galileo satellite ID;
- LOS refers to the line-of-sight satellite;
- $\hat{\rho}_k^{(i)}$, $\hat{\dot{\rho}}_k^{(i)}$ denote the EKF-predicted pseudorange and pseudorange rate measurements, respectively;
- $\boldsymbol{z}_{innov}$ refers to the measurement innovation vector for the VDFLL operation mode, including the code and carrier discriminator outputs, given in Eq. (5-26);
- $\boldsymbol{z}_{input}$ refers to the measurement input vector for the scalar tracking operation, comprising the pseudorange and pseudorange rate measurements after the scalar code and carrier NCO update per channel.

Figure 6-1. The complete design flow of the designed dual-constellation dual-frequency GNSS signal emulator.

The sequential functioning of the signal emulator operation can be clearly observed from the generation of the propagation delays to the EKF navigation filters for the two receiver architectures under study. However, it is important to highlight the fact that the EKF filter operation is initiated after the Weighted Least Square (WLS)-position convergence is reached at the initialization step. Furthermore, the last major block referring to the code and carrier feedback loop is part of the VDFLL mechanism and is performed after the navigation solution estimation, as noted in Figure 6-1.

The description of the GNSS signal emulator functional blocks, separated by dashed grey lines in Figure 6-1, is provided in details in the following sub-sections.

6.1.1. Loading the input parameters' files

The first block of the GNSS signal emulator performs the loading of the simulation input parameters that can be logically split into two sub-steps:

- Charging the configuration files including:
  - The main simulation parameters' text file containing:
    - The intermediate and sampling frequency;
    - Activation of single or multi constellation and frequency bands such as: GPS L1, GPS L5, Galileo E1, Galileo E5a&E5b;
    - The navigation solution update rate from $50\ Hz$ to $1\ Hz$;
    - A command indicating the activation of the autocorrelation function filtering;
    - Enabling or disabling the inclusion of temporary satellite outages, signal interferences and deformations;
    - Activation of the Weighted Least Square (WLS) solution used for the initialization of the EKF state vector prior to switching to the EKF navigation algorithm;
    - Generation of the ionosphere error based on the Klobuchar model parameters for GPS satellites and NeQuick for the Galileo constellation along with the 1st order Gauss-Markov variables used to model the ionosphere residual errors after correction;

- Activation and choice of the multipath propagation model that can be none, linear multipath and DLR urban environment multipath model;
- Choice of the mask angle for the GPS and Galileo satellites;
- The activation command for the VDFLL receiver processing;
- Satellite selection mode employed for the VDFLL EKF positioning algorithm, aiming at reducing the inter-channel errors propagation under harsh multipath reception conditions.

o The code and carrier tracking parameters for all the GPS/Galileo signals in terms of:

- RF filter bandwidth;
- Choice of the code DLL discriminator type (Dot Product and EMLP) along with the Early-Late chip spacing in chips, the DLL noise bandwidth in Hz and its integration time in second;
- Choice of the carrier FLL discriminator type (Cross-Product, Decision-directed cross-product, Differential Arctangent and Four-quadrant arctangent discriminators) and their associated parameters such as: the FLL noise bandwidth, FLL order and integration time;
- Choice of the carrier PLL discriminator type (Costas and Arctangent discriminators) and their associated parameters such as: the PLL noise bandwidth, PLL order and integration time;
- Carrier loop selection between three distinct options: FLL only (employed in the vectorized architecture), PLL only (implemented in the scalar tracking receiver) and a further upgrade to the FLL-aided PLL configuration;
- PLL-aided DLL configuration especially valid for high receiver dynamics.

o The receiver's motion file for the static and automotive receiver test cases. For the former test, the user's location is fixed in the ENAC's premises in terms of latitude, longitude and altitude coordinates. Whereas for the dynamic test, the GNSS emulator simulates the receiver's motion along a pre-defined trajectory at constant or varying velocities. For this purpose, a realistic user waypoint file, output from the Novatel SPAN receiver during a test campaign in Toulouse urban area, is fed to the designed GNSS emulator.

➢ Loading the GPS and Galileo constellation using the broadcast ephemeris files that can be downloaded from the Crustal Dynamics Data Information System (CDDIS) and International GNSS Service Multi-GNSS Experiment and Pilot project (IGS MGEX) websites, allowing the simulation of the true GPS constellation and complete Galileo one at the given simulation time. The ephemeris data consent the satellite position and its elevation angle computation that allows the discarding of the satellites under the specified elevation mask.

6.1.2. Code and Carrier Tracking process

As previously stated, the GNSS signal emulator is designed in a modular manner in order to allow an effective switch between the scalar and vector tracking architectures. The common code/carrier tracking blocks between the two implemented architectures are the correlation mathematical operation and code/carrier discriminators, which were previously detailed in section 3.5. The following differences can be envisaged between the scalar and vector tracking architectures in the tracking stage, as illustrated in Figure 6-1 and summarized in Table 6-1:

1) In the scalar tracking operation mode a carrier phase discriminator is used, whereas the proposed vector tracking algorithms operates on the carrier frequency discriminator output;
2) A 3rd order PLL and 1st order DLL-aided PLL per tracking channel, performing the carrier and code tracking tasks, are employed by the scalar tracking receiver according to the model already presented in section 3.5.3. Whereas, the code delay and carrier frequency updates for the VDFLL architecture are jointly computed for all the tracking channels in the navigation solution block based on the estimated navigation solution and fed back to the tracking block;
3) For the scalar tracking architecture, the satellite lock detection test is implemented through the classic C/N_0 estimator in section 3.5.3 and under outage conditions, a hot re-acquisition process of 1 second duration is applied with random initial code errors related to the L1 and E1 code autocorrelation sharpness and initial frequency errors equal to Doppler bin size of $25\ Hz$. Contrary to the scalar tracking configuration, the need of a re-acquisition algorithm is removed in the vector tracking configuration due to the special feedback loop;
4) The estimated code and carrier measurements for only the satellites passing the lock detection test, referred to as the locked satellites, are fed to the EKF navigation filter in the scalar configuration. On the contrary, a "feed all" code and Doppler measurements errors strategy to the navigation filter is adopted for the vector tracking algorithm. However in the presence of severe multipath conditions, a "LOS satellite selection" technique is proposed for the VDFLL architecture with the scope of minimizing the errors flow between the tracking channels. The description of the satellite selection process is provided in the following chapter.

Table 6-1. *Scalar and vector tracking architecture differences in the signal tracking stage*

Operations	Scalar Tracking	Vector Tracking	
Lock detection test	YES	NO	
Signal Reacquisition	YES	NO	
C/N_0 estimation	Sliding-window		
Feed measurements from:	Locked satellites	Tracked satellites	LOS selected satellites (multipath = ON)

The generated database of the received signal rays that are obtained from the urban multipath model, shown by the green block in Figure 6-1, are fed to the GNSS signal emulator at the correlator output level. Further details concerning the urban model simulation are provided in the following section.

6.1.2.1. Sliding-window C/N$_0$ estimation technique

Both the scalar and vector tracking navigation modules that are implemented in this thesis operate at $50\ Hz$ update rate. Since the EKF measurement covariance matrix $\boldsymbol{R_k}$ requires the tracking channels' C/N$_0$ estimations at the tracking loop integration rate (that is $50\ Hz$), a sliding-window C/N$_0$ estimation algorithm is developed whose workflow is shown in Figure 6-2.

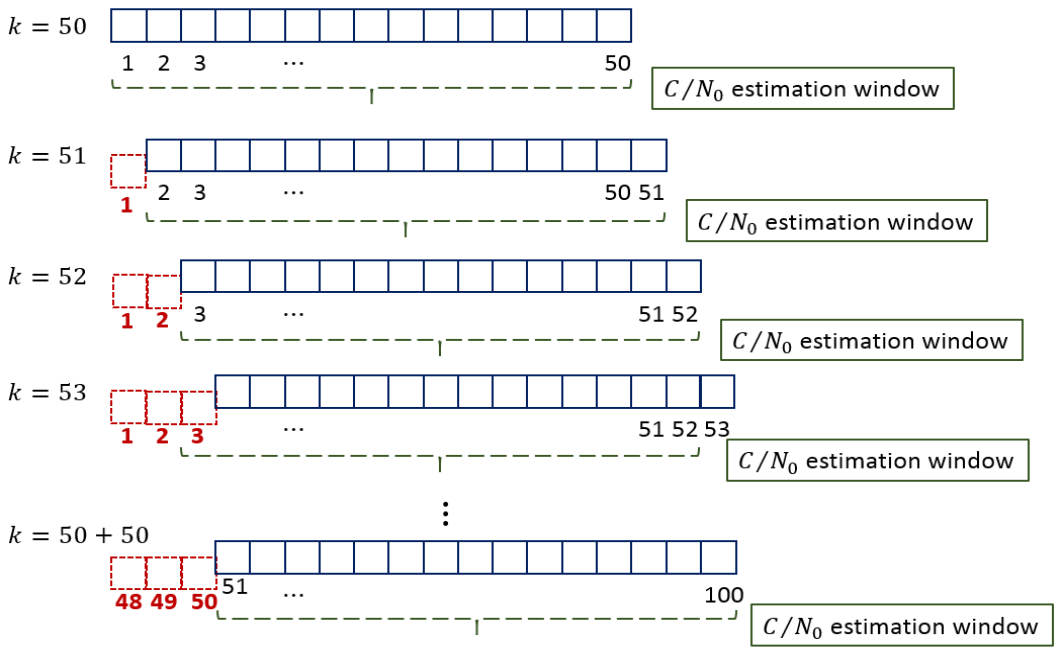

Figure 6-2. *The sliding-window C/N$_0$ estimation workflow during 50 integration intervals.*

The blue boxes in Figure 6-2 denote the signal-plus-noise narrowband power per coherent integration interval whereas the red boxes represent the "neglected" intervals as the sliding-windows passes to the successive epoch.

As it can be noted, the sliding-window mechanism is activated only after the 50^{th} integration epoch, which corresponds to the first output of the classic C/N$_0$ estimation technique, presented in Section 3.5.3. For each measurement interval *k*, starting from the $50 + 1^{th}$ integration epoch, the channel signal-plus-noise power is computed as:

$$CP_k = \sum_{k=1}^{K} \left[\left(\sum_{i=1}^{M} IP_i \right)_k^2 + \left(\sum_{i=1}^{M} QP_i \right)_k^2 \right] \qquad (6\text{-}2)$$

where $K = 50$ indicates the number of non-coherent integrations averaged over 1 second interval and $M = 20$ for GPS L1 C/A and Galileo E1-C pilot signals denotes the coherent accumulation intervals.

The estimated mean of the channel power, representing the code lock detector, is given by:

$$\mu_{CP,k} = \frac{1}{K} \cdot CP_k \qquad (6\text{-}3)$$

Whereas, the variance of the channel power set is expressed as:

$$\sigma_{CP,k}^2 = \frac{1}{K} \cdot \sum_{k=1}^{K} (CP_k - \mu_{CP,k})^2 \quad (6\text{-}4)$$

The normalized mean channel power can be computed as:

$$NMP_k = \frac{{\mu_{CP,k}}^2}{\sigma_{CP,k}^2} \quad (6\text{-}5)$$

Finally, the carrier-to-noise ratio is estimated according to the following relation:

$$C/N_{0_{est,k}} = 10\log_{10} \cdot \left(NMP_k - 1 + \sqrt[2]{NMP_k \cdot (NMP_k - 1)}\right) \quad (6\text{-}6)$$

6.1.2.2. Proposed Hot Re-acquisition model

For the scalar tracking architecture, the satellite lock detection test is implemented through the C/N_0 estimator with the threshold set at $25\ dB - Hz$ [Parkinson, 1996]. The satellites that do not pass the lock detection test are declared unlocked and their measurements are not fed to the navigation filter. In a conventional receiver, the satellites in this state should enter a re-acquisition mode, where for each "unlocked" channel a rough 2D search in the code delay and Doppler frequency domain is conducted in order to assess the signal presence [Gleason and Gebre-Egziabher, 2009].

In the developed signal emulator, a simplified hot re-acquisition process is implemented 1 second after the loss of lock detection. Afterwards, the tracking is re-initiated with the initial code and Doppler errors in line with a typical acquisition search bin size. The Doppler frequency uncertainty (ε_{freq}) at the initiation of the re-acquisition stage is related to the Doppler acquisition bin width as follows [Curran, 2010]:

$$\varepsilon_{freq} = \frac{1}{4 \cdot T_{i,freq}} = \frac{1}{4 \cdot 0.01} = 25\ Hz \quad (6\text{-}7)$$

where $T_{i,freq}$ is the FLL integration period.

Whereas, the code delay error uncertainty (ε_{code}) at the re-acquisition step is computed according to the L1 and E1 chip spacing (d_c) and autocorrelation function sharpness (α) as:

$$\varepsilon_{code} = \begin{cases} \frac{d_c}{\alpha} & with\ \alpha = 1 \quad for\ \ GPS\ L1\ BPSK(1) \\ \frac{d_c}{\alpha} & with\ \alpha = 3 \quad for\ GAL\ E1\ BOC(1,1) \end{cases} \quad (6\text{-}8)$$

The assumption made at this stage is that both the code delay and Doppler errors follow a uniform distribution, fully described by the code and carrier uncertainties described above. At the point when the lock detection test is passed, the channel goes into the tracking mode where the estimates of the code delay and the Doppler frequency are continuously refined.

6.2. Urban Propagation Channel Model

In this dissertation, an urban propagation channel model has been used to generate a representative of urban environment signal's reception conditions. This model, known as the DLR Land Mobile

Multipath Channel model (LMMC), was developed thanks to an extensive measurement campaign conducted by DLR in Munich urban and suburban areas in 2002. It was generated based on the statistical results gathered from the measurement campaign, which was characterized by using high time resolution permitting to distinguish the different received echoes. Therefore, the DLR model is a wideband propagation channel model where each LOS and multipath echo are considered separately [DLR, 2008]. Indeed, this model has been specifically designed to study the multipath effect in GNSS signals and is a freely accessible algorithm for academic purposes that can be downloaded from the DLR website.

6.2.1. Correlation Process description

The simulation tool under description is a high-fidelity GNSS receiver simulator that is based on the fine modeling of the correlator outputs. As such, it thus does not require the generation of the actual signals, but only of the corresponding correlator outputs. It is therefore extremely important to be able to reproduce very accurately the effect of the error sources of interest on the correlator outputs.

Furthermore, the LOS and NLOS echoes information is fed in the tracking stage at the correlator output level per each satellite in view, following classical models of the correlator outputs (for the m^{th} satellite):

$$\begin{aligned} IX_m(k) &= \sum_{i=1}^{N_{LOS}} A_{LOS,i}(k) \cdot R\left(\varepsilon_{\tau_{LOS,i}}(k) + d_X\right) \cdot \cos\left(\varepsilon_{\varphi_{LOS,i}}(k)\right) \cdot \operatorname{sinc}\left(\pi \cdot \varepsilon_{f_{D,LOS,i}}(k) \cdot T_{int}\right) \\ &+ \sum_{j=1}^{N_{NLOS}} A_{NLOS,j}(k) \cdot R\left(\varepsilon_{\tau_{NLOS,i}}(k) + d_X\right) \cdot \cos\left(\varepsilon_{\varphi_{NLOS,i}}(k)\right) \cdot \operatorname{sinc}\left(\pi \cdot \varepsilon_{f_{D,NLOS,i}}(k) \cdot T_{int}\right) + n_{IX}(k) \\ QX_m(k) &= \sum_{i=1}^{N_{LOS}} A_{LOS,i}(k) \cdot R\left(\varepsilon_{\tau_{LOS,i}}(k) + d_X\right) \cdot \sin\left(\varepsilon_{\varphi_{LOS,i}}(k)\right) \cdot \operatorname{sinc}\left(\pi \cdot \varepsilon_{f_{D,LOS,i}}(k) \cdot T_{int}\right) \\ &+ \sum_{j=1}^{N_{NLOS}} A_{NLOS,j}(k) \cdot R\left(\varepsilon_{\tau_{NLOS,i}}(k) + d_X\right) \cdot \sin\left(\varepsilon_{\varphi_{NLOS,i}}(k)\right) \cdot \operatorname{sinc}\left(\pi \cdot \varepsilon_{f_{D,NLOS,i}}(k) \cdot T_{int}\right) + n_{QX}(k) \end{aligned} \quad (6\text{-}9)$$

where:

- X indicates the Early (E), Prompt (P) and Late (L) code replicas shifted by d_X, depending on the chip spacing T_c as follows:

$$d_X = \begin{cases} -\dfrac{T_c}{2} & if\ X = E \\ 0 & if\ X = P \\ +\dfrac{T_c}{2} & if\ X = L \end{cases} \quad (6\text{-}10)$$

- The channel errors including the code delay, carrier phase and frequency errors $(\varepsilon_{\tau i,LOS/NLOS}, \varepsilon_{\varphi i,LOS/NLOS}, \varepsilon_{f_D i,LOS/NLOS})$, respectively computed as the difference between the LOS/NLOS related data $\left(\tau_{LOS/NLOS,i}, \varphi_{LOS/NLOS,i}, f_{D\,LOS/NLOS,i}\right)$ and the corresponding estimated values in the tracking loops per each channel, expressed as:

$$\begin{aligned}\varepsilon_{\tau_{LOS/NLOS,i}} &= \tau_{LOS/NLOS,i} - \tau_{est} \\ \varepsilon_{\varphi_{LOS/NLOS,i}} &= (\varphi_0 + \varphi_{LOS/NLOS,i}) - \varphi_{est} \\ \varepsilon_{f_{D\,LOS/NLOS,i}} &= f_{D\,LOS/NLOS,i} - f_{D\,est}\end{aligned} \quad (6\text{-}11)$$

  - where φ_0 denotes the signal's initial phase computed according to Eq. (4-14);
  - $\left(\tau_{LOS/NLOS,i}, \varphi_{LOS/NLOS,i}, f_{D_{LOS/NLOS,i}}\right)$ represents the LOS/NLOS echoes' relative delay, phase and Doppler frequency per each satellite, output from the DLR urban channel files.

- $n_{IX,m}$ and $n_{QX,m}$ represent the In Phase and Quadrature correlator output noise terms of the m^{th} tracked channel, respectively, added according to the correlator's noise covariance matrix.

The urban channel model description, providing the LOS/NLOS information fed into the correlator outputs, is detailed in the following sections.

6.2.2. Description of the Urban Channel Model

The DLR model is a hybrid statistic/deterministic mathematical propagation channel model. The statistical part refers to the generation of a random urban scenario from a given set of channel defining parameters. Once the complete urban scenario is defined, the impact of the propagation channel into the received GNSS signal is manly determined by using deterministic techniques. A detailed explanation is given below.

The random urban scenario generated from statistical parameters is completely defined by:

- Potential obstacles to the received GNSS signal such as trees, buildings, poles, etc;
- Receiver's trajectory;
- Satellite's position with respect to the user's trajectory and the generated obstacles (note that only one satellite can be defined at a time).

Therefore, the following parameters are loaded into the algorithm in order to define the scenario:

- The urban scenario parameters, required to reproduce a typical city street, which include the road width, buildings' height and the trees/poles' heights and diameters. All these obstacles are statistically generated.
- The receiver speed and heading angle;
- The satellite elevation and azimuth angles in degrees.

Figure 6-3 provides a graphical example of a constructed urban scenario. After defining the user's trajectory and satellite's relative position and once the scenario obstacles are statistically generated, the impact on the received GNSS signal is calculated. As said before, the attenuation, the phase and the delay associated to the LOS and multipath echoes are deterministically determined. The method used by the DLR team is ray tracing and geometric techniques. More specifically, the multipath (NLOS) echoes are generated in a one by one manner, where each multipath ray is associated with a reflector that has been generated following a statistical model. Furthermore, the number of echoes and their life span are statistical variables depending on the satellite elevation angle.

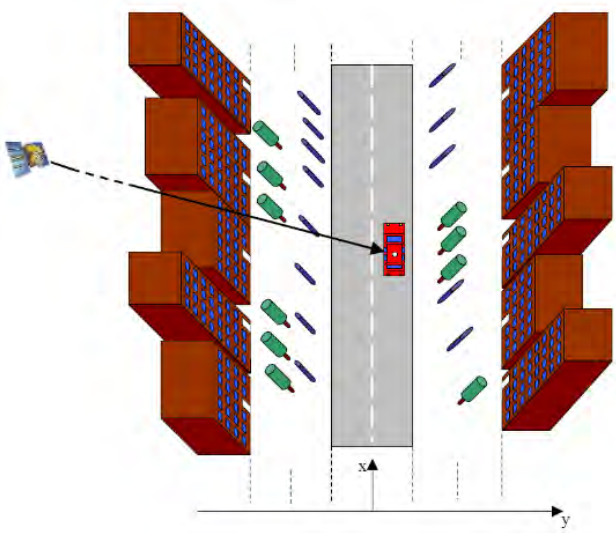

Figure 6-3. *Artificial urban scenario generated by the DLR urban propagation channel model [DLR, 2007].*

Another illustration of the DLR model car scenario generation based on the vehicle input parameters is provided in Figure 6-4.

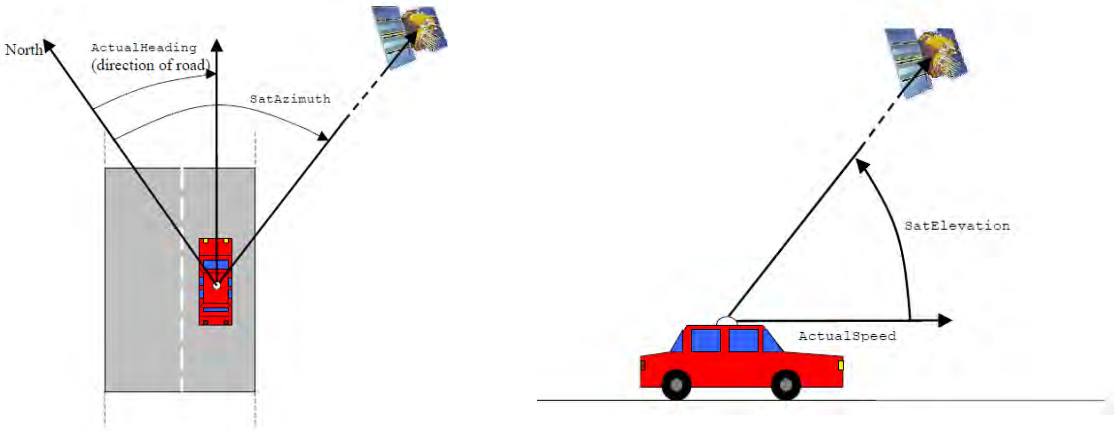

a) **b)**

Figure 6-4. *2D-plane visualization of the:* **a)** *satellite azimuth and vehicle heading angles;* **b)** *satellite elevation angel and vehicle actual speed vector [DLR, 2007].*

Finally, the statistical part of the DLR urban model comprises [DLR, 2008]:

- The house front, tree and lamp post generation in the synthetic environment;
- The position-dependent LOS signal power variations in the shadow of tree tops;
- The reflectors' position depending on the satellites azimuth and elevation angle;
- The mean power of echoes depending on their distance to the receiver and on the satellite elevation;
- The echoes lifespan and bandwidth depending on the satellite elevation,
- The number of coexisting echoes and the movement of the reflection points is also strictly dependent on the satellite elevation angle.

Whereas, the deterministic part of the model provides [DLR, 2008]:

- The diffraction of the LOS signal on houses, tree trunks and lamp posts;

- The delay of diffracted signals received in the shadow of houses;
- The mean attenuation through tree tops;
- The delay and Doppler shift trends of echo signals due to the receiver and reflector movement.

6.2.2.1. LOS and Multipath echoes modelling

The direct LOS ray follows a deterministic model determined by the house fronts, trees and lampposts found in its trajectory. Each of these obstacles are statistically generated and placed along the trajectory following a Gaussian distribution. In specifics, the house fronts attenuation is computed based on the knife edge model while the poles and tree trunk attenuation is modelled by a double knife edge model [Lehner and Steingass, 2005]. The house fronts-associated delays are deduced from the scenario geometry whereas the relative delays of the diffracted signals from the tree trunks and poles are neglected. In the DLR model, there are a few special cases when multiple LOS echoes (up to a maximum of three rays) are considered with LOS delays differing from zero due to the LOS diffraction at the house fronts. The multipath echoes are generated from the reflectors, which are initialized in random positions along the trajectory and radiating equally in any direction but with a given attenuation w.r.t the direct path. The attenuation associated to the echo generated by each reflector is statistically determined. From the results analysis of the measurement campaign, the envelope of each echo signal follows in average a Rician distribution [Steingass and Lehner, 2004].

6.2.2.2. Urban Scenario parameters

A large number of the model inputs are configurable including the user's distance from the road middle and the statistic parameters indicating the mean, variance and minimum/maximum values of the Gaussian distribution that characterize the buildings shaping (height, width and gap between two buildings) and trees and poles (height, diameter, distances from the road and building) [DLR, 2007]. The urban scenario parameters, set to reproduce the typical city center street, are summarized in Table 6-2:

Table 6-2. *Urban city center scenario parameters*

Parameters	Value	Comments
General		
Carrier Frequency	$1.57542 \cdot e^9\ Hz$	GPS L1 band
Sampling Frequency	50 Hz	Set according to the user's trajectory rate and signal tracking integration period
Operation mode		
User Type	"Car"	Car trajectory
Environment	"Urban"	Urban city street
User-related		
Antenna Height	$1.5\ m$	
Road Width	$5\ m$	
Distance from the middle of the road	$1\ m$	
Buildings		

Building Row1	"1"	Logical parameter indicating the building's presence in the road's left side
Building Row2	"1"	Logical parameter indicating the building's presence in the road's right side
Building Width	$\sim N(22,25)$	Gaussian-distributed with mean value $22\ m$ and standard deviation equal to $25\ m$
Building Height	$\sim N(13,6.4)$	Gaussian-distributed with mean value $13\ m$ and standard deviation equal to $6.4\ m$
Building Gap	$\sim N(11,7)$	Gaussian-distributed with mean value $11\ m$ and standard deviation equal to $7\ m$
Tree trunks		
Tree Row1	"1"	Logical parameter indicating the tree's presence in the road's left side
Tree Row2	"1"	Logical parameter indicating the tree's presence in the road's right side
Tree Height	$8\ m$	
Tree Diameter	$5\ m$	
Tree Trunk Length	$2\ m$	
Tree Trunk Diameter	$0.2\ m$	
Tree Row1 & Row2 distribution	$\sim N(40,20)$	Gaussian-distributed with mean value $40\ m$ and standard deviation equal to $20\ m$
Poles		
Pole Row1	"1"	Logical parameter indicating the poles' presence in the road's left side
Pole Row2	"1"	Logical parameter indicating the poles' presence in the road's right side
Pole Height	$10\ m$	
Pole Diameter	$0.2\ m$	
Pole Row1 & Row2 distribution	$\sim N(25,10)$	Gaussian-distributed with mean value $25\ m$ and standard deviation equal to $10\ m$

Moreover, only the reflected rays up to a maximum $-40\ dB$ attenuation with respect to the LOS are considered. Three main limitations of this urban channel model may be defined:

1) The generated urban channels are independent from each other. In fact, the urban environment conditions are generated separately for each GPS and Galileo tracked satellite by feeding their elevation and azimuth angles to the DLR urban channel;
2) The satellite position evolution is not considered in the DLR model;
3) The urban DLR propagation channel model is heavy and time-consuming.

6.2.2.3. DLR model Channel Impulse Response (CIR)

The generated database of the received signal rays, obtained from the DLR urban channel model, consists of time series of amplitude, delay and phase of the LOS ray and NLOS echoes received for each satellite per channel. In other words, the DLR channel model outputs are the following:

- The channel impact, defined by the number of echoes, the amplitude, the relative delay with respect to the direct signal and the phase of each generated echo;
- The relative delay between the LOS ray and each multipath echo, denoted by $\tau_{NLOS,j}$. In the DLR model, the LOS delay is equal to zero and is not null only when the LOS ray is diffracted by the house front.

Therefore, the DLR model output is the complex time-variant channel impulse response (CIR) with up to 80 discrete rays, having the following form [DLR, 2007]:

$$\begin{aligned} h_{urban}(t,\tau) &= \sum_{i=1}^{n_{LOS}} c_{LOS,i} \cdot \delta\left(t - \tau_{LOS,i}(t)\right) + \sum_{j=1}^{n_{NLOS}} c_{NLOS,j} \cdot \delta\left(t - \tau_{NLOS,j}(t)\right) \\ &= \sum_{i=i}^{n_{LOS}} A_{LOS,i} \cdot e^{j\varphi_{LOS,i}} \cdot \delta\left(t - \tau_{LOS,i}(t)\right) \\ &+ \sum_{i=i}^{n_{NLOS}} A_{NLOS,i} \cdot e^{j\varphi_{NLOS,i}} \cdot \delta\left(t - \tau_{NLOS,i}(t)\right) \end{aligned} \quad (6\text{-}12)$$

Where:

- n_{LOS} and n_{NLOS} denote the total number of LOS rays (up to 3 rays when diffracted at house fronts) and NLOS echoes, which is limited by the minimum accepted power level set to $-40\ dB$;
- $\left(A_{LOS}, \tau_{LOS}, \varphi_{LOS}\right)_i$ denotes the LOS rays' amplitude, delay in $[m]$, phase in $[rad]$ for $(i = 1 \div n_{LOS})$;
- $\left(A_{NLOS}, \tau_{NLOS}, \varphi_{NLOS}\right)_j$ denotes the NLOS echoes' amplitude, relative delay in $[m]$, phase in $[rad]$ for $(j = 1 \div n_{NLOS})$;
- t is the time instant at which the CIR is defined.

6.2.3. Customization of the DLR model outputs

To obtain a realistic vehicle urban scenario coherent with the reference car trajectory fed to the EKF navigation filter, the following customization were made to the DLR model:

- Firstly, the DLR urban trajectory was generated at a sampling frequency equal to the tracking loops update rate at $50\ Hz$;
- Secondly, this model was adapted in such a manner that it can also provide the Doppler frequency of the LOS rays and NLOS echoes ($f_{D_{LOS/NLOS}}$). Thus, the modified DLR output vector for each epoch *k* is defined as:

$$mult_k = \left[\left(A_{LOS}, \tau_{LOS}, \varphi_{LOS}, f_{D_{LOS}}\right)_i \vdots \left(A_{NLOS}, \tau_{NLOS}, \varphi_{NLOS}, f_{D_{NLOS}}\right)_j\right] \quad (6\text{-}13)$$

In the DLR model, the LOS ray Doppler frequency is computed based on the LOS relative phase change. In fact, this phase change is directly translated from the vehicle movement vector via geometric relations, depending on the receiver's velocity, the bearing angle (expressed as the difference between the vehicle heading and the satellite azimuth angle) and the satellite elevation angle, as depicted in Figure 6-4. Contrary to LOS rays, the Doppler frequency calculation for the reflected rays is not a straightforward procedure due to their random generation process following the statistical model. Thus, different echoes may be generated between two consecutive epochs and they are randomly ordered in the output vector. To cope with this scenario, an algorithm capable of identifying the echoes repetition between two epochs and further computing their associated Doppler frequencies was developed, as depicted in Figure 6-5.

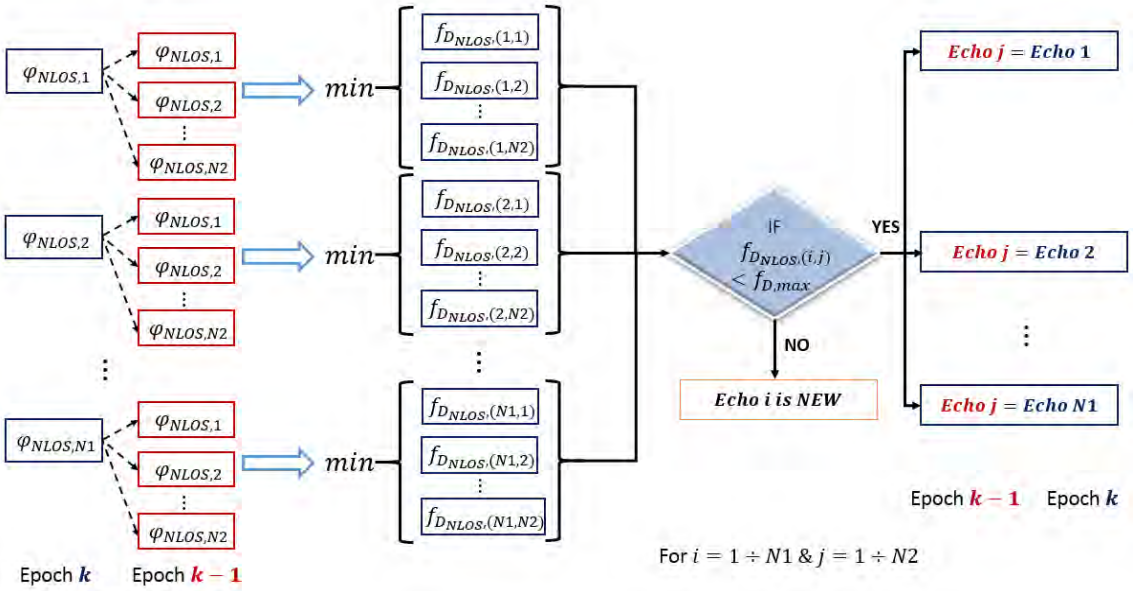

Figure 6-5. *The followed scheme to identify the NLOS echoes repetition in two consecutive epochs* $k-1 \rightarrow k$ *and to compute the associated Doppler frequency.*

For each NLOS echo generated in the current epoch k, illustrated by the blue boxes in Figure 6-5, a Doppler frequency is calculated w.r.t to each NLOS echo already present in the model outputs from the previous epoch $k-1$, according to:

$$f_{D_{NLOS(i,j)}}(k) = \frac{\left(\varphi_{NLOS,i}(k) - \varphi_{NLOS,j}(k-1)\right)}{2\pi \cdot T} \; for \; [i \in (1, N1) \; \& \; j \in (1, N2)] \qquad (6\text{-}14)$$

where:

- $\varphi_{NLOS,i/j}$ indicates the NLOS echo phase for the current/previous epoch $N1/N2$ generated echoes, respectively;
- T is the DLR model generation period, expressed in $[s]$, set equal to the code/carrier integration period.

The NLOS echo repetition between two consecutive epochs $(k-1) \rightarrow k$, is identified by the minimum Doppler frequency value of all the possible echoes' couples obtained from these two epochs, expressed by their indices (i_k, j_{k-1}). Furthermore, an addition test is performed that aims at the identification of new randomly generated echoes. A new echo is detected when the Doppler

frequencies computed as the phase change w.r.t to all the previous epoch $N2$ echoes' phases exceed the maximum Doppler frequency, calculated as:

$$f_{D_{max}}(k) = \frac{f_{L1}}{c} \cdot v_s \cdot \cos(\theta)\ [Hz] \qquad (6\text{-}15)$$

Where:

- v_s denotes the vehicle current speed in $\left[\frac{m}{s}\right]$;
- θ is the satellite elevation angle in $[rad]$;
- $f_{L1} = 1.57542\ GHz$ is the L1 carrier frequency and c is the light speed in $\left[\frac{m}{s}\right]$.

6.3. Description of the Navigation algorithm

Following the GNSS emulator workflow in the second part of Figure 6-1, a clear difference in the navigation level between the scalar and vector operation modes can be observed. In fact, the KF navigation filter in the scalar receiver operates on the locked satellites only whereas the VDFLL algorithm takes use of the code and carrier measurements coming from all the satellites in view (referred to tracked satellites in Figure 6-1) or the selected ones when the satellite selection algorithm is active as illustrated in green in Figure 6-1. In both operation modes, the pseudorange and pseudorange rate observations from the locked (scalar case) and tracked (vector tracking), constitute the measurement input vector for the WLS navigation algorithm. The WLS technique, operative only at the initialization step and that was already detailed in section 4.3.1, solves iteratively the navigation solution around the state vector error until the position error norm is sufficiently small. The achievement of this condition ends the WLS solution and triggers the initiation of the EKF navigation algorithm and its state vector initialization to the WLS-estimated 8×1 state vector ($\boldsymbol{X_0} = \boldsymbol{X_{WLS}}$).

The main differences between the two architectures under study become evident in EKF structure change when the ionosphere residual estimation procedure is activated.

1) The VDFLL state vector is expanded with the ionosphere residual error per tracking channel, as presented in Eq. (5-8), while the classic PVT state vector is conserved for the scalar architecture, as detailed in Section 4.3.2;

2) As a direct consequence of the inclusion of the ionosphere residual states, the initial state covariance matrix $\boldsymbol{P_{VDFLL}}(0)$ of the VDFLL architecture is augmented with the residuals uncertainties for the N tracked satellites, obtained from the Klobuchar (GPS) or NeQuick (Galileo) correction models, respectively provided in Eq. (3-7) and (3-11), and is expressed as:

$$\boldsymbol{P_{VDFLL,iono}}(0) = diag[\sigma^{2\ (1)}_{b_{iono,k}}, \cdots, \sigma^{2\ (i)}_{b_{iono,k}}, \cdots, \sigma^{2\ (N)}_{b_{iono,k}}]_{8+N} \qquad (6\text{-}16)$$

3) The VDFLL process noise covariance $\boldsymbol{Q}_{VDFLL,k}$ is also altered and can be considered as an enhancement of the scalar EKF process noise covariance matrix with the ionospheric error driven process noises for each satellite channel from $i = 1 \div N$ according to the relation given in Eq. (5-11);

4) The measurement covariance matrix representations for the two receiver architectures exhibit major differences:

   - When omitting the biases contribution, the code/carrier tracking error variances in the open-loop configuration are fed to the VDFLL measurement covariance matrix $\boldsymbol{R_{VDFLL,k}}$, since the code/carrier feedback is closed after the EKF position update. Whereas for the scalar tracking operation mode, the classic DLL and PLL tracking error variances are included into the scalar measurement covariance matrix $\boldsymbol{R_{ST,k}}$ for each locked satellite using the relations from Eq. (4-30) - (4-32);
   - However in the presence of the ionosphere residuals, the scalar measurement covariance matrix $\boldsymbol{R_{ST,k}}$ is inflated with the ionosphere residual and residual rates error variance terms $\left(\sigma^{2\ (i)}_{b_{iono,k}}, \sigma^{2\ (i)}_{\dot{b}_{iono,k}}\right)$. Concerning the VDFLL architecture, only the measurement covariance matrix states $\boldsymbol{R_{VDFLL,k}}$ related to the Doppler measurements are inflated since the ionosphere residual impact on the code measurements is being estimated. Thus, the measurement covariance matrixes for the two operation modes have the following terms in the main diagonal:

$$\boldsymbol{R_{ST,iono}}(k) = \begin{cases} \sigma^{2\,(i)}_{DLL}(k) + \sigma^{2\ (i)}_{b_{iono,k}} & for\ 1 \le i \le N_{locked} \\ \sigma^{2\,(i)}_{PLL}(k) + \sigma^{2\ (i)}_{\dot{b}_{iono,k}} & for\ 1 \le i \le N_{locked} \end{cases} \qquad (6\text{-}17)$$

   and,

$$\boldsymbol{R_{VDFLL,iono}}(k) = \begin{cases} \sigma^{2\,(i)}_{\delta\rho_{VDFLL}}(k) & for\ 1 \le i \le N_{tracked} \\ \sigma^{2\,(i)}_{\delta\dot{\rho}_{VDFLL}}(k) + \sigma^{2\ (i)}_{\dot{b}_{iono,k}} & for\ 1 \le i \le N_{tracked} \end{cases} \qquad (6\text{-}18)$$

   where:

   - $(\sigma^{2\,(i)}_{DLL}, \sigma^{2\,(i)}_{PLL})\ (k)$ denote the DLL and PLL loop error variances, modelling the pseudorange and pseudorange rate measurement errors, respectively, presented in [Betz and Kolodziejski, 2000] and [Kaplan and Hegarty, 2006];
   - $\left(\sigma^{2\,(i)}_{\delta\rho_{VDFLL}}, \sigma^{2\,(i)}_{\delta\rho_{VDFLL}}\right)\ (k)$ denote the code and carrier discriminators open-loop error variances, respectively, defined in Eq. (5-16) and (5-17);
   - $\left(\sigma^{2\ (i)}_{b_{iono,k}}, \sigma^{2\ (i)}_{\dot{b}_{iono,k}}\right)$ denote the ionosphere residual and residual rate variances, given in Eq. (5-3) and (5-7);
   - $N_{locked}, N_{tracked}$ are the total number of GPS and Galileo locked and tracked (in-view) channels for the scalar and vector tracking architectures, respectively.

5) The leading difference between the scalar and vectorized navigation filter designs relies on the measurement innovation step. Regarding the scalar EKF navigation filter, the measurement innovation is computed as the difference between the measurement input vector, comprising the code and Doppler measurements obtained at the tracking stage after the NCO update, and the EKF-predicted measurements as $(\boldsymbol{z_{innov,k}} = \boldsymbol{z_{input,k}} - \boldsymbol{z_{pred,k}})$. On

the contrary, the code and carrier discriminators errors per tracking channel are fed directly to the VDFLL EKF filter as its innovation vector.

The remaining EKF filter state prediction and measurement update steps are the same between the two operation modes. In the scalar tracking architecture, the final task performed by the EKF navigation filter is the state estimate update ($\boldsymbol{X_{k|k}}$). Since in the VDFLL architecture, the positioning and tracking tasks are combined and performed by the EKF navigation filter, the updated state vector estimation will ensure the "vectorized" code/carrier NCO update computation in the feedback loop to the tracking channels, as illustrated in the green block in Figure 6-1 and given in Section 5.3.5.

6.4. Conclusions

The aim of this chapter was the presentation of the developed dual-constellation GPS/Galileo emulator, incorporating the scalar and proposed vector tracking architectures, and capable of performing the tracking and navigation tasks in a realistic urban propagation channel model.

The overall concept of the GNSS signal emulator, which simulates the GNSS signals at the correlator output, along with the evident benefits by employing simulated data w.r.t real measurements were provided in section 6.1 that are listed below:

- A faster processing achieved by omitting the correlation operation that represents the most time-consuming task of a real GNSS receiver;
- The total control on the simulation parameters including the satellites constellation and atmospheric effects generation, the receiver tracking parameters configuration, the inclusion of different user's motion files, the user environment and GNSS signals' characteristics;
- The testing flexibility of new tracking and navigation filters' configurations, as it is the case for the proposed VDFLL architecture, providing the mean for finely evaluating the tracking and navigation performance in different conditions;
- Possibility to test the overall capability of the vectorized configuration concerning the fully-deployed GPS/Galileo satellite constellations, which is not the case when using the real measurements from the limited Galileo satellites geometry.

The processing blocks of the dual-constellation signal emulator, from the measurement generation process to the navigation algorithms, were detailed in section 6.1. The attention was directed to the description of the sliding-window C/N_0 estimation algorithm, required for the computation of the measurement covariance matrix $\boldsymbol{R_k}$ for the two architectures. Moreover, the simplified hot 1 second re-acquisition process initiated after the loss-of-lock detection in the scalar tracking architecture, was also described in details in section 6.1.

The fundamental part of this chapter was constituted by the correlator output remodeling in order to include the LOS/NLOS echoes information in terms of amplitude, relative delay, phase and Doppler frequency at the correlator output level. This process along with the description of the wideband DLR urban propagation channel model, including the urban scenario parameters and LOS/NLOS echoes modelling were detailed in section 6.2. Furthermore, the DLR urban channel model was adapted to meet the requirements of the scalar and vector tracking architectures. For this matter, the multipath

parameters were generated at the same sampling rate as the tracking loop update at $50\ Hz$ and also, an efficient and simple algorithm was used to compute the echoes Doppler frequency based on the phase comparison between two consecutive epochs.

The major differences between the scalar (used as benchmark) and vector tracking receivers' navigation algorithms were summarized in section 6.3. The crucial distinction between the two EKF filters relies in fact on the ionosphere residual estimation process implemented for the VDFLL architecture that is associated with the augmentation of its state vector with the ionosphere residuals per tracked satellite. As a direct consequence, the VDFLL state and measurement covariance matrixes, are altered in order to accommodate the ionosphere residual-related uncertainties. It is important to mention that no knowledge of the ionosphere residuals is assumed in the VDFLL EKF initialization step and that the EKF filter operation is initiated for both architectures after the WLS-estimated position convergence is achieved. These remarks will be later referred to in the simulation results section.

7. Simulation Results

This chapter examines the performance of the proposed vector tracking algorithm in urban environment in the presence of multipath and ionosphere residual error reception. It aims at investigating the performance of the implemented VDFLL solution by comparing it to the conventional scalar tracking receiver both in the navigation solution- and tracking channels estimation domain for different test configurations. The main differences between the two architectures rely on the KF design and the measurement processing manner, already provided in Chapter 4 and 5.

The first part of the chapter provides the global view of the test description, comprising the car trajectory profile and the tracking channels/navigation module parameters for the two architectures under study.

In section 7.2, the VDFLL algorithm validation in the presence of ionosphere residual errors in both the navigation and channel domains is performed via Monte Carlo (MC) simulation.

Section 7.3 extends the performance comparison between the scalar tracking and VDFLL receiver configurations to the complete urban environment representative, characterized by the multipath and ionosphere residuals presence. Herein, the VDFLL capability in estimating the ionosphere residual errors on each tracking channel, according to the Gauss-Markov state vector and dynamic matrix model detailed in chapter 5, is assessed.

Last but not least, the performance assessment is concluded in section 7.4 with the severe urban condition test that is characterized by strong satellite outages. For this configuration, the satellite selection mechanism is activated for the VDFLL architecture with the objective of increasing the position solution and channel estimation reliability in limited number of observations.

Finally, the chapter conclusions are drawn in section 7.5.

7.1. Test Setup

7.1.1. Simulated Scenarios

In this thesis, the tests are performed on a simulated car trajectory in Toulouse urban area with the following characteristics:

- The car trajectory corresponds to a real car trajectory generated from the data collected during a real test campaign in Toulouse urban area, by using a NovAtel's SPAN receiver mounted on the car. The recorded trajectory of $600\ s$ duration is presented in Figure 7-1.
- The signal reception conditions are simulated by the developed GNSS emulator described in Chapter 6.

Figure 7-1. *The reference car trajectory in Toulouse city center*

Concerning the generation of the signal reception conditions, the tests herein presented simulate the signal reception of GPS and Galileo constellations in the L1 band, assuming a binary phase shift keying BPSK(1) modulation for GPS L1 C/A signal and a binary offset carrier modulation BOC(1,1) for a simplified Galileo E1 pilot signal. In the simulated test scenarios, the GPS and Galileo constellations are generated from the RINEX files, which show that there are maximally 13 simultaneously tracked GPS L1 and Galileo E1 channels during the 10 minutes urban trajectory. The satellites skyplot representation, illustrating the elevation and azimuth angles of the visible satellites, is provided in Figure 7-2.

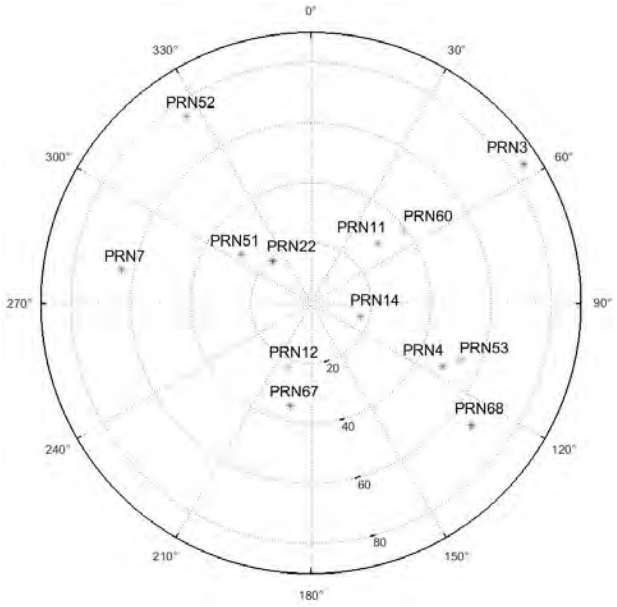

Figure 7-2. *The GPS and Galileo satellites skyplot.*

Finally, depending on the generated signal reception conditions, different scenarios can be simulated. In this study, the performance analysis is conducted in an extensive manner for three different test scenarios. The test scenarios are defined by the generated source of errors in addition to the thermal noise which is always present.

The lists of scenarios is given below:

- ***Scenario 1***: *Receiver testing in the presence of ionosphere residual errors only*;
- ***Scenario 2***: *Receiver testing in complete urban environment representative, including both multipath and ionosphere residual errors presence*;
- ***Scenario 3***: *VDFLL "Stress test", referring to bad satellite constellation geometries and reduced observations.*

7.1.2. Receiver's Tracking and Navigation parameters

The receiver parameters used during the tests, defining the scalar (ST) and the vector tracking (VT) loop design as well as their navigation filter configurations, are summarized in Table 7-1.

Table 7-1. *Tracking loops and navigation module test parameters*

Parameters	ST	VT
General		
RF filter bandwidth $[\mathbf{MHz}]$	24 (double-sided)	
I&D period $[\mathbf{s}]$	0.02	
L1/E1 Code delay tracking		
DLL order	*1st*	*N/A**
DLL configuration	*Carrier-aided DLL*	*N/A*
GPS L1 chip spacing $(\mathbf{d_{C-L1}})$ $[\mathbf{chip}]$	*0.5*	
GAL E1 chip spacing $(\mathbf{d_{C-E1}})$ $[\mathbf{chip}]$	*0.2*	
Discriminator type	Early Minus Late Power (EMLP)	
DLL update period $[\mathbf{s}]$	0.02	*N/A*
DLL noise bandwidth $(\mathbf{B_{DLL-n}})$ $[\mathbf{Hz}]$	1	
Carrier phase/frequency tracking		
Carrier estimation	*Phase*	*Frequency*
PLL order	3	*N/A*
PLL update period $[\mathbf{s}]$	0.02	*N/A*
PLL noise bandwidth $(\mathbf{B_{PLL-n}})$ $[\mathbf{Hz}]$	10	*N/A*
Discriminator type	*Atan2*	*Cross Product (CP)*
Navigation filter		
Initialization	*Weighted Least Square (WLS)*	
Type	*EKF*	
Nr of States (base configuration)	8	
State vector type	*PVT*	
Observations	*Pseudoranges/ranges rates*	*Code/carrier discriminator outputs (as innovations)*
Nr. of measurements	$2 \cdot$ *nr of locked satellites*	$2 \cdot$ *nr of tracked satellites*
Satellite selection	*N/A*	*Active*
Ionosphere residual estimation	*N/A*	*Active*
Nr. of states (ionosphere active)	8	$8 +$ *nr of satellites in-view*
PVT update rate $[\mathbf{Hz}]$	50	
Channel Feedback Loop	*Loop-based*	*EKF navigation solution-based*

Measurement covariance matrix	*Closed-loop*	*Open-loop*
Code delay period $[s]$	*N/A*	0.02
Carrier frequency period $[s]$	*N/A*	0.01
*- Not active		

Two important reminders must be made regarding the implementation of the two receiver architectures under study:

- Firstly, in order to initialize the vector tracking loop parameters, the scalar tracking operation that employs a DLL for the code delay tracking and a 3rd order PLL for the carrier phase estimation, must be conducted first;
- Secondly, for both receiver configurations, the initial PVT state vector for the EKF navigation filter is set accordingly to the Weighted Least Square (WLS) estimated solution after convergence.

7.1.3. Description of the used Parameters and Statistics

A detailed performance assessment of the proposed VDFLL algorithm in comparison to the scalar tracking receiver configuration is performed in degraded signal reception conditions in two different levels:

- ***Navigation level*:** expressed in terms of user's navigation solution estimation accuracy in the vehicle navigation frame (along- and cross- track coordinates);
- ***Channel level***: indicated by the code delay and carrier Doppler frequency estimation errors, which are expressed in a different manner for the scalar and vector tracking architectures.

Concerning the scalar tracking (ST) architecture, the code delay error $\left(\varepsilon_{\tau}^{(i)}(k)\right)$ at epoch k for the i^{th} GPS/Galileo satellite in-view is computed as follows:

$$\begin{aligned}\varepsilon_{\tau,ST}^{(i)}(k) &= \tau_0^{(i)}(k) - \tau_{est,ST}^{(i)}(k) \\ &= \frac{1}{c}\cdot\left(R_0^{(i)}(k) + b_{Rx}(k) - b_s^{(i)}(k)\right) - \tau_{est,ST}^{(i)}(k) \quad [m]\end{aligned} \tag{7-1}$$

where:

- $R_0^{(i)}(k) = \sqrt[2]{\left(x_s^{(i)} - x_0\right)^2 + \left(y_s^{(i)} - y_0\right)^2 + \left(z_s^{(i)} - z_0\right)^2}\,(k)$ denotes the true satellite-user geometric distance, expressed in ECEF frame in $[m]$;
- b_{Rx} and $b_s^{(i)}$ denote the user's and i^{th} satellite clock biases, respectively, expressed in $[m]$;
- $\tau_{est,ST}^{(i)}$ denotes the DLL-estimated code delay including the ionosphere residual bias and expressed in $[m]$;

A different approach is adopted for the derivation of the Doppler frequency error for the scalar tracking architecture, since it employs a 3rd order PLL for the carrier phase estimation. Recalling that the Doppler frequency measurement can be obtained by differentiating the carrier phase

observations of two consecutive epochs, the Doppler frequency error can be computed according to Eq. (4-17):

$$\begin{aligned}\varepsilon_{f_{D,st}}^{(i)}(k) &= f_{D}{}_{0}^{(i)}(k) - f_{D}{}_{est,ST}^{(i)}(k) \\ &= \frac{\left(\varphi_0^{(i)}(k) - \varphi_0^{(i)}(k-1)\right) - \left(\varphi_{est,ST}^{(i)}(k) - \varphi_{est,ST}^{(i)}(k-1)\right)}{2\pi \cdot T}(k) \quad [Hz]\end{aligned} \qquad (7\text{-}2)$$

where:

- $\varphi_0^{(i)}$ denotes the true carrier phase of the i^{th} satellite, that includes the clock bias and ionosphere residual contributions as shown in Eq. (4-14);
- $f_{D}{}_{est,ST}^{(i)}$ represents the Doppler frequency estimation, computed as the PLL-estimated carrier phase $\left(\varphi_{est,ST}^{(i)}\right)$ change in two consecutive epochs.

When referring to the VDFLL architecture, the code delay error $\left(\varepsilon_{\tau,VDFLL}^{(i)}(k)\right)$ at epoch k for the i^{th} GPS/Galileo satellite in-view is computed as follows:

$$\begin{aligned}\varepsilon_{\tau,VDFLL}^{(i)}(k) &= \tau_0^{(i)}(k) - \tau_{est,VDFLL}^{(i)}(k) \\ &= \frac{1}{c} \cdot \left[\left(R_0^{(i)}(k) + b_{Rx}(k) - b_s^{(i)}(k)\right) + b_{iono}^{(i)}(k) - \left(\hat{R}_k^{(i)} + \hat{b}_{Rx}(k) + \hat{b}_{iono}^{(i)}(k)\right)\right] \\ &= \frac{1}{c} \cdot \left[\left(R_0^{(i)}(k) - \hat{R}_k^{(i)} + b_{Rx}(k) - \hat{b}_{Rx}(k) - b_s^{(i)}(k)\right) + \left(b_{iono}^{(i)} - \hat{b}_{iono}^{(i)}(k)\right)\right]\end{aligned} \qquad (7\text{-}3)$$

where:

- $\tau_{est,VDFLL}^{(i)}(k)$ denotes the VDFLL-estimated code delay at the measurement prediction stage, computed in Eq. (5-33);
- $b_{iono}^{(i)}(k)$ and $\hat{b}_{iono}^{(i)}(k)$ denote the true and VDFLL-estimated (inside the state vector) ionosphere residuals of the i^{th} satellite.

The clear difference between the code delay errors for the two architectures, stands on the appearance of the ionosphere residual estimation error $\left(b_{iono}^{(i)} - \hat{b}_{iono}^{(i)}(k)\right)$ that is due to the VDFLL algorithm design in order to estimate the ionosphere residual.

Whereas, the Doppler frequency error for the VDFLL architecture is deduced from the VDFLL-predicted pseudorange rate defined in Eq. (5-34) and is provided by:

$$\begin{aligned}\varepsilon_{f_{D,st}}^{(i)}(k) &= f_{D}{}_{0}^{(i)}(k) - f_{D}{}_{est,VDFLL}^{(i)}(k) \\ &= \frac{\left(\varphi_0^{(i)}(k) - \varphi_0^{(i)}(k-1)\right)}{2\pi \cdot T} - f_{D}{}_{est,VDFLL}^{(i)}(k) \quad [Hz]\end{aligned} \qquad (7\text{-}4)$$

For the above two categories, the following statistical parameters are computed as a function of time along the car trajectory, including:

- The mean of the estimation error;
- The Root Mean Square of the absolute estimation errors, referred to as the empirical quadratic mean RMS;
- The $95-$ and $99-$ percentiles $(95\,\%, 99\,\%)$, representing the accuracy confidence levels, bounding the absolute estimation errors' values.

The following sub-sections present the simulation results for each of the test scenarios given above.

7.2. Scenario 1: Presence of the Ionosphere residuals only

7.2.1. Objective

The objective of this test scenario is to assess in detail the position and channel estimation performance of the two tracking receiver architectures in an open sky environment. Furthermore, the test conducted in this section aims at validating the proposed VDFLL algorithm capability in dealing with the ionosphere residual errors.

7.2.2. Scenario characteristics

More specifically, in this scenario only two errors' sources are considered, which indeed are not perfectly corrected by external/internal information or models as it is the case for the satellite clock correction. Indeed, these errors' sources are the thermal noise and the ionospheric residuals, with the later appearing in the code measurements even after the application of the Kobluchar model for GPS L1 C/A signals and the NeQuick model for Galileo E1 OS signals, already presented in section 3.1 and 4.1.

7.2.3. Methodology

In order to achieve a detailed performance assessment of the two EKF navigation filter configurations in this scenario, 30 Monte Carlo simulations runs were conducted with the same car trajectory presented in section 7.1. Considering that the EKF navigations solution is estimated at a $50\ Hz$ rate and the car trajectory duration is 600 seconds, then the interval on which the position and channel domain statistics are computed contains 900000 estimation error values per each parameter under study. Indeed, it may be said that the chosen number of Monte Carlo runs is quite sufficient for validating the proposed vectorized architecture for the used urban car trajectory. For each simulation, a new draw of ionosphere residual errors and therefore GNSS measurements is generated and the initial simulation date is also changed within the scope of obtaining a different satellite geometry during each run.

Concerning the navigation error comparison, the probability distribution function (PDF) representation has been chosen since it provides a clear insight of the error statistics and their boundings. For a proper validation of the scalar and vector tracking architectures, the Monte Carlo simulations have been applied to a reduced number of observations starting from a maximum number of 7 satellites to 4 satellites in view, which represents the minimum EKF filter requirement for the navigation solution convergence. It must be noted that for 3 satellites only, the navigation solution slowly diverges and thus it cannot be used for the purpose of this analysis.

It must be also reminded that in the initialization step of the VDFLL architecture, there is no ionosphere residual knowledge considered in the state vector. Therefore, at the first time instant all the ionosphere residual states are set to zero and as a direct consequence the initial VDFLL state

covariance matrix $\boldsymbol{P_{VDFLL}}(0)$ is augmented with the residuals uncertainties for the N tracked satellites, defined in section 6.1.

7.2.4. Results

The next part provides an overview of the test results firstly in the navigation domain, in terms of PVT error PDFs and a detailed statistics' table and afterwards, focusing on the code and carrier estimation errors dependency on the satellites' elevation and bearing angles.

7.2.4.1. Monte Carlo Results in the Navigation Domain

In this subsection, the performance analysis focuses on the navigation solution errors only. The PDF of the EKF estimation errors concerning the 2-D along and cross track position and velocity errors are illustrated in Figure 7-3 and Figure 7-4, respectively. Whereas the receiver's clock bias and drift errors' PDFs for the two architectures under study are shown in Figure 7-5 a) and b), respectively. The navigation errors' PDFs are illustrated for both the VDFLL (in blue) and Scalar tracking (ST) + EKF filter (in red) architectures based on the PVT solution computed from 7 satellites (top left) to 4 satellites in view (bottom right). Furthermore, the 95% percentiles (or 2σ error bounds) are illustrated in blue and red dashed lines for the VDFLL and ST+EKF configurations, respectively. The statistical parameters, regarding the conducted Monte Carlo tests' results, are presented in Table 7-2.

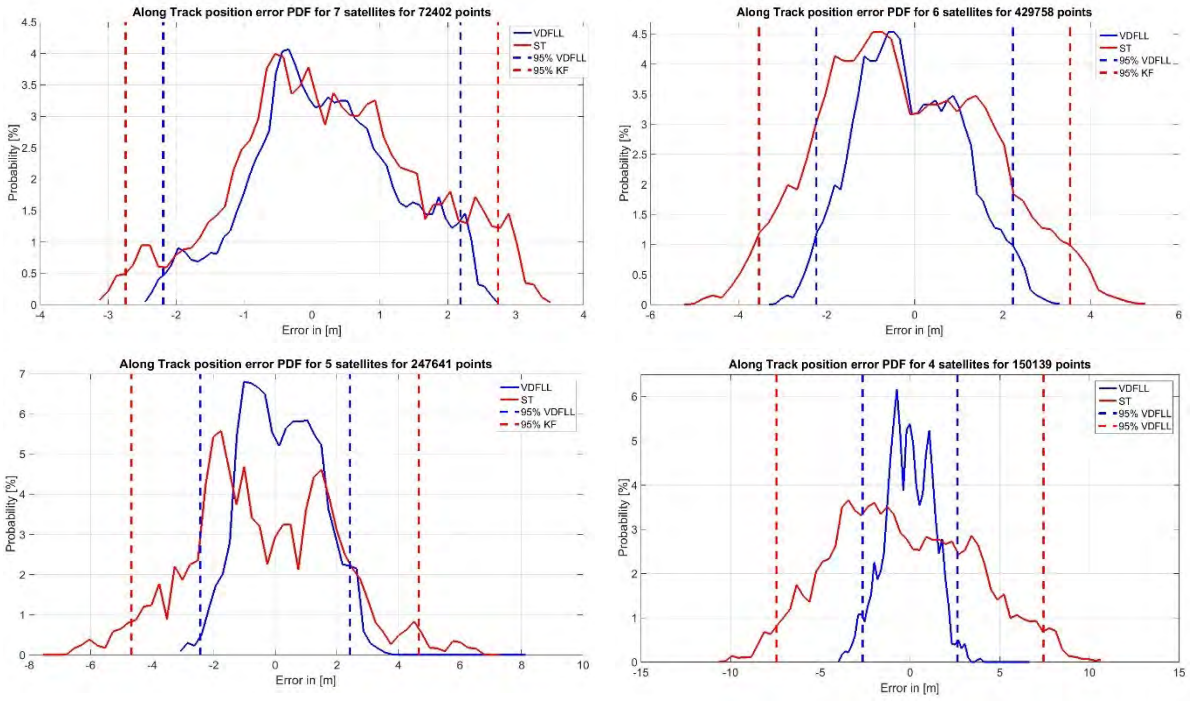

a)

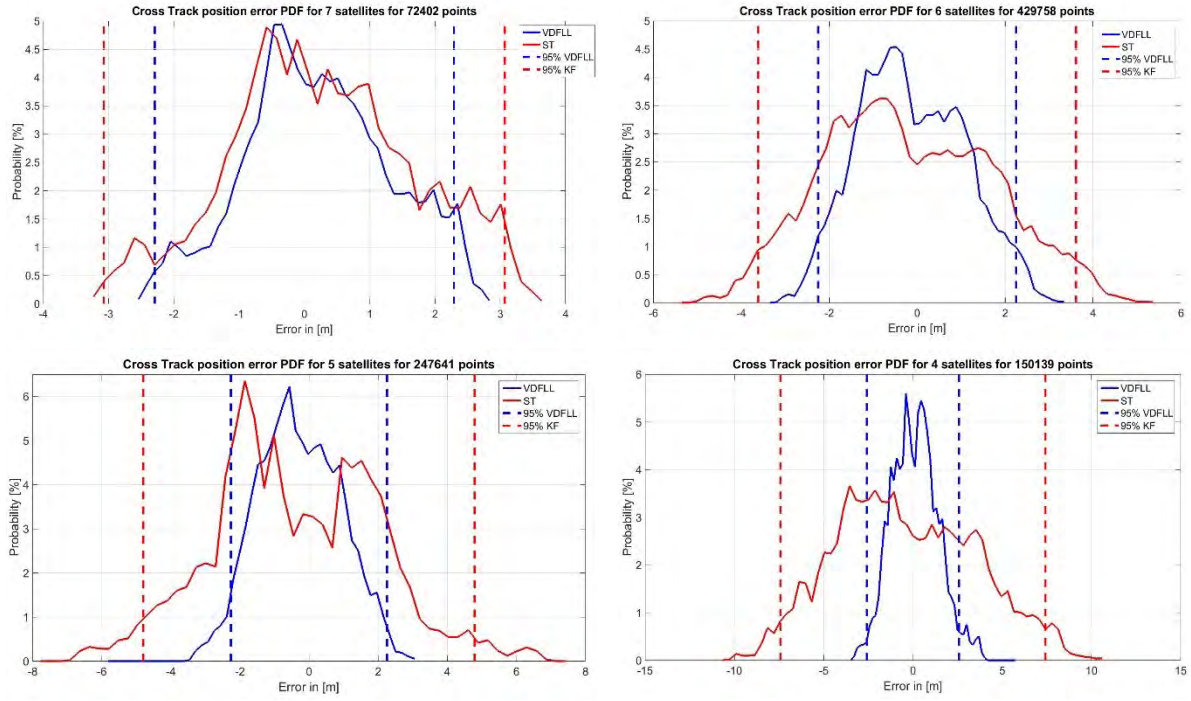

b)

Figure 7-3. ***a)*** *Along- and* ***b)*** *Cross track position errors PDFs from Monte Carlo simulations.*

An overall observation that can be made based on the PDFs curves for each position estimation error, is the very slight resemblance to the normal distribution PDF pattern due to the not-properly mitigated (for the ST+EKF filter) and not-perfectly estimated (for the VDFLL architecture) ionosphere residuals. From the plots in Figure 7-3, it can be seen that the VDFLL architecture exhibits a better positioning performance w.r.t the scalar tracking receiver for each number of satellites case. Indeed, a significant position estimation degradation in both along and cross track coordinates is exhibited by the ST+EKF navigation filter (red curve) with the reduction of the number of observations from 7 to 4 satellites in-view. This degradation becomes even more evident when only 4 satellites are used for the navigation solution estimation, which is related to the inclusion of the bare minimum number of measurements for the correct filter operation that at the same time are also significantly affected by the ionosphere residual errors. This performance deterioration is also reflected by the increase of the ST+EKF position error covariance bounds (in red) from $2.74\ m$ (along track) when seven satellites are used for the navigation solution, up to nearly 3 times more going to $7.44\ m$ for 4 satellites in-view from Table 7-2.

On the contrary, the VDFLL technique conserves a stable position estimation within $2.7\ m$ 95%–percentile bounds (see Table 7-2). The reasons behind the VDFLL EKF stability in the navigation domain are twofold. Firstly, the VDFLL EKF filter is modified with the objective of estimating the ionosphere residual errors by augmenting the state vector X_{VDFLL} with the residual states per tracked channel and also by modifying the discrete state transition matrix with the inclusion of residual's Gauss-Markov power decaying functions, as already described in Chapter 5. Whereas, no ionosphere residual estimation process is performed from the scalar tracking receiver which leads to a larger impact of the residuals in the PVT solution. Secondly, the code and carrier NCO updates in the feedback loop, computed from the position and velocity estimations projected in the pseudorange and pseudorange rate domain, encompass the ionosphere residual error corrections. This ensures the position

estimation error reduction in a recursive manner from the current to the following measurement epoch.

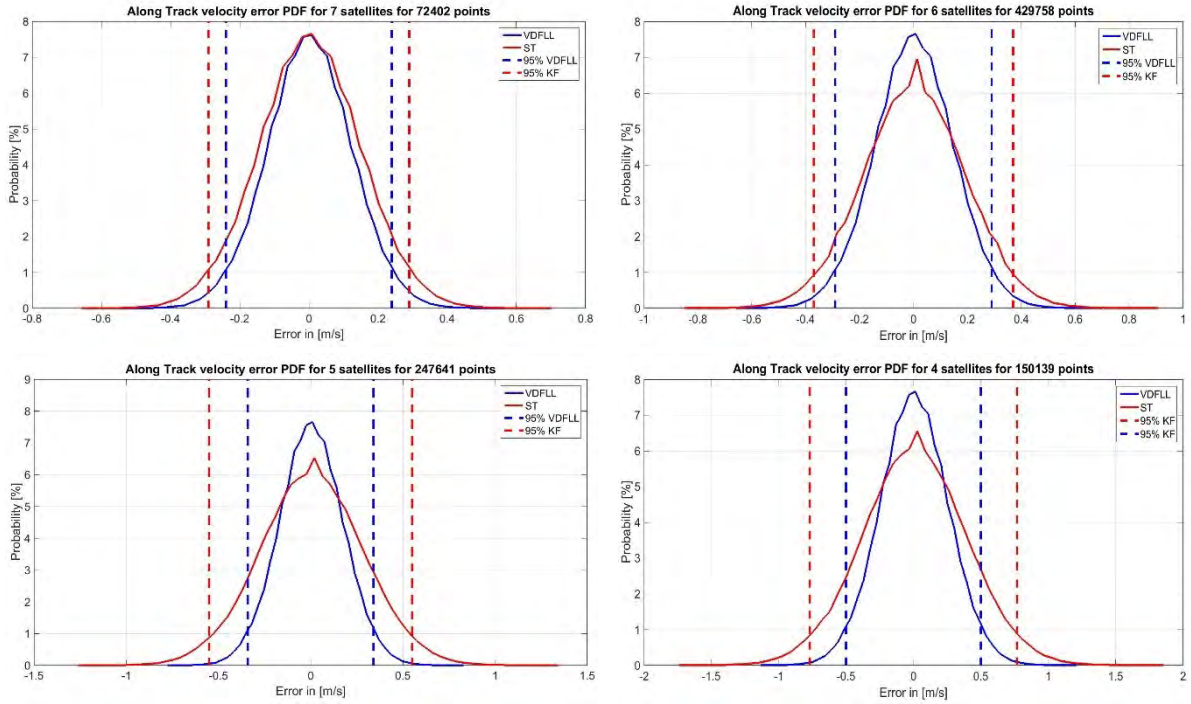

a)

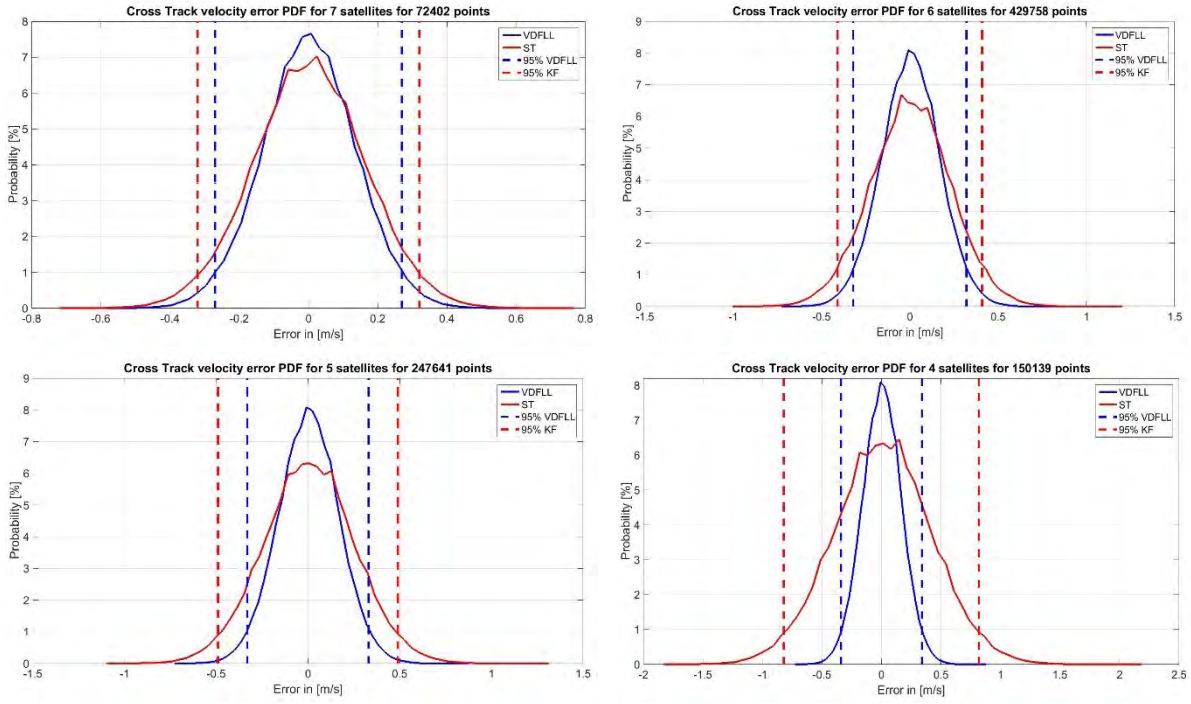

b)

Figure 7-4. **a)** Along- and **b)** Cross track velocity errors PDFs from Monte Carlo simulations.

A higher VDFLL performance is also noticed in the along and cross track velocity estimates but at a lower order of magnitude compared to the position domain, as illustrated in Figure 7-4. This can be explained by the slow variation in time of the ionosphere residuals, therefore affecting less the Doppler measurements. However, VDFLL provides better user's dynamics estimation even for reduced

number of observables, as it can be seen for the 4 satellites scenario in the bottom right plots. This is reflected at the twice lower VDFLL velocity error bounds (in blue) against the ST+EKF ones (in red) in the extreme case of only 4 visible satellites. These results are exploited in details in Table 7-2. Furthermore, the nearly normal distribution-shape of the velocity PDFs curves is related to the Gaussian distribution property of the ionosphere residual rates, computed as the derivative of the ionosphere residual errors that are modelled as 1st order Gauss-Markov processes.

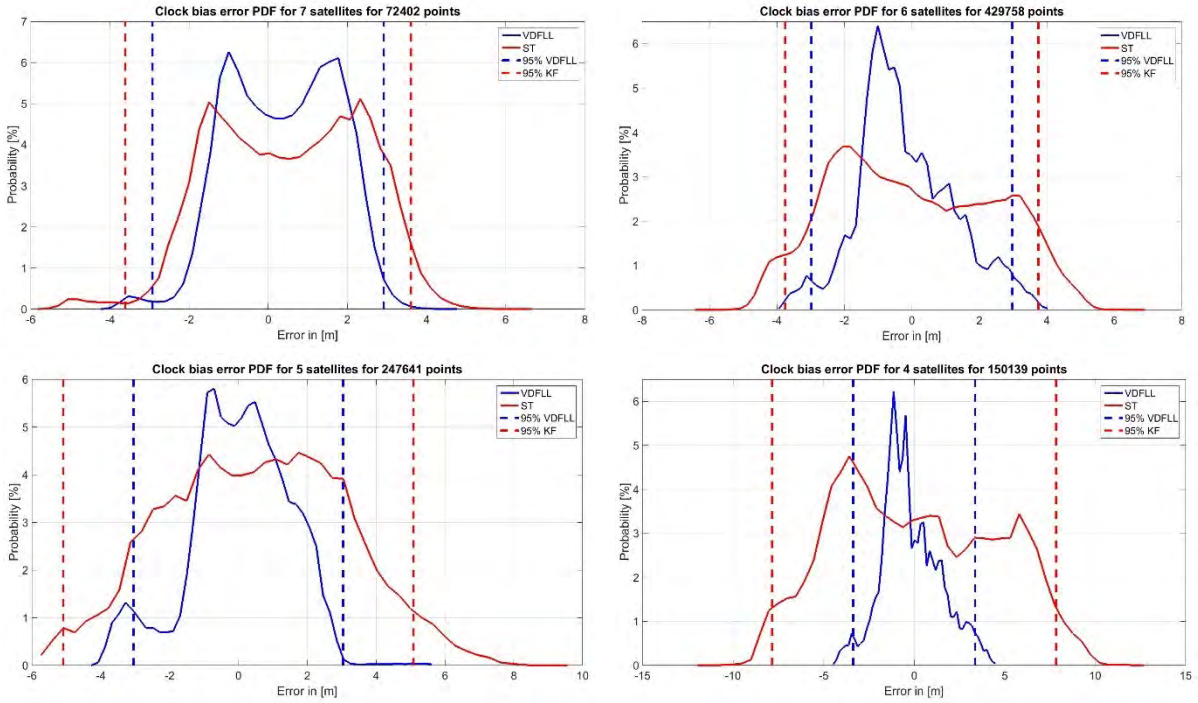

a)

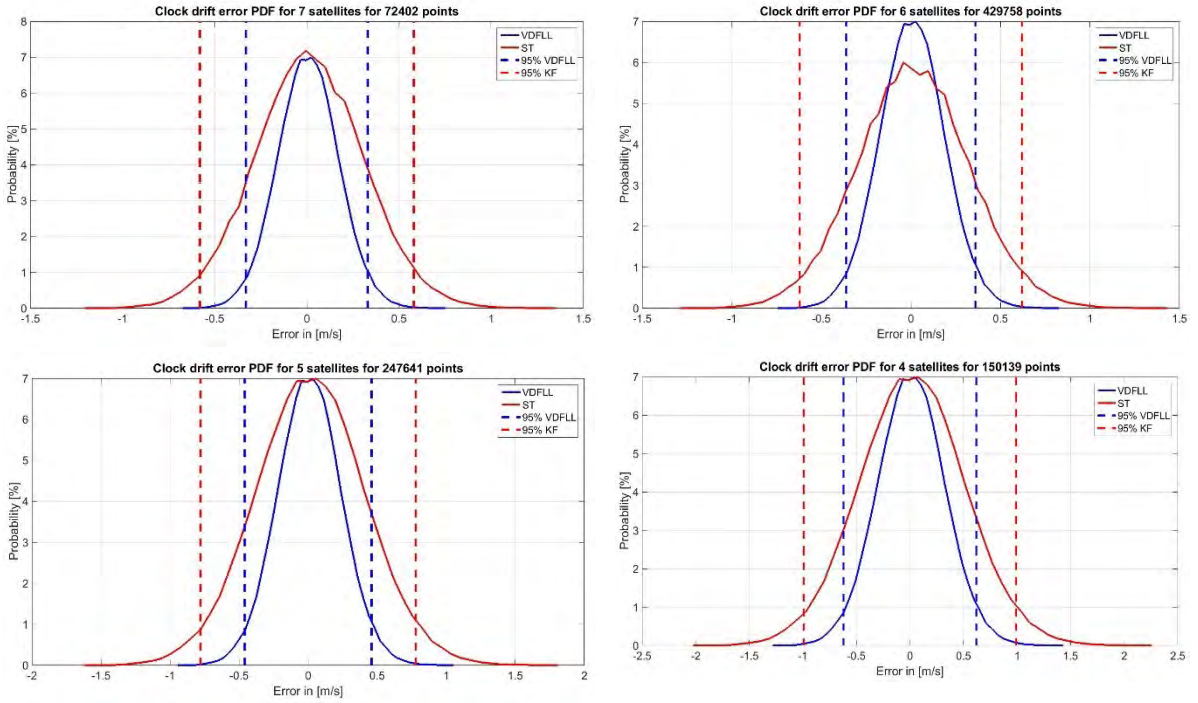

b)

Figure 7-5. ***a)*** *Clock bias and* ***b)*** *Clock drift errors PDFs from Monte Carlo simulations.*

The most marked VDFLL superiority concerns the receiver's clock bias estimation in the presence of few available measurements, as can be seen in Figure 7-5 a). When carefully observing the clock bias error PDFs for both the vectorized and scalar receiver operation modes, it can be noticed that the clock bias estimation error magnitude exceeds the position errors one. In fact, the pseudorange measurement errors are mostly projected to the least observable EKF state that is the user's clock bias. Moreover, these errors become more evident in the presence of the ionosphere residuals which explains the larger clock bias errors (up to 2.5 times for the 4 satellites scenario in Table 7-2) from the scalar tracking receiver that is not capable of observing/estimating these residuals.

Concerning the clock drift estimation errors in Figure 7-5 b), the same statements presented for the velocity estimation characteristic hold. This may be related to the translation chain between the carrier frequency errors, comprising the ionosphere residual rates, and the velocity + clock drift states. However, this reasoning will be validated when presenting the channel errors' results in the following sub-section.

The detailed statistical parameters summarizing the Monte Carlo results are presented in Table 7-2.

Table 7-2. *Navigation estimation error statistics for the two architectures under study.*

			$N=7$		$N=6$		$N=5$		$N=4$	
			ST	**VT**	**ST**	**VT**	**ST**	**VT**	**ST**	**VT**
POSITION	**Along Track**	Mean	0.1	0.1	0.2	0.1	0.4	0.2	0.7	0.4
		RMS	1.4	1.1	1.9	1.2	2.4	1.2	4	1.4
		95%	2.7	2.2	3.5	2.2	4.7	2.5	7.4	2.6
		99%	3.4	2.4	4.1	2.6	6.1	2.9	8.6	3.2
	Cross Track	Mean	0.1	0.5	0.2	0.1	0.4	0.3	0.8	0.5
		RMS	1.6	1.1	1.9	1.2	2.4	1.3	3.9	1.5
		95%	3.1	2.4	3.6	2.3	4.8	2.4	7.4	2.6
		99%	3.8	2.5	4.2	2.6	6.3	2.9	8.7	3.5
VELOCITY	**Along Track**	Mean	~0	~0	~0	~0	~0	~0	~0	~0
		RMS	0.2	0.1	0.2	0.1	0.3	0.2	0.4	0.3
		95%	0.3	0.2	0.4	0.3	0.6	0.3	0.8	0.5
		99%	0.4	0.3	0.5	0.4	0.7	0.5	1.1	0.7
	Cross Track	Mean	~0	~0	~0	~0	~0	~0	~0	~0
		RMS	0.1	0.1	0.2	0.1	0.4	0.2	0.7	0.3
		95%	0.3	0.2	0.4	0.3	0.5	0.3	0.8	0.4
		99%	0.4	0.4	0.5	0.4	0.7	0.4	1.1	0.5
CLOCK	**Bias**	Mean	0.3	0.2	0.1	0.2	0.5	0.1	0.6	0.2
		RMS	2	1.7	2.6	1.3	2.7	1.5	4.5	1.6
		95%	3.6	3	3.8	3	5.1	3.1	7.9	3.4
		99%	4.4	3.1	4.8	3.2	6.3	3.7	9.1	4.1
	Drift	Mean	~0	~0	~0	~0	~0	~0	~0	~0
		RMS	0.3	0.2	0.3	0.2	0.4	0.2	0.5	0.3
		95%	0.6	0.3	0.6	0.4	0.8	0.5	1	0.6
		99%	0.8	0.6	0.8	0.5	1.1	0.6	1.3	0.8

7.2.4.2. Monte Carlo Results for the Tracking Channels

The tracking channels' estimation errors RMS for the two architectures under comparison are illustrated via the contour plots in Figure 7-6, as a function of the satellites elevation and bearing angle.

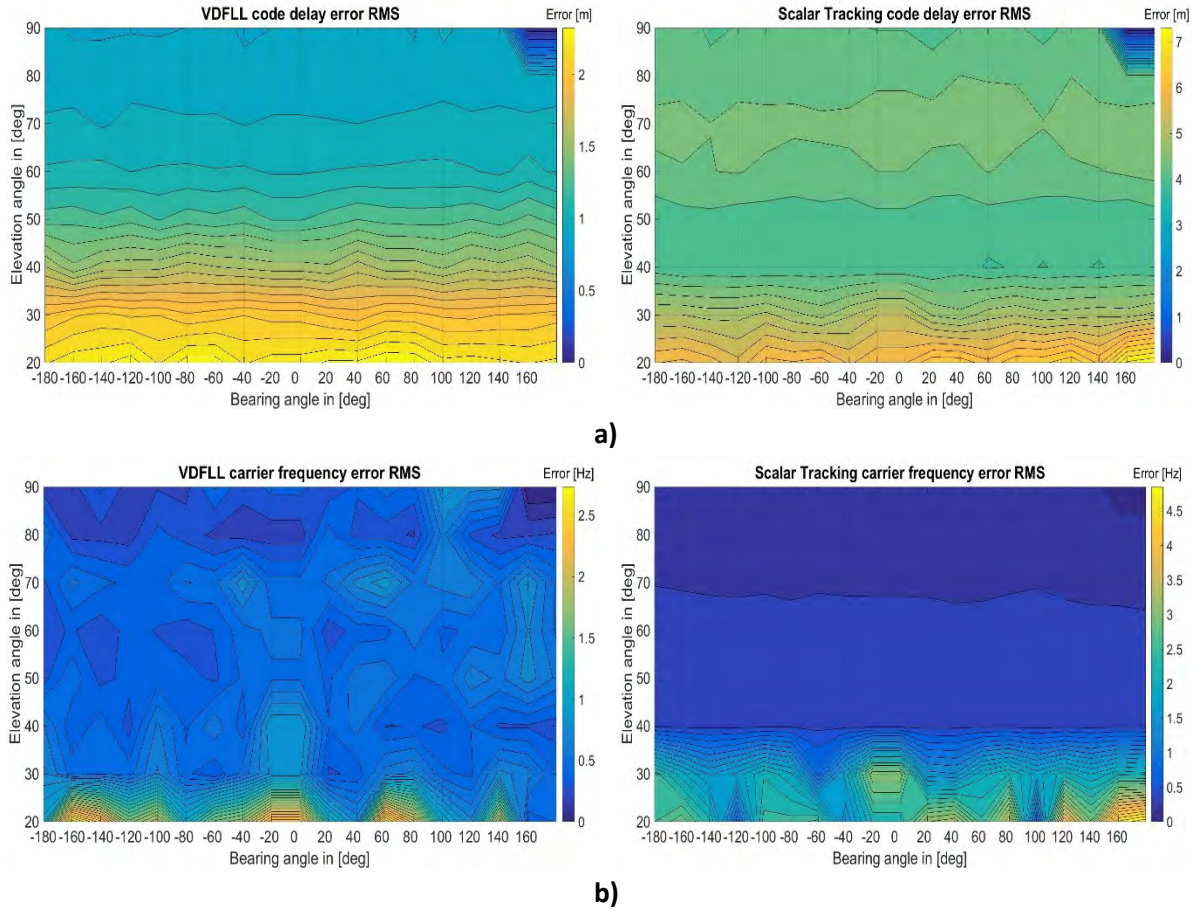

Figure 7-6. ***a)*** *Code delay and* ***b)*** *Carrier frequency errors RMS from Monte Carlo simulations.*

From the contour plots of both the code delay- and carrier frequency error RMS, respectively illustrated in Figure 7-6 a) and b), a significant dependence on the satellite elevation angle is clearly apparent. In fact as illustrated by the bright yellow areas, the code delay- and carrier frequency errors are more dominant in the low elevation region since the ionosphere diffraction effects are larger for low elevation angles. Furthermore when observing Figure 7-6 b), a relation between the carrier frequency errors and the bearing angle (vehicle heading – satellite azimuth angle) can be determined for both architectures. The likely reason for this behavior is that the Doppler frequency depends on the vehicle orientation along the trajectory that is translated into a change of the vehicle heading angle.

What clearly differentiates the two architectures is in fact the order of magnitude of the code delay- and carrier frequency estimation errors. As it can be observed in the first two plots in Figure 7-6 a), the VDFLL code delay estimations are far less erroneous w.r.t the scalar tracking estimations for the overall covered area. The VDFLL superiority in the code delay estimation, shown in the left upper plot, becomes more evident in low elevation region $(20^{\circ} - 30^{\circ})$ with a maximum error of $2.5\,m$ that is three times less than the scalar tracking code delay error. This is due to the VDFLL capability of estimating the ionosphere residual errors and therefore, reducing their impact in the code delay

errors. Furthermore, the VDFLL code delay error RMS decrease when passing to high elevation angles is related to the better satellite geometry that is further translated into an increased observability through the EKF measurement matrix. In other words, high elevation satellites are less likely to introduce biases in the position estimation and therefore, providing a more accurate feedback to the tracking channels.

The proposed vector tracking technique surpasses the scalar tracking counterpart also in terms of the accuracy in estimating the carrier frequency error, as shown in Figure 7-6 b). This comes from the fact that the source of the ionosphere residual rate, the ionosphere residual errors, are correctly estimated and therefore, nearly cancelling out their effect. However, the VDFLL performance improvement in the Doppler frequency level is of a lower order compared to the code delay estimation improvement. This might be due to the slow ionosphere residual variation with time, which is reflected in a lower impact of the ionosphere residual rates in the Doppler measurements for both architectures. Quite interesting is indeed the VDFLL frequency error RMS dispersion up to high elevation angles that is not quite evident for the scalar tracking configuration. This illustrates one of the major drawbacks of vector tracking, being the inter-channel errors coupling. It must be noted that the dark blue areas in the upper right regions are in fact related to the lack of satellite observations.

7.2.5. Conclusions on Scenario 1

In this section, the performance comparison in the navigation and channel level between the VDFLL and scalar tracking receiver configurations was performed in an open sky environment where only the ionosphere residuals were considered. In order to assess in detail the performances of the two architectures, 30 Monte Carlo simulations at $50\ Hz$ sampling rate were run with the same urban car trajectory but with a different satellite geometry and ionosphere residuals draw.

The contour plots of the tracking channels' errors RMS demonstrated the VDFLL capability in estimating the ionosphere residuals that in fact is reflected by the nearly 3 times lower code error RMS for the VDFLL technique w.r.t scalar tracking receiver. VDFLL also outperforms the scalar tracking technique in the Doppler frequency estimation but at a lower order w.r.t to the code delay estimation, due to the slow variation in time of the ionosphere residuals. Moreover, these contour plots also proved our expectation regarding a certain correlation between the channel errors' and the satellite elevation angle: the higher the elevation angle is, the lower the code and carrier estimations are. It was interesting to observe the dependence of the Doppler frequency estimation on the bearing angle for both configurations. This is due to the Doppler frequency variation caused by the change of the vehicle orientation that is observed via the heading angle change.

The better VDFLL code and carrier frequency estimations w.r.t the conventional receiver are further translated in the navigation domain. Indeed, lower position and clock bias estimation errors and tighter covariance bounds are marked for the VDFLL architecture, when observing the PDF plots and statistics in Table 7-2, even with the reduction of the number of observations up to a minimum of 4 required measurements for the correct operation of the EKF filter. The proposed vectorized architecture outruns the scalar receiver even when referring to the velocity and clock drift estimations but in less evident manner compared to the position/clock bias values. The logic behind this behavior is strictly linked to the lower Doppler frequency errors due to the slowly amplitude changing of the ionosphere residuals, as mentioned in the channel comments above.

7.3. Scenario 2: Performance Assessment in Urban Environment

7.3.1. Objective

This section continues the performance assessment of the two receiver architectures but for a complete urban environment representative, comprising both the inclusion of the multipath channels' parameters from the DLR urban model into the GNSS signal emulator and the presence of the ionosphere residual errors. As previously stated in VDFLL algorithm description, the ionosphere residual errors affecting the tracking channels are estimated by the VDFLL navigation filter.

7.3.2. Scenario characteristics

The simulated reception conditions are that of an automotive car trajectory in multipath signal reception condition and in the presence of ionosphere residuals. During the reference car trajectory, in total 13 GPS and Galileo satellites are constantly in view and being tracked by the receiver, as it was illustrated in the skyplot from Figure 7-2.

The multipath reception conditions are generated by the DLR channel generation program described in section 6.2.2. Figure 7-7 illustrates the channel impulse response (CIR) by showing the multipath power delay profiles (PDPs) for each tracked GPS and Galileo channel along the urban car trajectory of ten minutes duration.

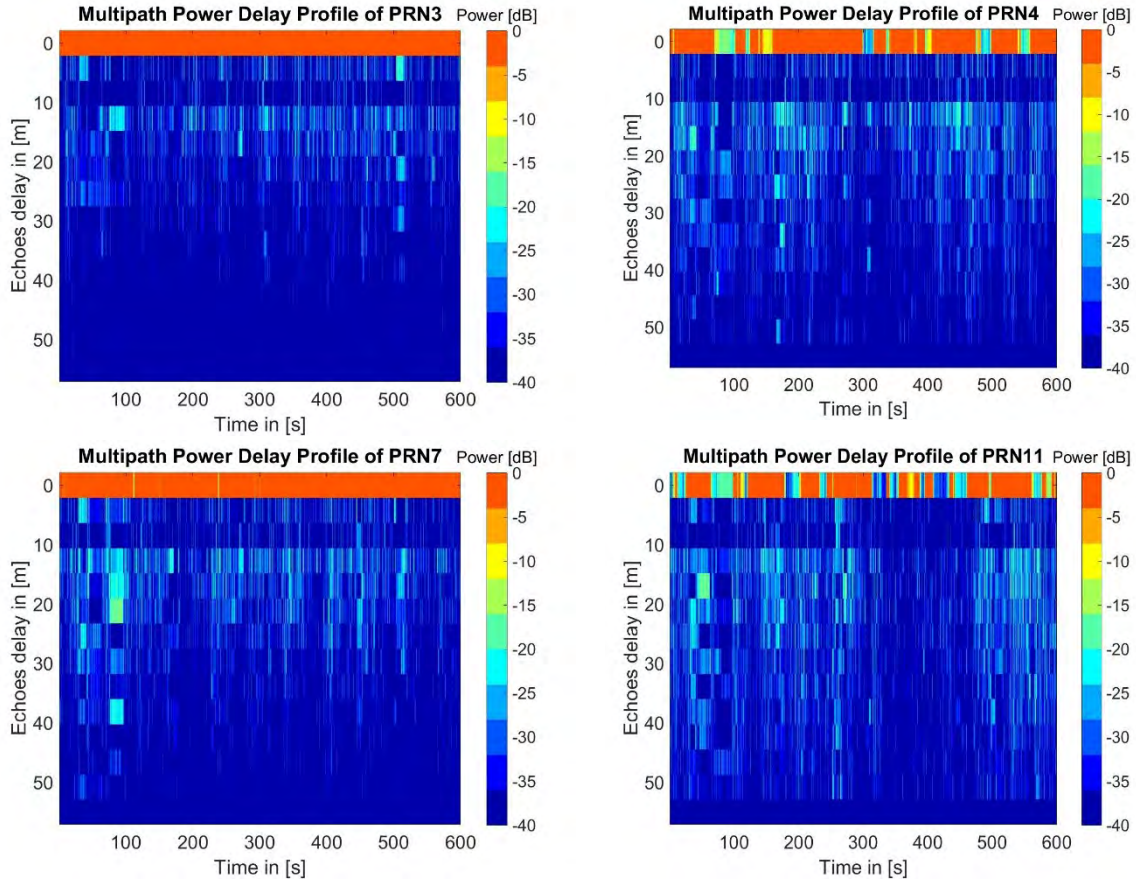

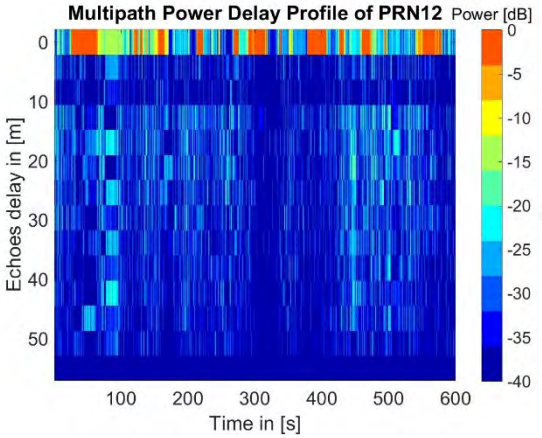
Multipath Power Delay Profile of PRN12 Power [dB]
Echoes delay in [m]
Time in [s]

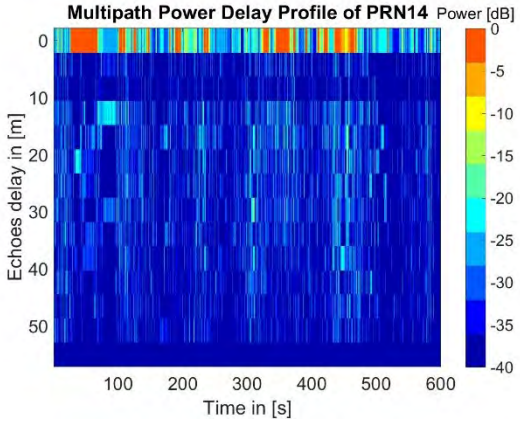
Multipath Power Delay Profile of PRN14 Power [dB]
Echoes delay in [m]
Time in [s]

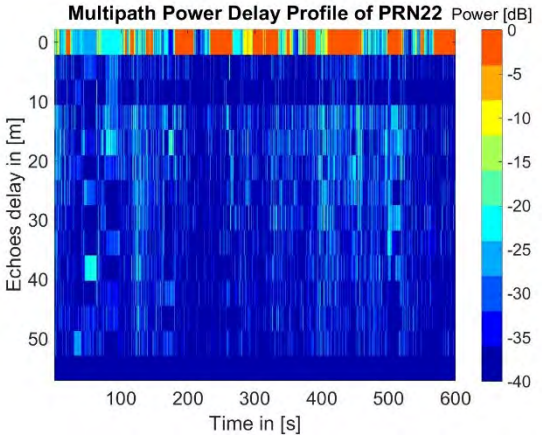
Multipath Power Delay Profile of PRN22 Power [dB]
Echoes delay in [m]
Time in [s]

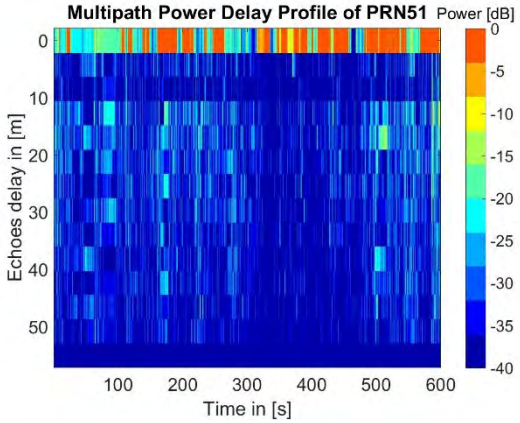
Multipath Power Delay Profile of PRN51 Power [dB]
Echoes delay in [m]
Time in [s]

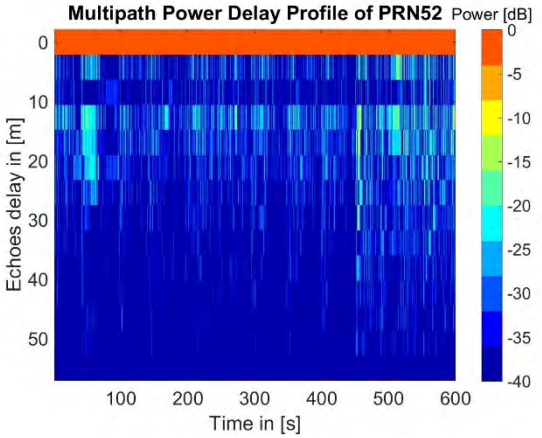
Multipath Power Delay Profile of PRN52 Power [dB]
Echoes delay in [m]
Time in [s]

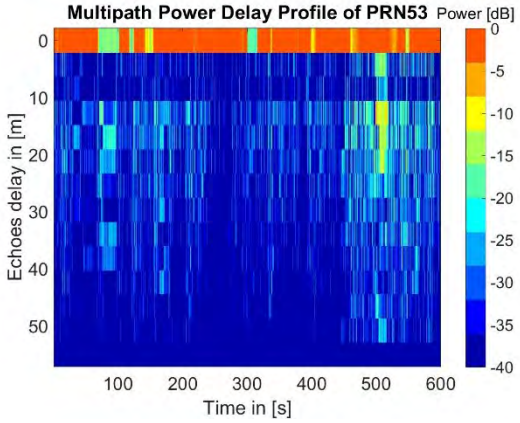
Multipath Power Delay Profile of PRN53 Power [dB]
Echoes delay in [m]
Time in [s]

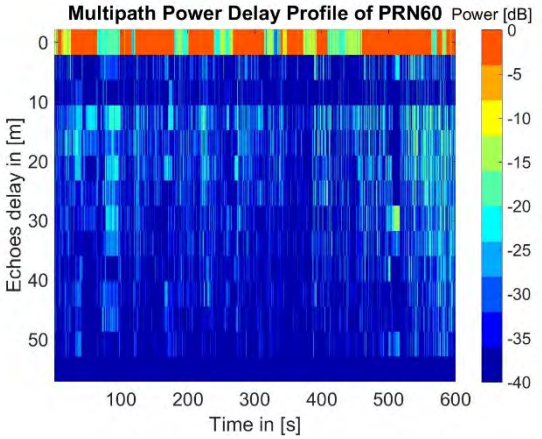
Multipath Power Delay Profile of PRN60 Power [dB]
Echoes delay in [m]
Time in [s]

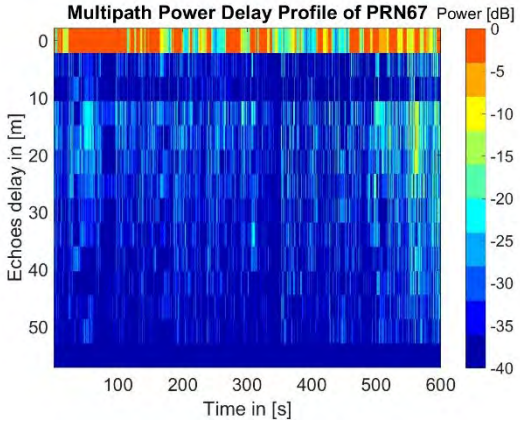
Multipath Power Delay Profile of PRN67 Power [dB]
Echoes delay in [m]
Time in [s]

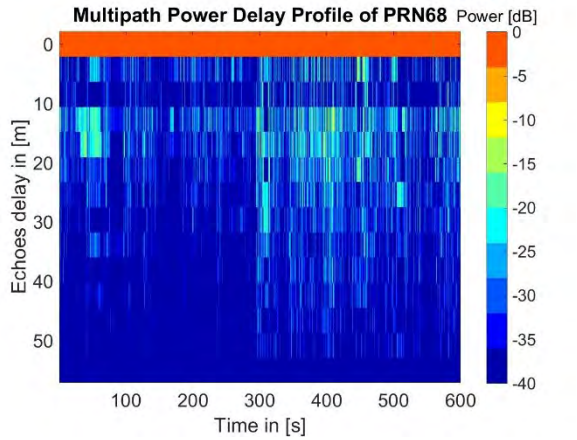

Figure 7-7. *The multipath PDPs for all the tracked satellites along the car trajectory.*

The PDPs show the attenuation of the received multipath echoes power and are represented in 2D figures that can be further interpreted as follows:

- *X axis*: denotes the channel evolution in time along the trajectory, expressed in $[s]$;
- *Y axis*: denotes the time difference, expressed in $[m]$ between the multipath echoes arrival with respect to the theoretical direct path signal. It must be noted that the delay is indeed presented in relative terms with respect to the theoretical time of arrival of the direct path at $0\ ns$;
- *Color*: is an indicator of the multipath echo's power attenuation w.r.t. the ideal open sky LOS power, which does not suffer any attenuation except for the ideal propagation loses that are only dependent on the signal carrier frequency and travelled distance.

The LOS and NLOS echoes information, comprising their amplitude, code delay, phase and Doppler frequency, are integrated in the signal emulator at the correlator output level according to the model provided in Eq. (6-9).

After observing the code delay statistics at the output of the DLR urban model, the code delay bin for the LOS ray has been chosen to include delays up to $5\ m$, whereas, all the other echoes exhibiting delays superior to that threshold are equally distributed in the NLOS code delay bins. Finally, the color code of the PDP plots goes from the dark blue, representing low multipath signal power (starting from $-40\ dB$), up to the highest signal power in the red label.

Therefore, the PDP represents a clear indicator of LOS and NLOS signal presence when observing the accumulated power in the near echo region (from $0 - 5\ m$). In other words, only the strong red color in this area denotes the LOS ray presence. Based on this distinction criteria, all the tracked satellites may be distributed into three different categories such as:

- *LOS satellites*: grouping those satellites characterized by the presence of LOS signals along the vehicle motion, such as: GPS PRN 3 and 7, and Galileo 52 and 68. These satellites are also the closest to the zenith and are less impacted by the urban obstacles and foliage;
- *Moderate LOS satellites*: including the satellites with varying LOS signal-to-NLOS echoes reception but still conserving the LOS dominance along most of the trajectory, such as: GPS PRN 4 and 11, and Galileo PRN 53 and 60;

- *NLOS satellites*: containing the satellites, whose multipath PDPs lack the presence of the direct LOS signal reception. GPS PRN 12, 14, 22 and Galileo PRN 51, 67 naturally fall into this category.

This satellite categorization is conserved and furtherly recalled in the following sub-sections.

7.3.3. Methodology

In this test scenario, only one simulation was conducted with the same car trajectory presented in section 7.1, in multipath and ionosphere residuals presence and with the same GPS/Galileo constellation geometry. As it was the case for the previous test, the EKF filter operation for the two architectures is initiated only after the convergence of the WLS-estimated position solution has been reached. Moreover, no knowledge of the ionosphere residuals is considered in the initialization step of the VDFLL EKF state vector (ionosphere residuals' states set to zero) and thus, the initial state covariance matrix is inflated by the residuals variance, similarly to the MC test in section 7.2.

7.3.4. Results

The following sub-section is dedicated to the provision of the comparison results in the navigation level, in terms of PVT errors along the trajectory, and further on code and carrier estimation errors along with their distribution pattern. The description of the results in both levels is concluded with their respective tables of statistics.

7.3.4.1. Navigation Level Analysis in Urban Environment

The number of GPS and Galileo LOS satellites in multipath condition along the car trajectory is illustrated in Figure 7-8. Herein, the LOS indicator for each satellite is defined by the LOS ray power ratio with the accumulated power of all the received echoes. In other words, the satellite is declared LOS when the LOS/NLOS echoes power ratio exceeds the threshold that in logarithmic scale is set to $-20\ dB$. Of particular interest are the two areas included in the red circle and dotted blue rectangle, which represent the sudden decrease of the number of LOS satellites in view. Moreover, the red area 1 is of double importance since it coincides both with the EKF filter initialization period and with the strongest outage event, leading to the presence of only three LOS satellites for the navigation solution computation.

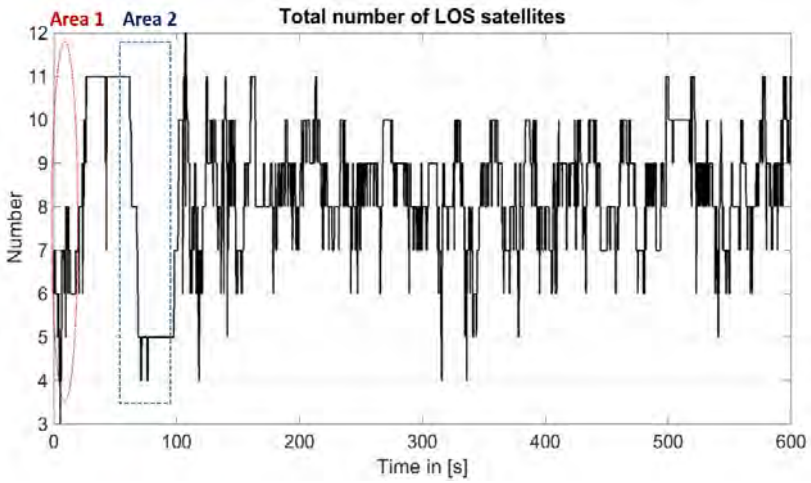

Figure 7-8. *GPS and Galileo constellations geometry in multipath condition for both architectures.*

The position and velocity error comparison between the scalar tracking (ST) + EKF positioning module and the VDFLL algorithm, both operating at $50\ Hz$ update rate, are presented in Figure 7-9 and Figure 7-10. Both figures present the EKF estimation errors along the entire trajectory in the vehicle frame, for the along track- in a) and cross track coordinates in b). Moreover, the blue and red dotted curves represent the $2 \cdot \sigma_{EKF}$ bounds, respectively for the VDFLL and ST receiver configurations, where σ_{EKF} is the estimation error covariance estimated by the Kalman filter. The position results while the car is driving through the downtown area are shown on the left side of the plots in Figure 7-9. Whereas, the right plots in the figures below show a magnified view of navigation solution errors inside area 1 with the objective of clearly viewing the EKF filter convergence interval.

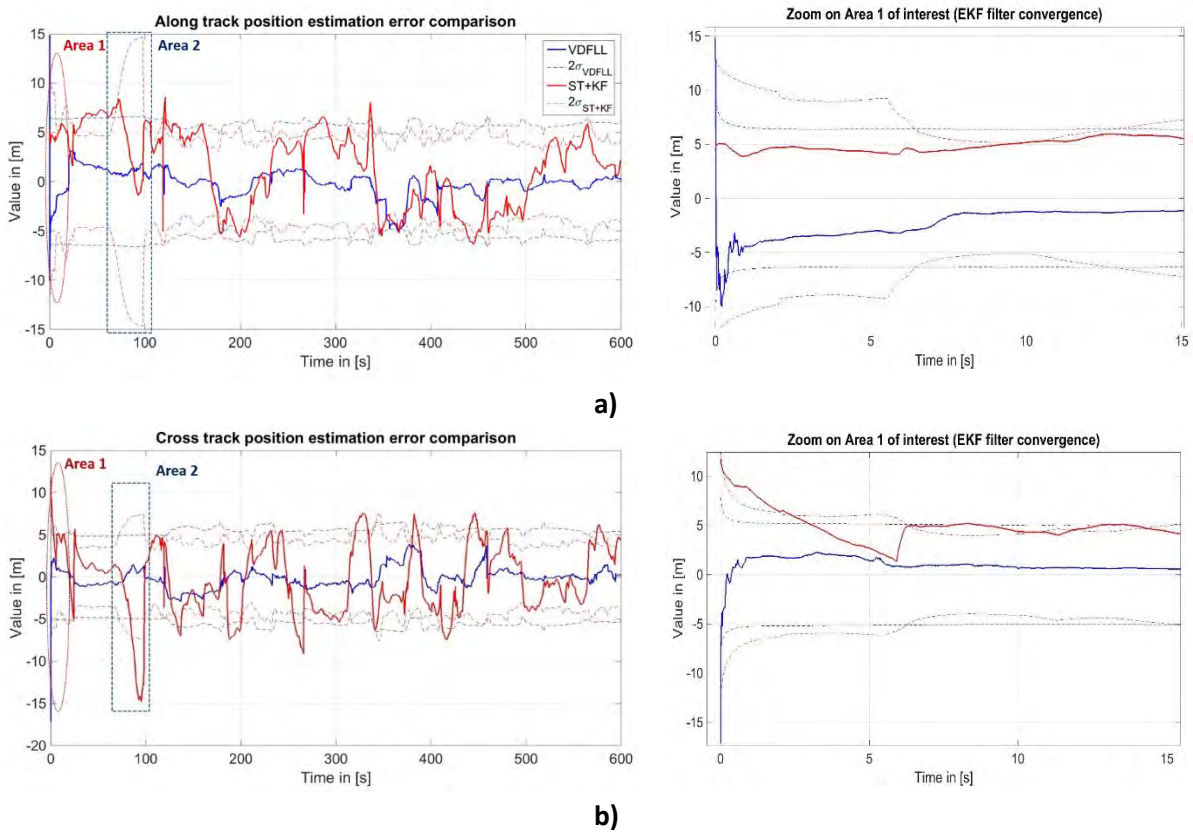

Figure 7-9. *Position performance overview in the presence of multipath and ionosphere residual errors (Scalar Tracking VS VDFLL).*

According to the position error evolution in time from Figure 7-9, three main observations can be made:

- Firstly, the VDFLL position estimation across all the car trajectory is more stable than the ST+KF estimation, which undergoes strong variations due to the lack of observability of the ionosphere residuals and to the multipath-introduced code delay errors;
- Secondly, the VDFLL covariance bounds estimated by the EKF filter constantly confine the estimation error, representing a clear indicator of the good filter tuning. On the contrary, the scalar receiver's position estimation is not perfectly bordered within the ST+KF $2 \cdot \sigma_{EKF}$ bounds as a result of unestimated biases still present in the navigation solution. These results are even confirmed by the position error statistics from Table 7-3 where it can be noted the

3 times lower VDFLL position error RMS both along and cross track w.r.t to the ST + EKF receiver (with a $4\ m$ position error RMS). Moreover, these findings can also be compared to the results obtained from the test in only multipath conditions in Appendix D.2;

- Thirdly, the fast VDFLL filter convergence after the initialization process, as illustrated in the zoomed view of area 1, proves its capability of decently estimating the ionosphere residuals contributions and therefore, reducing the position error. In fact, the zoomed plot of area 1 illustrates the fast VDFLL-estimated position convergence within 1 second that based on the EKF filter rate coincides with 50 measurement epochs. The along and cross track position error decrease for the WLS-estimated position to a nearly zero estimation error is due to the joint position and tracking estimation process achieved by the VDFLL algorithm.

Of particular interest is the position error comparison within the area 2 rectangle in the presence of only 4 LOS satellites, which coincides with the lowest number of observations that are fed to the EKF filter. This satellite outage event results in a large ST+KF estimated position error up to $13\ m$ in the across track coordinate (see Table 7-3). As a normal response to this event, the ST+KF covariance bounds are significantly increased to cope with the higher uncertainty toward the only four "good" measurements but that still include ionosphere residual errors. During this outage interval, the VDFLL filter performs a forward propagation of the state vector that later drives the code/carrier NCO updates in the feedback loop, aiding in this way the channel errors correction. As soon as the LOS satellite signals become available, the vector tracking algorithm can further correct the state vector error accumulated during the outage period. As expected when introducing more reliable pseudorange measurements, the position errors and their estimation uncertainties are reduced. This explains the quasi-irrelevant VDFLL position covariance increase.

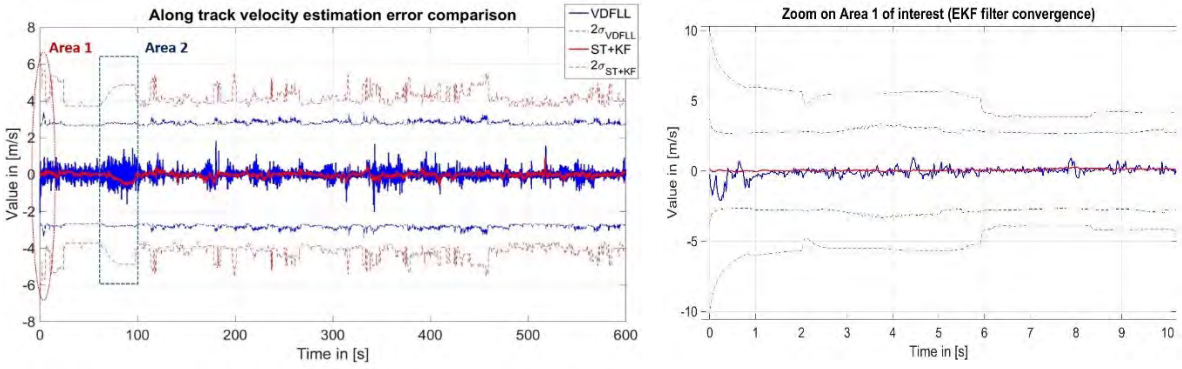

a)

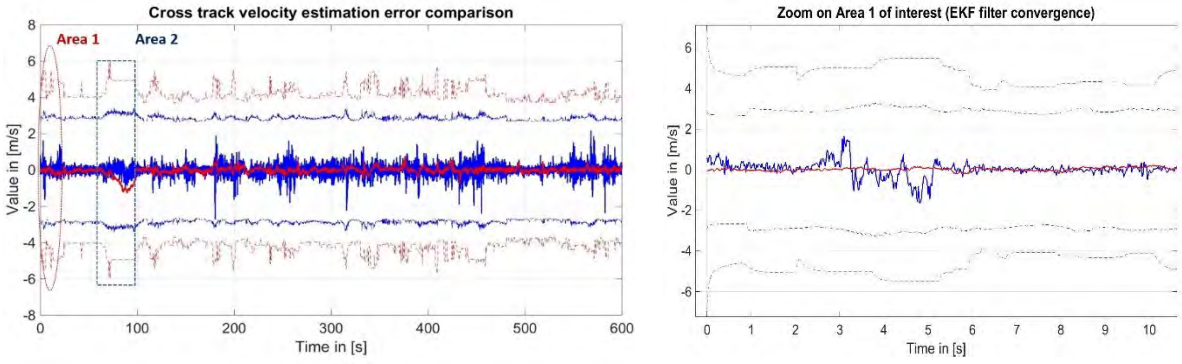

b)

Figure 7-10. *Velocity performance overview in the presence of multipath and ionosphere residual errors (Scalar Tracking VS VDFLL).*

Figure 7-10 illustrates the contribution provided by the ionosphere residual rates along with the multipath effect on the velocity estimation. Similarly to the previous section, the velocity estimation errors for the two receiver configurations are dominated by the noise and seem to follow zero-centered Gaussian distributions that is partially due to the 1st order Gauss-Markov distribution of the ionosphere residual errors. The VDFLL-estimated along and cross track velocities are noisier compared to the ST+EKF estimations, which is related to the use of frequency discriminators whereas PLLs are employed by the scalar receiver.

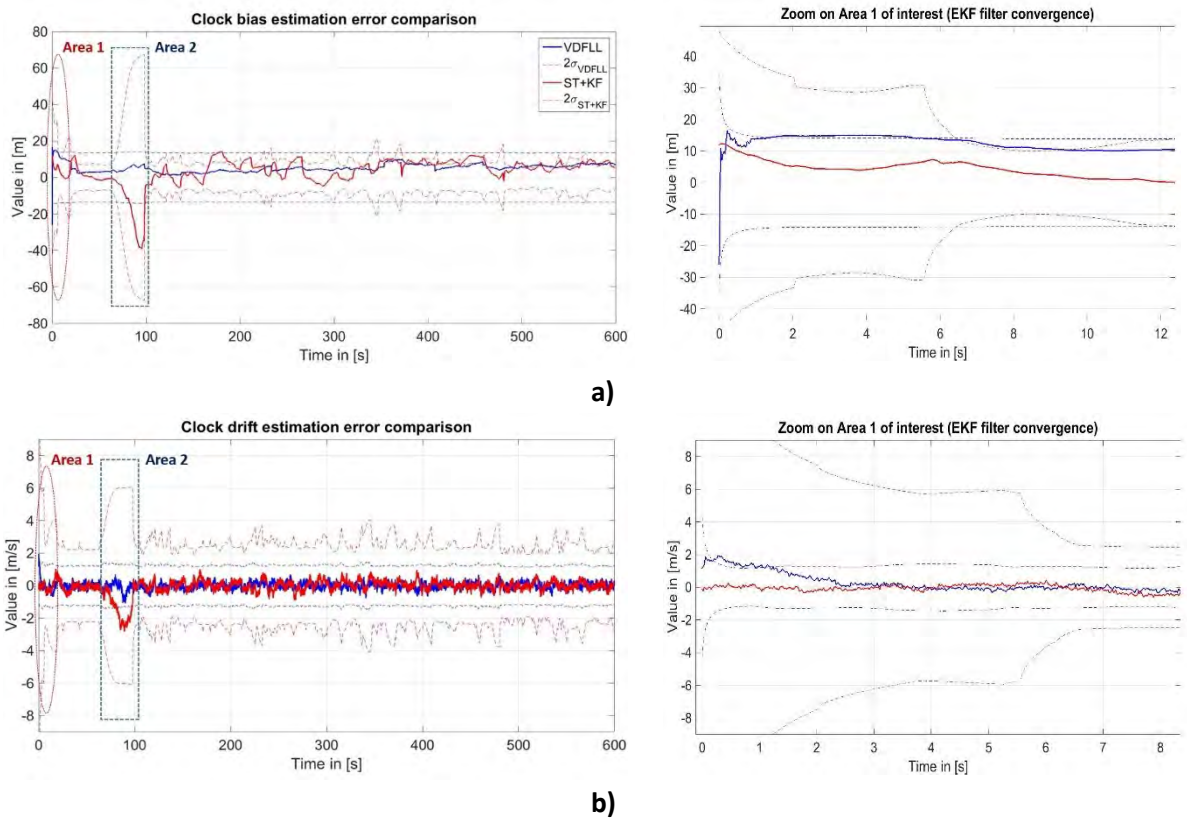

Figure 7-11. *User's clock states performance overview in the presence of multipath and ionosphere residual errors (Scalar Tracking VS VDFLL).*

Contrary to the ST+KF receiver operation mode, the proposed VDFLL technique ensures stable user's clock bias estimation during the overall trajectory, as shown in Figure 7-11. In the magnified view of the EKF filter initialization period, illustrated on the top right plot of Figure 7-11, it can be noted the fast VDFLL clock bias correction from the initial $20\ m$ error, coming from the WLS estimation, to a stable clock bias estimation at the $10\ m$ level. This non-zero convergence of the clock bias is majorly caused by the VDFLL principle of operation based on the joint tracking and navigation tasks that are performed by the EKF filter. This means that the error presence in the position estimation, which is used to generate the NCO update, inserts an error on the code delay estimation that is absorbed by the clock and ionosphere residual states since the filter cannot separate them.

Concerning the clock drift estimation performance, the same comments presented for the velocity terms are valid due to their relation embedded in the pseudorange rate measurement. Moreover, very small differences are noted between the two architectures in terms of velocity RMS and

percentiles bounds, referring to the statistics in Table 7-3. However, noisier estimations are observed from both receiver configurations w.r.t the performance analysis in multipath condition only, detailed in Appendix D.2. This noise addition is related to the presence of the ionosphere residual rate errors in the pseudorange rate measurements, which are linked to the velocity and clock drift states. Moreover, the reduction of locked satellites number occurring inside the area 2 window causes the increase of the clock drift error and its associated covariance for the scalar tracking receiver.

The navigation statistics results in the complete urban environment representative are illustrated in Table 7-3.

Table 7-3. *Navigation estimation error statistics in the presence of multipath and ionosphere errors.*

	VDFLL				Scalar Tracking (ST) + EKF			
	Mean	**RMS**	**95 %**	**99 %**	**Mean**	**RMS**	**95 %**	**99 %**
Position states								
Along track position error $[m]$	0.2	1.4	3.1	4.6	1.5	4.2	6.9	8.6
Cross track position error $[m]$	0.1	1.2	2.5	3.5	0.5	4.3	7.2	13.2
Velocity states								
Along track velocity error $[m/s]$	~0	0.2	0.5	0.8	~0	0.2	0.3	0.5
Cross track velocity error $[m/s]$	~0	0.3	0.6	0.9	~0	0.2	0.4	1.1
Clock states								
Clock bias error $[m]$	2.2	3.7	7.4	11.2	3.6	8.3	12.2	35.2
Clock drift error $[m/s]$	~0	0.2	0.4	0.7	~0	0.5	0.7	2.3

Once more, the VDFLL capability in correctly estimating the navigation solution in multipath and ionosphere residual errors presence is confirmed within a $95\ \%$ position error of $3\ m$. Better clock bias estimation statistics are also observed for the VDFLL technique with an approximately 3 times lower RMS w.r.t the scalar receiver configuration.

7.3.4.2. Channel Level Analysis in Urban Environment

The performance analysis between the Scalar Tracking (ST) and VDFLL is now extended to the signal level, expressed by the code delay and carrier frequency estimation errors along the car trajectory. Recalling the LOS/NLOS satellites' categorization based on their PDP profiles, the tracking channel errors' along with their errors distribution are presented for the VDFLL and ST techniques for a LOS, moderate LOS and NLOS satellite in this exact order from Figure 7-12 to Figure 7-14.

For a better understanding of the channel errors comparison, the code delay and carrier frequency errors distributions for each satellite category are also illustrated. Furthermore, the quantile-quantile (Q-Q) plots are also used in this thesis for the channels' error characterization, knowing that the Q-Q plots represent the best graphical tool widely used in statistics to identify the probability distribution of the variables under study. The Q-Q plot is a probability plot capable of comparing two probability distributions by plotting their quantiles against each other. When the points of the Q-Q plot lie on the line $y = x$, this means that two distributions being compared are identical.

7.3.4.2.1. Channel errors comparison for a LOS satellite

In this subsection, the performance comparison in the channel level is performed for the LOS GPS PRN3 satellite, characterized by the red color in its PDP profile from Figure 7-7 and situated at a high elevation angle of 84°, referring to the skyplot in Figure 7-2.

The code delay error comparison for the LOS GPS PRN3, provided in the left plot of Figure 7-12 a), confirm the VDFLL better performance expectation w.r.t the ST loop that is especially manifested concerning the code delay estimation. This is purely related to VDFLL's principle of operation, for which the code delay correction is generated from the estimated user's position. Logically, a lower position error leads to a more accurate code delay estimation, which becomes even more evident for high-elevation LOS satellites. However, similar carrier frequency estimation errors are observed for the two techniques, as depicted in the right plot, due to the low ionosphere effect on high elevation satellites and also, related to the lower reflection and diffraction probability of the LOS ray for high elevation satellites.

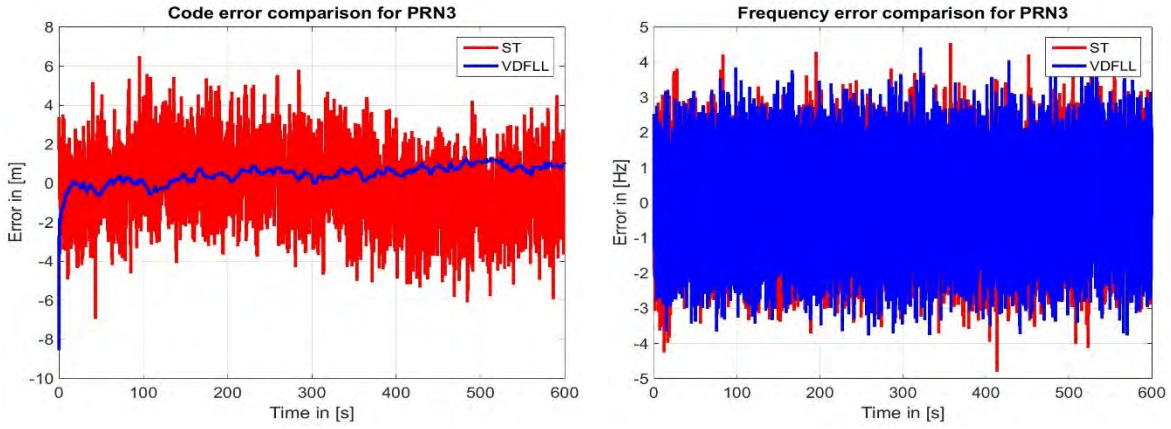

a)

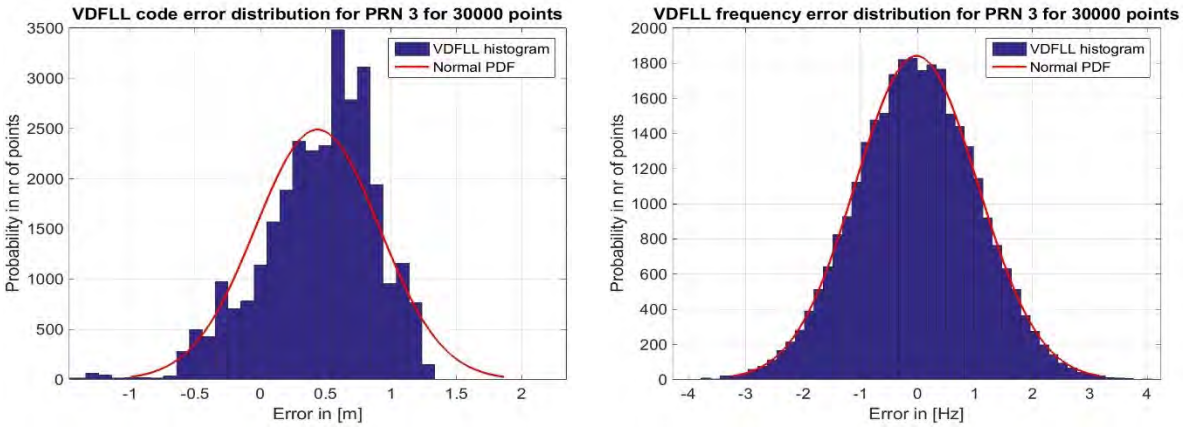

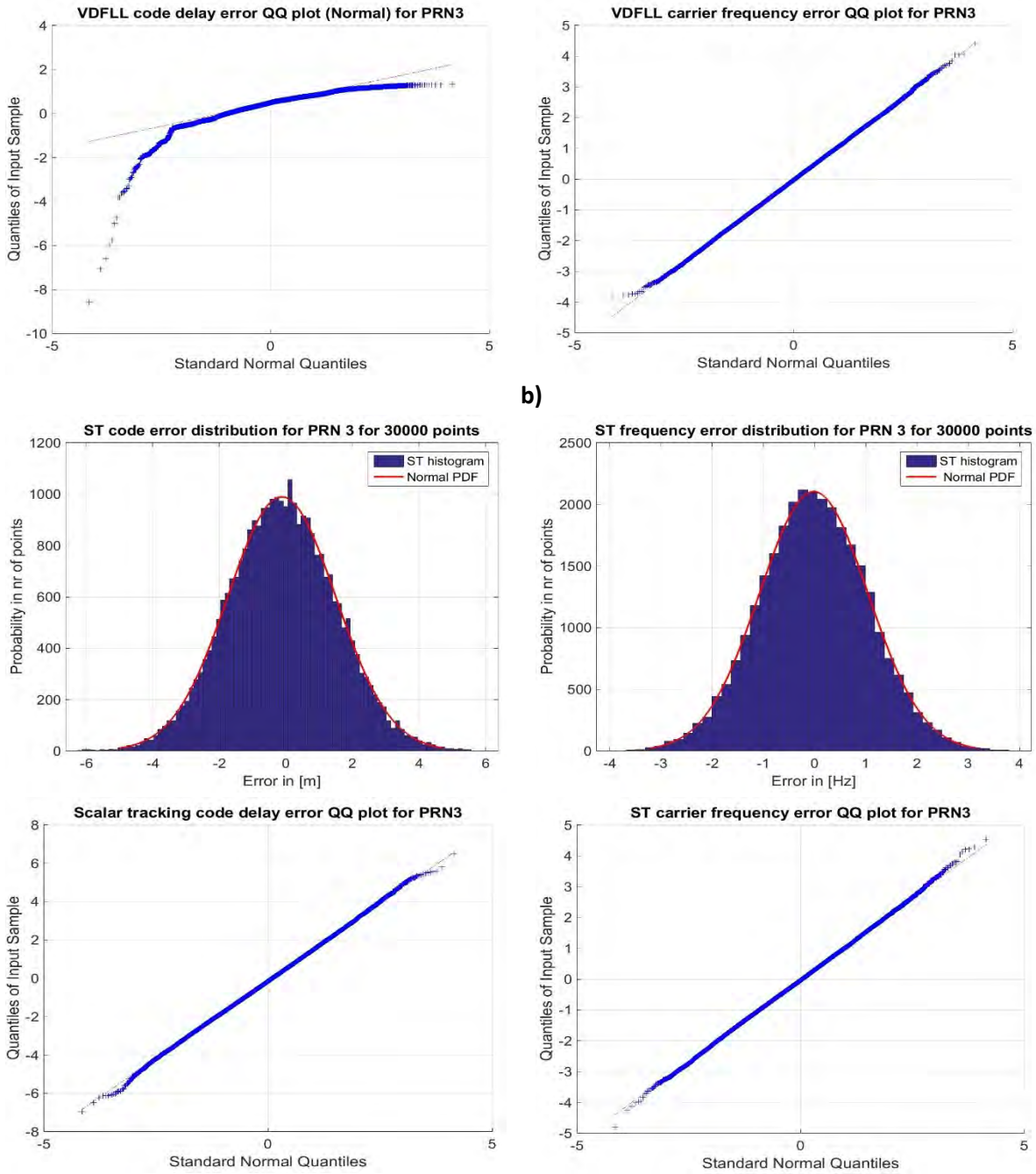

Figure 7-12. *Performance comparison in the tracking channel level for one LOS satellite in ionosphere and multipath reception condition.*

Regarding the channel errors' distribution for the VDFLL and ST architectures, shown respectively in Figure 7-12 b) and c), it may be noticed that the best distribution fit for the VDFLL- and ST- estimated code/carrier errors for a LOS satellite is the normal (Gaussian) distribution that is even more marked for the carrier estimation error distributions. The VDFLL code error histogram and more precisely its Q-Q plot, provided in the left plots of Figure 7-12 b), show a deformation of the Gaussian distribution. This can be explained by the translation of the biased position and the residual errors, remaining from the ionosphere residual estimation, from the position domain to the channel level via the EKF-estimated code NCO update. On the contrary, the Gaussian distribution property of the ST-estimated

code delay error remains untouched since the channel tracking and position computation tasks are separately performed.

7.3.4.2.2. Channel errors comparison for a moderate LOS satellite

Now, the channel level performance assessment is extended to a moderate LOS satellite (ex: GPS PRN4), which provides the LOS ray during most of the car trajectory as depicted in the PDP profile from Figure 7-7 and situated at a mid-elevation altitude of 52°, referring to the skyplot in Figure 7-2.

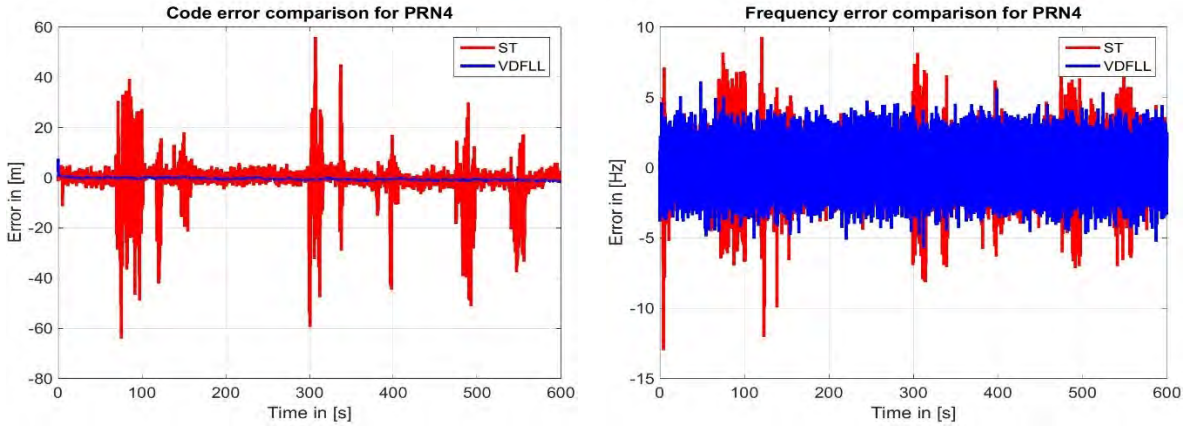

a)

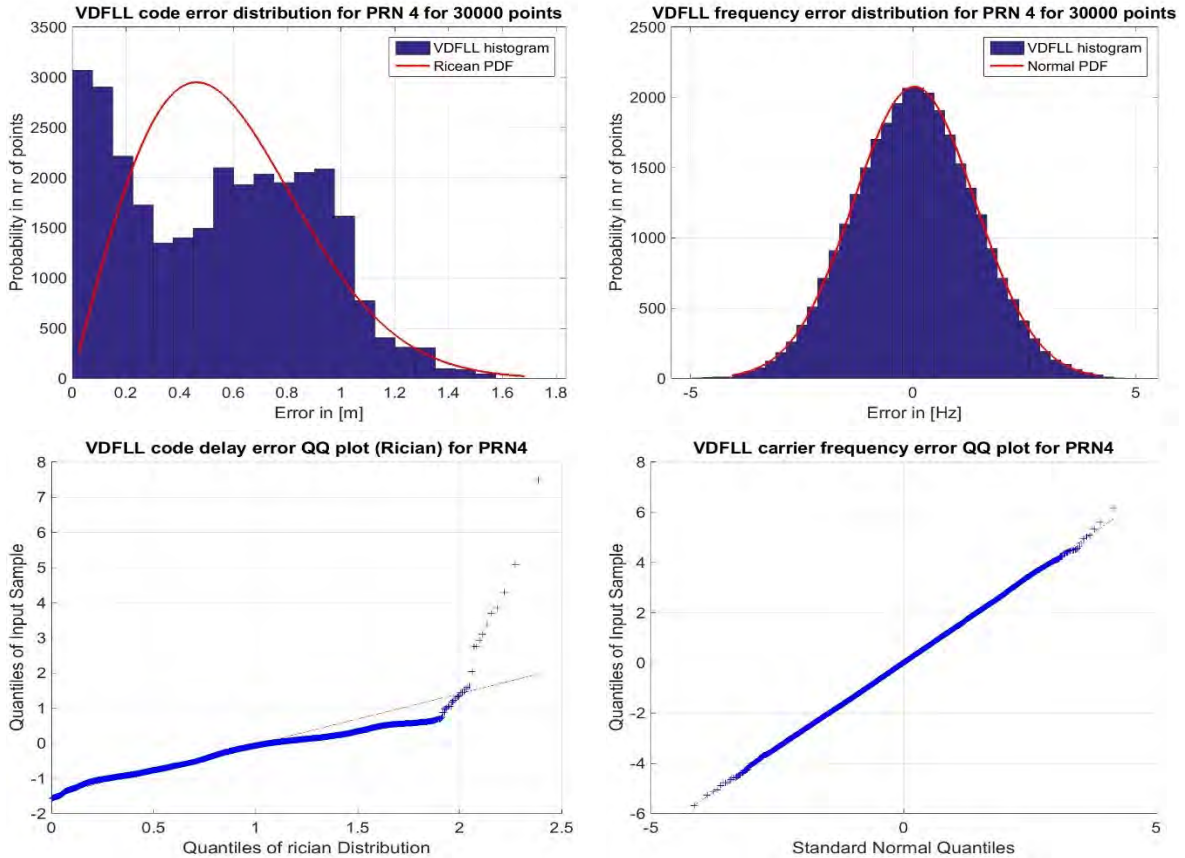

b)

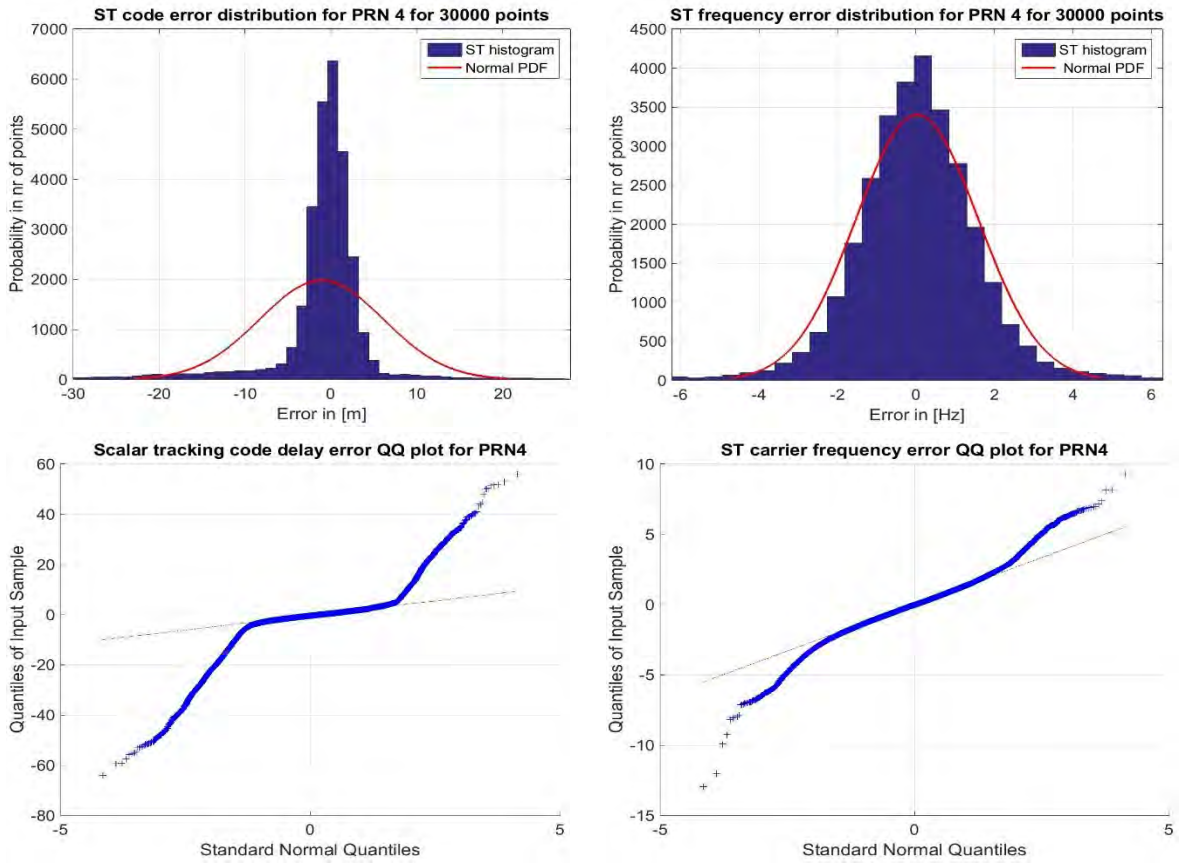

c)

Figure 7-13. *Performance comparison in the tracking channel level for one moderate LOS satellite in ionosphere and multipath reception condition.*

The VDFLL supremacy becomes evident for both the code and carrier tracking processes of a moderate LOS satellite, characterized by frequent LOS to NLOS transitions along the trajectory, as shown in Figure 7-13. The LOS signal blockage defined by the $40\ dB$ signal power drop and by the green/blue PDP regions at $100\ s$, $300\ s$ and around $475\ s$ in Figure 7-7, is reflected by significant code delay errors increase for the scalar tracking operation, as it can be seen in the left plot of Figure 7-13 a). On the contrary, the accurate and stable VDFLL code delay estimation is assured even during these signal power drops. The VDFLL stability is confirmed even for the Doppler frequency estimation but at a lower magnitude w.r.t the code delay estimation. This VDFLL superiority is achieved by the channel aiding characteristic of the VDFLL technique.

Even though the VDFLL code and carrier estimation are far more stable compared to the ST configuration, the LOS blockage occurrences introduce significant code delay and carrier frequency biases that affect the distribution function of the two architectures, as illustrated in Figure 7-13 b) and c). Indeed, the Gaussian distribution still persists for the ST code- and frequency errors in the LOS signal presence but is totally altered during LOS signal blockages, as shown in Figure 7-13 c). The definition of the best distribution fit to the VDFLL code and frequency errors is not at all an easy task due to the difficulty in determining the exact mathematical relation concerning the channel's coupling via the EKF-estimated position. However through several tests, the Rician bivariate distribution is the only known distribution that remotely fits the VDFLL code error distribution, as illustrated in the left plots from Figure 7-13 b). Moreover, the VDFLL frequency estimations are noisier due to the Gaussian-

distributed ionosphere residual rates that are expressed as the derivative of the 1st order Gauss-Markov ionosphere residual process.

7.3.4.2.3. Channel errors comparison for a NLOS satellite

The last performance comparison, regarding the code and carrier estimation errors for the two receiver architectures, is dedicated to the pure NLOS satellite category. Observing the multipath PDP profile from Figure 7-7, the Galileo PRN 51 does represent one of the worst tracked satellite that passes recurrently in loss-of-lock condition.

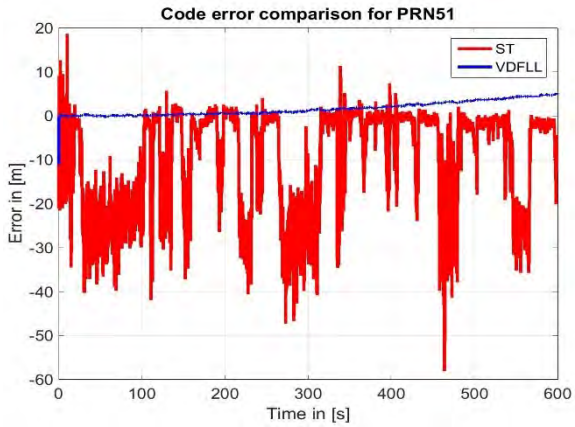

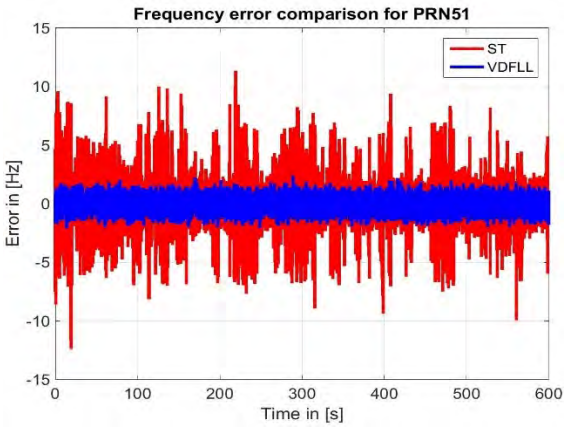

a)

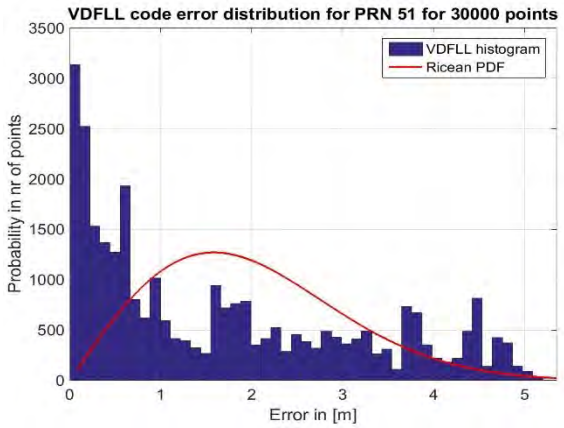

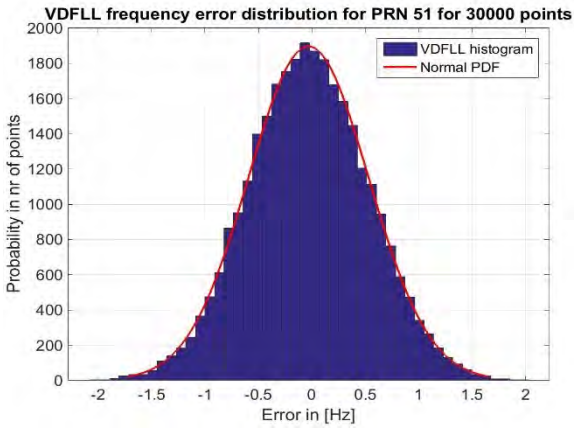

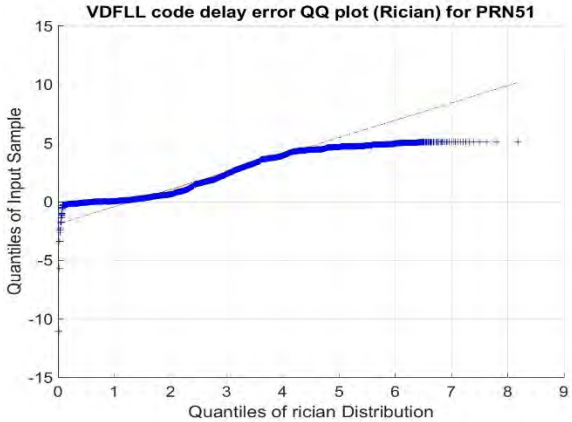

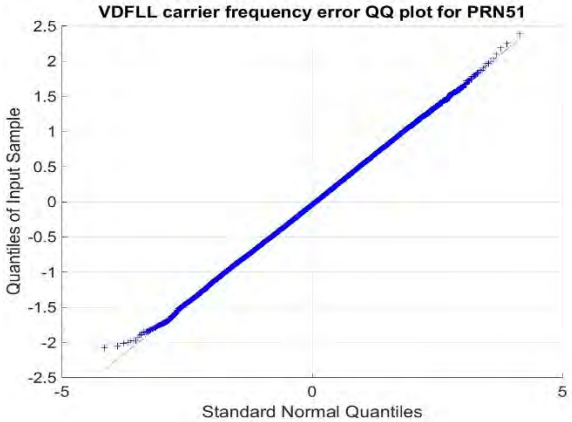

b)

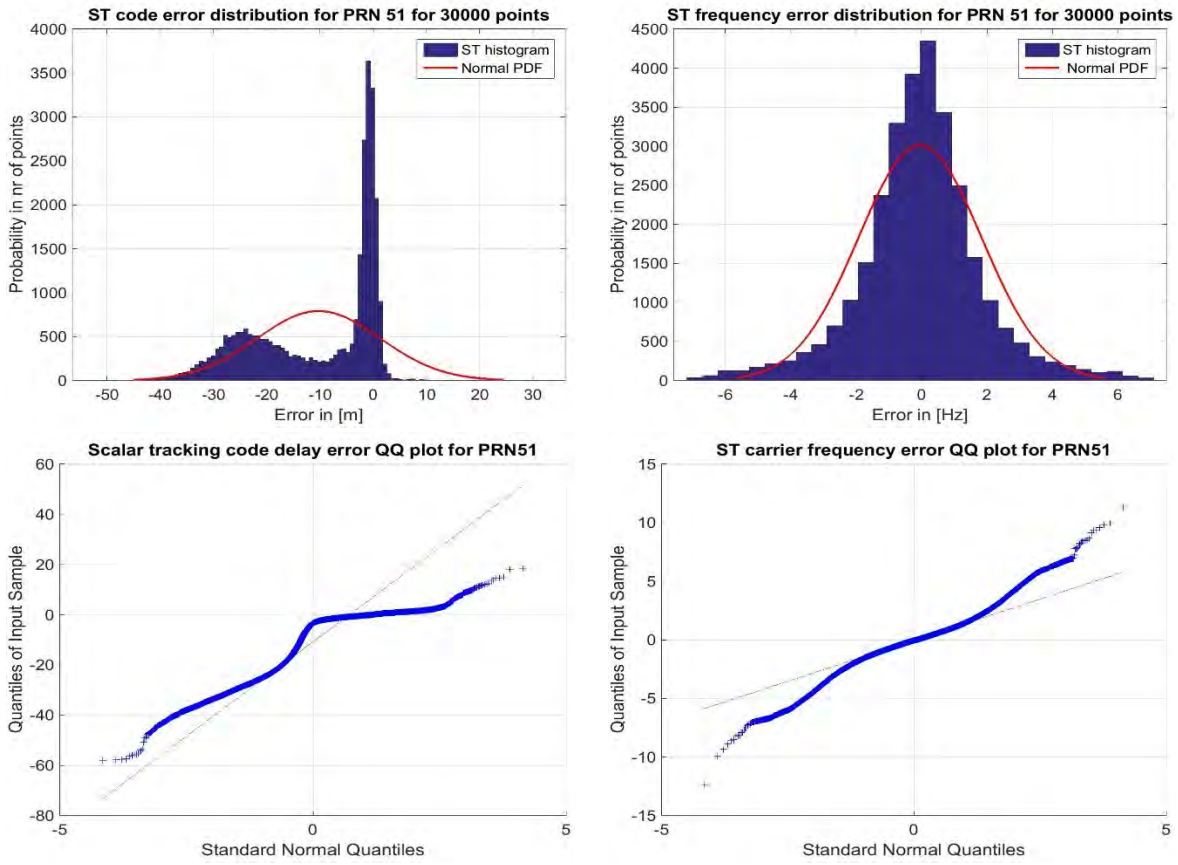

c)

Figure 7-14. *Performance comparison in the tracking channel level for a NLOS satellite in ionosphere and multipath reception condition.*

Based on the multipath PDP profile of Galileo PRN51 in Figure 7-7, three major and with large duration satellite blockages may be observed in the first $100\ s$, after $300\ s$ and at around the $375\ s$, with the last event representing the shortest LOS-to-NLOS transition but characterized by the highest power decrease up to $-40\ dB$. These strong satellite blockage events are clearly distinguished by the increase of the code delay and carrier frequency (at a lower magnitude) estimation errors for the scalar tracking receiver, illustrated by the red curve in Figure 7-14 a). In the scalar tracking configuration, the NLOS satellite tracking process is interrupted after the lock detection test failure, which triggers the start of the $1\ s$ hot re-acquisition process according to the model provided in section 6.1.2. Indeed, the code loss-of-lock condition occurs when the code delay error exceeds the discriminator chip spacing, which is set to $0.5\ chips = 149\ m$ for GPS L1 and $0.2\ chips = 58\ m$ for the Galileo E1 signals as provided in Table 7-1. Returning to the code delay estimation error plot in Figure 7-14 a), it can be seen that these loss-of-lock event takes place one single time for the Galileo PRN51 at the 375^{th} epoch. These loss-of-lock occurrences do also seriously affect the ST code and frequency errors histogram and therefore, transforming the ST Q-Q plots which are less Gaussian compared to the moderate LOS satellite due to the NLOS-induced biases, as illustrated in Figure 7-14 c).

On the contrary, as it can be pointed out in Figure 7-14 a), the code/carrier tracking estimation process is continuously carried on by the VDFLL architecture (in blue) based on the mutual channel aiding via the NCO feedback loop. Hence, a VDFLL code estimation error increase is noticed after the occurrence

of the satellite blockage in the middle of trajectory (at $300\ s$). Whereas, no significant effects of the NLOS transition are observed in the frequency estimation.

7.3.4.2.4. Channels' errors statistics

The performance comparison in terms of channel error statistics in the presence of multipath and ionosphere residuals, for the three LOS, moderate LOS and NLOS satellites presented above, are provided in Table 7-4.

Table 7-4. *Channel error statistics in the presence of multipath and ionosphere errors.*

	Vector Tracking (VT)				Scalar Tracking (ST)			
	Mean	**RMS**	**95 %**	**99 %**	**Mean**	**RMS**	**95 %**	**99 %**
Category 1: LOS satellites (Ex: GPS PRN 3)								
Code error $[m]$	0.4	0.6	1.3	1.5	0.1	1.6	3.3	4.3
Frequency error $[Hz]$	~0	1.1	2.1	2.7	~0	1	2.2	2.9
Category 2: Moderate LOS satellites (Ex: GPS PRN 4)								
Code error $[m]$	0.5	0.9	1.6	1.7	0.9	8.1	19.3	36.4
Frequency error $[Hz]$	~0	1.4	2.7	3.5	~0	1.6	3.1	5.2
Category 3: NLOS satellites (Ex: Galileo PRN 51)								
Code error $[m]$	1.7	2.2	4.1	4.8	9.9	15.8	31.2	38.5
Frequency error $[Hz]$	~0	1.9	2.3	2.9	~0	1.9	4.2	6.5

The first remark that can be made is the quasi-equivalent carrier frequency estimation performance between the two architectures for the LOS and moderate LOS satellites, but with a more accurate frequency estimation from the VDFLL concerning the NLOS channels. However, striking performance differences are observed in the code delay estimation between the VDFLL and ST techniques, with the former ensuring a stable code delay estimation even when tracking pure NLOS satellites. Indeed, the VDFLL code delay estimations are nearly 10 times more precise w.r.t the scalar tracking operation mode. This represents an evident confirmation of the channel aiding characteristic of the VDFLL algorithm and also its capability in estimating the ionosphere residuals.

7.3.4.2.5. VDFLL Ionosphere residuals' estimation performance

The detailed comparison in the channel level cannot be considered complete without verifying the VDFLL capability in estimating the ionosphere residuals and following their evolution in time. To this scope, the VDFLL-estimated ionosphere residual evolution in time (in blue) compared to the true one (in black) on the left and the ionosphere residual error covariance for a LOS, a moderate LOS and a NLOS satellite on the right side are illustrated in Figure 7-15.

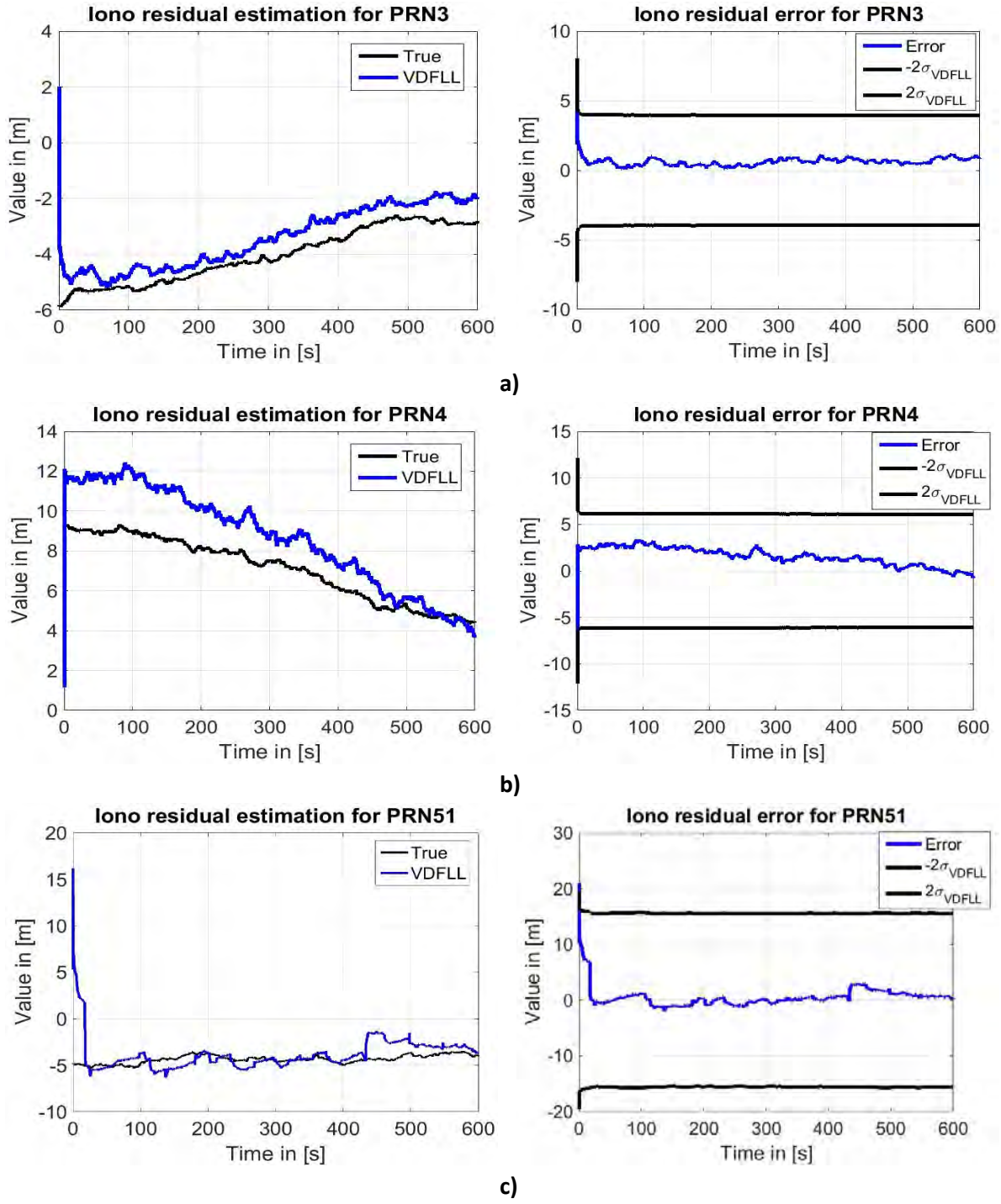

Figure 7-15. *VDFLL ionosphere residual error estimation for a:* ***a)*** *LOS,* ***b)*** *Moderate LOS and* ***c)*** *NLOS satellite.*

Observing the plots from Figure 7-15, it can be noticed the fast convergence of the VDFLL-estimated ionosphere residual states to the true ionosphere residuals, even without any prior knowledge of these residuals in the VDFLL EKF initialization step. Furthermore, the VDFLL technique is capable of following the ionosphere residual evolution in time, regardless of the LOS/NLOS satellite category, and correcting them up to a certain level in the pseudorange measurements. Nevertheless, certain biases of around 2 m that are illustrated in the right error plots for the moderate LOS and NLOS satellite from Figure 7-15 b) and c), still remain after the ionosphere residual estimation. This result is expected due

to the difficulty in observing the ionosphere residuals as separate states from the pseudorange measurements.

7.3.5. Conclusions on Scenario 2

This section focused on the performance assessment in the navigation and channel level of the dual-constellation GPS/Galileo VDFLL and scalar tracking receiver configurations in urban environment, characterized by the multipath signal reception and the ionosphere residuals presence. In this scenario, one simulation was conducted with the urban car trajectory shown in Figure 7-1 and by feeding at the GNSS emulator's correlator output level the multipath data generated from the urban channel model defined in section 6.2.

The results showed the VDFLL superiority in the navigation domain, with an emphasis on the position and clock bias estimation. Indeed, nearly three times lower position and clock bias estimation error fluctuations in time were observed for the VDFLL architecture w.r.t the scalar receiver configuration, also confirmed by the RMS error values in the table of statistics. Furthermore, the VDFLL reactivity was noted during satellite outage intervals that are characterized by a reduction of the number of the observations. During these intervals, an accurate navigation solution estimation is assured by the VDFLL filter thanks to the code/carrier NCO updates driven by the position and velocity estimations. Slightly better velocities and clock drift estimations are obtained from the vector tracking receiver w.r.t the scalar tracking configuration, related to the limited multipath impact on the Doppler measurements and also to the slow variation of the ionosphere residuals.

The performance comparison was further extended to the code and carrier estimation analysis along with their error statistics for the LOS, moderate LOS and NLOS satellite categories, defined according to the received multipath signal power illustrated via the Power Delay Profiles (PDPs). The VDFLL tracking robustness becomes evident especially in the code delay tracking for moderate LOS and NLOS satellites that experience large signal power drops. During these satellite blockage intervals, the scalar code tracking process is interrupted due the code loss-of-lock and the hot $1\ s$ re-acquisition process is directly started. On the contrary, the tracking process is continuously performed by the VDFLL receiver based on the channel aiding. The channel error statistics illustrated approximately 10 times more precise code delay estimations w.r.t the scalar tracking operation mode when referring to the NLOS satellites. However, nearly-equivalent carrier frequency estimations are observed between the two architectures when tracking LOS and moderate LOS satellites.

7.4. Scenario 3: Performance Assessment in Severe Urban Conditions

7.4.1. Objective

The last performed test aims at the performance comparison of the two receiver configurations in severe urban conditions, characterized by long satellite outage intervals that are translated into reduced number of observables fed to the navigation filters. Indeed, this "stress test" is conducted with main objective in testing the limits of the VDFLL algorithm both in the navigation and channel level.

7.4.2. Scenario characteristics

Herein, the severe urban conditions are simulated by using only the GPS L1 signals that are still under multipath reception and in the presence of ionosphere residual errors. The GPS constellation geometry used in this test along the same urban car trajectory is shown in Figure 7-16.

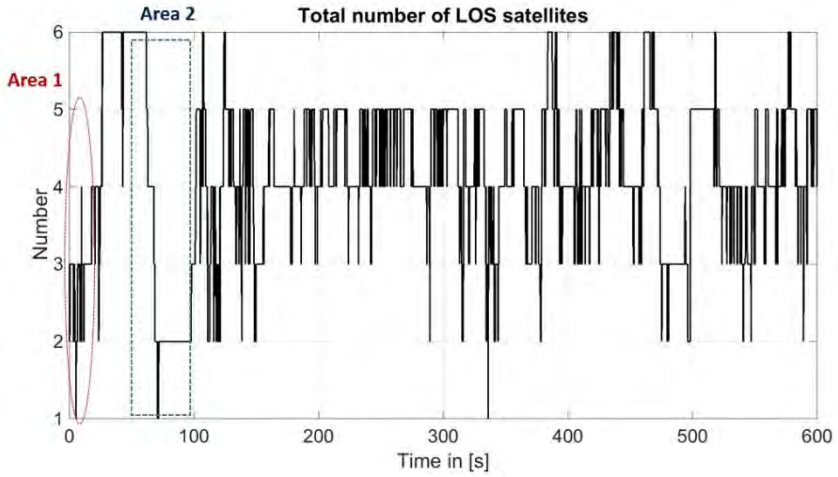

Figure 7-16. *GPS satellites visibility in harsh urban conditions.*

As in the previous sections, the navigation performance analysis will be mostly focused on two regions along the car trajectory, which are illustrated by the red circle and dotted blue rectangle and that are representative of harsh urban conditions. As it can be seen, only one LOS satellite is being tracked by the two architectures in the two regions of interest (area 1 and 2).

7.4.3. Methodology

Similarly to the previous test scenario, only one simulation was conducted with the same car trajectory presented in section 7.1, in multipath and ionosphere residuals presence but this time only the GPS constellation is active in order to limit the number of observations. Again, the EKF filter operation starts after the WLS position solution convergence and for the VDFLL EKF filter, the initial residual states are supposed to be unknown and therefore, set to zero.

The particularity of this last test relies on the implementation of two different VDFLL operation modes. The first VDFLL operation mode is the same one used in the previous, based on the “feed all measurements” principle, where all the pseudoranges and Doppler measurements coming from both LOS and NLOS satellites are included in the VDFLL navigation filter. Whereas, the second operation mode consists on feeding to the EKF filter the measurements coming from only “good” satellites. This approach is called the *satellite selection* and is proposed within the objective of increasing the VDFLL efficiency in these harsh urban conditions. The block diagram representation of the satellite selection technique is shown in Figure 7-17.

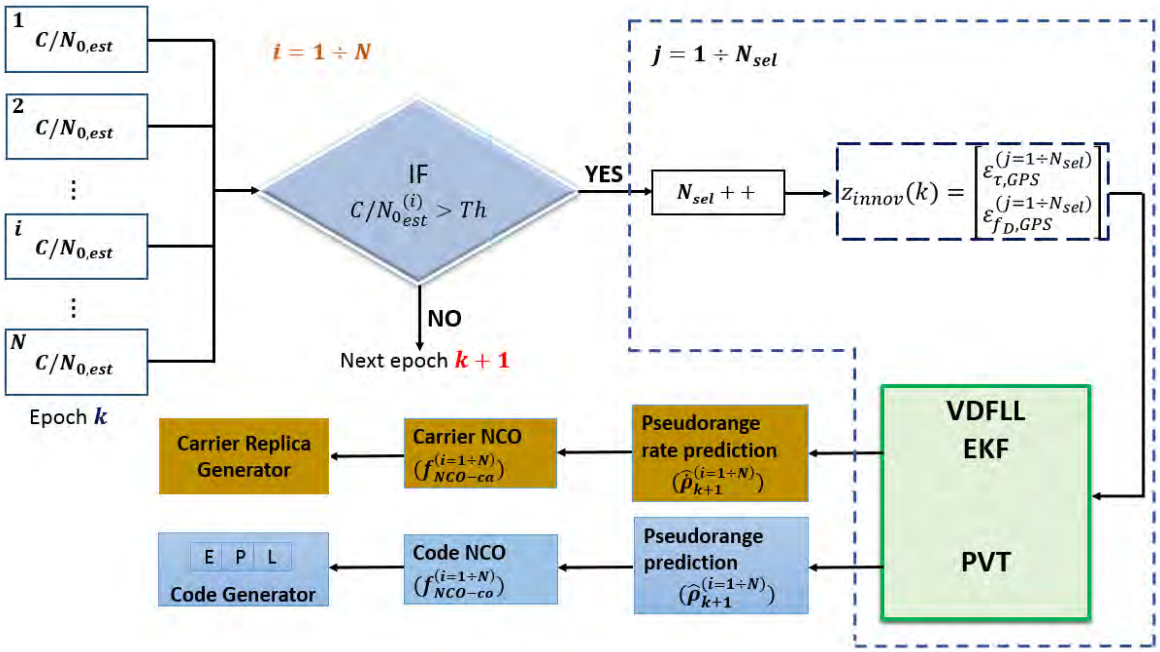

Th – threshold

N – Total number of satellites

N_{sel} – number of selected satellites

Figure 7-17. *Block diagram representation of the satellite selection technique.*

The satellite selection technique basically consists on feeding into the EKF filter the code and carrier innovations, included in the z_{innov} vector, from only a set of chosen (selected) satellites that have successfully passed the C/N_0 test. In other words, only those satellites having an estimated carrier-to-noise ration that exceeds the chosen threshold of $25\,dB-Hz$, which represents the urban environment indicator according to [Seco-Granados et al., 2012], will be further used for the position estimation. Therefore, the VDFLL EKF state vector innovation process and navigation solution estimation is driven only by the "best" tracked satellites $(j = 1 \div N_{sel})$ knowing that the satellites with the higher C/N_0 estimation are more likely to represent LOS satellites. Thus, a reduction of the position error also limits the channels' error flow via the NCO feedback loop to all the tracked satellites. Finally, this approach significantly increases the accuracy and reliability of the navigation solution by trusting its navigation and channels estimation tasks only to the LOS satellites, which are indeed less susceptible to the measurements biases.

7.4.4. Results in harsh urban environment

Following the same organization as in the previous sections, the navigation performance analysis will be mostly focused on two regions along the car trajectory, which are illustrated by the red circle and dotted blue rectangle that are representative of harsh urban conditions. As it can be seen, only one LOS satellite is being tracked (while the remaining 6 satellites are in NLOS conditions) by the two architectures in the two regions of interest (area 1 and 2).

7.4.4.1. Navigation Level Analysis

The performance comparison results between the scalar and VDFLL receiver architectures in the navigation level are jointly presented for the “feed all” and “satellite selection” VDFLL operation modes. This approach allows a better and detailed analysis of the pros and cons provided by these two configurations. Furthermore, only the position and clock bias estimation errors are herein analyzed since they represent the majorly effected states from the multipath and ionosphere residuals, as it was seen in the previous test scenario.

7.4.4.1.1. Results under no satellite selection operation for the VDFLL

The position results along the car trajectory, where no satellite selection operation is performed for the VDFLL architecture, are illustrated for the along and cross track coordinates on the left side of Figure 7-18 a) and b), respectively. Whereas, the top and bottom right plots illustrate a zoomed view of navigation solution errors inside area 1 and 2, denoting the EKF filter initialization period and the satellite outages, respectively.

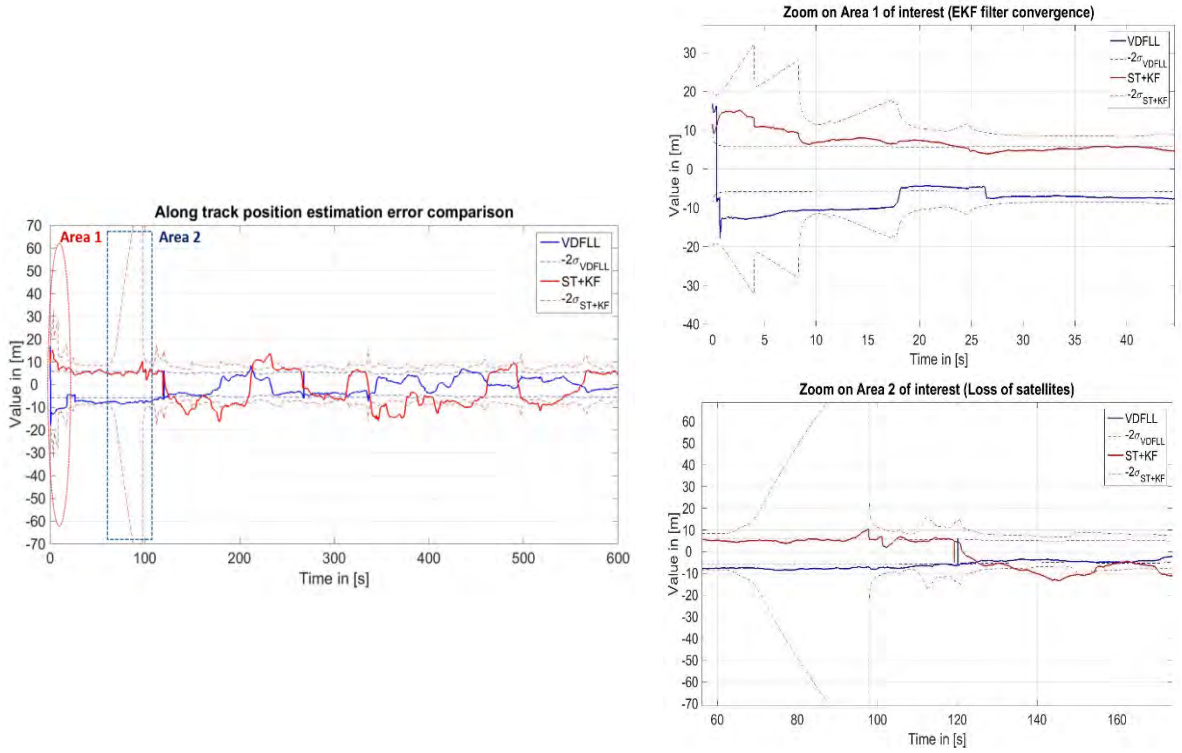

a)

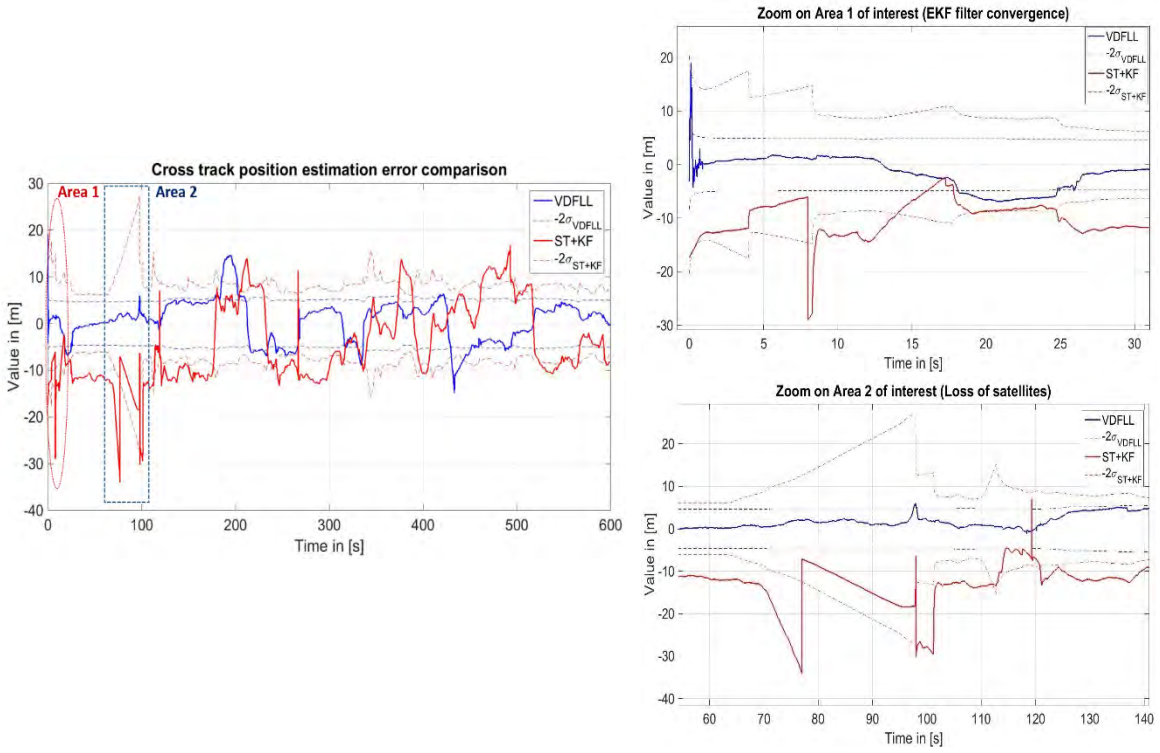

b)

Figure 7-18. *2D Position performance overview in severe urban conditions (No satellite selection for VDFLL).*

The general remark when observing the position error plots is the high position error variation for both the scalar and VDFLL architectures. Observing the magnified view of area 1 both for the along and cross track coordinate in Figure 7-18 a) and b), respectively, it can be easily noted the convergence of the two EKF filters toward a biased position of approximately $13\,m$. For the scalar tracking

architecture (in red) this result is quite logical, since during area 1 period (see Figure 7-18) there is only one locked satellite, which is totally insufficient to provide a decent position estimation. Whereas, a different explanation holds for the VDFLL architecture. Indeed during this period, there are more biased measurements coming from the 6 NLOS satellites w.r.t to the observations from the only LOS satellite and therefore, reducing the VDFLL EKF capability of correcting the position bias.

During the second severe outage, starting after the 70^{th} second as illustrated inside the red area 2, the sudden decrease from six to one LOS satellite is associated with the sudden covariance bound increase for the two architectures, as a logic filter reaction in terms of positioning error uncertainty. However, a certain position estimation reliability is noted for the VDFLL architecture, since the VDFLL position error is perfectly bordered by the VDFLL covariance bounds along the overall trajectory. The opposite holds for the ST+EKF-estimated position error that is constantly trespassing its uncertainty bounds, more visible in the cross track plot in Figure 7-18 b) leading to an error of nearly $33\ m$. Nevertheless, at the end of these outage interval after $110\ s$ and with the inclusion of new measurements with the reappearance of the previous NLOS satellites, the ST+EKF position error decreases and the uncertainty bounds are tightened. However a nearly $10\ m$ position bias still persists.

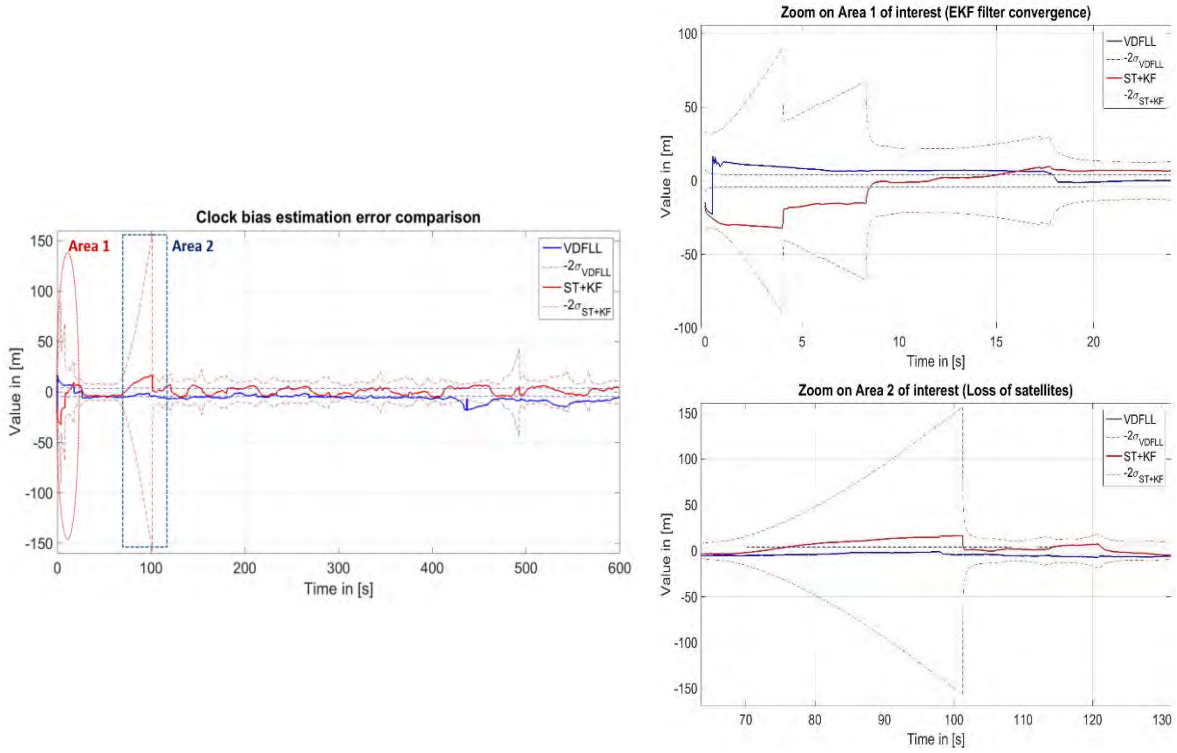

Figure 7-19. *User's clock bias performance overview in severe urban conditions (No Satellite selection for VDFLL).*

The most marked performance differences between the ST+EKF and VDFLL receiver configurations are noticed for the clock bias estimation, as illustrated in Figure 7-19. Again, a lack of clock bias estimation convergence is noted for both the receiver configurations during the initial period (in area 1), illustrated in the top right plot. The largest clock estimation error is registered for the scalar receiver configuration during the severe satellite outage period inside area 2. Indeed during this interval, the ST+KF covariance bounds explode up to the $150\ m$ level due to the large inflation of the Kalman gain. On the contrary, the VDFLL filter performs a forward propagation of the state vector that later drives

the code/carrier NCO updates in the feedback loop, aiding in this way the channel errors correction. Furthermore in the VDFLL case, the clock bias estimation errors are divided between the clock and ionosphere residual states, which explains the lower clock bias estimation error.

7.4.4.1.2. Results under the satellite selection operation for the VDFLL

In order to cope with these severe urban conditions, the satellite selection technique that was presented in Figure 7-17 is activated for the VDFLL algorithm. The same figure representation from the previous section is conserved.

The position results along the car trajectory are shown for the along and cross track coordinates on the left side of Figure 7-20 a) and b), respectively. Whereas, on the right side the magnified view of the areas of interest (area 1 and 2) are presented.

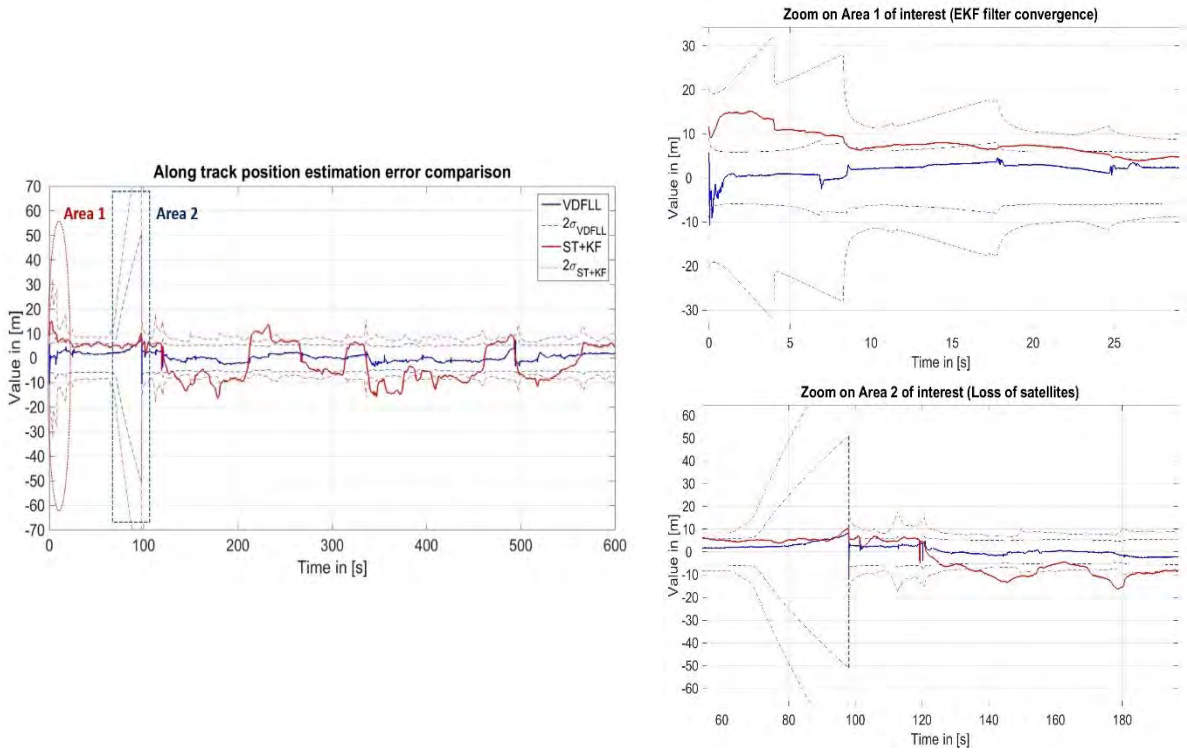

a)

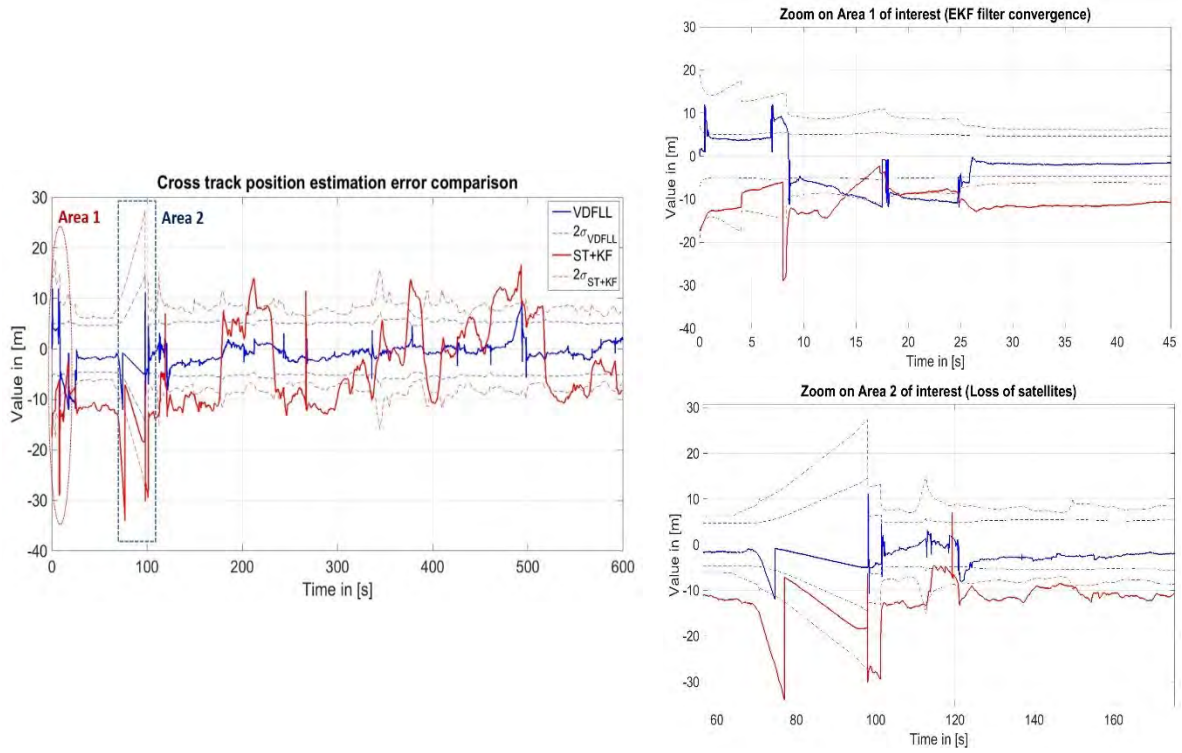

b)

Figure 7-20. *2D Position performance overview in severe urban conditions (Active satellite selection for VDFLL).*

The first clear observation that can be made when comparing the VDFLL position estimation in its two different operation modes with and without the activation of the satellite selection procedure, shown respectively in Figure 7-18 and Figure 7-20, is the lower VDFLL position error oscillation for both position coordinates when the satellite selection algorithm is used. Moreover, the VDFLL position error is perfectly bordered by the VDFLL covariance bounds along the overall trajectory, contrary to the ST+KF-estimated position error that is constantly trespassing its uncertainty bounds. This might be explained by the fact that the biased measurements from the NLOS satellites, which do not pass the C/N_0 test of the satellite selection process, are not included into the VDFLL navigation filter. In other words, the state vector innovation process is carried on by the LOS satellites only. Moreover, a faster position convergence of the VDFLL EKF filter in the initialization step (area 1) is observed when the satellite selection is performed w.r.t to the "feed all" VDFLL principle depicted in Figure 7-18. However, a fast position error increase is observed at the $8^{th}s$ in the zoomed area 1 by the ST+EKF architecture (in red) but also from the VDFLL algorithm, due to the inclusion of only one LOS satellite in the both the navigation solutions. During this period, the VDFLL filter performs recursively only the state propagation since the measurement innovation information that is achieved only by one LOS satellite is quite limited. This clearly denotes an operation limit of the VDFLL EKF filter in the satellite selection operation mode.

When referring to the second long outage interval from $75 - 100\ s$, illustrated in the zoomed area 2 plot, it can be noted a fast position error raise associated with larger covariance bounds for the two architectures. Hence, this $10\ m$ error is fast corrected by the VDFLL algorithm with the inclusion of new observations from the reappearing satellites that once more reflects the VDFLL reactivity

property. On the contrary, the ST+EKF position estimation from nearly $34\ m$ error slowly converges toward a biased position of around $12\ m$.

The performance comparison between the scalar and vector tracking receivers, with the later adopting the satellite selection technique, regarding the clock bias estimation is illustrated in Figure 7-21.

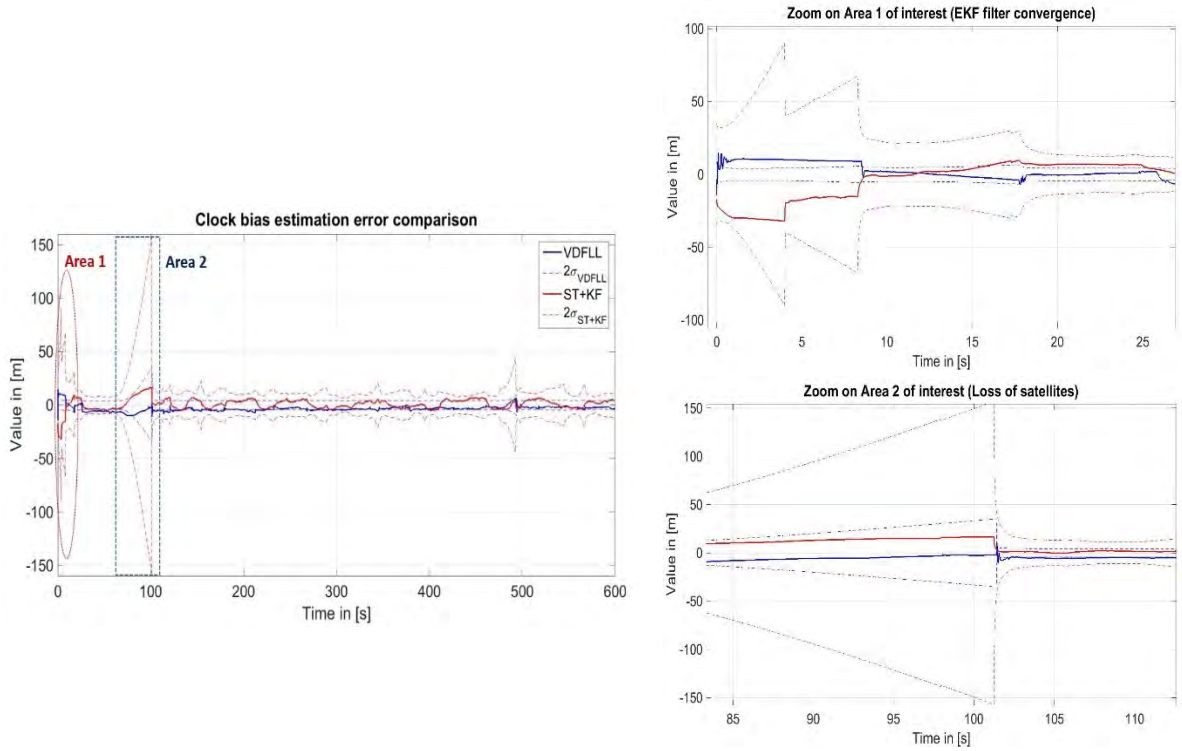

Figure 7-21. *User's clock bias performance overview in severe urban conditions (Active satellite selection for VDFLL).*

Concerning the performance comparison between the two architectures, the same comments made in the previous section are still valid. When observing the clock bias performance for the VDFLL satellite selection case in Figure 7-21 and comparing it with the classic VDFLL operation results from Figure 7-19, no significant improvement is noted. In fact it is quite difficult to clearly mark any performance improvement of the satellite selection due to the higher error magnitude of the ST+EKF clock bias estimation. For this matter, the focus shall be directed to the position and clock bias error statistics that are revealed in Table 7-5.

Table 7-5. *Position and clock bias estimation error statistics in harsh urban conditions.*

			ST+EKF	VDFLL (classic)	VDFLL (satellite selection)
POSITION	Along Track	Mean	1.4	0.9	0.5
		RMS	7.7	4.7	1.8
		95%	13.4	8.1	3.2
		99%	14.8	13.9	5.6
	Cross Track	Mean	4.4	0.6	0.9
		RMS	9.5	4.5	2.4
		95%	13.6	8.3	5.1
		99%	26.1	15.4	10.1
Clock Bias		Mean	1.1	5.7	3.4
		RMS	6.3	5.2	4.2
		95%	15.4	12.8	6.7
		99%	24.4	16.8	9.7

As expected, the results show clearly the better positioning performance of the VDFLL architecture, regardless of its operation mode, noted by a twice lower RMS error for the both the along and cross track coordinates. However, a biased clock estimation centered at $3.4\ m$ and $5.7\ m$ is observed for the two VDFLL configurations, respectively. The position and clock bias estimation statistics do mark the evident benefits in employing the satellite selection algorithm in harsh urban conditions. Indeed, lower errors' variation (represented by the RMS parameter) and tighter covariance bounds (denoted by the 95 and 99 percentiles) are marked by the VDFLL architecture when employing the satellite selection technique. This clearly reflects the advantage of the satellite selection process, by focalizing the navigation estimation and NCO update tasks to the best (with the highest C/N_0) satellites, whose measurements are less affected by biases.

7.4.4.2. Channel Level Analysis

After the detailed performance analysis in the navigation domain, our attention is now directed to the channels errors performance assessment. The channel errors obtained from the VDFLL architecture in its two configurations (classic and satellite selection) are both much lower and thus nearly not distinguishable w.r.t the larger scale ST errors. Therefore, only the VDFLL channels' errors in the satellite selection operation mode are shown in the following figures. However, the detailed representation of the channels' errors statistics obtained from the two VDFLL operation modes and the ST receiver configuration are provided in Table 7-6.

The channel estimation errors along with their errors distributions for the code delay in a) and carrier frequency errors in b) are presented for the VDFLL and ST techniques for a LOS, a moderate LOS and a NLOS satellite in this exact order from Figure 7-22 to Figure 7-24.

7.4.4.2.1. Channel errors comparison for a LOS satellite

The performance comparison between the VDFLL architecture employing the satellite selection procedure and the ST receiver is performed in the channel level for the LOS GPS PRN3 satellite, as

illustrated in Figure 7-22. This satellite is situated at a high elevation angle of 84°, referring to the skyplot in Figure 7-2.

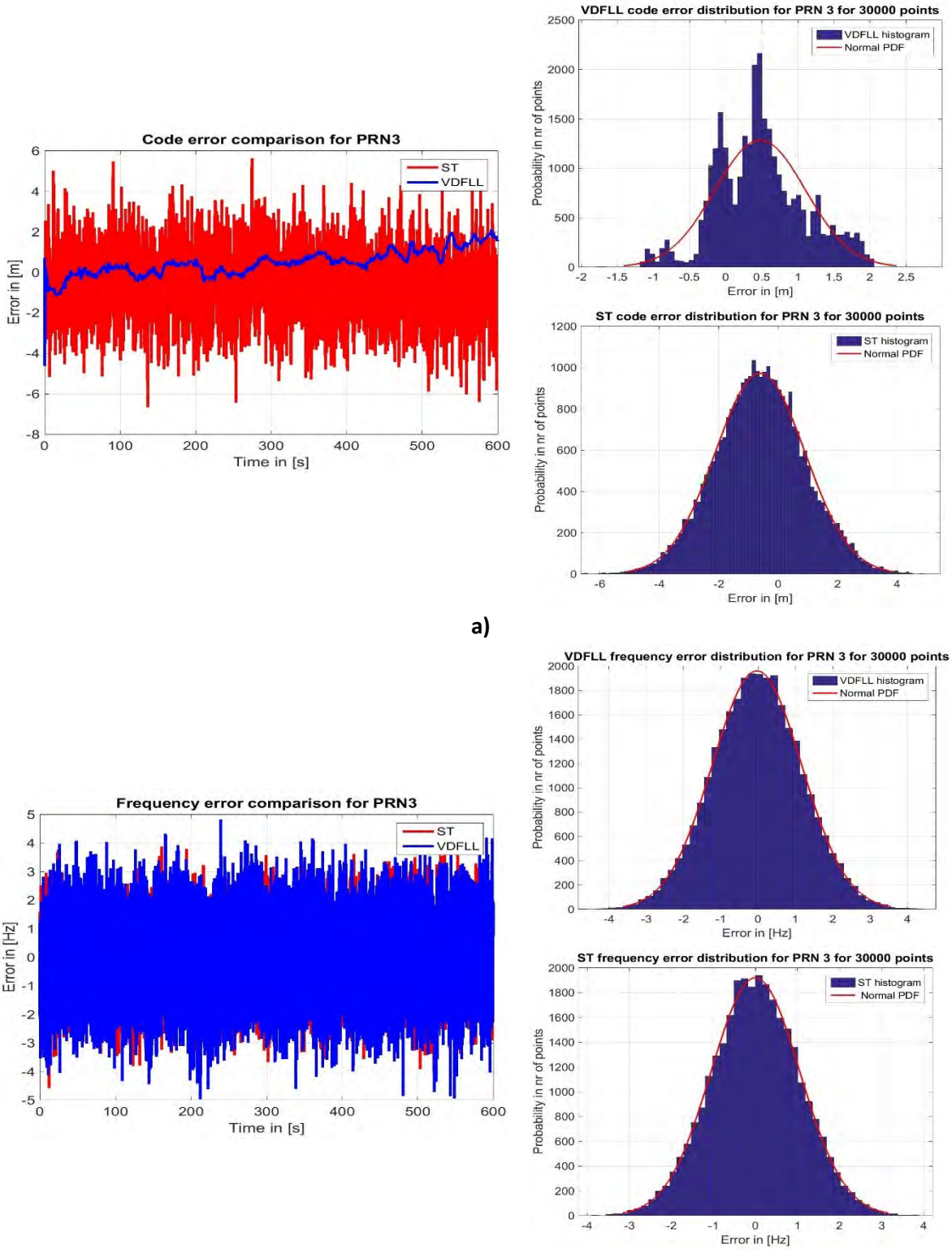

Figure 7-22. *Performance comparison in the tracking channel level for one LOS satellite in harsh urban environment.*

The code delay error comparison for the LOS GPS PRN3, provided in the left plot of Figure 7-22 a), shows a higher code delay estimation accuracy for the VDFLL algorithm. However, a slightly drifting trend is observed starting from $310\ s$ that coincides with a severe satellite outage event, as it can be seen in Figure 7-16. During this event, a $10\ m$ position error increase occurs as it can be observed in Figure 7-20. Since the VDFLL code NCO update is computed based on the position estimation, this bias is further projected in the channel level through the feedback loop. This phenomena is also reflected into the non-Gaussian distribution of the VDFLL-estimated code error in the top right plot of Figure 7-22 a). On the contrary, the ST-estimated code delay is noisier and zero-centered but not biased (referring to the right bottom plot from Figure 7-22 a)) since the code tracking process is performed in a closed-loop manner, regardless of the navigation solution estimation.

However, nearly equivalent carrier frequency estimation errors that are zero-mean and Gaussian distributed are observed for the two architectures, as depicted in Figure 7-22 b). These low frequency estimation errors are mostly related to vehicle dynamics, since the other error sources such as the ionosphere residuals and multipath errors have a minimal impact on high elevation satellites.

7.4.4.2.2. Channel errors comparison for a moderate LOS satellite

In this sub-section, the channel level assessment is performed for GPS PRN4 that falls into the moderate LOS satellite category, as shown in the PDP profile in Figure 7-7. The herein performed analysis will be also referred to the channel error investigation made for the urban environment test concerning the dual-constellation receiver in the previous section 7.3.4.2. The code delay and carrier frequency estimation errors comparison between the VDFLL (under satellite selection) and the scalar tracking technique for GPS PRN4 satellite are shown in Figure 7-23.

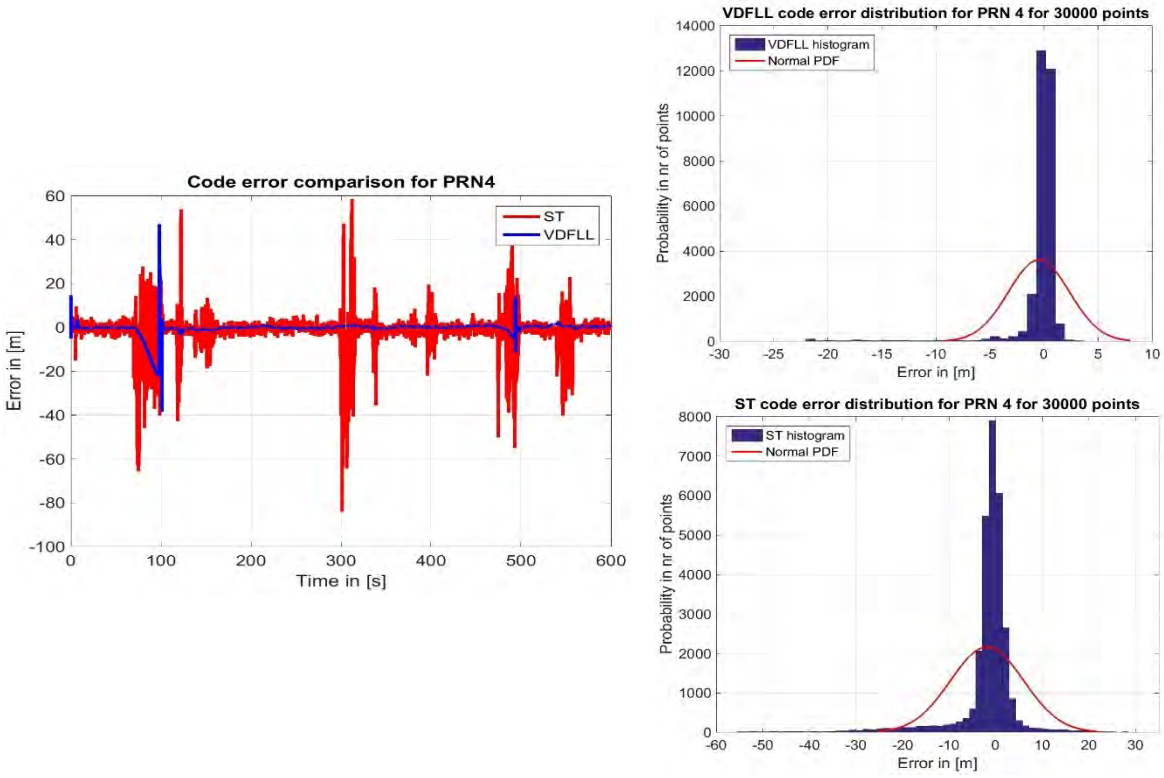

a)

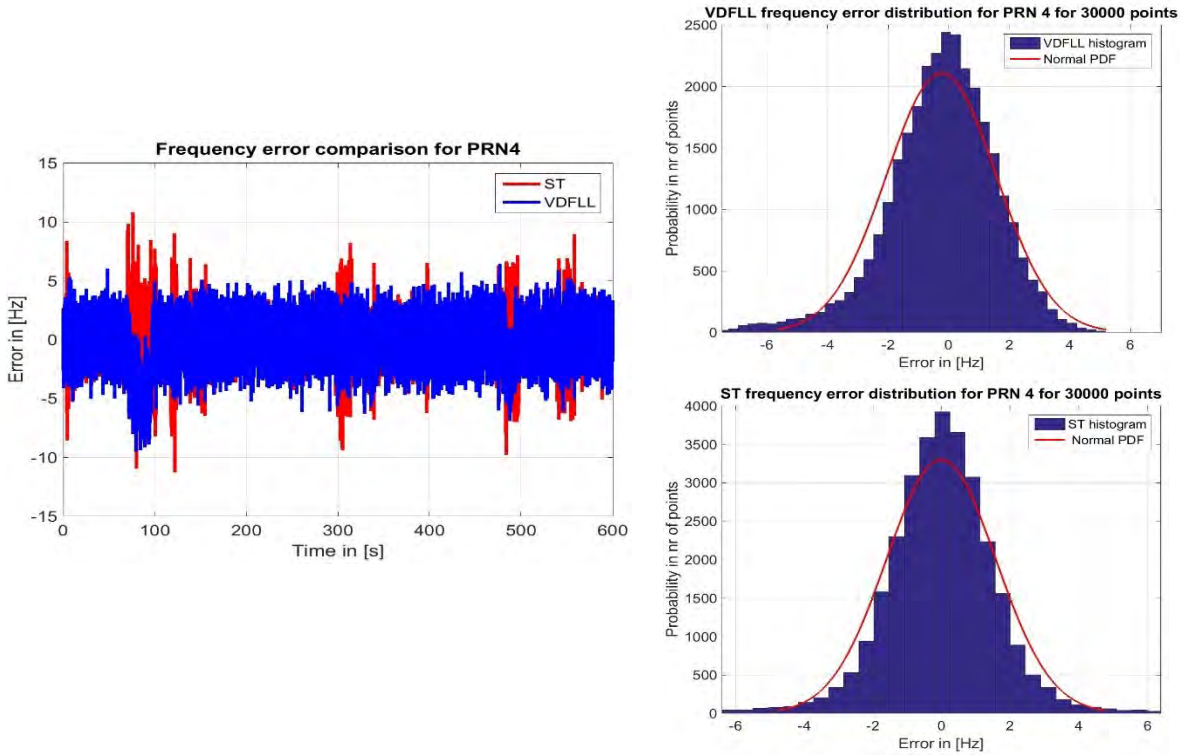

b)

Figure 7-23. *Performance comparison in the tracking channel level for one moderate LOS satellite in harsh urban environment.*

The strong signal power drops by approximately $40\ dB$ after $100\ s$, $300\ s$ and around the $475\ s$, illustrated by the red to green/blue transition when observing the GPS PRN4 PDP profile in Figure 7-7, are manifested by the large code delay errors for the scalar tracking configuration (in red) as shown in Figure 7-23 a). The same error increase is also observed for the ST carrier estimation but at a much lower scale due to the reduced multipath and ionosphere residual effects on the Doppler measurements.

When observing the code delay- and carrier frequency error evolution for the VDFLL architecture (in blue) provided in Figure 7-23 a) and b), respectively, two short-duration jumps are noted after $100\ s$ and $475\ s$. The reason for this behavior is dedicated to the presence of a single LOS satellite for the first jump, and due to the fast variation of the visible satellites in the second one, as shown in Figure 7-16. In fact, this limited number of observations is not sufficient to provide an accurate position estimation, since the VDFLL filter is forced to estimate a $(8 +$ number of ionosphere residuals) state vector with only one or two sets of measurements. This VDFLL performance decrease somehow contradicts the stability during outage events that was seen in Figure 7-13 for the dual-constellation VDFLL architecture. This performance difference lies in fact on the channel aiding property that is not entirely exploited from the VDFLL algorithm (satellite selection operation) in severe urban conditions and during satellite blockages due to the limited number of observations. However with the reappearance of the previously blocked satellites, the channels errors are reduced due to the inclusion of more measurements into the VDFLL EKF filter. The higher code estimation accuracy from the VDFLL architecture can also be remarked by lower error scale in the histogram plots in Figure 7-23 a).

7.4.4.2.3. Channel errors comparison for a NLOS satellite

The performance assessment in the channel level between the VDFLL and ST receiver configurations in harsh urban environment, which is characterized by poor satellite visibility, is concluded with the NLOS satellite analysis illustrated in Figure 7-24.

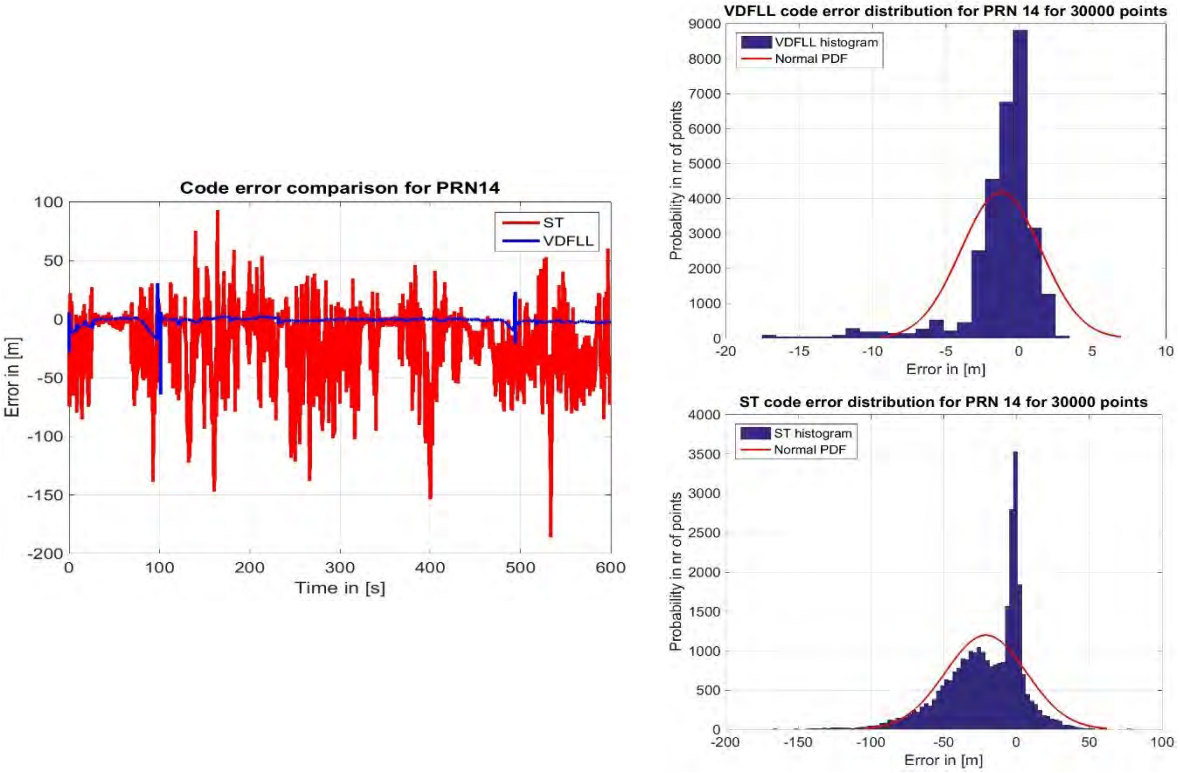

a)

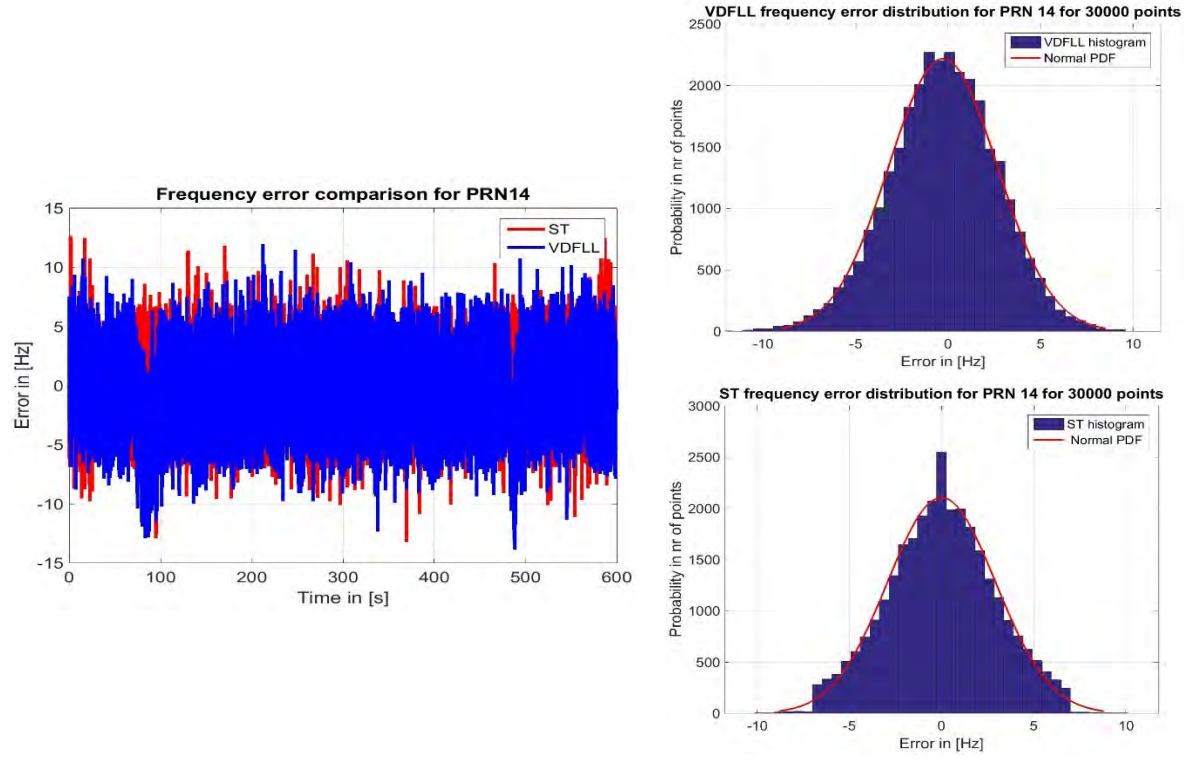

b)

Figure 7-24. *Performance comparison in the tracking channel level for one NLOS satellite in harsh urban environment.*

GPS PRN14 exhibits numerous signal power drops along the car trajectory as it can be easily noted from the blue areas in the first delay bin $(0 \text{ to } 5\ m)$ of its PDP profile in Figure 7-7. These signal power declines due to the LOS signal blockage significantly affect the scalar code tracking loops, which fail to correctly estimate the code delay. These events induce large code delay estimation errors for the scalar tracking receiver, illustrated by the red curve in Figure 7-24 a), mostly observed in five different epochs $(\sim 100\ s, 180\ s, 275\ s, 400\ s \text{ and } 530\ s)$.

The code delay errors exceeding the linear tracking domain of the code discriminator, defined by the correlator chip spacing that in this implementation is set to $0.5\ chips = 149\ m$ (see Table 7-1), correspond to a biased response of the code discriminator. Thus, a code loss-of-lock occurs that further launches the start of $1\ s$ hot re-acquisition process according to the model provided in section 6.1.2. These large code errors are also noticed by high non-zero centered peaks in the ST code error histogram provided in the bottom plot of Figure 7-24 a).

On the contrary, as it can be pointed out in Figure 7-24 a), the code tracking estimation process is continuously carried on by the VDFLL architecture (in blue), insensitive to the signal power decrease. This is due to the fact that the code (and carrier) tracking process for the VDFLL architecture in the satellite selection procedure, is achieved by VDFLL EKF filter using the code innovations from the satellites passing the C/N_0 test from Figure 7-17. This is the reason why increased code/carrier estimation errors are observed only in two epochs at around $(75 \text{ and } 480\ s)$, similarly to the GPS PRN 4 case in the previous section, coinciding with the presence of only one LOS satellite that cannot ensure a correct position estimation and therefore, biasing the code NCO update to each tracking channel in the feedback loop. Beside these two epochs, where a clear frequency error hump for the VDFLL configuration (in blue) is observed, the carrier frequency is correctly estimated within $\sim 5\ Hz$ 3σ bound when referring to the histograms in Figure 7-24 b).

7.4.4.2.4. Channels' errors statistics

The channel error statistics for the scalar tracking (ST) and the two VDFLL architectures, namely the classic VDFLL (based on the "feed all" principle) and the proposed VDFLL technique with the satellite selection procedure, for the three LOS, moderate LOS and NLOS satellites presented above, are summarized in Table 7-6.

Table 7-6. *Channel error statistics in severe urban conditions.*

		ST	VDFLL (classic)	VDFLL (satellite selection)
Category 1: LOS satellite (Ex: GPS PRN3)				
Code error $[m]$	Mean	0.6	1	0.5
	RMS	1.6	1.3	0.8
	95%	3.4	2.5	1.7
	99%	4.4	3.4	1.9
Frequency error $[Hz]$	Mean	~0	~0	~0
	RMS	1.1	1.3	1.2
	95%	2.1	2.6	2.3
	99%	2.7	3.2	3.1
Category 2: Moderate LOS satellite (Ex: GPS PRN4)				
Code error $[m]$	Mean	1.9	1.1	0.6
	RMS	8.1	4.6	3
	95%	19.8	6.3	3.5
	99%	39.5	17.5	11.7
Frequency error $[Hz]$	Mean	~0	0.9	0.2
	RMS	1.6	1.4	1.3
	95%	3.2	2.5	2.3
	99%	5.4	5.1	4.9
Category 3: NLOS satellite (Ex: GPS PRN14)				
Code error $[m]$	Mean	21	4.4	2.4
	RMS	38.9	5.2	3.5
	95%	72.7	7.1	4.8
	99%	105.2	18.7	12.4
Frequency error $[Hz]$	Mean	~0	0.1	0.3
	RMS	2.9	3.2	2.9
	95%	5.9	6	5.8
	99%	6.8	8.1	7.8

Herein, the performance analysis will be stipulated in two comparison levels: firstly, commenting the ST error statistics w.r.t to the two VDFLL configurations, and secondly, observing the differences between the classic and satellite selection-based VDFLL architectures.

From a global observation of the table results, the code/carrier tracking accuracy for the VDFLL architectures can be obviously noticed. However, no meaningful improvement is brought by the VDFLL architectures in the code delay tracking process for LOS satellites, since they are less susceptible toward the ionosphere residuals (lower for high elevations as shown in Figure 7-6) and to the direct signal blockage. Equivalent performance between the ST and VDFLL architectures also concerning the carrier frequency tracking for the same reasons are observed as detailed in section 7.3.

However, the performance gain in employing the VDFLL architectures w.r.t the ST technique becomes evident in the code delay estimation for the moderate LOS (GPS PRN4) and NLOS satellite (GPS PRN14). Indeed, twice lower code error variations (indicated by the RMS value) and more than three times lower 2σ bounds (denoted by the $95\ \%$ percentile) are exhibited from the VDFLL configuration against the ST technique for the moderate LOS (GPS PRN4) satellite. This performance difference is even more enhanced when referring to the code delay tracking for the NLOS satellites, characterized by frequent code loss-of-locks. In fact, the VDFLL-estimated code delays are much less biased compared to the ST-estimations, which is reflected by the approximately six and ten times lower RMS and $95\ \%$ bounds, respectively, when using the vector tracking algorithm for the NLOS GPS PRN14 satellite. These satisfying code estimation results are a proof of concept of the VDFLL tracking robustness in signal-constrained environments.

When focusing on the comparative analysis only between the two VDFLL architectures, a $2-3\ m$ improvement is observed in the code delay estimation and also associated with tighter $95\ \%$ and $99\ \%$ coder error bounds when employing the satellite selection process. This performance originates at the limitation of the channel's error flow since the position estimation and the tracking tasks are computed by the high C/N_0 (thus less biased) satellites.

7.4.5. Conclusions on Scenario 3

The last performed test, aiming at examining the operational limits of the VDFLL receiver architecture both in the navigation and channel level, is performed in harsh urban conditions with very limited number of observables. This scenario is generated by using only the GPS L1 signals (single constellation) that are still affected by multipath and ionosphere residuals, as for the previous test scenario. In order to cope with the severe urban conditions, a different configuration of the VDFLL architecture referred to as the satellite selection was proposed. The satellite selection algorithm, consisting on feeding to the VDFLL filter the measurement innovations coming from the high C/N_0 ($> 25\ dB-Hz$) satellites, was presented in section 7.4.3. Therefore, the performance comparison in the navigation and channel level was performed for the two VDFLL architectures (classic + satellite selection) and the scalar tracking receiver.

Once more, the two VDFLL architectures outperformed the scalar tracking receiver concerning both the position and clock bias estimations in severe urban conditions. Regarding the performance comparison between the two vectorized configurations, lower errors variation (denoted also by the RMS value) and tighter error bounds (characterized by the 95 and 99 percentiles) were observed by the satellite selection operation mode of the VDFLL architecture. This better performance is explained by the satellite selection property, consisting in concentrating the navigation solution estimation and the NCO update process to the LOS satellites that are less affected by the ionosphere and multipath effects.

Regarding the channel level performance assessment, the VDFLL tracking robustness was confirmed particularly by assuring nearly 10 times lower code delay estimation errors w.r.t scalar tracking when tracking NLOS satellites. Contrary to initiation of the hot re-acquisition process during satellite blockages in the scalar tracking receiver, the continuous code/frequency tracking was guaranteed by the two VDFLL configurations. However, better frequency estimations were provided from the VDFLL architectures w.r.t scalar tracking technique but at much lower order of magnitude compared to the code delays estimation. Concerning the comparative analysis only between the two VDFLL

architectures, a $2-3\,m$ improvement was noted in the code delay estimation and also associated with tighter $95\,\%$ and $99\,\%$ coder error bounds when employing the satellite selection process.

7.5. Conclusions

This chapter tackled the accuracy performance assessment of the proposed dual-constellation GPS/Galileo single-frequency L1/E1 VDFLL architecture in reference to the scalar receiver configuration in a simulated urban environment. For this matter, an extensive performance comparison for different test scenarios was performed in the system level, in terms of the user's navigation solution estimation accuracy in the vehicle frame and in the channel level, represented by the code delay and Doppler frequency estimation errors.

In Section 7.1, the dynamic car trajectory along with the test parameters related to the scalar (ST) and vector tracking (VT) loop design and their respective navigation filter configurations were introduced. Moreover, the formulation of the code delay and carrier frequency estimation errors was done for both architectures, noting that the ionosphere residuals are estimated only by the VT algorithm.

The validation of the VDFLL algorithm in the presence of ionosphere residual errors was performed via Monte Carlo (MC) simulation in section 7.2. For each MC simulation, a new draw of ionosphere residual errors is generated and the initial simulation date is also changed within the scope of obtaining a different satellite geometry during each run. The PDF representation of the position, velocity and receiver's clock errors along with the navigation statistics (in terms of mean, RMS, 95- and 99-percentiles) demonstrated the VDFLL capability in decently (with certain remaining biases) estimating the ionosphere residual errors. The VDFLL superiority against the scalar tracking receiver was also proved in the channel level for both the code delay and carrier frequency estimation errors, with the VDFLL channels' estimations being far less erroneous overall the coverage area, especially when referring to the code delay errors. An interesting result was the dependence of the ST- and VDFLL-estimated carrier frequency errors on the bearing angle. This behavior is a reflection of the Doppler frequency relation with the vehicle orientation that is exhibited by its heading angle change as part of the satellite-user bearing angle calculation.

In section 7.3, the performance analysis of the two architectures under study was extended to the complete urban environment representative, comprising both the ionosphere residuals and the simulated multipath reception conditions, with the later obtained from the adapted DLR urban channel model and added at the correlator level into the developed GNSS signal emulator. In this test, the same car trajectory and GPS/Galileo constellation geometry were preserved. The performance analysis was extended to the signal level in terms of code delay and Doppler frequency estimation errors for LOS, moderate LOS and NLOS satellites, which were defined according to the computed Power Delay Profiles (PDPs).

The channel errors results verified the robustness of the proposed VDFLL technique, which is dedicated to its capability in properly estimating the ionosphere residual errors due to their large correlation time and also due to the EKF-estimated position and channels update. This VDFLL tracking robustness becomes even more evident regarding the code delay tracking for moderate and NLOS satellites that do frequently experience important signal power drops. During these outage intervals,

the scalar tracking process is totally interrupted after the failure of the code lock detection test and the re-acquisition process is immediately initiated. The contrary may be stated for the VDFLL algorithm, where the code/carrier tracking estimation process is continuously pursued based on the mutual channel aiding. Great attention was directed toward the analysis of the code delay- and carrier frequency errors distributions with an emphasis on the Q-Q plot representation, which is a powerful graphical tool in identifying the errors distribution function. Noticeable differences concerning the distribution functions are recognized between the two architectures and also for the LOS, moderate LOS and NLOS satellites. The Q-Q plots demonstrated the nearly- Gaussian property of the carrier frequency errors for both the scalar tracking (ST) and vector tracking (VT) techniques. However, a stronger Gaussian feature is seen for the VDFLL carrier frequency errors distribution due to the channels noise sharing related to the ionosphere residual rate effect on the Doppler measurements. When referring to the code delay errors, the presence of biases due to channels' errors coupling make it really difficult to establish VDFLL code tracking error distribution (fairy Ricean) concerning the moderate LOS and NLOS satellites. Whereas, the code delay errors from high elevation LOS satellites are approximately Gaussian-distributed. The word approximately is used since certain code delay error histogram deformations are present and caused by the errors flow between the VDFLL tracking channels. Regarding the ST code delay errors, the finding of the proper distribution fit represents an extremely hard task due to the numerous code loss-of-lock occurrences.

The VDFLL superiority was also reconfirmed in the navigation domain, especially when referring to the position and clock bias estimation accuracies. Nearly twice lower position and clock bias estimation error variations were observed for the VDFLL architecture w.r.t the scalar receiver configuration, also confirmed by the RMS error values in the table of statistics. Moreover, the VDFLL reactivity was noted during satellite outage intervals that are characterized by a reduction of the number of observations. During these intervals, an accurate navigation solution estimation is assured by the VDFLL filter thanks to the code/carrier NCO updates driven by the position and velocity estimations. Slightly better velocities and clock drift estimations are obtained from the vector tracking receiver w.r.t the scalar tracking configuration, related to the limited multipath impact on the Doppler measurements and also to the slow variation of the ionosphere residuals.

The final performed test, aiming at the VDFLL navigation and channel estimation performance evaluation in harsh urban conditions, was detailed in section 7.4. The severe urban conditions are reproduced by the use of the GPS L1 signals (single constellation) only along the car trajectory, assuring a limited number of tracked satellites, whose measurements are still affected by multipath and ionosphere residual errors.

In order to cope with the severe urban conditions, a different configuration of the VDFLL architecture referred to as the satellite selection was proposed. The satellite selection algorithm, consisting on feeding to the VDFLL filter the measurement innovations coming from the high C/N_0 ($> 25\ dB - Hz$), satellites was presented in section 7.4.3. Therefore, the performance comparison in the navigation and channel level was performed for the two VDFLL architectures (classic + satellite selection) and the scalar tracking receiver.

The position results once more certified the VDFLL superiority in the provision of a continuous coverage and a valid navigation solution throughout the dense urban canyon scenario. Multiple position and clock bias estimation jumps of nearly $30\ m$ were reported from the scalar tracking receiver during the significant GPS outages, when sometimes only one or two LOS satellites are

available. Whereas, smaller position errors up to $10\,m$ magnitude were observed from the VDFLL architecture during the same outage periods. This position error increase is due to the insufficient measurements set required to estimate the $(8+$ number of tracked satellites) state vector. Furthermore, lower position/clock bias errors and tighter covariance bounds were noted for the satellite selection operation w.r.t to the classic (feed all measurements) VDFLL architecture. This better performance is explained by the satellite selection property, consisting in concentrating the navigation solution estimation and the NCO update process to the LOS satellites that are less probably affected by the ionosphere and multipath effects. A better position estimation induces lower code delay estimation errors in the VDFLL EKF-estimated NCO updates and this was indeed observed for the VDFLL under satellite selection operation. Limited improvements were observed both in the frequency (channel level) and velocity/clock drift estimations due to the limited multipath and ionosphere residual impact on the Doppler measurements.

8. Conclusions and Perspectives

This chapter summarizes the main conclusions of the work conducted in this dissertation and provides several recommendation for future research in this field.

8.1. Conclusions

The work performed in this dissertation is developed in the context of the GNSS use in urban environment. The urban environment is particularly challenging to the GNSS signal reception, where multipath and direct signal blockage significantly affect the signal processing and thus, introducing great errors in the pseudorange and carrier measurements that further degrade the position accuracy and availability. In this context and aiming at the improvement of the receiver's robustness, advanced signal processing or aiding techniques are required. For this matter, the focus of this thesis was oriented to the vector tracking architectures that represent viable techniques for reducing the multipath interference and NLOS signal reception impact due to the merge of the signal tracking and navigation solution estimation tasks via the navigation filter.

This Ph.D. thesis focused on the design of a dual-constellation GPS/Galileo and single-frequency L1/E1 band vector tracking architecture for automotive usage in urban environment. The choice behind the implementation of dual-constellation but single-frequency vectorized architecture was twofold. Firstly, the introduction of the Galileo satellite measurements assures an increased position accuracy and navigation solution availability in signal-constrained environments. Secondly, the choice of a single frequency band architecture is within the objective of a reduced architecture complexity and conserving the low-cost feasibility criteria of the mobile user's receiver module. The objective of this thesis was the detailed performance assessment of the designed vector tracking architecture with respect to the conventional scalar tracking receiver in an urban environment representative.

Since this research work was conducted in the framework of a European-funded project, the attention was obviously directed toward the integration of the US GPS and European Galileo system signals in the designed receiver architecture. In addition, the description of the GPS L1 C/A and Galileo E1-C (pilot) signals, which are considered in the framework of the Ph.D. thesis, were presented in terms of their modulation scheme, code period and spectrum properties in Chapter 2. Two main characteristics of the Galileo E1 signal were provided such as: the availability of the pilot channel in the quadrature branch and the use of the subcarrier Binary Offset Carrier (BOC) modulation.

In order to provide a detailed performance investigation of the proposed vector tracking algorithm in urban environment, several simulation tests have been conducted by employing a realistic dual-constellation dual-frequency GNSS signal emulator comprising the navigation module. The developed GNSS signal emulator, simulating in this research work the GPS L1 C/A and Galileo E1-C signals of interest at the correlator output level, was described in Chapter 6. The simulation option against the use of real measurements was chosen in this dissertation due to the testing flexibility offered by the former in terms of new tracking techniques and different navigation filter's configurations, as it is the case of the designed vectorized receiver architecture. Indeed, the GNSS signal emulator allows the

total control on the simulation parameters comprising the user environment and GNSS signal's characteristics, the generation of the signal propagation delays, the inclusion of different user's motion files etc.

The implemented signal emulator is entirely configurable and comprises three main modules such as: the generation of the propagation delays and measurement errors, the code/carrier signal tracking unit and the navigation processor. Among all the possible propagation delay sources, the ionosphere delay represents the major atmosphere-induced delay to the code measurements after the correction of the satellite clock error. The use of single L1 band signals does not permit the correction of the ionosphere delays and therefore, the use of the Klobuchar (GPS) and NeQuick (Galileo) ionosphere correction models is required. The resultant ionosphere residual was modelled according to the civil aviation standard as a first-order Gauss Markov process having an exponentially decaying autocorrelation function and a large correlation time of $1800\ s$, as was detailed in the first part of Chapter 3. Whereas, the second part of this chapter was dedicated to the description of the code (DLL) and carrier (PLL/FLL) tracking loops with the emphasis on the discriminator functions' description and the errors analysis aiming at the provision of the DLL/PLL error variance models. These code/carrier closed-loop tracking error variances were later used to model the measurement covariance matrix of the scalar receiver's navigation filter.

The central part of the GNSS signal emulator is constituted by the navigation processor that is implemented via an Extended Kalman Filter (EKF) for both the scalar and vector tracking receiver configurations but differing in the state and observation models. Another interest of the GNSS signal emulator is that it offers the possibility to efficiently switch between the two EKF-based navigation algorithms, which are initiated only after the Weighted Least Square (WLS)-estimated position convergence is achieved.

Chapter 4 introduced the detailed mathematical formulation of the WLS and EKF navigation estimators in terms of the absolute Position, Velocity and Time (PVT) eight-state vector expressed in the ECEF frame and the non-linear measurement model. The dual-constellation receiver configuration logically implies the presence of two receiver clock bias terms w.r.t the GPS and Galileo time. However, it was demonstrated that assuming the inter-constellation clock variation as accurately known, only one receiver's clock bias term can characterize both the GPS and Galileo measurements. This result indeed simplified the navigation solution due to the reduction of the number of states that need to be estimated. Furthermore, the pseudorange and pseudorange rate measurements (in the presence of ionosphere residuals) of the locked satellites that are estimated from the DLL and PLL, respectively, constitute the measurement input vector for the scalar EKF navigation filter. Due to the presence of the ionosphere residuals in the corrected measurements, the scalar measurement covariance matrix already including the DLL/PLL error variances was inflated with the ionosphere residual and residual rates error variance terms, as it was shown in Chapter 4.

This research work has placed in the spotlight the dual-constellation vector tracking technique in signal-constrained environment. For this purpose, a detailed state-of-the-art on vector tracking techniques along with their provided advantages and disadvantages has been realized and an overview of the possible configurations was detailed in Chapter 5. Finally, the Vector Delay Frequency Lock Loop (VDFLL) was chosen among the other candidates, since this architecture ensures a better receiver's dynamics estimation due to the joint code delay and Doppler carrier frequency tracking for all the satellites in-view performed by the common navigation filter. Two main differences are noticed between the VDFLL and scalar tracking architectures according to their operation principle. Firstly, the

the VDFLL architecture operates on the "feed all" concept, consisting in including the code/carrier discriminator outputs from all the satellites in-view (or tracked) as the measurement vector of the EKF filter. Secondly, the VDFLL code/carrier NCO update loop is driven by the EKF-estimated navigation solution and thus, exploiting the tracking channels aiding property. This loop closure after the navigation solution estimation implies the inclusion of the open-loop code/carrier discriminator error variances into the VDFLL measurement covariance matrix.

One of the novelties of this dissertation relies on the design of a dual-constellation GPS/Galileo single frequency L1/E1 VDFLL architecture for the urban environment conditions and that provides the estimation of the ionosphere residuals affecting the incoming pseudorange observations. Therefore in this work, another crucial distinction between the EKF navigation filters for the scalar and vector tracking receivers arises due to the ionosphere residual estimation process implemented for the VDFLL architecture. This is associated with the augmentation of the VDFLL state vector with the ionosphere residuals per each tracked satellite. As a direct consequence, the VDFLL process and measurement noise covariance matrixes, were altered accordingly to accommodate the ionosphere residual-related uncertainties as were derived in Chapter 5. Furthermore, the open-loop code/carrier error variance models are indeed sufficient to incorporate the multipath-induced error variations on the code and Doppler measurements since these effects are reflected at the decrease of the carrier-to-noise rate estimation. The detailed flowchart of the designed VDFLL architecture and the relation between the state and observation model were exposed in this chapter. Last but not least, the VDFLL NCO feedback to the code/carrier tracking loops along with the measurements' model were also detailed.

The most sensitive part of the signal emulator development is the generation of a representative of urban environment signal's reception conditions that was detailed in the second part of Chapter 6. The DLR Land Mobile Multipath Channel model (LMMC), representing a wideband propagation channel model that was developed thanks to a precise and extensive measurement campaign in urban environment, was used in this thesis. The urban environment conditions were generated separately for each GPS and Galileo tracked satellite by feeding their elevation/azimuth angles and the reference car trajectory to the DLR urban channel. The generated channel model samples in terms of LOS/NLOS amplitude, delay, phase and Doppler frequency have been stored and directly fed to the emulator at the correlator level. The urban channel model has been customized to meet the requirements of the scalar and vector tracking architectures. For this matter, the multipath parameters were generated at the same sampling rate as the tracking loop update at $50\ Hz$ and also, an efficient algorithm was used to compute the echoes' Doppler frequency due to their random generation process following the statistical model. At last, the formulation of the modified correlator outputs that integrates the LOS and NLOS echoes data to the signal emulator has been also determined in this chapter.

The aim of this thesis was the detailed performance assessment of the proposed dual-constellation GPS/Galileo single-frequency L1/E1 VDFLL architecture in reference to the scalar receiver configuration in urban environment representative. A variety of test scenarios were conducted with the same car trajectory in Toulouse city center but differing in terms of the generated error sources in addition to the always present thermal noise, as detailed in Chapter 7. These tests were employed to study the proposed VDFLL algorithm performance in comparison to the scalar tracking receiver serving as a benchmark. An extensive performance comparison was performed in the navigation level, in terms of the user's navigation solution estimation accuracy in the vehicle frame and in the channel level, represented by the code delay and Doppler frequency estimation errors. In addition, the

performance analysis was accomplished by the use of several statistical tools and parameters including the Q-Q plot, the Probability and Cumulative Distribution Functions (PDF/CDF) along with the mean, RMS and the 95- and 99-percentiles statistics.

The first performance analysis was performed in the presence of only ionosphere residuals via Monte Carlo (MC) simulations, with a different ionosphere residual draw and satellite geometry in each run. Aiming at the validation of the two receiver architectures, the Monte Carlo simulations have been applied to the single constellation case, characterized by a reduced number of observations from a maximum of 7 satellites to 4 satellites in view, with the lower limit representing the minimum EKF filter requirement for the navigation solution convergence. When observing the navigation errors' PDF plots and their statistics, it was shown that the designed VDFLL algorithm outperformed the scalar tracking receiver in terms of the PVT estimation accuracy. Indeed, approximately three time lower position and clock bias estimation errors and tighter error covariance bounds are noticed for the VDFLL architecture w.r.t the scalar tracking + EKF receiver, even for reduced number of measurements. This clearly reflects the capability of the designed VDFLL technique in estimating the ionosphere residuals and therefore, reducing their impact in the navigation solution estimation.

The VDFLL performance improvement is also noticed in the velocity and clock drift estimation but at a lower magnitude compared to the position/clock bias estimation due to the slowly time-varying ionosphere residuals. The tracking channels' errors RMS demonstrated the VDFLL capability in estimating the ionosphere residuals that is in fact observed by lower code delay estimation error RMS for the VDFLL technique w.r.t scalar tracking technique. Concerning the Doppler frequency estimation, slightly better estimation are noted for the VDFLL architecture due to the low ionosphere residual impact on the Doppler observations.

The VDFLL superiority against the scalar tracking receiver was also confirmed in the urban environment representative, comprising both the ionosphere residuals and multipath reception conditions, with the later generated by the modified DLR urban channel model and further added at the correlator output level of the signal emulator. Concerning the navigation level analysis, particular attention was dedicated to two time intervals such as the EKF initialization period in the beginning of the car trajectory and a strong satellite outage interval in the middle of the trajectory that is represented by only 4 satellites in-view for the navigation solution estimation. In such conditions, three main VDFLL features are remarked regarding the PVT estimation namely the reactivity, stability and reliability. The VDFLL reactivity is denoted by the fast position solution convergence in the initialization period and by the fast position error decrease in the satellites reappearance after the satellite outage event. Whereas, the VDFLL stability is denoted by the slow position error variations in time that is also noticed during the satellite outages within a $4\,m$ position error RMS. Last but not least, the VDFLL EKF-estimated position error covariance bounds constantly confine the estimation error. This represents a clear indicator of VDFLL navigation solution reliability, which is preferable for urban applications that demand high integrity requirements. All these considerations are also valid for the VDFLL velocity and clock drift estimations but less evident due to lower impact of the ionosphere and multipath effects on the pseudorange rate measurements.

A detailed performance investigation was performed in the signal level in terms of code delay and Doppler frequency estimation errors for LOS, moderate LOS and NLOS satellites, which were defined according to the computed Power Delay Profiles (PDPs). The channel error results revealed the VDFLL tracking robustness especially referring to the code delay estimation for moderate LOS and NLOS

satellites that experience significant signal power drops. This is a direct consequence of the accurate VDFLL-estimated position that is further projected via the LOS vector onto the code replica in the feedback loop. During these satellite blockage intervals, the scalar code tracking process was interrupted due the code loss-of-lock, triggering the start of the hot $1\ s$ re-acquisition process that was described in Chapter 6. On the contrary, the tracking process is continuously performed by the VDFLL receiver based on the channel aiding.

A final test, aiming at testing the VDFLL limits concerning the navigation and channel estimations, was performed for severe urban conditions. These harsh urban conditions were reproduced by the use of only the GPS L1 signals (single constellation) along the car trajectory, assuring a limited number of tracked satellites, whose measurements are still affected by multipath and ionosphere residual errors. In this conditions, another VDFLL architecture configuration known as the VDFLL satellite selection was proposed. The satellite selection algorithm, consisting on feeding to the VDFLL filter the measurement innovations coming from the high C/N_0 satellites was presented in the last chapter. The position and clock bias estimation error results certified the VDFLL superiority in terms of position availability and accuracy throughout the dense urban canyon scenario.

During a stretch of the car trajectory characterized by powerful GPS satellite outages, in the presence of one or two LOS satellites, multiple position and clock bias estimation jumps of up to $40\ m$ were observed by the scalar tracking + EKF receiver. On the contrary, higher navigation solution accuracies with lower oscillations in time were observed for the two VDFLL (classic + satellite selection) architectures. However, evident benefits in employing the satellite selection algorithm are marked in the lower position and clock bias estimation errors (represented by the RMS parameter) and tighter covariance bounds (denoted by the 95 and 99 percentiles). This clearly reflects the advantage of the satellite selection process, by focalizing the navigation estimation and NCO update tasks to the best (with the highest C/N_0) satellites, whose measurements are less affected by biases. Moreover, better code delay estimations, confined at the $5\ m$ 95-percentiles error level even for NLOS satellites, were obtained from the VDFLL architecture in the satellite selection operation mode related to the higher position accuracy that drives the code NCO update.

8.2. Perspectives for Future Work

Starting from the research made in this Ph.D., further studies can be conducted on four different domains that are: tracking, positioning, integration and integrity monitoring.

In this dissertation, the performance assessment of the proposed vector tracking architecture was conducted in simulated urban environment, which offered the possibility of analyzing in detail the impact of each error source separately and jointly both on the navigation and channel levels. However, the use of real data would allow further tests on the developed algorithm and is crucial to finalize the validation of the VDFLL technique in urban environment.

After this consideration, recommendations on these four axes are further detailed.

- **Tracking domain:**

In this thesis, the non-coherent vector tracking algorithm was considered since only the Doppler frequencies from all the satellites in-view are jointly tracked by the EKF navigation filter whereas, the phase of the carrier signals is not tracked. Therefore, extending the vector tracking process toward the carrier phase estimation constitutes an interesting research topic. However, the vectorized PLL (VPLL) that integrates the carrier phases into the Kalman filter represents several challenging issues that need to be addressed. First, the estimated user position is not sufficiently accurate to predict the carrier phase ambiguity, related to the impact of the propagation delays and other possible biases. Moreover, the carrier phase of the received signals is more susceptible to multipath interference and LOS blockages. Due to the tracking channels' coupling at the navigation level for the vectorized architecture, a disturbance or bias in one carrier phase is propagated and could potentially affect the phase estimation of the other channels. From all these considerations, it can be seen that the correct operation of the VPLL technique in urban environments, where low C/N_0 ratios are encountered, represents an ambitious task.

Another research subject in the tracking domain can be the implementation of the cascaded vector tracking architecture. It basically consists on including a L1/E1 EKF local filter per tracking channel in charge of estimating the tracking errors for that channel along with the central EKF filter that provides the navigation solution estimation and computes the NCO update in the feedback loop. The benefits of this approach are twofold. Firstly, this configuration can reduce the order of the navigation filter state vector and also the rate of the measurement innovations' inclusion in the central filter. Secondly, the use of a local filter at the channel level may significantly reduce the errors coupling between the tracking channels.

Moreover, the current implementation of the dual-constellation GPS/Galileo single frequency L1/E1 can be broadened to the dual-frequency operation through the inclusion of the L5/E5a/E5b signals. This dual-frequency combination can totally remove the first order ionospheric delay but leaving the high order terms that have an insignificant effect on the measurements. However, the dual-frequency architecture does not properly fit with the low-cost receiver requirement for urban applications.

- **Position domain:**

The navigation filter used for both the scalar tracking and VDFLL receiver configurations was an Extended Kalman Filter (EKF). However, another possible filter implementation such as the Unscented Kalman Filter (UKF) could be studied in the future. The employ of the UKF might be appealing in the case of highly non-linear observation functions since no linearization of the system models is required. Indeed, the UKF applies a deterministic sampling technique to select a set of sigma (samples) points, capturing the true mean and covariance of the random state vector. Afterwards, these sigma points are propagated through non-linear functions that remove the requirement to calculate the Jacobians for the linearization process that is a costly operation [Zhu et al., 2015]. This implementation also removes the Gaussianity assumption of the measurement errors, interesting in the presence of multipath conditions. The UKF filter is of particular interest when dealing with highly non-linear observation functions, as it is the case for the GNSS hybridization with inertial and video sensors. However, this technique significantly augments the computational load due to the sigma points' propagations procedure. In this dissertation, the UKF equation have been implemented and thus, offering the possibility to switch between the EKF and UKF architectures. Nevertheless, this approach was not considered in this thesis since the code/Doppler measurement functions are slightly nonlinear.

Another point that can be further refined concerns the measurement error modelling due to multipath and LOS blockages. In this dissertation, the multipath error modelling was briefly conducted by generating different urban scenarios based on the DLR urban channel model but with the same urban trajectory. This data was later used to determine the code delay error variance due to the recorded multipath effects that were added at the correlator output level of the signal emulator. Yet no changes have been applied to the open-loop discriminator error variances in the proposed VDFLL technique since the multipath impact on the measurements is observed at the estimated C/N_0 level. However, an extensive urban measurement campaign is necessary for the multipath error modelling, which represents a demanding task knowing that multipath errors are strictly dependent on the user trajectory and urban obstacles.

- **Integration domain:**

A possible way to improve the navigation solution accuracy in multipath conditions and only NLOS signal reception, is the GNSS measurement fusion with other sensors having complementary advantages. Generally for land vehicle navigation, the most widely used hybridization algorithms consist on coupling the GNSS code/Doppler measurements with the inertial and/or odometric data. Indeed, the use of Inertial Navigation Systems (INS) that typically comprise the accelerometers and gyroscopes' sensors assures the availability and continuity of the navigation solution even when the GNSS measurements are severely corrupted or even unavailable during satellite outage periods. However, the navigation performance obtained from the GNSS/INS integration depends a lot on the quality of the inertial sensor. Moreover, the inclusion of the odometric sensor in the hybridized solution, which measures the distance travelled by the vehicle, increases the number of observations and may help to limit the drift of the INS system.

As it was described in Chapter 5, vector tracking was seen as an initial step toward the ultra-tight (deep) GNSS/INSS integration that can be simply achieved by upgrading the EKF navigation filter toward an integrated GNSS/INS filter. The included inertial sensor will now be in charge of performing the state propagation stage, while the GNSS measurement innovations will provide the state vector update. Nonetheless, the ultra-tight GNSS/INS coupling is associated with the increase of the state vector order that is later reflected into an increased architecture complexity.

The GNSS/INS integration can also be expanded to the inclusion of additional sensors such as the video camera, which in the past years has gained a particular attention in the navigation applications. Two different video sensors can be identified based on their operation principle, namely the video Fisheye camera and the Simultaneous Localization and Mapping (SLAM) technique. The Fisheye camera is used for the GNSS LOS satellite detection in order to perform the NLOS rejection and thus, discard the erroneous measurements at the source prior to their inclusion in the navigation filter. In other words, this strategy can be thought of as a satellite selection process at the observation level. This technique was first proposed in [Attia et al., 2010] and its integration in the receiver architecture were provided in [Shytermeja et al., 2014] and [Shytermeja et al., 2017]. Whereas in the GNSS/SLAM camera integration, the vehicle heading measurement is provided by the SLAM camera in the vision frame through feature matching techniques. Features geo-referencing and the EKF state vector augmentation with the camera scale factors are required in this fusion.

- **Integrity monitoring:**

Another topic for future research is the integrity monitoring for the vector tracking architecture, which is of great importance for safety-critical and liability-critical land vehicle applications such as the road user charging (RUC). However, this represents a very complex operation for vector tracking techniques since signal tracking is jointly done by the navigation filter and thus, a fault in one channel can be propagated to the other tracking channels. Therefore, the single fault assumption considered in typical integrity monitoring techniques such as Receiver Autonomous Integrity Monitoring (RAIM) and Aircraft Autonomous Integrity Monitoring (AAIM) algorithms is not valid anymore in vector tracking architecture. Thus, the road toward the proposal of an integrity monitoring technique for the vector tracking receiver should pass through two major steps. Firstly, a measurement consistency check must be done at the code/carrier discriminator output level in order to identify the possible faulty channels. Secondly, the definition of the threat models for severe multipath conditions and LOS satellite blockages along with their probability of occurrence is required.

References

[Abbott and Lillo, 2003] A.S. Abbott and W.E. Lillo, *Global Positioning Systems and Intertial Measuring Unit Ultratight Coupling Method*, Feb. 2003, no. US 6,516,021 B1, pp. 18.

[Attia et al., 2010] D. Attia, C. Meurie, Y. Ruichek, J. Marais and A. Flancquart, *Image analysis based real time detection of satellites reception state*, 2010, pp. 1651–1656.

[Avila-Rodriguez et al., 2006] J.-A. Avila-Rodriguez, S. Wallner, G. Hein, E. Rebeyrol, O. Julien, C. Macabiau, L. Ries, A. De Latour, L. Lestarquit and J.-L. Issler, *CBOC – an Implementation of MBOC*, in Proceedings of CNES Workshop, Oct. 2006.

[Bastide, 2004] F. Bastide, *Galileo E5a/E5b and GPS L5 Acquisition Time Statistical Characterization and Application to Civil Aviation*, in Proceedings of ION GNSS, Sep. 2004.

[Betz, 2002] J.W. Betz, *Effect of Linear Time-Invariant Distortions on RNSS Code Tracking Accuracy*, in Proceedings of ION GPS, Sep. 2002.

[Betz and Kolodziejski, 2000] J.W. Betz and K.R. Kolodziejski, *Extended Theory of Early-Late Code Tracking for a Bandlimited GPS Receiver*, May 2000.

[Bevly, 2014] D. Bevly, *Navigation for Land Based Applications*, Sep. 2014.

[Bhattacharyya, 2012] S. Bhattacharyya, *Performance and Integrity Analysis of the Vector Tracking Architecture of GNSS Receivers*, Ph.D. Thesis, University of Minnesota, , 2012.

[Borre et al., 2007] K. Borre, D.M. Akos, N. Bertelsen, P. Rinder and S.H. Jensen, *A software-defined GPS and Galileo receiver: a single-frequency approach*, 2007.

[Brown and Hwang, 1996] R.. Brown and P.Y.. Hwang, *Introduction to Random Signals and Applied Kalman Filtering*, 1996.

[Curran, 2010] J.T. Curran, *Weak signal digital GNSS tracking algorithms*, Ph.D. Thesis, Department of Electrical and Electronic Engineering, National University of Ireland, , 2010.

[Di Giovanni and Radicella, 1990] G. Di Giovanni and S. Radicella, *An analytical model of the electron density profile in the ionosphere*, published in Advances in Space Research, 1990, vol. 10, pp. 27–30.

[Dierendonck et al., 1992] V.A. Dierendonck, P. Fenton and T. Ford, *Theory and performance of narrow correlator spacing in a GPS receiver*, published in Navigation, 1992, vol. 39, pp. 265–283.

[DLR, 2007] DLR, *Technical Note on the Implementation of the Land Mobile Satellite Channel Model - Software Usage*, Jul. 2007.

[DLR, 2008] DLR, *Technical Note on the Land Mobile Satellite Channel Model - Interface Control Document*, May 2008.

[Dovis and Mulassano, 2009] F. Dovis and P. Mulassano, *Introduction to Global Navigation Satellite Systems*, published in Politecnico I Torio, 2009.

[EUROCAE, 2010] EUROCAE, *MOPS for Airborne Open Service Galileo Satellite Receiving Equipment*, 2010.

[European Commission, 2016] European Commission, *European GNSS (Galileo) Open Service-Ionospheric Correction Algorithm for Galileo Single Frequency Users*, 2016.

[Farrell, 1998] J. Farrell, *Radical Streamlining of GPS/INS*, in Proceedings of ION GPS, Sep. 1998.

[Gleason and Gebre-Egziabher, 2009] S. Gleason and D. Gebre-Egziabher, *GNSS applications and methods*, 2009.

[Gold, 1967] R. Gold, *Optimal Binary Sequences for Spread Spectrum Multiplexing*, Oct. 1967, vol. 13, pp. 619–621.

[GPS.gov, 2006] GPS.gov, *Joint Statement on Galileo and GPS Signal Optimization By the European Commission (EC) and the United States (US)*, Mar. 2006.

[GPS.gov, 2008] GPS.gov, *Global Positioning System Standard Positioning Service Performance Standard*, Sep. 2008.

[GPS.gov, 2013] GPS.gov, *Navstar GPS Space Segment/Navigation User Interfaces, Interface Specification IS-GPS-200 Rev. D, IRN-200H*, Sep. 2013.

[GPS.gov, 2016] GPS.gov, *GPS.gov website available at http://www.gps.gov/systems/gps/*, Dec. 2016.

[Grewal et al., 2007] M.S. Grewal, R.W. Lawrence and P.A. Angus, *Global positioning systems, inertial navigation, and integration*, 2007.

[Groves, 2013] P.D. Groves, *Principles of GNSS, inertial, and multisensor integrated navigation systems*, 2013.

[GSA, 2010] GSA, *European GNSS (Galileo) Open Service, Signal In Space Interface Control Document*, 2010.

[GSA, 2016] GSA, *Galileo system description website at https://www.gsa.europa.eu/european-gnss/galileo/galileo-european-global-satellite-based-navigation-system*, 2016.

[GSA, 2017] GSA, *GNSS Market Report 2017- Issue 5*, 2017.

[Hegarty and Van Dierendonck, 1999] C. Hegarty and A.J. Van Dierendonck, *Civil GPS/WAAS Signal Design and Interference Environment at 1176.45 MHz: Results of RTCA SC159 WG1 Activities*, in Proceedings of ION GPS, Sep. 1999.

[ICAO, 2006] ICAO, *ICAO Convention - Annex 10: Aeronautical Telecommunications - Volume 1: Radio Navigation Aids*, 2006.

[ICAO, 2009] ICAO, *MOPS for GPS/ABAS Airborne Equipment*, Apr. 2009.

[Irsigler and Eissfeller, 2003] M. Irsigler and B. Eissfeller, *Comparison of Multipath Mitigation Techniques with Consideration of Future Signal Structures*, in Proceedings of ION GPS/GNSS, Sep. 2003.

[Jovancevic et al., 2004] A. Jovancevic, A. Brown, S. Ganguly, J. Noronha and B. Sirpatil, *Ultra Tight Coupling Implementation Using Real Time Software Receiver*, in Proceedings of ION GNSS, Sep. 2004.

[Julien, 2006] O. Julien, *Design of Galileo L1F receiver tracking loops*, 2006.

[Julien, 2006] O. Julien, *Design of Galileo L1F receiver tracking loops*, Ph.D. Thesis, University of Calgary, Canada, 2006.

[Julien et al., 2004] O. Julien, G. Lachapelle and M.E. Cannon, *A new multipath and noise mitigation technique using data/data-less navigation signals*, 2004, pp. 8–19.

[Julien et al., 2006] O. Julien, C. Macabiau, L. Ries and J.-L. Issler, *1-Bit processing of composite BOC (CBOC) signals*, in Proceedings of CNES-ESA Workshop, Oct. 2006.

[Kalman, 1960] R.E. Kalman, *New Approach to Linear Filtering and Prediction Problems,* Mar. 1960.

[Kaplan and Hegarty, 2006] D.E. Kaplan and J.C. Hegarty, *Understanding GPS: Principles and Applications. Second edition*, 2006.

[Kaplan and Hegarty, 2006] E.D. Kaplan and C.J. Hegarty, *Understanding GPS: principles and applications - Book*, 2006.

[Klobuchar, 1987] J.A. Klobuchar, *Ionospheric Time-Delay Algorithm for Single-Frequency GPS Users*, published in Aerospace and Electronic Systems, IEEE Transactions on, 1987, pp. 325–331.

[Lashley, 2009] M. Lashley, *Modeling and Performance Analysis of GPS Vector Tracking Algorithms*, Ph.D. Thesis, Auburn University, , 2009.

[Lashley et al., 2010] M. Lashley, D.M. Bevly and J.Y. Hung, *A valid comparison of vector and scalar tracking loops*, 2010, pp. 464–474.

[Lehner and Steingass, 2005] A. Lehner and A. Steingass, *A novel channel model for land mobile satellite navigation*, 2005, pp. 2132–2138.

[Macabiau et al., 2003] C. Macabiau, L. Ries, F. Bastide and J.-L. Issler, *GPS L5 Receiver Implementation Issues*, in Proceedings of ION GPS/GNSS, Sep. 2003.

[Misra, P., 2001] Misra, P., *Global Positioning System, Signals, Measurements and Performance*, 2001.

[Navipedia-GLO, 2016] Navipedia-GLO, *GLONASS Future and Evolutions*, 2016.

[Nunes and Sousa, 2014] F. Nunes and F. Sousa, *Practical Simulation of GNSS Signals in the Presence of Ionospheric Scintillation*, in Proceedings of IEEE/ION PLANS, May 2014.

[Pagot, 2016] J.-B. Pagot, *Modeling and Monitoring of New GNSS Signal Distortions in the Context of Civil Aviation*, Ph.D. Thesis, Institut National Polytechnique de Toulouse, Toulouse, France, Dec. 2016.

[Pany et al., 2005] T. Pany, R. Kaniuth and B. Eissfeller, *Deep Integration of Navigation Solution and Signal Processing*, in Proceedings of ION GNSS, Sep. 2005.

[Paonni et al., 2010] M. Paonni, M. Anghileri, S. Wallner, J.-Á. Ávila-Rodríguez and B. Eissfeller, *Performance Assessment of GNSS Signals in terms of Time to First Fix for Cold, Warm and Hot Start*, in Proceedings of ION ITM, Jan. 2010.

[Parkinson, 1996] B.W. Parkinson, *Progress in Astronautics and Aeronautics: Global Positioning System: Theory and Applications*, 1996, vol. 2.

[Petovello and Lachapelle, 2006] M. Petovello and G. Lachapelle, *Comparison of vector-based software receiver implementations with application to ultra-tight GPS/INS integration*, 2006.

[RTCA, 2006] RTCA, *DO 301 - MOPS for GNSS Airborne Active Antenna Equipment for the L1 Frequency Band (ke28je2)*, Dec. 2006.

[Salos, 2012] D. Salos, *Integrity Monitoring Applied to the Reception of Gnss Signals in Urban Environments*, Ph.D. Thesis, Institut National Polytechnique de Toulouse, , 2012.

[Seco-Granados et al., 2012] G. Seco-Granados, J.A. López-Salcedo, D. Jiménez-Baños and G. López-Risueño, *Challenges in indoor global navigation satellite systems: Unveiling its core features in signal processing*, published in Signal Processing Magazine, IEEE, 2012, vol. 29, pp. 108–131.

[Shytermeja et al., 2014] E. Shytermeja, A. Garcia-Pena and O. Julien, *Proposed architecture for integrity monitoring of a GNSS/MEMS system with a Fisheye camera in urban environment*, in Proceedings of International Conference on Localization and GNSS (ICL-GNSS), 2014, pp. 1–6.

[Shytermeja et al., 2017] E. Shytermeja, M.J. Pasnikowski, O. Julien and M.T. Lopez, *GNSS Quality of Service in Urban Environment*, Mar. 2017, pp. 79–105.

[Soloviev et al., 2004] A. Soloviev, S. Gunawardena and F. Van Graas, *Deeply Integrated GPS/Low-Cost IMU for Low CNR Signal Processing: Flight Test Results and Real Time Implementation*, in Proceedings of ION GNSS, Sep. 2004.

[Sousa and Nunes, 2014] F. Sousa and F. Nunes, *Performance Analysis of a VDFLL GNSS Receiver Architecture under Ionospheric Scintillation and Multipath Conditions*, in Proceedings of IEEE/ION PLANS, May 2014.

[Spilker et al., 1998] J. Spilker, H. Martin and B. Parkinson, *A Family of Split Spectrum GPS Civil Signals*, in Proceedings of ION GPS, Sep. 1998.

[Steingass and Lehner, 2004] A. Steingass and A. Lehner, *Measuring the Navigation Multipath Channel – A Statistical Analysis*, in Proceedings of ION GNSS, Sep. 2004.

[Stephens and Thomas, 1995] S.A. Stephens and J.B. Thomas, *Controlled-root formulation for digital phase-locked loops*, 1995, pp. 78–95.

[Taylor and Barnes, 2005] J. Taylor and E. Barnes, *GPS Current Signal-in-Space Navigation Performance*, in Proceedings of ION NTM, Jan. 2005.

[Winkel, 2003] J. Winkel, *Modeling and Simulating GNSS Signal Structures and Receivers*, Ph.D. Thesis, Universität der Bundeswehr München, , 2003.

[Won et al., 2009] J.-H. Won, D. Dötterböck and B. Eissfeller, *Performance Comparison of Different Forms of Kalman Filter Approach for a Vector-Based GNSS Signal Tracking Loop*, in Proceedings of ION GNSS, Sep. 2009.

[Zhu et al., 2015] F. Zhu, Y. Zhang, X. Su, H. Li and H. Guo, *GNSS position estimation based on Unscented Kalman Filter*, in Proceedings of ICOM), 2015.

Appendix A. Scalar Tracking Error Variance

This appendix aims at describing the model used in this dissertation to estimate the variance and the covariance of correlator outputs.

This appendix is divided in three sections. Firstly, the theoretical derivation of the correlator noise variance is presented. Secondly, the correlated noise covariance matrix of three correlator pairs is provided in details. Last but not least, the code and carrier NCO update calculation for the scalar tracking receiver is detailed.

A.1 Derivation of the Correlator Noise Variance

The received signal r from each satellite in-view, after the carrier wipe-off process, is expressed in the continuous-time domain as:

$$r(t) = A \cdot d(t-\tau) \cdot c(t-\tau) \cdot e^{j(2\pi \cdot \varepsilon_{f_D} \cdot t + \varepsilon_\varphi)} + n(t) \qquad \textit{(A-1)}$$

where:

- A denotes the signal amplitude;
- $d(t-\tau)$ denotes the navigation data stream;
- $c(t-\tau)$ is the signal PRN code;
- τ is the unknown signal delay that has to be estimated by the receiver;
- ε_φ is the received signal phase error;
- ε_{f_D} represents the Doppler frequency error of the received signal;
- $n(t)$ is the signal noise.

The received signal is further correlated with the receiver's generated code replica $c(t-\hat{\tau})$ and after being accumulated during the T integration period within the data bit transition, it yields:

$$\tilde{r}(t) = \frac{A}{T} \cdot \int_0^T c(t-\tau) \cdot c(t-\hat{\tau}) \cdot e^{j(2\pi \cdot \varepsilon_{f_D} \cdot t + \varepsilon_\varphi)} dt \qquad \textit{(A-2)}$$

The correlator outputs at the end of the integration interval $t = kT$ for the Early (E), Prompt (P) and Late (L) correlators are expressed as a combination of the in-phase and quadrature signal contributions $S_{I,Q,k}$ and their respective noise contributions $\eta_{I,Q,k}$ as:

$$\begin{aligned} Z_{(E,L,P),k} &= S_{(E,L,P),k} + n_{(E,L,P),k} \\ &= (S_{I-(E,L,P),k} + j \cdot S_{Q-(E,L,P),k}) + (n_{I-(E,L,P),k} + j \cdot n_{Q-(E,L,P),k}) \end{aligned} \qquad \textit{(A-3)}$$

In other words, the I and Q correlator output branches of the complex signal Z can be expressed as:

$$\begin{aligned} Z_{I,k} &= \mathrm{Re}\{Z_{(E,L,P),k}\} = S_{I,k} + n_{I,k} \\ Z_{Q,k} &= \mathrm{Im}\{Z_{(E,L,P),k}\} = S_{Q,k} + n_{Q,k} \end{aligned} \tag{A-4}$$

Developing the signal contributions from Eq. (A-2), for the Prompt correlator output only, the following expression is obtained:

$$\begin{aligned} S_{P,k} &= \frac{A}{T} \cdot \int_0^T c(t-\tau) \cdot c(t-\hat{\tau}) \cdot e^{j(2\pi \cdot \varepsilon_{f_D} \cdot t + \varepsilon_\varphi)}\, dt \\ &= \frac{A}{T} \cdot \int_0^T 1 \cdot e^{j(2\pi \cdot \varepsilon_{f_D} \cdot t + \varepsilon_\varphi)} dt \\ &= \frac{A}{T} \cdot e^{j\varphi} \cdot \int_0^T e^{j(2\pi \cdot \varepsilon_{f_D} \cdot t)} dt \\ &= \frac{A}{T} \cdot e^{j\varphi} \cdot \frac{e^{j(2\pi \cdot \varepsilon_{f_D} \cdot T)} - 1}{j(2\pi \cdot \varepsilon_{f_D} \cdot T)} \\ &= \frac{A}{T} \cdot e^{j\varphi} \cdot \frac{e^{j(\pi \cdot \varepsilon_{f_D} \cdot T)}(e^{j(\pi \cdot \varepsilon_{f_D} \cdot T)} - e^{-j(\pi \cdot \varepsilon_{f_D} \cdot T)})}{j(2\pi \cdot \varepsilon_{f_D} \cdot T)} \\ &= \frac{A}{T} \cdot e^{j\varphi} \cdot \frac{2j \cdot \sin(\pi \cdot \varepsilon_{f_D} \cdot T)}{j(2\pi \cdot \varepsilon_{f_D} \cdot T)} \\ &= \frac{A}{T} \cdot e^{j\Delta\theta_{com}} \cdot \mathrm{sinc}(\pi \cdot \varepsilon_{f_D} \cdot T) \end{aligned} \tag{A-5}$$

where $\Delta\theta_{com} = \varepsilon_\varphi + \pi \cdot \varepsilon_{f_D} \cdot T$.

The noise samples n_k affecting the in-phase and quadrature correlator outputs are given by [Misra, P., 2001]:

$$\begin{aligned} n_{I,k} &= \frac{\sqrt[2]{2}}{T} \cdot \int_0^T n(t) \cdot c(t-\hat{\tau}) \cdot \cos(2\pi \cdot (f_{IF} + \hat{f}_D) \cdot t + \hat{\varphi}) \\ n_{Q,k} &= \frac{\sqrt[2]{2}}{T} \cdot \int_0^T n(t) \cdot c(t-\hat{\tau}) \cdot \sin(2\pi \cdot (f_{IF} + \hat{f}_D) \cdot t + \hat{\varphi}) \end{aligned} \tag{A-6}$$

The mean value of the in-phase and quadrature noise samples is computed as follows:

$$\begin{aligned} E\{n_{I,k}\} = E\{n_{Q,k}\} &= E\left\{ \frac{\sqrt[2]{2}}{T} \cdot \int_0^T n(t) \cdot c(t-\hat{\tau}) \cdot \cos(2\pi \cdot (f_{IF} + \hat{f}_D) \cdot t + \hat{\varphi}) \right\} \\ &= \frac{\sqrt[2]{2}}{T} \cdot E\left\{ \int_0^T n(t) \cdot c(t-\hat{\tau}) \cdot \cos(2\pi \cdot (f_{IF} + \hat{f}_D) \cdot t + \hat{\varphi}) \right\} \end{aligned} \tag{A-7}$$

Since the noise vector $n(t)$ is modelled as an additive white Gaussian noise with zero mean, then $E\{n(t)\} = 0$ and therefore:

$$E\{n_{I,k}\} = E\{n_{Q,k}\} = 0 \tag{A-8}$$

On the other hand, the variance of the in-phase and quadrature noise samples are expressed as:

$$\begin{aligned} var\{n_{I,k}\} = var\{n_{Q,k}\} = & \; E\left\{\left(n_{I,k} - E\{n_{I,k}\}\right)^2\right\} = E\{n_{I,k}^2\} \\ & = E\{\frac{\sqrt[2]{2}}{T} \cdot \int_0^T n(t) \cdot c(t-\hat{\tau}) \cdot \cos(2\pi \cdot (f_{IF} + \hat{f}_D) \cdot t + \hat{\varphi}) dt \\ & \cdot \frac{\sqrt[2]{2}}{T} \cdot \int_0^T n(s) \cdot c(s-\hat{\tau}) \cdot \cos(2\pi \cdot (f_{IF} + \hat{f}_D) \cdot t + \hat{\varphi})\, ds\} \\ & = \frac{2}{T^2} \cdot \int_0^T \int_0^T E\{n(t) \cdot n(s)\} \cdot c(t-\hat{\tau}) \cdot c(s-\hat{\tau}) \\ & \cdot \cos\left(2\pi \cdot \left(f + \hat{f}_D\right) \cdot t + \hat{\theta}_n\right) \cdot \cos\left(2\pi \cdot \left(f + \hat{f}_D\right) \cdot s + \hat{\theta}_n\right)\, dt\, ds \end{aligned} \tag{A-9}$$

Since the carrier frequency f, varies more quickly than the code c, then the two frequency terms will average to zero and the expression above may be written as:

$$\begin{aligned} var\{n_{I,k}\} &= \frac{1}{T^2} \cdot \int_0^T \int_0^T E\{n(t) \cdot n(s)\} \cdot c(t-\hat{\tau}) \cdot c(s-\hat{\tau}) dt\, ds \\ &= \frac{1}{T^2} \cdot \int_0^T \int_0^T \frac{N_0}{2} \cdot \delta(t-s) \cdot c(t-\hat{\tau}) \cdot c(s-\hat{\tau}) dt\, ds \\ &= \frac{N_0}{4T^2} \cdot \int_0^T \int_0^T c(t-\hat{\tau}) \cdot c(s-\hat{\tau}) dt\, ds \\ &= \frac{N_0}{4T} \end{aligned} \tag{A-10}$$

where δ denotes the Dirac's function.

Summarizing, the noise variance at the in-phase and quadrature correlator outputs is given by:

$$\sigma^2 = var\{n_{I,k}\} = var\{n_{Q,k}\} = \frac{N_0}{4T} \tag{A-11}$$

for which $N_0 = k_b \cdot T_{sys}$ is the Gaussian noise density in $dBW - Hz$ where:

- $k_b = -228.6 \frac{dBW-Hz}{K}$ is the Boltzmann constant;
- T_{sys} is the system noise temperature in Kelvin scale.

A.2 Computation of the Noise Covariance Matrix

Assuming the correct evaluation of the data bit transition and neglecting the carrier phase and frequency errors contributions, the correlator model becomes:

$$\begin{aligned} I(\varepsilon_\tau) &= A \cdot R_c(\varepsilon_\tau) + n_I \\ Q(\varepsilon_\tau) &= A \cdot R_c(\varepsilon_\tau) + n_Q \end{aligned} \tag{A-12}$$

where:

- A is the received signal amplitude related to the signal power through the expression $A = \sqrt[2]{\frac{P}{2}}$;
- R_c is the correlation function of the filtered incoming code with the local spreading code, embedding all the propagation channel effects;
- ε_τ is the signal's code error in $[chips]$ expressed as the difference between the true (unknown) code delay and its locally-estimated counterpart ($\hat{\tau}$);
- n_I and n_Q are the noises at the in-phase and quadrature branches, respectively, assumed independent Gaussian-distributed and with the same power level.

Herein, only the noise variance of the in-phase correlator outputs is calculated. The same computation holds also for the quadrature-phase correlator.

The noise correlation function at the correlator output is defined by [Julien, 2006] through the use of inverse Fourier transform FFT^{-1} as:

$$\begin{aligned} R_{n_I}(\varepsilon_\tau) &= \frac{1}{2} \cdot \frac{N_0}{2T} \cdot \int_{-\infty}^{+\infty} |H_{RF}(f)|^2 \cdot r_{RO}(f) \cdot r_{RO}^*(f) \cdot e^{i \cdot 2\pi \cdot f \cdot \tau} \cdot d\tau \\ &= \frac{N_0}{4 \cdot T} \cdot FFT^{-1}[|H_{RF}(f)|^2 \cdot r_{RO}(f) \cdot r_{RO}^*(f)] \end{aligned} \quad \textit{(A-13)}$$

where

- $r_{RO}(f)$ is the Fourier transform of the local replica signal;
- $H_{RF}(f)$ is the RF filter transfer function (assuming to be equal to the pre-correlation filter);
- FFT^{-1} is the inverse Fourier transform.

In order to simplify the notation in Eq. (A-13), the correlation term R_m is introduced, and further substituted into Eq. (A-13):

$$R_{n_I}(\delta\tau) = \frac{N_0}{4 \cdot T} \cdot R_m(\tau) \quad \textit{(A-14)}$$

The noise standard deviation at the in-phase prompt correlator output is computed as the noise-signal power ratio given by:

$$\sigma(n_I) = \sqrt[2]{\frac{P_{n_I}}{P_s}} = \sqrt[2]{\frac{R_{n_I}}{A^2 \cdot R_s^2}} = \sqrt[2]{\frac{R_{n_I}}{\frac{P}{2} \cdot R_s^2}} = \sqrt[2]{\frac{2 \cdot R_{n_I}}{P \cdot R_s^2}} \quad \textit{(A-15)}$$

where R_s denotes the signal correlation function.

By introducing the relation between the signal power P and the carrier-to-noise ratio C/N_0 given in $dB - Hz$ as:

$$P = \frac{C}{\frac{N_0}{4 \cdot T}} = \frac{C}{N_0} \cdot 4 \cdot T \quad \textit{(A-16)}$$

The expression in Eq. (A-15) can now be rewritten as:

$$\sigma(n_I) = \sqrt[2]{\frac{2 \cdot R_{n_I}}{P \cdot R_s^2}} = \sqrt[2]{\frac{1}{2 \cdot T \cdot 10^{\left(\frac{C}{N_0}\right)/10}} \cdot \frac{R_{n_I}}{R_s^2}} \qquad \textit{(A-17)}$$

When the correlators output power is equally split between the two branches, thus $A = 1/2$, the correlator noise standard deviation value is twice higher:

$$\sigma(n_I) = \sqrt[2]{\frac{2 \cdot 2 \cdot R_{n_I}}{P \cdot R_s^2}} = \sqrt[2]{\frac{1}{T \cdot 10^{\left(\frac{C}{N_0}\right)/10}} \cdot \frac{R_{n_I}}{R_s^2}} \qquad \textit{(A-18)}$$

The noise correlation function value R_{n_I} follows clearly the signal correlation property, therefore $R_{n_I} \approx 1$. Finally, the noise variance for the three code correlators outputs, namely Early, Prompt and Late, can be computed as:

$$\begin{aligned}
\sigma(n_{IP}) &= \sqrt[2]{\frac{1}{2 \cdot T \cdot 10^{\left(\frac{C}{N_0}\right)/10}} \cdot \frac{1}{R_s^2(\varepsilon_\tau = 0)}} \\
\sigma(n_{IE}) &= \sqrt[2]{\frac{1}{2 \cdot T \cdot 10^{\left(\frac{C}{N_0}\right)/10}} \cdot \frac{1}{R_s^2\left(\varepsilon_\tau = -\frac{d_c \cdot T_c}{2}\right)}} = \frac{\sigma(n_{IP})}{R_{s,E}} \\
\sigma(n_{IL}) &= \sqrt[2]{\frac{1}{2 \cdot T \cdot 10^{\left(\frac{C}{N_0}\right)/10}} \cdot \frac{1}{R_s^2\left(\varepsilon_\tau = -\frac{d_c \cdot T_c}{2}\right)}} = \frac{\sigma(n_{IP})}{R_{s,L}}
\end{aligned} \qquad \textit{(A-19)}$$

Similarly, the relations of Eq. (A-19) hold for the quadrature-phase correlator branch. In order to correctly generate the noise contribution, it must be taken into account its correlation property among the correlator outputs (denoted by $x, y = E, P, L$). For this scope, the covariance can be obtained from the noise correlation function:

$$\begin{aligned}
cov\left(n_{I_x}, n_{I_y}\right) &= E\left[\left(n_{I_x} - E\left(n_{I_x}\right)\right) \cdot \left(n_{I_y} - E\left(n_{I_y}\right)\right)\right] \\
&= E\left(n_{I_x} \cdot n_{I_y}\right) - E\left(n_{I_x}\right) \cdot E\left(n_{I_y}\right)
\end{aligned} \qquad \textit{(A-20)}$$

Recalling that the noise at the correlation output is modelled as a random variable following a Gaussian distribution with zero mean and variance $\left(n_I \sim N\left(0, \sigma_{n_I}^2\right)\right)$, the expression of Eq. (A-20) becomes:

$$cov\left(n_{I_x}, n_{I_y}\right) = E\left(n_{I_x} \cdot n_{I_y}\right) = \frac{R_{n_I}(x - y)}{I_x \cdot I_y} \qquad \textit{(A-21)}$$

Substituting the expression in Eq. (A-18) into Eq. (A-21), the following relation is obtained:

$$cov\left(n_{I_x}, n_{I_y}\right) = \frac{R_{n_I}(x - y)}{I_x \cdot I_y} = \frac{1}{2 \cdot T \cdot 10^{C/N_0(dB-Hz)/10}} \cdot \frac{R_n(x - y)}{R_s(x) \cdot R_s(y)} \qquad \textit{(A-22)}$$

Finally, the noise covariance for the three correlator outputs along the in-phase branch are computed in Table A-1.

Table A-1. *Correlators' noise cross-correlation.*

	IE	**IP**	**IL**
IE	$R_n(IP-IP)=R_n(0)$	$R_n(IP-IE)=R_n\left(\frac{d_c\cdot T_c}{2}\right)$	$R_n(IL-IE)=R_n(d_c\cdot T_c)$
IP	$R_n(IE-IP)=R_n\left(-\frac{d_c\cdot T_c}{2}\right)$	$R_n(IP-IP)=R_n(0)$	$R_n(IL-IP)=R_n\left(\frac{d_c\cdot T_c}{2}\right)$
IL	$R_n(IE-IL)=R_n(-d_c\cdot T_c)$	$R_n(IP-IL)=R_n\left(-\frac{d_c\cdot T_c}{2}\right)$	$R_n(IL-IL)=R_n(0)$

The correlators' noise cross-correlation may be expressed in matrix format as:

$$R_{n_{3\times3}}=\begin{bmatrix} R_n(0) & R_n\left(\frac{d_c\cdot T_c}{2}\right) & R_n(d_c\cdot T_c) \\ R_n\left(-\frac{d_c\cdot T_c}{2}\right) & R_n(0) & R_n\left(\frac{d_c\cdot T_c}{2}\right) \\ R_n(-d_c\cdot T_c) & R_n\left(-\frac{d_c\cdot T_c}{2}\right) & R_n(0) \end{bmatrix} \quad \textit{(A-23)}$$

where $(d_c\cdot T_c)$ denotes the E-L chip spacing in unit of $[chips]$.

A.3 Code and Carrier NCO update

The loop filters objective is the discriminators output filtering for noise reduction purposes. The loop filter's output is subtracted from the original input signal to produce a correction factor, which is fed back into the receiver's channels in a closed loop process so as to update the current estimations [Kaplan and Hegarty, 2006]. Moreover, the code and carrier tracking response to the user dynamics depends on the loop's order and bandwidth. The loop's discrete signal update relating the filtered signal to the input one is presented via the *z*-transform operator. The frequency response of the tracking loop is obtained by [Stephens and Thomas, 1995]:

$$\hat{r}_z(z)=H_z(z)\cdot r_z(z) \quad \textit{(A-24)}$$

where $\hat{r}_z(z)$ and $r_z(z)$ are the *z*-transforms of the model and input signals, respectively and $H_z(z)$ denotes the closed-loop transfer function that is defined by:

$$H_z(z)=\frac{W(z)-(z-1)^N}{(z-1)^N} \quad \textit{(A-25)}$$

where:

$$\begin{aligned} W(z) &= (z-1)^N+(z-1)^{N-1}\cdot K_1+z\cdot(z-1)^N\cdot K_2+\cdots+z^{N-1}\cdot K_N \\ &= (z-1)^N+\sum_{i=1}^{N}(z-i)^{N-i}\cdot K_i\cdot z^{i-1} \end{aligned} \quad \textit{(A-26)}$$

Since this research work is focused on GNSS-based automotive applications, a 3rd order PLL and 1st order DLL are implemented for the scalar tracking receiver. Therefore, the PLL NCO update is computed according to the relations in Eq. (A-24) - (A-26)as follows:

$$\begin{aligned}\hat{\varphi}_z(z) &= H_z(z)\cdot\delta\varphi_z(z)\\ &= \frac{(z-1)^3+(z-1)^2\cdot K_1+z\cdot(z-1)\cdot K_2+z^2\cdot K_3-(z-1)^3}{(z-1)^3}\cdot D_{PLL}(z)\end{aligned} \quad \textit{(A-27)}$$

for which $D_{PLL}(z)$ represents the *z*-transform of the carrier phase discriminator.

By developing the relation and factorizing the common terms, the following relation is obtained:

$$\hat{\varphi}_z(z)\cdot(z^3-3z^2+3z+1) = [z^2\cdot(K_1+K_2+K_3)-z\cdot(2\cdot K_1+K_2)+K_1]\cdot D_{PLL}(z) \quad \textit{(A-28)}$$

Furthermore,

$$\begin{aligned}z^3\cdot\hat{\varphi}_z(z)-3z^2\cdot\hat{\varphi}_z(z)+3z\cdot\hat{\varphi}_z(z)+1 = {} & z^2\cdot(K_1+K_2+K_3)\cdot D_{PLL}(z)\\ & -z\cdot(2\cdot K_1+K_2)\cdot D_{PLL}(z)+K_1\cdot D_{PLL}(z)\end{aligned} \quad \textit{(A-29)}$$

Passing in the discrete time domain, the closed-loop PLL NCO update becomes:

$$\begin{aligned}\hat{\varphi}(k-3)-3\hat{\varphi}(k-2)+3\hat{\varphi}(k-1)+\hat{\varphi}(k) = {} & (K_1+K_2+K_3)\cdot D_{PLL}(k-2)\\ & -(2\cdot K_1+K_2)\cdot D_{PLL}(k-1)+K_1\cdot D_{PLL}(k)\end{aligned} \quad \textit{(A-30)}$$

For simplicity, let us substitute the right side of Eq. (A-30) by $M = (K_1+K_2+K_3)\cdot D_{PLL}(k-2) - (2\cdot K_1+K_2)\cdot D_{PLL}(k-1)+K_1\cdot D_{PLL}(k)$.

Re-expressing the left side of the relation above and dividing both sides by $(2\cdot\pi\cdot T_{PLL})$ where T_{PLL} indicated the PLL loop update interval, the 3rd order PLL NCO loop update $\left(f_{NCO,PLL}\right)$ is given by:

$$\begin{aligned}\frac{\left[\left(\hat{\varphi}(k)-\hat{\varphi}(k-1)\right)-2\left(\hat{\varphi}(k-1)-\hat{\varphi}(k-2)\right)-\left(\hat{\varphi}(k-2)-\hat{\varphi}(k-3)\right)\right]}{2\cdot\pi\cdot T_{PLL}} &= \frac{M}{2\cdot\pi\cdot T_{PLL}}\\ f_{NCO,PLL}(k)-2\cdot f_{NCO,PLL}(k-1)-f_{NCO,PLL}(k-2) &= \frac{M}{2\cdot\pi\cdot T_{PLL}}\end{aligned} \quad \textit{(A-31)}$$

As it can be clearly seen, the carrier phase NCO update when employing a 3rd order PLL loop depends on the carrier phase NCO and discriminator outputs from the two previous epochs and is computed as follows:

$$\begin{aligned}f_{NCO,PLL}(k) &= 2\cdot f_{NCO,PLL}(k-1)+f_{NCO,PLL}(k-2)\\ &= \frac{(K_1+K_2+K_3)\cdot D_{PLL}(k-2)-(2\cdot K_1+K_2)\cdot D_{PLL}(k-1)+K_1\cdot D_{PLL}(k)}{2\cdot\pi\cdot T_{PLL}}\end{aligned} \quad \textit{(A-32)}$$

In a similar manner, the 1st order DLL NCO update is given by:

$$f_{NCO,DLL}(k) = K_1\cdot D_{DLL}(k) \quad \textit{(A-33)}$$

where the 1st order loop coefficient $K_1 = 4\cdot B_{L-DLL/PLL}\cdot T_{DLL/PLL}$ is computed accordingly to the filter's loop bandwidth B_L and update interval T for the code and phase loops, respectively, while the second and third order loop coefficients (K_2, K_3) computation is detailed in [Kaplan and Hegarty, 2006].

Appendix B. Navigation Solution Estimators

This appendix provides the detailed description of the Weighted Least Square (WLS) navigation solution, starting firstly by the presentation of the WLS estimation principle and later with the derivation of the WLS state error covariance.

B.1 Weighted Least Squares (WLS) Estimation principle

Defining by $\boldsymbol{x} = [x_1\ x_2 \cdots x_M]^T$ the column state vector containing M unknowns that need to be estimated and $\boldsymbol{z} = [z_1\ z_2 \cdots z_M]^T$ the measurement residuals related to the state vector $\boldsymbol{x}$, the linear relation between the two vectors is described by the expression:

$$\boldsymbol{z} = \boldsymbol{H} \cdot \boldsymbol{x} + \boldsymbol{\varepsilon} \tag{B-1}$$

where $\boldsymbol{\varepsilon} = [\varepsilon_1\ \varepsilon_2 \cdots \varepsilon_N]^T$ denotes the measurement residuals errors and $\boldsymbol{H}$ is the $N \times M$ observation matrix relating the measurements to the states.

The best-fit solution of the state vector unknowns is the maximum likelihood estimate of $\boldsymbol{x}$ is defined as [Kaplan and Hegarty, 2006]:

$$\hat{\boldsymbol{x}} = \ argmax_{\boldsymbol{x}} \left\{ p\left(\frac{\boldsymbol{z}}{\boldsymbol{x}}\right) \right\} \tag{B-2}$$

Where $p\left(\frac{\boldsymbol{z}}{\boldsymbol{x}}\right)$ is the probability density function of the measurement **z** for the unknown **x**.

Considering that the measurement residual errors are Gaussian-distributed with zero-mean and covariance matrix $\boldsymbol{R_{N\times N}}$, then the maximum likelihood estimate is computed as:

$$\begin{aligned} \hat{\boldsymbol{x}} &= argmax_{\boldsymbol{x}} \left\{ \frac{\mathbf{1}}{(2\pi)^{N/2} \cdot \sqrt[2]{\boldsymbol{R_{N\times N}}}} exp\left[-\frac{1}{2} \cdot (\boldsymbol{z} - \boldsymbol{H} \cdot \boldsymbol{x})^{\boldsymbol{T}} \cdot \boldsymbol{R}_{\boldsymbol{N\times N}}^{-\mathbf{1}} \cdot (\boldsymbol{z} - \boldsymbol{H} \cdot \boldsymbol{x}) \right] \right\} \\ &= argmin_{\boldsymbol{x}} \left\{ (\boldsymbol{z} - \boldsymbol{H} \cdot \boldsymbol{x})^{\boldsymbol{T}} \cdot \boldsymbol{R}_{\boldsymbol{N\times N}}^{-\mathbf{1}} \cdot (\boldsymbol{z} - \boldsymbol{H} \cdot \boldsymbol{x}) \right\} \end{aligned} \tag{B-3}$$

The weighted least square solution is obtained by differentiating the expression above w.r.t to the state estimation $\hat{\boldsymbol{x}}$ as:

$$\frac{d}{d\hat{\boldsymbol{x}}} \left\{ (\boldsymbol{z} - \boldsymbol{H} \cdot \boldsymbol{x})^{\boldsymbol{T}} \cdot \boldsymbol{R}_{\boldsymbol{N\times N}}^{-\mathbf{1}} \cdot (\boldsymbol{z} - \boldsymbol{H} \cdot \boldsymbol{x}) \right\} = \left(\boldsymbol{H}^{\boldsymbol{T}} \boldsymbol{R}^{-\mathbf{1}} \boldsymbol{H} \right)^{-\mathbf{1}} \boldsymbol{H}^{\boldsymbol{T}} \boldsymbol{R}^{-\mathbf{1}} \cdot \boldsymbol{z} \tag{B-4}$$

Denoting as $\boldsymbol{K} = \left(\boldsymbol{H}^{\boldsymbol{T}} \boldsymbol{R}^{-\mathbf{1}} \boldsymbol{H} \right)^{-\mathbf{1}} \boldsymbol{H}^{\boldsymbol{T}} \boldsymbol{R}^{-\mathbf{1}}$, the WLS state vector estimate is provided by:

$$\hat{\boldsymbol{x}} = \ \boldsymbol{K} \cdot \boldsymbol{z} \tag{B-5}$$

B.2 WLS State Error Covariance matrix

Let $\boldsymbol{\epsilon}$ be the state estimation error vector given by:

$$\boldsymbol{\epsilon} = \hat{\boldsymbol{x}} - \boldsymbol{x} \tag{B-6}$$

The relationship between the user's estimation error vector ($\boldsymbol{\epsilon}$) and the measurement error vector ($\boldsymbol{\varepsilon}$) is obtained by substituting the expressions in Eq. (B-1) and (B-4) into Eq. (B-6) as:

$$\begin{aligned} \boldsymbol{\epsilon} &= \boldsymbol{K} \cdot \boldsymbol{z} - \boldsymbol{x} \\ &= \left(\boldsymbol{H^T R^{-1} H}\right)^{-1} \boldsymbol{H^T R^{-1}} \cdot (\boldsymbol{H} \cdot \boldsymbol{x} + \boldsymbol{\varepsilon}) - \boldsymbol{x} \\ &= \left(\boldsymbol{H^T R^{-1} H}\right)^{-1} \boldsymbol{H^T R^{-1}} \cdot \boldsymbol{\varepsilon} \\ &= \boldsymbol{K} \cdot \boldsymbol{\varepsilon} \end{aligned} \tag{B-7}$$

The estimation error covariance matrix is defined as:

$$cov\{\boldsymbol{\epsilon}\} = E\{\boldsymbol{\epsilon} \cdot \boldsymbol{\epsilon^T}\} - E\{\boldsymbol{\epsilon}\} \cdot E\{\boldsymbol{\epsilon}\}^T \tag{B-8}$$

Introducing the relations of Eq. (B-7) into Eq. (B-8), the covariance matrix can be rewritten as:

$$cov\{\boldsymbol{\epsilon}\} = E\{(\boldsymbol{K} \cdot \boldsymbol{\varepsilon}) \cdot (\boldsymbol{K} \cdot \boldsymbol{\varepsilon})^{\boldsymbol{T}}\} - E\{\boldsymbol{K} \cdot \boldsymbol{\varepsilon}\} \cdot E\{\boldsymbol{K} \cdot \boldsymbol{\varepsilon}\}^T \tag{B-9}$$

By developing the first term, the following expression is obtained:

$$\begin{aligned} E\{(\boldsymbol{K} \cdot \boldsymbol{\varepsilon}) \cdot (\boldsymbol{K} \cdot \boldsymbol{\varepsilon})^{\boldsymbol{T}}\} &= E\{\boldsymbol{K} \cdot \boldsymbol{\varepsilon} \cdot \boldsymbol{\varepsilon^T} \cdot \boldsymbol{K^T}\} \\ &= E\{\boldsymbol{K}\} \cdot E\{\boldsymbol{\varepsilon} \cdot \boldsymbol{\varepsilon^T}\} \cdot E\{\boldsymbol{K^T}\} \\ &= \boldsymbol{K} \cdot \boldsymbol{R} \cdot \boldsymbol{K^T} \end{aligned} \tag{B-10}$$

Developing the second term:

$$\begin{aligned} E\{\boldsymbol{K} \cdot \boldsymbol{\varepsilon}\} \cdot E\{\boldsymbol{K} \cdot \boldsymbol{\varepsilon}\}^T &= K \cdot E\{\boldsymbol{\varepsilon}\} + K \cdot E\{\boldsymbol{\varepsilon}\}^T \\ &= 0 \end{aligned} \tag{B-11}$$

Therefore the estimation error covariance matrix is given by:

$$cov\{\boldsymbol{\epsilon}\} = \boldsymbol{K} \cdot \boldsymbol{R} \cdot \boldsymbol{K^T} = (\boldsymbol{H^T} \cdot \boldsymbol{R^{-1}} \cdot \boldsymbol{H})^{-1} \tag{B-12}$$

Appendix C. Open-Loop Tracking Variance Models

This appendix aims provides the derivation of the open-loop variance models for the EMLP code and Cross Product (CP) carrier frequency discriminators, which constitute the measurement covariance matrix entries for the proposed VDFLL architecture.

C.1 The open-loop variance model of the code EMLP discriminator

The resulting complex signal at the output of the front-end stage, after baseband and low-pass filtering, is given by:

$$r(\tau, f_D, \varphi) = A \cdot d(t-\tau) \cdot c(t-\tau) \cdot e^{[j(\pi \cdot (f_{IF}+f_D) \cdot t + \varphi)]} + n(t) \qquad \textit{(C-1)}$$

where:

- A is the signal's amplitude;
- d is the navigation data;
- c refers to the signal PRN code;
- τ is the signal transit time from satellite i to the user's receiver;
- φ is the carrier signal phase;
- f_{IF}, f_D represent the carrier's Intermediate and the Doppler frequency, respectively;
- $n(t)$ represents the additive white Gaussian noise (AWGN) with power spectrum density equal to ${N_0}/{2}$.

The complex Early correlator output, obtained by correlating the incoming signal $r(\tau, f_D, \varphi)$ with the advanced code replica $c\left(t - \hat{\tau} - \frac{d_c \cdot T_c}{2}\right)$, can be written as:

$$\begin{aligned} E = IE + j \cdot QE &= \frac{1}{T_{int}} \int_0^{T_{int}} r(\tau, f_D, \varphi) \cdot c\left(t - \hat{\tau} - \frac{d_c \cdot T_c}{2}\right) dt \\ &= \frac{A}{T_{int}} \int_0^{T_{int}} d(t-\tau) \cdot c(t-\tau) \cdot c\left(t - \hat{\tau} - \frac{d_c \cdot T_c}{2}\right) \cdot e^{[j(\pi \cdot (f_D - \hat{f}_D) \cdot t + \varepsilon_\varphi)]} dt + n_E \end{aligned} \qquad \textit{(C-2)}$$

Assuming that the coherent integration does not occur during data bit transitions and that the Doppler frequency error is very small $\left(\varepsilon_{f_D} = f_D - \hat{f}_D \approx 0\right)$, by applying the linearity property of the integral operation the relation in Eq.(C-2) can be re-expressed as follows:

$$E = \frac{A}{T_{int}} \cdot d(t-\tau) \cdot e^{(j \cdot \varepsilon_\varphi)} \cdot \int_0^{T_{int}} c(t-\tau) \cdot c\left(t - \hat{\tau} - \frac{d_c \cdot T_c}{2}\right) dt + n_E$$
$$= A \cdot d(t-\tau) \cdot e^{(j \cdot \varepsilon_\varphi)} \cdot R_c\left(\varepsilon_\tau - \frac{d_c \cdot T_c}{2}\right) + n_E \qquad \textit{(C-3)}$$

where:

- $\varepsilon_\tau = \tau - \hat{\tau}$ denotes the PRN code delay error;
- R_c denotes the code autocorrelation function;
- $d_c \cdot T_c$ refers to the E-L chip spacing with d_c representing the fraction of chip spacing and T_c denotes the code chip period;

Similarly, the Late correlator output is given by:

$$L = IL + j \cdot QL$$
$$= A \cdot d(t-\tau) \cdot e^{(j \cdot \varepsilon_\varphi)} \cdot R_c\left(\varepsilon_\tau + \frac{d_c \cdot T_c}{2}\right) + n_L \qquad \textit{(C-4)}$$

The components of the complex noise for the Early and Late code correlator outputs $n_{E,L} = n_{IE,IL} + j \cdot n_{QE,QL}$ are independent zero-mean Gaussian random variables with variance $\sigma_n^2 = {N_0}/{4 \cdot T_{int}}$ as shown in Appendix A.1.

In this thesis, the Early Minus Late Power (EMLP) code discriminator is used, whose response after normalization is given by:

$$D_{EMLP,norm}(\varepsilon_\tau) = \frac{(IE^2 + QE^2) - (IL^2 + QL^2)}{(IE^2 + QE^2) + (IL^2 + QL^2)} \qquad \textit{(C-5)}$$

Neglecting the noise contributions, the normalized code discriminator yields:

$$D_{EMLP,norm}(\varepsilon_\tau) = \frac{P}{2} \cdot \frac{R_c^2\left(\varepsilon_\tau - d_c \cdot \frac{T_c}{2}\right) - R_c^2\left(\varepsilon_\tau + d_c \cdot \frac{T_c}{2}\right)}{R_c^2\left(\varepsilon_\tau - d_c \cdot \frac{T_c}{2}\right) + R_c^2\left(\varepsilon_\tau + d_c \cdot \frac{T_c}{2}\right)} \qquad \textit{(C-6)}$$

where P represents the incoming signal power.

For $|\varepsilon_\tau| \ll T_c$, the code autocorrelation function R_c can be approximated by:

$$R_c(\varepsilon_\tau) = 1 - \alpha \cdot |\varepsilon_\tau| \qquad \textit{(C-7)}$$

where α corresponds to the absolute slope of the code autocorrelation function around the main peak that is $\alpha_{GPS,L1} = 1/T_c$ for the GPS L1 BPSK(1) signal, $\alpha_{Gal,BOC} = 3/T_c$ for the Galileo E1 BOC(1,1) signal and $\alpha_{Gal,CBOC(6,1,1/11)} = (53 + 2\sqrt[2]{10})/11 \cdot T_c$ for the Galileo CBOC(6,1,1/11) pilot signal [Sousa and Nunes, 2014].

Substituting the simplified code autocorrelation expression from Eq. (C-7) into (C-6) and denoting for simplicity the E-L spacing as $\Delta = d_c \cdot T_c$, the normalized EMLP discriminator function can be expressed as:

$$
\begin{aligned}
D_{EMLP,norm}(\varepsilon_\tau) &= \frac{\left[R_c\left(\varepsilon_\tau - \frac{\Delta}{2}\right) - R_c\left(\varepsilon_\tau + \frac{\Delta}{2}\right)\right] \cdot \left[R_c\left(\varepsilon_\tau - \frac{\Delta}{2}\right) + R_c\left(\varepsilon_\tau + \frac{\Delta}{2}\right)\right]}{R_c^2\left(\varepsilon_\tau - \frac{\Delta}{2}\right) + R_c^2\left(\varepsilon_\tau + \frac{\Delta}{2}\right)} \\
&\approx \frac{P}{2} \cdot \frac{[2 \cdot \alpha \cdot \varepsilon_\tau] \cdot [2 - \alpha \cdot \Delta]}{\left(1 - \alpha \cdot \frac{\Delta}{2} + 1 - \alpha \cdot \frac{\Delta}{2}\right)^2} \\
&= \frac{P \cdot \alpha \cdot \varepsilon_\tau}{(2 - \alpha \cdot \Delta)}
\end{aligned}
\qquad \text{(C-8)}
$$

For easiness of treatment, the code EMLP discriminator may be expressed as follows [Misra, P., 2001]:

$$
\varepsilon_{\tau-EMLP} = \frac{\left(Z_{IE}^2 + Z_{QE}^2\right) - \left(Z_{IL}^2 + Z_{QL}^2\right)}{\left(Z_{IE}^2 + Z_{QE}^2\right) + \left(Z_{IL}^2 + Z_{QL}^2\right)} \qquad \text{(C-9)}
$$

Where the incoming signal Z at a given epoch k, for both the in-phase and quadrature branches, includes both the signal and noise contributions, expressed as:

$$
Z_k = S_k + n_k \qquad \text{(C-10)}
$$

According to the incoming signal expression in Eq. (C-10), the normalized EMLP code discriminator can be re-written as follows:

$$
\varepsilon_{\tau-EMLP} = \frac{\left[|(S_{IE} + n_{IE})|^2 + \left|\left(S_{QE} + n_{QE}\right)\right|^2\right] - \left[|(S_{IL} + n_{IL})|^2 + \left|\left(S_{QL} + n_{QL}\right)\right|^2\right]}{\left[|(S_{IE} + n_{IE})|^2 + \left|\left(S_{QE} + n_{QE}\right)\right|^2\right] + \left[|(S_{IL} + n_{IL})|^2 + \left|\left(S_{QL} + n_{QL}\right)\right|^2\right]} \qquad \text{(C-11)}
$$

For simplicity, the following substitution for the nominator and denominator are made:

$$
\begin{aligned}
A &= \left[|(S_{IE} + n_{IE})|^2 + \left|\left(S_{QE} + n_{QE}\right)\right|^2\right] - \left[|(S_{IL} + n_{IL})|^2 + \left|\left(S_{QL} + n_{QL}\right)\right|^2\right] \\
B &= \left[|(S_{IE} + n_{IE})|^2 + \left|\left(S_{QE} + n_{QE}\right)\right|^2\right] + \left[|(S_{IL} + n_{IL})|^2 + \left|\left(S_{QL} + n_{QL}\right)\right|^2\right]
\end{aligned}
\qquad \text{(C-12)}
$$

Developing the above relations, the following expressions are obtained:

$$
\begin{aligned}
A &= \left[|(S_{IE} + n_{IE})|^2 + \left|\left(S_{QE} + n_{QE}\right)\right|^2\right] - \left[|(S_{IL} + n_{IL})|^2 + \left|\left(S_{QL} + n_{QL}\right)\right|^2\right] \\
&= S_{IE}^2 + 2 \cdot S_{IE} \cdot n_{IE} + n_{IE}^2 + S_{QE}^2 + 2 \cdot S_{QE} \cdot n_{QE} + n_{QE}^2 - S_{IL}^2 - 2 \cdot S_{IL} \cdot n_{IL} \\
&\quad - n_{IL}^2 - S_{QL}^2 - 2 \cdot S_{QL} \cdot n_{QL} - n_{QL}^2
\end{aligned}
\qquad \text{(C-13)}
$$

and,

$$
\begin{aligned}
B &= \left[|(S_{IE} + n_{IE})|^2 + \left|\left(S_{QE} + n_{QE}\right)\right|^2\right] - \left[|(S_{IL} + n_{IL})|^2 + \left|\left(S_{QL} + n_{QL}\right)\right|^2\right] \\
&= S_{IE}^2 + 2 \cdot S_{IE} \cdot n_{IE} + n_{IE}^2 + S_{QE}^2 + 2 \cdot S_{QE} \cdot n_{QE} + n_{QE}^2 + S_{IL}^2 + 2 \cdot S_{IL} \cdot n_{IL} \\
&\quad + n_{IL}^2 + S_{QL}^2 + 2 \cdot S_{QL} \cdot n_{QL} + n_{QL}^2
\end{aligned}
\qquad \text{(C-14)}
$$

where the signal and noise contributions are given by:

$$
\begin{aligned}
S_{IE} &= \mathrm{Re}\{\tilde{S}_E\} = \frac{A}{2}\cdot R_c\left(\varepsilon_\tau - \frac{\Delta}{2}\right)\cdot\cos\left(2\pi\cdot\varepsilon_{f_D}\cdot T + \varepsilon_\varphi\right)\\
S_{QE} &= \mathrm{Im}\{\tilde{S}_E\} = \frac{A}{2}\cdot R_c\left(\varepsilon_\tau + \frac{\Delta}{2}\right)\cdot\sin\left(2\pi\cdot\varepsilon_{f_D}\cdot T + \varepsilon_\varphi\right)\\
S_{IL} &= \mathrm{Re}\{\tilde{S}_L\} = \frac{A}{2}\cdot R_c\left(\varepsilon_\tau - \frac{\Delta}{2}\right)\cdot\cos\left(2\pi\cdot\varepsilon_{f_D}\cdot T + \varepsilon_\varphi\right)\\
S_{QL} &= \mathrm{Im}\{\tilde{S}_L\} = \frac{A}{2}\cdot R_c\left(\varepsilon_\tau + \frac{\Delta}{2}\right)\cdot\sin\left(2\pi\cdot\varepsilon_{f_D}\cdot T + \varepsilon_\varphi\right)\\
n_{IE} &= \mathrm{Re}\{\tilde{n}_E\} \quad , \quad n_{QE} = \mathrm{Im}\{\tilde{n}_E\}\\
n_{IL} &= \mathrm{Im}\{\tilde{n}_L\} \quad , \quad n_{QL} = \mathrm{Im}\{\tilde{n}_L\}
\end{aligned}
\qquad \textit{(C-15)}
$$

For which the operators Re and Im refer to the real and imaginary components of the complex signal (with the symbol ∼).

The expectance of the discriminator output is obtained by averaging the signal and noise contributions that yields the final error signal given as follows:

$$
\begin{aligned}
E\{\varepsilon_{\tau-EMLP}\} &= \frac{E\left\{\left[|(S_{IE}+n_{IE})|^2 + \left|\left(S_{QE}+n_{QE}\right)\right|^2\right] - \left[|(S_{IL}+n_{IL})|^2 + \left|\left(S_{QL}+n_{QL}\right)\right|^2\right]\right\}}{E\left\{\left[|(S_{IE}+n_{IE})|^2 + \left|\left(S_{QE}+n_{QE}\right)\right|^2\right] + \left[|(S_{IL}+n_{IL})|^2 + \left|\left(S_{QL}+n_{QL}\right)\right|^2\right]\right\}}\\
&= \frac{E\{A\}}{E\{B\}}
\end{aligned}
\qquad \textit{(C-16)}
$$

Substituting the relations from Eq. (C-13) and Eq. (C-14) into Eq. (C-16), the EMLP nominator and denominator expectances can be further developed as follows:

$$
\begin{aligned}
E\{A\} &= E\left\{\left[|(S_{IE}+n_{IE})|^2 + \left|\left(S_{QE}+n_{QE}\right)\right|^2\right] - \left[|(S_{IL}+n_{IL})|^2 + \left|\left(S_{QL}+n_{QL}\right)\right|^2\right]\right\}\\
&= E\{S_{IE}^2\} + 2\cdot E\{S_{IE}\}\cdot E\{n_{IE}\} + E\{n_{IE}^2\} + E\{S_{QE}^2\} + 2\cdot E\{S_{QE}\}\cdot E\{n_{QE}\} + E\{n_{QE}^2\}\\
&-E\{S_{IL}^2\} - 2\cdot E\{S_{IL}\}\cdot E\{n_{IL}\} - E\{n_{IL}^2\} - E\{S_{QL}^2\} - 2\cdot E\{S_{QL}\}\cdot E\{n_{QL}\} - E\{n_{QL}^2\}\\
&= S_{IE}^2 + 2\cdot S_{IE}\cdot E\{n_{IE}\} + E\{n_{IE}^2\} + S_{QE}^2 + 2\cdot S_{QE}\cdot E\{n_{QE}\} + E\{n_{QE}^2\} - S_{IL}^2\\
&-2\cdot S_{IL}\cdot E\{n_{IL}\} - S_{QL}^2 - 2\cdot S_{QL}\cdot E\{n_{QL}\} - E\{n_{QL}^2\}
\end{aligned}
\qquad \textit{(C-17)}
$$

and similarly for the denominator term:

$$
\begin{aligned}
E\{B\} &= E\left\{\left[|(S_{IE}+n_{IE})|^2 + \left|\left(S_{QE}+n_{QE}\right)\right|^2\right] + \left[|(S_{IL}+n_{IL})|^2 + \left|\left(S_{QL}+n_{QL}\right)\right|^2\right]\right\}\\
&= E\{S_{IE}^2\} + 2\cdot E\{S_{IE}\}\cdot E\{n_{IE}\} + E\{n_{IE}^2\} + E\{S_{QE}^2\} + 2\cdot E\{S_{QE}\}\cdot E\{n_{QE}\} + E\{n_{QE}^2\}\\
&+E\{S_{IL}^2\} + 2\cdot E\{S_{IL}\}\cdot E\{n_{IL}\} + E\{n_{IL}^2\} + E\{S_{QL}^2\} + 2\cdot E\{S_{QL}\}\cdot E\{n_{QL}\} + E\{n_{QL}^2\}\\
&= S_{IE}^2 + 2\cdot S_{IE}\cdot E\{n_{IE}\} + E\{n_{IE}^2\} + S_{QE}^2 + 2\cdot S_{QE}\cdot E\{n_{QE}\} + E\{n_{QE}^2\} + S_{IL}^2\\
&+2\cdot S_{IL}\cdot E\{n_{IL}\} + S_{QL}^2 + 2\cdot S_{QL}\cdot E\{n_{QL}\} + E\{n_{QL}^2\}
\end{aligned}
\qquad \textit{(C-18)}
$$

The Early and Late signal and noise contributions denoted by S_E, S_L and n_E, n_L, respectively, are given by:

$$
\begin{aligned}
|S_E|^2 &= S_{IE}^2 + S_{QE}^2 = \frac{A^2}{4} \cdot R_c^2\left(\varepsilon_\tau - \frac{\Delta}{2}\right) \\
|S_L|^2 &= S_{IL}^2 + S_{QL}^2 = \frac{A^2}{4} \cdot R_c^2\left(\varepsilon_\tau + \frac{\Delta}{2}\right) \\
|n_E|^2 &= n_{IE}^2 + n_{QE}^2 \\
|n_L|^2 &= n_{IL}^2 + n_{QL}^2
\end{aligned}
\qquad \textit{(C-19)}
$$

Knowing that the noise samples follow an additive zero-mean white Gaussian distribution, we may write:

$$
\begin{aligned}
E\{n_{IE}\} = E\{n_{IL}\} = E\{n_{QE}\} = E\{n_{QL}\} = 0 \\
var\{n_E\} = var\{n_L\} = E\{(n_E - E\{n_E\})^2\} = E\{n_E^2\} = \frac{N_0}{2 \cdot T}
\end{aligned}
\qquad \textit{(C-20)}
$$

Applying the signal and noise relations from Eq. (C-19) and (C-20) into Eq. (C-17) and (C-18), the EMLP discriminator expectance is given by:

$$
\begin{aligned}
E\{A\} &= S_{IE}^2 + S_{QE}^2 - \left(S_{IL}^2 + S_{QL}^2\right) + E\{n_{IE}^2\} + E\{n_{QE}^2\} - \left(E\{n_{IL}^2\} + E\{n_{QL}^2\}\right) \\
&= S_E^2 - S_L^2 + E\{n_E^2\} - E\{n_L^2\} \\
&= S_E^2 - S_L^2 \\
&= \frac{A^2}{4} \cdot \left[R_c^2\left(\varepsilon_\tau - \frac{\Delta}{2}\right) - R_c^2\left(\varepsilon_\tau + \frac{\Delta}{2}\right)\right] \\
&= \frac{A^2}{4} \cdot \left[\left(R_c\left(\varepsilon_\tau - \frac{\Delta}{2}\right) - R_c\left(\varepsilon_\tau + \frac{\Delta}{2}\right)\right) \cdot \left(R_c\left(\varepsilon_\tau - \frac{\Delta}{2}\right) + R_c\left(\varepsilon_\tau + \frac{\Delta}{2}\right)\right)\right] \\
&= \frac{A^2}{2} \cdot \alpha \cdot \varepsilon_\tau \cdot (2 - \alpha \cdot \Delta)
\end{aligned}
\qquad \textit{(C-21)}
$$

And,

$$
\begin{aligned}
E\{B\} &= S_{IE}^2 + S_{QE}^2 + S_{IL}^2 + S_{QL}^2 + E\{n_{IE}^2\} + E\{n_{QE}^2\} + E\{n_{IL}^2\} + E\{n_{QL}^2\} \\
&= S_E^2 + S_L^2 + E\{n_E^2\} + E\{n_L^2\} \\
&= \frac{A^2}{4} \cdot \left[R_c^2\left(\varepsilon_\tau - \frac{\Delta}{2}\right) + R_c^2\left(\varepsilon_\tau + \frac{\Delta}{2}\right)\right] + \frac{N_0}{T} \\
&= \frac{A^2}{4} \cdot \left(1 - \frac{\alpha \cdot \Delta}{2} - 1 - \frac{\alpha \cdot \Delta}{2}\right)^2 + \frac{N_0}{T} \\
&= \frac{A^2}{4} \cdot (2 - \alpha \cdot \Delta)^2 + \frac{N_0}{T}
\end{aligned}
\qquad \textit{(C-22)}
$$

Finally, the noise expectance of the un-normalized and normalized EMLP discriminator are respectively given as:

$$
\begin{aligned}
E\{\varepsilon_{\tau-EMLP,un-norm}\} &= \frac{A^2}{2} \cdot \alpha \cdot \varepsilon_\tau \cdot (2 - \alpha \cdot \Delta) \\
E\{\varepsilon_{\tau-EMLP,norm}\} &= \frac{A^2}{4} \cdot (2 - \alpha \cdot \Delta)^2 + \frac{N_0}{T}
\end{aligned}
\qquad \textit{(C-23)}
$$

The variance of the EMLP discriminator noise samples can be computed as follows:

$$\begin{aligned} var\{\varepsilon_{\tau-EMLP}\} &= E\{(\varepsilon_{\tau-EMLP} - E\{\varepsilon_{\tau-EMLP}\})^2\} \\ &= E\{\varepsilon^2_{\tau-EMLP}\} - 2\cdot E\{\varepsilon_{\tau-EMLP}\cdot E\{\varepsilon_{\tau-EMLP}\}\} + E^2\{\varepsilon_{\tau-EMLP}\} \\ &= E\{\varepsilon^2_{\tau-EMLP}\} - 2\cdot E\{\varepsilon_{\tau-EMLP}\}\cdot E\{\varepsilon_{\tau-EMLP}\} + E^2\{\varepsilon_{\tau-EMLP}\} \\ &= E\{\varepsilon^2_{\tau-EMLP}\} - E^2\{\varepsilon_{\tau-EMLP}\} \end{aligned} \quad \textit{(C-24)}$$

The first term is computed as follows:

$$\begin{aligned} E\{\varepsilon^2_{\tau-EMLP}\} &= E\left\{\left[\left|(S_{IE}+n_{IE})\right|^2 + \left|\left(S_{QE}+n_{QE}\right)\right|^2\right] - \left[\left|(S_{IL}+n_{IL})\right|^2 + \left|\left(S_{QL}+n_{QL}\right)\right|^2\right]\right\}^2 \\ &= E\{S_E^2 + 2\cdot S_{IE}\cdot E\{n_{IE}\} + E\{n_{IE}^2\} + S_{QE}^2 + 2\cdot S_{QE}\cdot E\{n_{QE}\} + E\{n_{QE}^2\} - S_L^2 \\ &-2\cdot S_{IL}\cdot E\{n_{IL}\} - 2\cdot S_{QL}\cdot E\{n_{QL}\} - E\{n_{QL}^2\}\}^2 \end{aligned} \quad \textit{(C-25)}$$

Recalling that the In-phase (I) and Quadrature (Q) noise samples and their early (E) and late (L) contributions are mutually uncorrelated, the following relations hold:

$$E\{n_{x_1y_1}\cdot n_{x_2y_2}\} = 0 \qquad for\ x_1,x_2 = \{I,Q\}\ \&\ y_1,y_2 = \{E,L\}\ \&\ (x_1 \neq x_2)\&(y_1 \neq y_2) \quad \textit{(C-26)}$$

The expectation of the additive white Gaussian noise samples raised in the third and fourth power are detailed below.

$E\{n_{xy}^3\}$ can be computed based on the concept of *moment coefficient of skewness* of a random variable that is the third standardized moment, denoted by γ_1 and defined as:

$$\gamma_1 = E\left\{\left(\frac{X-E(X)}{\mathrm{var}(X)}\right)^3\right\} = E\left\{\left(\frac{X-\mu}{\sigma}\right)^3\right\} = \frac{\mu_3}{\sigma^3} \quad \textit{(C-27)}$$

where:

- μ is the mean value of the Gaussian-distributed random variable X ($\mu = 0$);
- σ denotes its standart deviation;
- μ_3 represents the third central moment that for a Gaussian distribution is $\mu_3 = 0$.

The formula expressing the skewness in terms of $E(X^3)$ in Eq. (C-27) can be expanded as follows:

$$\begin{aligned} \gamma_1 &= E\left\{\left(\frac{X-E(X)}{\mathrm{var}(X)}\right)^3\right\} \\ &= \frac{E(X^3) - 3\cdot\mu\cdot E(X^2) + 3\cdot\mu^2\cdot E(X) - \mu^3}{\sigma^3} \\ &= \frac{E(X^3) - 3\cdot\mu\cdot\left(E(X^2) - \mu\cdot E(X)\right) - \mu^3}{\sigma^3} \\ &= \frac{E(X^3) - 3\cdot\mu\cdot\sigma^2 - \mu^3}{\sigma^3} \end{aligned} \quad \textit{(C-28)}$$

Combining Eq. (C-27) and (C-28), the following expression is obtained:

$$\frac{\mu_3}{\sigma^3} = \frac{E(X^3) - 3\cdot\mu\cdot\sigma^2 - \mu^3}{\sigma^3} \quad \textit{(C-29)}$$

Herein, the random variable X represents the additive white Gaussian noise samples that are characterized by a zero third central moment ($\mu_3 = 0$), thus:

$$0 = \frac{E(X^3)}{\sigma^3} \rightarrow E(X^3) = 0 \qquad \textit{(C-30)}$$

Therefore,

$$E\{n_{xy}^3\} = 0 \qquad \textit{(C-31)}$$

On the other side, $E\{n_E^4\}$ and $E\{n_L^4\}$ can be computed based on the concept of *kurtosis*, defined as the measure or "peakedness" of the probability distribution of a random variable and represented from the fourth standardized moment, denoted by β_2 and defined as [Brown and Hwang, 1996]:

$$\beta_2 = E\left\{\left(\frac{X - E(X)}{\mathrm{var}(X)}\right)^4\right\} = E\left\{\left(\frac{X-\mu}{\sigma}\right)^4\right\} = \frac{\mu_4}{\sigma^4} \qquad \textit{(C-32)}$$

where μ_4 represents the fourth central moment that for a Gaussian distribution is $\mu_4 = 3 \cdot \sigma^4$.

The relation expressing the skewness in terms of $E(X^4)$ in Eq. (C-32) can be expanded as follows:

$$\begin{aligned} \beta_2 &= E\left\{\left(\frac{X-\mu}{\sigma}\right)^4\right\} \\ &= \frac{E(X^4) - 4\cdot\mu\cdot E(X^3) + 6\cdot\mu^2\cdot E(X^2) - 4\cdot\mu^3\cdot E\{X\} + \mu^4}{\sigma^4} \\ &= \frac{E(X^4)}{\sigma^4} \end{aligned} \qquad \textit{(C-33)}$$

By substituting Eq. (C-30) into (C-33) and recalling that the noise sample are zero-mean Gaussian distributed, the following relation can be written:

$$3 = \frac{E(X^4)}{\sigma^4} \rightarrow E(X^4) = 3 \cdot \sigma^4 \qquad \textit{(C-34)}$$

Finally,

$$E\{\tilde{\eta}_E^4\} = E\{\tilde{\eta}_L^4\} = 3 \cdot \sigma^4 = 3 \cdot \left(\frac{N_0}{2T}\right)^2 \qquad \textit{(C-35)}$$

Substituting the relations given in Eq. (C-26), (C-31) and (C-35) into Eq. (C-24) and (C-25) and after further developments, the EMLP discriminator noise variance in the open-loop configuration is expressed by:

$$var\{\varepsilon_{\tau-EMLP}\} = \sigma^2_{\varepsilon_{\tau-EMLP}} = \frac{\Delta}{2\cdot\alpha\cdot\left(C/N_0\right)\cdot T_{int}} = \frac{d\cdot T_c}{2\cdot\alpha\cdot\left(C/N_0\right)\cdot T_{int}} \qquad \textit{(C-36)}$$

C.2 The open-loop variance model of the frequency Cross-Product discriminator (CP)

The Cross Product discriminator, noted as CP, is in fact reputed to be the most computationally efficient frequency discriminator and is defined as:

$$CP(k) = \frac{IP(k-1) \cdot QP(k) - IP(k) \cdot QP(k-1)}{t_k - t_{k-1}} \quad \textit{(C-37)}$$

Or,

$$CP(k) = \frac{IP(k-1) \cdot QP(k) - IP(k) \cdot QP(k-1)}{T_{int}} \quad \textit{(C-38)}$$

Where:

- $T_{int} = t_k - t_{k-1}$ is the integration period between the two successive epochs $k-1$ and k;
- IP and QP are the in-phase and quadrature prompt signal samples.

The output frequency error $\varepsilon_{CP}(k)$ is a sinusoidal function of successive phase errors and depends on the signal amplitude. For easiness of treatment, the Cross Product FLL discriminator may be expressed as follows [Misra, P., 2001]:

$$\varepsilon_{CPD}(k) = Z_{I,k-1} \cdot Z_{Q,k} - Z_{I,k} \cdot Z_{Q,k-1} \quad \textit{(C-39)}$$

Where the incoming signal Z, for both the in-phase and quadrature branches, includes both the signal and noise contributions, expressed as:

$$Z_k = S_k + n_k \quad \textit{(C-40)}$$

The expectance of the discriminator output is obtained by averaging the signal and noise contributions that yields the final error signal given as follows:

$$\begin{aligned} E(\varepsilon_{CP}) &= E\left(Z_{I,k-1} \cdot Z_{Q,k} - Z_{I,k} \cdot Z_{Q,k-1}\right) \\ &= E\left[(S_{I,k-1} + n_{I,k-1}) \cdot (S_{Q,k} + n_{Q,k}) - (S_{I,k} + n_{I,k}) \cdot (S_{Q,k-1} + n_{Q,k-1})\right] \\ &= E[(S_{I,k-1} \cdot S_{Q,k}) + (S_{I,k-1} \cdot n_{Q,k}) + (S_{Q,k} \cdot n_{I,k-1}) + (n_{I,k-1} \cdot n_{Q,k}) - \cdots \\ &-(S_{I,k} \cdot S_{Q,k-1}) - (S_{I,k} \cdot n_{Q,k-1}) - (S_{Q,k-1} \cdot n_{I,k}) - (n_{I,k-1} \cdot n_{Q,k})] \\ &= E\{S_{I,k-1} \cdot S_{Q,k}\} + S_{I,n-1} \cdot E\{n_{Q,k}\} + S_{Q,n} \cdot E\{n_{I,k-1}\} + E\{n_{I,k-1} \cdot n_{Q,k}\} - \\ &-E\{S_{I,k} \cdot S_{Q,k-1}\} - S_{I,k} \cdot E\{n_{Q,k-1}\} - S_{Q,k-1} \cdot E\{n_{I,k}\} - E\{n_{I,k-1} \cdot n_{Q,k}\} \end{aligned} \quad \textit{(C-41)}$$

Recalling that the in-phase and quadrature noise samples are modelled as independent and uncorrelated Gaussian-distributed variables with expectation $E\{n_{I,k}\} = E\{n_{Q,k}\} = 0$ and $E\{n_{I,k} \cdot n_{Q,k}\} = 0$, the expression above can be reduced to:

$$E(\varepsilon_{CP}) = E\left\{S_{I,k-1} \cdot S_{Q,k} - S_{I,k} \cdot S_{Q,k-1}\right\} \quad \textit{(C-42)}$$

In the error analysis of the Cross Product FLL discriminator, we assume a very small frequency error Δf_D, which in commercial GPS receiver means that $\varepsilon_{f_D} < 200\ Hz$, and this brings that $sinc(\pi \cdot \varepsilon_{f_D} \cdot T) \sim 1$. However, the received signal phase is still under the influence of the frequency error and can be expressed as the sum of the initial phase error ε_{φ_0} and the frequency error term multiplied by the integration time as:

$$\varepsilon_{\varphi} = \varepsilon_{\varphi_0} + \pi \cdot \varepsilon_{f_D} \cdot T \quad \textit{(C-43)}$$

Therefore, the expectation of the Cross Product discriminator error can be expanded as:

$$\begin{aligned} E\{\varepsilon_{CPD}\} &= E\{S_{I,k-1}\cdot S_{Q,k} - S_{I,k}\cdot S_{Q,k-1}\} \\ &= A\cdot[\cos\left(\varepsilon_{\varphi_0}+\pi\cdot(k-1)\cdot\varepsilon_{f_D}\cdot T\right)\cdot\sin\left(\varepsilon_{\varphi_0}+\pi\cdot k\cdot\varepsilon_{f_D}\cdot T\right) \\ &-\cos\left(\varepsilon_{\varphi_0}+\pi\cdot k\cdot\varepsilon_{f_D}\cdot T\right)\cdot\sin\left(\varepsilon_{\varphi_0}+\pi\cdot(k-1)\cdot\varepsilon_{f_D}\cdot T\right)] \end{aligned} \quad \textit{(C-44)}$$

Using the following trigonometric identity:

$$\sin\alpha\cdot\cos\beta-\cos\alpha\cdot\sin\beta=\sin(\alpha-\beta)\approx\alpha-\beta \quad \textit{(C-45)}$$

Finally,

$$\begin{aligned} E\{\varepsilon_{CPD}\} &= E\{S_{I,k-1}\cdot S_{Q,k} - S_{I,k}\cdot S_{Q,k-1}\} \\ &= A\cdot\left[\cos(\varepsilon_{\varphi_{k-1}})\cdot\sin(\varepsilon_{\varphi_k})-\cos(\varepsilon_{\varphi_k})\cdot\sin(\varepsilon_{\varphi_{k-1}})\right] \\ &= A\cdot\sin(\varepsilon_{\varphi_k}-\varepsilon_{\varphi_{k-1}}) \\ &= A\cdot\sin(\pi\cdot\varepsilon_{f_D}\cdot T) \\ &= A\cdot(\pi\cdot\varepsilon_{f_D}\cdot T) \end{aligned} \quad \textit{(C-46)}$$

The variance of the discriminator error is computed based on the following relation [Misra, P., 2001]:

$$\mathrm{var}(X)=E\{X^2\}-(E\{X\})^2, \quad \textit{(C-47)}$$

where the second term $(E\{X\})^2$ has been already calculated in Eq. (C-46). Therefore, the first term $E\{X^2\}$ has to be computed as:

$$\begin{aligned} E\{{\varepsilon_{CPD}}^2\} &= E\left\{\left(Z_{I,k-1}\cdot Z_{Q,k}-Z_{I,k}\cdot Z_{Q,k-1}\right)^2\right\} \\ &= E\left\{\left(Z_{I,k-1}\cdot Z_{Q,k}-Z_{I,k}\cdot Z_{Q,k-1}\right)\cdot\left(Z_{I,k-1}\cdot Z_{Q,k}-Z_{I,k}\cdot Z_{Q,k-1}\right)\right\} \\ &= E\left\{{Z^2}_{I,k-1}\cdot{Z^2}_{Q,k}\right\}-2\cdot E\{Z_{I,k-1}\cdot Z_{I,k}\cdot Z_{Q,k-1}\cdot Z_{Q,k}\} \\ &+E\left\{{Z^2}_{I,k}\cdot{Z^2}_{Q,k-1}\right\} \end{aligned} \quad \textit{(C-48)}$$

The first term is developed as follows:

$$\begin{aligned} E\left\{{Z^2}_{I,k-1}\cdot{Z^2}_{Q,k}\right\} &= E\{(S_{I,k-1}+n_{I,k-1})^2\cdot(S_{Q,k}+n_{Q,k})^2\} \\ &= E\{({S^2}_{I,k-1}+2\cdot S_{I,k-1}\cdot n_{I,k-1}+{n^2}_{I,k-1})\cdot\cdots \\ &\cdot({S^2}_{Q,k}+2\cdot S_{Q,k}\cdot n_{Q,k}+{n^2}_{Q,k})\} \\ &= E\left\{{S^2}_{I,k-1}\cdot{S^2}_{Q,k}\right\}+2\cdot E\left\{{S^2}_{I,k-1}\cdot S_{Q,k}\cdot n_{Q,k}\right\}+E\left\{{S^2}_{I,k-1}\cdot{n^2}_{Q,k}\right\} \\ &+2\cdot E\left\{S_{I,k-1}\cdot{S^2}_{Q,k}\cdot n_{I,k-1}\right\}+4\cdot E\left\{S_{I,k-1}\cdot S_{Q,k}\cdot n_{I,k-1}\cdot n_{Q,k}\right\} \\ &+2\cdot E\left\{S_{I,k-1}\cdot{n^2}_{Q,k}\cdot n_{I,k-1}\right\}+E\left\{{n^2}_{I,k-1}\cdot{S^2}_{Q,k}\right\} \\ &+2\cdot E\left\{S_{Q,k}\cdot{n^2}_{I,k-1}\cdot n_{Q,k}\right\}+E\left\{{n^2}_{I,k-1}\cdot{n^2}_{Q,k}\right\} \end{aligned} \quad \textit{(C-49)}$$

Recalling that:

$$\begin{aligned} E\{c\} &= c \\ E\{a\cdot n_{(I,Q),k}\} &= a\cdot E\{n_{(I,Q),k}\}=0 \\ E\{n_I\cdot n_Q\} &= E\{n_I\}\cdot E\{n_Q\}=0 \\ E\{n_I^2\cdot n_Q^2\} &= E\{n_I^2\}\cdot E\{n_Q^2\}=\sigma^4 \end{aligned} \quad \textit{(C-50)}$$

The first term is then reduced to:

$$E\left\{{Z^2}_{I,k-1}\cdot{Z^2}_{Q,k}\right\}={S^2}_{I,k-1}\cdot{S^2}_{Q,k}+\sigma^2\cdot{S^2}_{I,k-1}+\sigma^2\cdot{S^2}_{Q,k}+\sigma^4 \quad \textit{(C-51)}$$

Passing now to the second term of Eq. (C-48):

$$
\begin{aligned}
E\{Z_{I,k-1}\cdot Z_{I,k}\cdot Z_{Q,k-1}\cdot Z_{Q,k}\} &= E\{(S_{I,k-1}+n_{I,k-1})\cdot(S_{I,k}+n_{I,k})\cdot(S_{Q,k-1}+n_{Q,k-1})\cdot(S_{Q,k}+n_{Q,k})\}\\
&= E\{(S_{I,k-1}\cdot S_{I,k}+S_{I,k-1}\cdot n_{I,k}+S_{I,k}\cdot n_{I,k-1}+n_{I,k-1}\cdot n_{I,k})\cdot\cdots\\
&\cdot(S_{Q,k-1}\cdot S_{Q,k}+S_{Q,k-1}\cdot n_{Q,k}+S_{Q,k}\cdot n_{Q,k-1}+n_{Q,k-1}\cdot n_{Q,k})\}\\
&= (S_{I,k-1}\cdot S_{I,k}\cdot S_{Q,k-1}\cdot S_{Q,k}+S_{I,k-1}\cdot S_{I,k}\cdot S_{Q,k-1}\cdot E\{n_{Q,k}\}\\
&+S_{I,k-1}\cdot S_{I,k}\cdot S_{Q,k}\cdot E\{n_{Q,k-1}\}+S_{I,k-1}\cdot S_{I,k}\cdot E\{n_{Q,k-1}\}\cdot E\{n_{Q,k}\})\\
&+(S_{I,k-1}\cdot S_{Q,k-1}\cdot S_{Q,k}\cdot E\{n_{I,k}\}+S_{I,k-1}\cdot S_{Q,k-1}\cdot E\{n_{I,k}\}\cdot E\{n_{Q,k}\}\\
&+S_{I,k-1}\cdot S_{Q,k}\cdot E\{n_{I,k}\}\cdot E\{n_{Q,k-1}\}+S_{I,k-1}\cdot E\{n_{I,k}\}\cdot E\{n_{Q,k-1}\cdot n_{Q,k}\}\\
&+\big(S_{I,k}\cdot S_{Q,k-1}\cdot S_{Q,k}\cdot E\{n_{I,k-1}\}+S_{I,k}\cdot S_{Q,k-1}\cdot E\{n_{I,k-1}\}\cdot E\{n_{Q,k}\}\\
&+S_{I,k}\cdot S_{Q,k}\cdot E\{n_{I,k-1}\}\cdot E\{n_{Q,k-1}\}+S_{I,k}\cdot E\{n_{I,k-1}\}\cdot E\{n_{Q,k-1}\cdot n_{Q,k}\})\\
&+(S_{Q,k-1}\cdot S_{Q,k}\cdot E\{n_{I,k-1}\}\cdot E\{n_{I,k}\}+S_{Q,k-1}\cdot E\{n_{I,k-1}\cdot n_{I,k}\}\cdot E\{n_{Q,k}\}\\
&+S_{Q,k}\cdot E\{n_{I,k-1}\cdot n_{I,k}\}\cdot E\{n_{Q,k-1}\}+E\{n_{I,k-1}\cdot n_{I,k}\}\cdot E\{n_{Q,k-1}\cdot n_{Q,k}\})
\end{aligned}
\qquad \textit{(C-52)}
$$

By applying the relations of Eq. (C-51) into Eq. (C-52), the following expression is obtained:

$$
\begin{aligned}
E\{Z_{I,k-1}\cdot Z_{I,k}\cdot Z_{Q,k-1}\cdot Z_{Q,k}\} &= S_{I,k-1}\cdot S_{I,k}\cdot S_{Q,k-1}\cdot S_{Q,k}+S_{I,k-1}\cdot S_{I,k}\cdot\sigma^2\\
&+S_{Q,k-1}\cdot S_{Q,k}\cdot\sigma^2+\sigma^4
\end{aligned}
\qquad \textit{(C-53)}
$$

Similarly, the third term is summarized below:

$$
E\{{Z^2}_{I,k}\cdot {Z^2}_{Q,k-1}\} = {S^2}_{I,k}\cdot {S^2}_{Q,k-1}+\sigma^2\cdot {S^2}_{I,k}+\sigma^2\cdot {S^2}_{Q,k-1}+\sigma^4 \qquad \textit{(C-54)}
$$

Substituting the three developed terms of Eq. (C-51), (C-53) and (C-54) into Eq. (C-48), it can be observed that the first product consisting of the signal contributions only, will sum to the square mean value of the error signal. Finally, the variance of the Cross Product discriminator output is given by:

$$
var\{\varepsilon_{CPD}\} = C\cdot\sigma^2+\sigma^4 \qquad \textit{(C-55)}
$$

Finally, the normalized Cross Product (CP) discriminator error variance is computed as follows:

$$
\begin{aligned}
var\{\varepsilon_{CPD-normalized}\} &= \frac{var\{\varepsilon_{CPD}\}}{\left(\frac{\partial E\{\varepsilon_{CPD}\}}{\partial\varepsilon_{f_D}}\right)^2}\\
&= \frac{C\cdot\sigma^2+\sigma^4}{\left(\frac{\partial(\pi\cdot C\cdot\varepsilon_{f_D}\cdot T)}{\partial\varepsilon_{f_D}}\right)^2}\\
&= \frac{C\cdot\sigma^2+\sigma^4}{\left(\frac{\partial(\pi\cdot C\cdot\varepsilon_{f_D}\cdot T)}{\partial\varepsilon_{f_D}}\right)^2}\\
&= \frac{C\sigma^2\cdot\left(1+\frac{\sigma^4}{C\sigma^2}\right)}{\pi^2\cdot C^2\cdot T^2}\\
&= \frac{1}{\pi^2\cdot C/N_0\cdot T^3}\cdot\left(1+\frac{1}{T\cdot C/N_0}\right)
\end{aligned}
\qquad \textit{(C-56)}
$$

Appendix D. Additional Results on the Performance Assessment

This appendix completes the performance assessment of the scalar and vector tracking receiver configurations by providing extra results and plots both in the navigation and channel domain. This appendix is divided in two sections. The first one, provides a different representation of the Monte Carlo performance analysis in the navigation level by means of the Cumulative Distribution Functions (CDFs) used for both the scalar and vector tracking receiver architectures. Secondly, the performance comparison results expressed in the navigation and channel level are provided in the presence of multipath conditions only.

D.1 Monte Carlo additional results in the position domain

In the current part, the performance analysis focuses on the navigation solution errors only. The cumulative distribution function (CDF) of the EKF estimation errors concerning the 2-D position, velocity errors and the receiver's clock bias and drift states for the VDFLL EKF (in blue) and Scalar tracking (ST) + EKF filter (in red) are respectively provided in Figure D-1, Figure D-2 and Figure D-3.

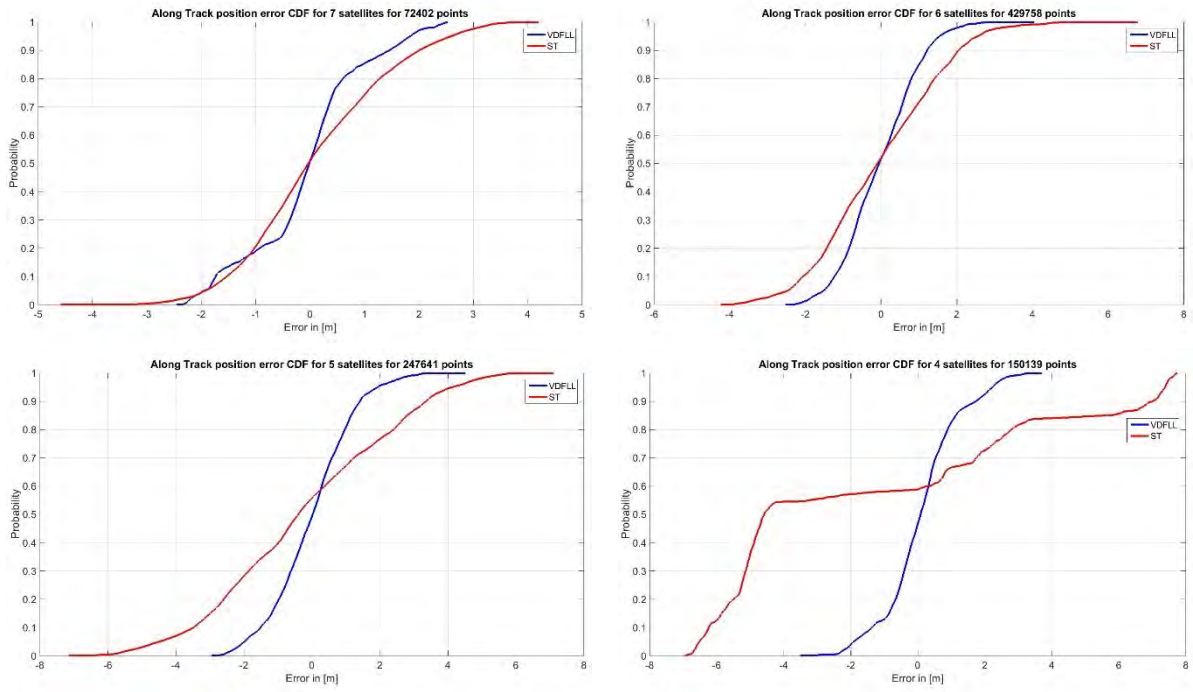

a)

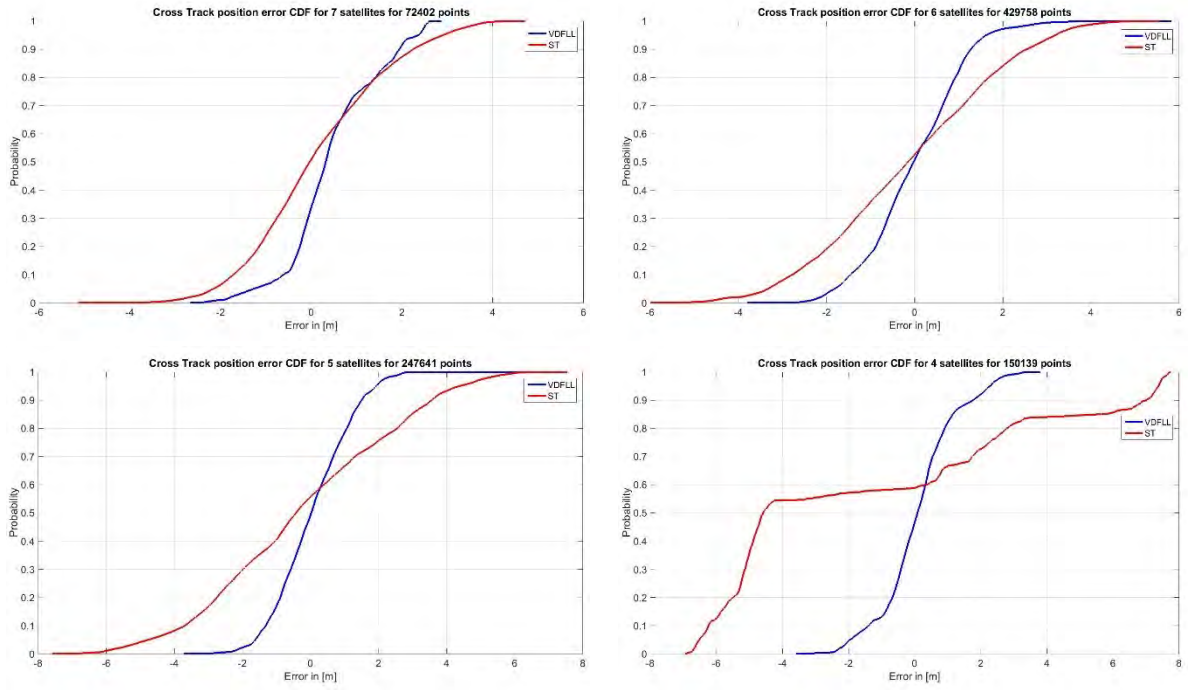

b)

Figure D-1. ***a)*** *Along- and* ***b)*** *Cross track position errors CDFs from Monte Carlo simulations.*

The CDF representation of the navigation errors provides a clear insight of the error statistics and their bounding. For a proper validation of the scalar and vector tracking architectures, the Monte Carlo simulations have been applied to a reduced number of observations starting from a maximum number of 7 satellites (top left) to 4 satellites in view (bottom right), which represents the minimum EKF filter requirement for the navigation solution convergence.

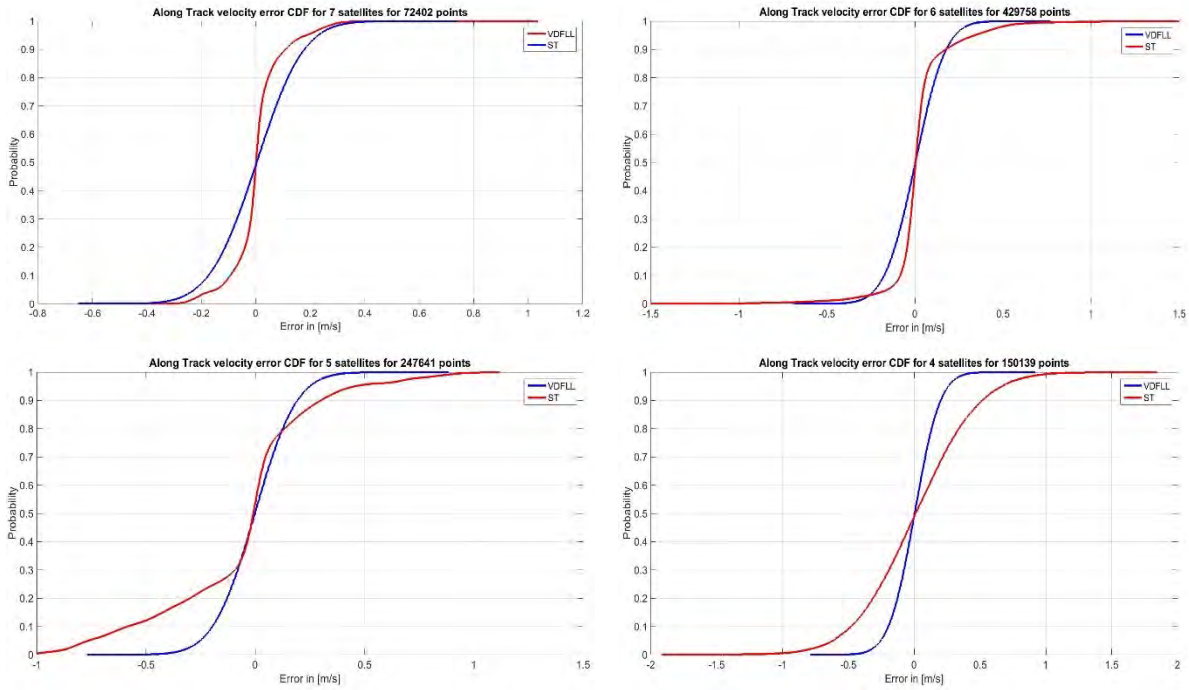

a)

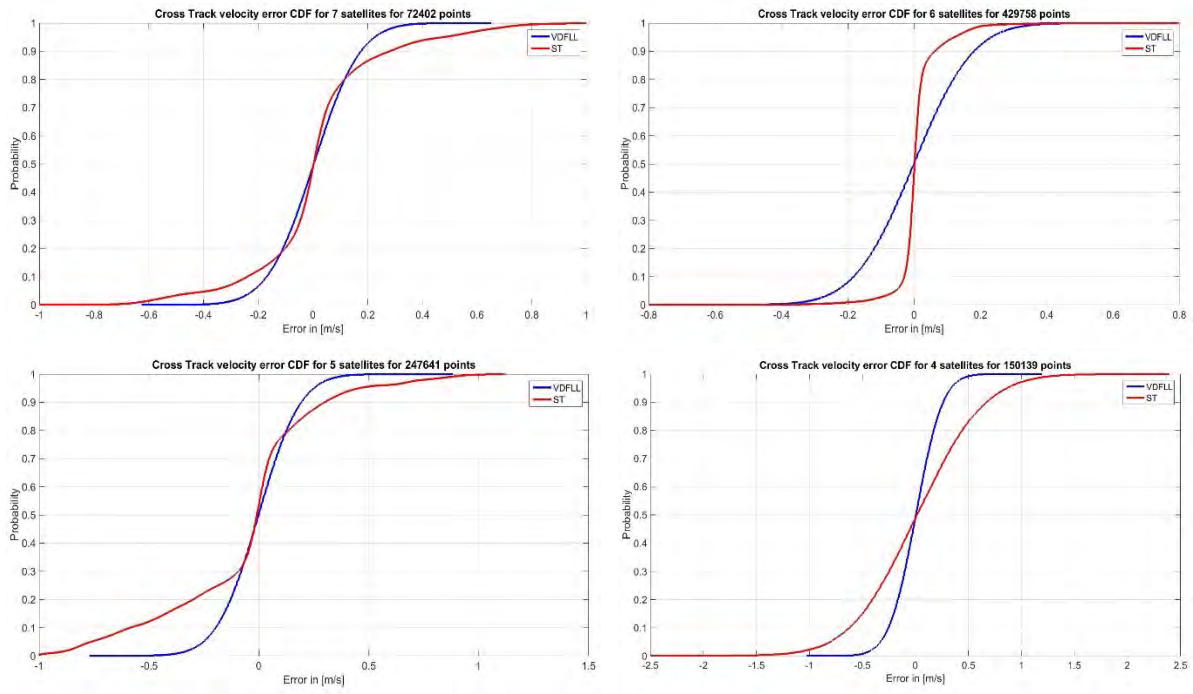

b)

Figure D-2. ***a)*** *Along- and* ***b)*** *Cross track velocity errors CDFs from Monte Carlo simulations.*

An overall observation that can be made based on the CDFs curves for each estimation error, is that they quietly resemble to the CDF pattern of a normal distribution. In fact, this remark suits correctly to the EKF Gaussian distribution assumption concerning the process and measurement noises. Observing the plots in Figure D-1, a significant position estimation degradation in both along and cross track coordinates is exhibited by the ST+EKF navigation filter (red curve) with the reduction of the number of observations from 7 to 4 satellites in-view. This degradation becomes even more evident when only 4 satellites are used for the navigation solution estimation, which is related to the inclusion of the bare minimum number of measurements for the correct filter operation that at the same time are also significantly affected by the ionosphere residual errors.

On the contrary, the VDFLL technique conserves a stable position estimation within the $2.75\ m$ 95 – percentile bound, giving the impression of being nearly insensitive to the reduction of number of tracked satellites. The reasons behind the VDFLL EKF stability in the navigation domain are twofold. Firstly, the VDFLL EKF filter is modified with the objective of estimating the ionosphere residual errors by augmenting the state vector X_{VDFLL} with the residual states per tracked channel and also by modifying the discrete state transition matrix with the inclusion of residual's Gauss-Markov power decaying functions, as already described in Chapter 5. Secondly, the code and carrier NCO updates in the feedback loop, computed from the position and velocity estimations projected in the pseudorange and pseudorange rate domain, encompass the ionosphere residual error corrections. This ensures the position estimation error reduction in a recursive manner from the current to the following measurement epoch.

A slightly better performance of the VDFLL technique is also noticed in the along and cross track velocity estimations, as illustrated in Figure D-2. This equivalent performance between the two architectures can be explained by the slow variation in time of the ionosphere residuals. Furthermore, the perfect S-shape of the velocity CDFs curves is related to the Gaussian distribution property of the

ionosphere residual rates, computed as the derivative of the ionosphere residual errors that are modelled as 1st order Gauss-Markov processes.

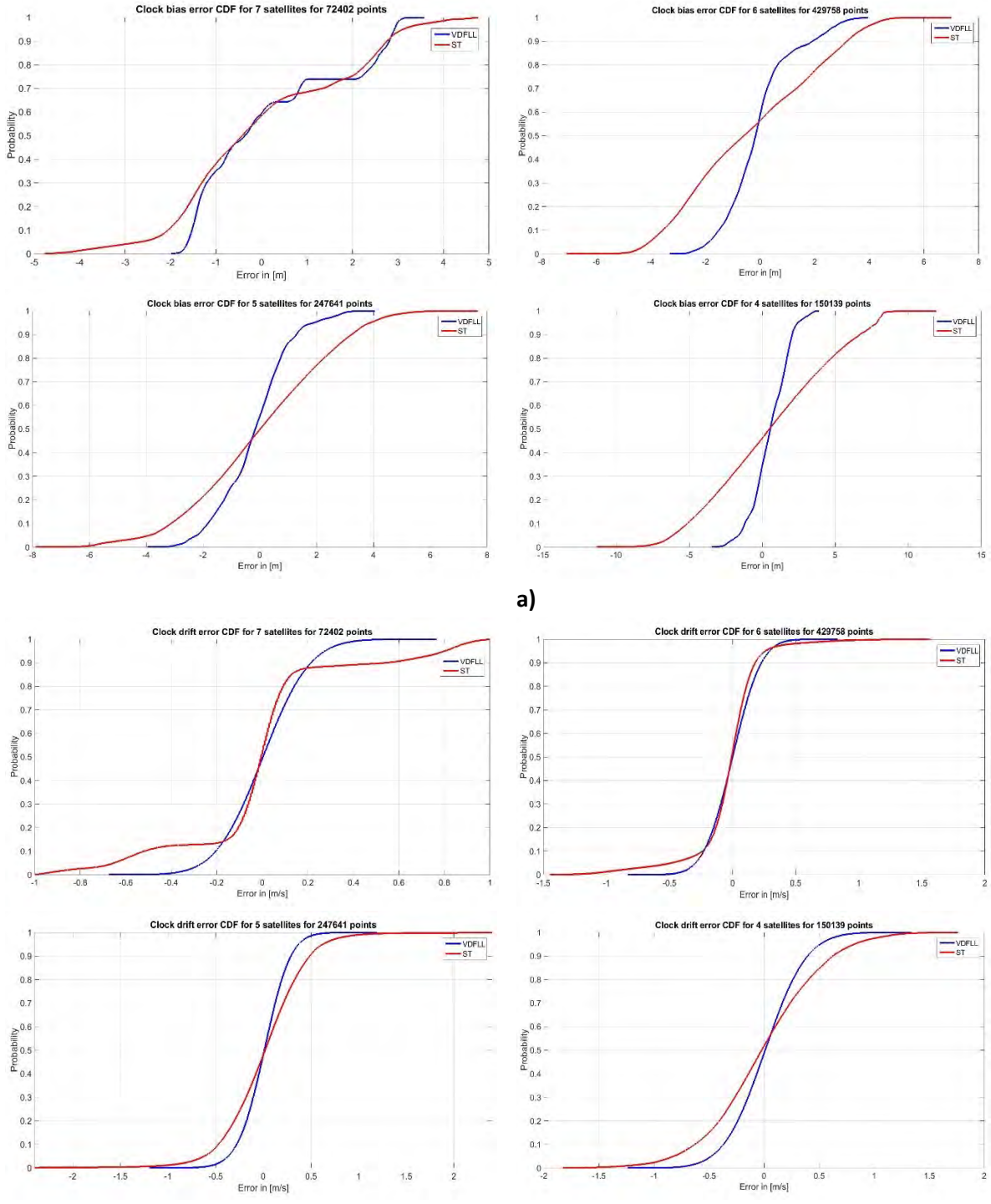

Figure D-3. ***a)*** *Clock bias and* ***b)*** *Clock drift errors CDFs from Monte Carlo simulations.*

The most marked VDFLL superiority concerns the receiver's clock bias estimation in the presence of few available measurements, as can be seen in Figure D-3 a). When carefully observing the clock bias error CDFs for both the vectorized and scalar receiver operation modes, it can be noticed that the clock bias estimation error magnitude exceeds the position errors. In fact, all the unestimated or not correctly estimated position errors are projected to the least observable state that is the user's clock

bias. This logic is also verified by the clock bias CDF curves deformation, which is particularly evident for the first plot in Figure D-3 a) due to the lower number of Monte Carlo points when 7 satellites are being processed w.r.t the other cases.

Concerning the clock drift estimation errors in Figure D-3 b), comparable performance can be identified between the two techniques, which is similar to the velocity estimation characteristic. Finally, it may be concluded that a direct translation chain between the code delay errors that include the ionosphere residuals contribution and the position + clock bias states exists. The same direct relation holds between the carrier frequency errors, comprising the ionosphere residual rates, and the velocity + clock drift states.

D.2 Performance Assessment in Multipath condition

D.2.1. Objective

This test aims at the performance comparison of the two receiver configurations in urban conditions characterized by the multipath reception conditions and LOS blockage events, with the later that are translated into reduced number of observables fed to the navigation filters. Furthermore, in this test the measurements are not affected from the ionosphere residuals.

D.2.2. Scenario characteristics

The simulated reception conditions are that of an automotive car trajectory in multipath signal reception condition. During the reference car trajectory, in total 13 GPS and Galileo satellites are constantly in view and being tracked by the receiver, as it was illustrated in the skyplot from Figure 7-2. As previously stated in section 7.3, the multipath reception conditions are generated by the DLR channel generation program described in section 6.2.2. Moreover, the channel impulse response (CIR) by showing the multipath power delay profiles (PDPs) for each tracked GPS and Galileo channels along the urban car trajectory of ten minutes duration are illustrated in Figure 7-7.

D.2.3. Methodology

In this test scenario, only one simulation was conducted with the same car trajectory presented in section 7.1, in multipath reception conditions and with the same GPS/Galileo constellation geometry. As it was the case for the previous tests in chapter 7, the EKF filter operation for the two architectures is initiated only after the convergence of the WLS-estimated position solution has been reached.

D.2.4. Results in Multipath environment

The following sub-section is dedicated to the provision of the comparison results in the navigation level, in terms of PVT errors along the trajectory, and further on code and carrier estimation errors along with their distribution pattern. The results description in both levels are concluded with their respective tables of statistics.

D.2.4.1. Navigation Level Analysis

The GPS and Galileo constellation geometry in multipath condition along the car trajectory is illustrated in Figure D-4. Of particular interest are the two areas included in the red circle and dotted blue rectangle, which represent the sudden decrease of the number of LOS satellites in view. Moreover, the red area 1 is of double importance since it coincides both with the EKF filter initialization period and also with the strongest outage event, leading to the presence of only three LOS satellites for the position computation.

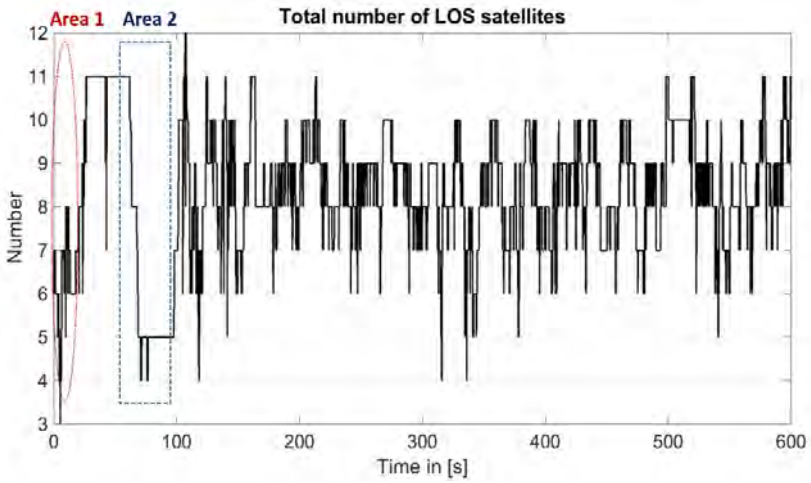

Figure D-4. *GPS and Galileo constellations geometry in multipath condition.*

The position and velocity error comparison between the scalar tracking (ST) + EKF positioning module and the VDFLL algorithm, both operating at $50\ Hz$ update rate, are presented in Figure D-5 and Figure D-6. Both figures present the EKF estimation errors along the entire trajectory in the vehicle frame, for the along track- in a) and cross track coordinates in b). Moreover, the blue and red dotted curves represent the $2 \cdot \sigma_{EKF}$ bounds, respectively for the VDFLL and ST+EKF receiver configurations, where σ_{EKF} is the estimation error covariance estimated by the Kalman filter. The position results while the car is driving through the downtown area are shown on the left side of the plots in Figure D-5. Whereas, the right plots in the figures below show a magnified view of navigation solution errors inside area 1 with the objective of clearly viewing the EKF filter convergence interval.

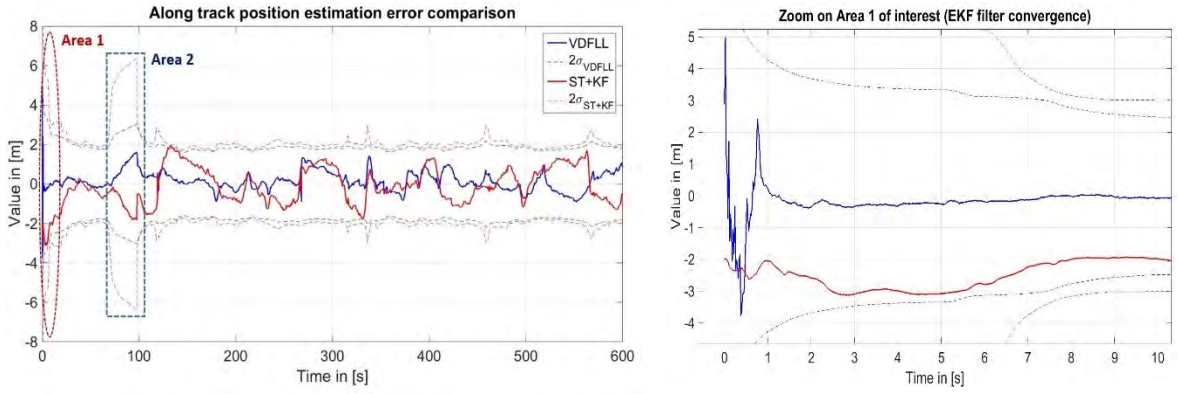

a)

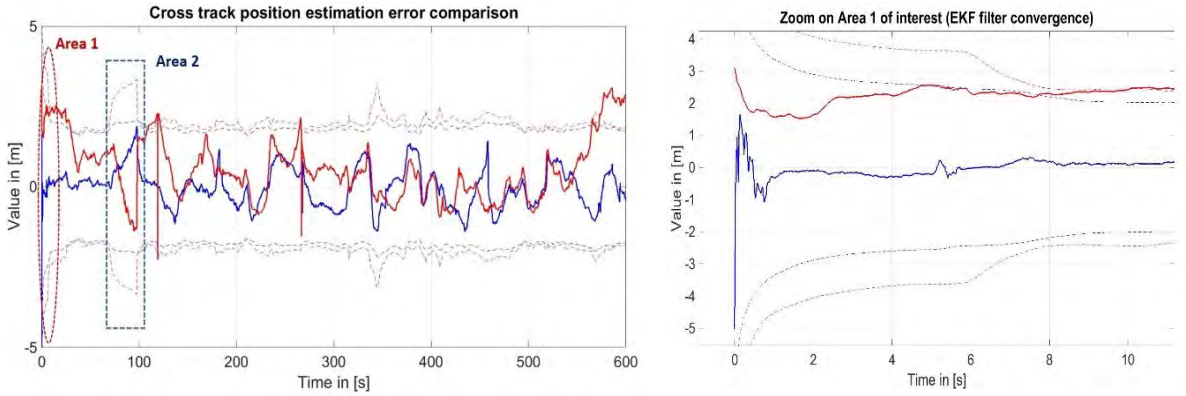

b)

Figure D-5. *Position performance overview in multipath condition (Scalar Tracking VS VDFLL).*

When observing the position error plots in Figure D-5, three main VDFLL superiorities compared to the ST+KF receiver configuration are remarked, such as: stability, reliability and reactivity. The first is justified by the low position error fluctuations in time. Whereas, the VDFLL position reliability is explained by the position error limiting within the $2 \cdot \sigma_{EKF}$ covariance borders along the trajectory and also in the occurrence of severe outage conditions, as it is the case around the 100^{th} epoch depicted in the dotted blue area 2. Last but not least, the VDFLL reactivity consists in the fast estimation error correction during the filter's initialization period (area 1) and after the occurrence of satellite outages (area 2). In fact, the zoomed plot of area 1 illustrates the fast VDFLL-estimated position convergence within 1 second that based on the EKF filter rate coincides with 50 measurement epochs. The along and cross track position error decrease from $5\ m$ at the first EKF epoch, which is the outcome of the WLS algorithm, to a nearly zero estimation error is due to the joint position and tracking estimation process achieved by the VDFLL algorithm. On the contrary, the position errors reported by the ST+KF receiver are biased and remain uncorrected since the code tracking loops are totally independent from the navigation solution.

When the vehicle enters the dense urban region from the $75^{th} - 100^{th}$ epoch, confined in the area 2 rectangle, the received GNSS signals are significantly attenuated by the urban obstacles, forcing the navigation filter to compute the position solution by using the measurements provided from only 4 "good" LOS satellites. Therefore, a sudden position error increase associated with the covariance borders raise for the two filters are observed. However, the VDFLL covariance increase is twice lower when comparing it to the ST+KF module due to the VDFLL capability of effectively ignoring the erroneous NLOS measurements through properly de-weighting them via its measurement covariance matrix R and also due to the code NCO update computed based on the navigation solution estimation. During this interval, the VDFLL filter performs a forward propagation of the state vector that later drives the code/carrier NCO updates in the feedback loop, aiding in this way the channel errors correction. As soon as the LOS satellite signals become available, the vector tracking algorithm can further correct the state vector error accumulated during the outage period. As expected when introducing more reliable pseudorange measurements, the position errors and their estimation uncertainties are reduced.

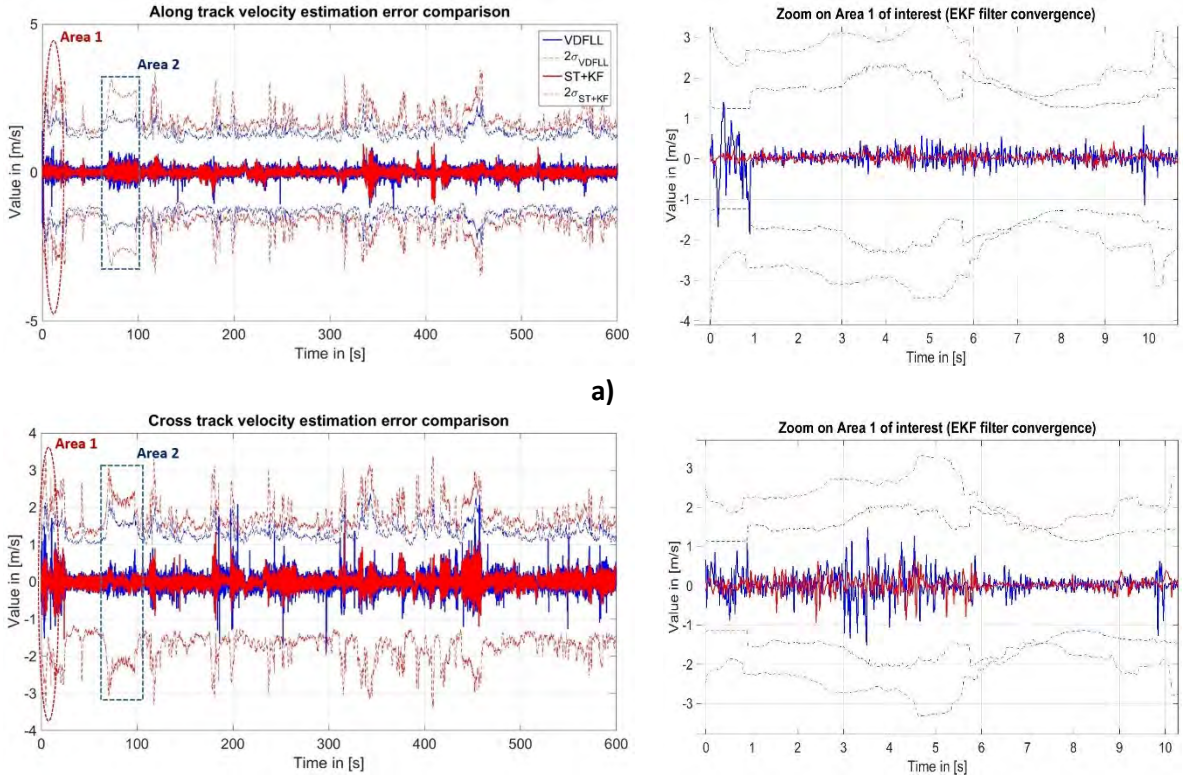

Figure D-6. *Velocity performance overview in multipath condition (Scalar Tracking VS VDFLL).*

The velocity performance overview in Figure D-6 evidences obvious differences in comparison to the position error evolution in time shown previously in Figure D-5. Indeed, the velocity estimation errors for the two receiver configurations are dominated by the noise and seem to follow zero-centered Gaussian distributions. The most evident explanation to this behavior is that the fast multipath condition variations along the car trajectory are interpreted by the carrier tracking loops as noise components, which are also masked from the Gaussian noise added at the correlator outputs. The VDFLL filter convergence characteristic remains valid even for the velocity estimation, as illustrated in the first second of the magnified area 1 plot on the right. However, the VDFLL-estimated along and cross track velocities are slightly noisier then the ST+KF counterparts, which is related to the VDFLL channel's errors coupling that is introduced by the VDFLL technique.

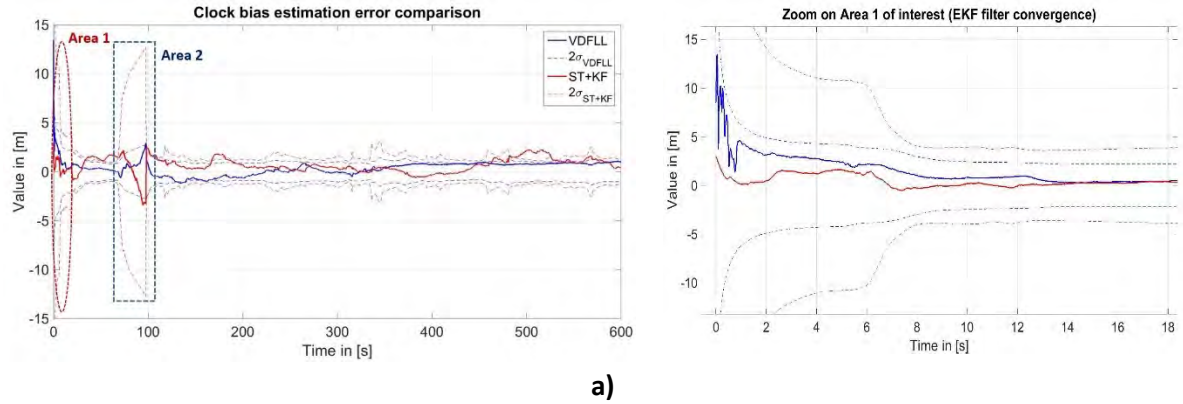

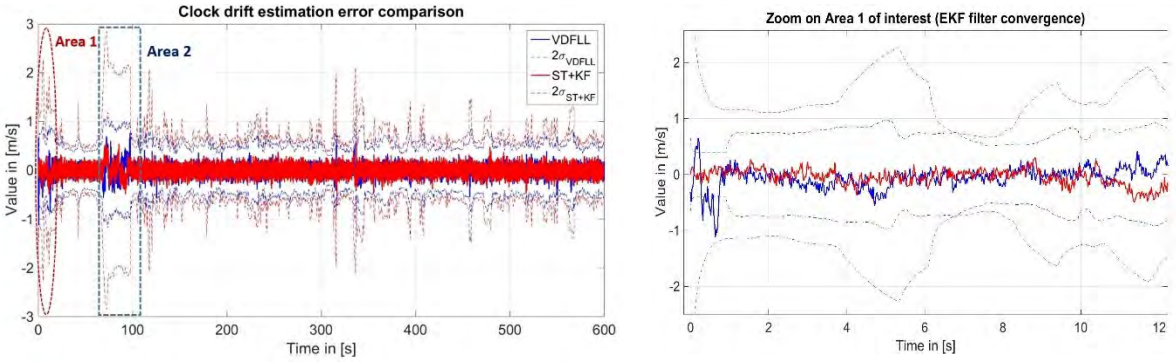

b)

Figure D-7. *Clock states performance overview in multipath condition (Scalar Tracking VS VDFLL)*

The receiver's clock performance comparison, expressed in terms of the user's clock bias and clock drift estimation errors, are respectively depicted in Figure D-7 a) and b). When jointly comparing the position-, velocity- and clock estimation errors evolution in time, two direct correlations may be drawn:

$$\begin{aligned} \varepsilon_\tau &\rightarrow \rho \rightarrow [p_a, p_c, b_u] \\ \varepsilon_{f_D} &\rightarrow \dot{\rho} \rightarrow [v_a, v_c, \dot{b}_u] \end{aligned} \tag{D-1}$$

where:

- $[\varepsilon_\tau, \varepsilon_{f_D}]$ – are the code delay and Doppler frequency errors;
- $[\rho, \dot{\rho}]$ – are the pseudorange and pseudorange rate (Doppler) measurements;
- $[p_a, p_c]$ – denote the vehicle's along and cross track position errors;
- $[v_a, v_c]$ – denote the vehicle's along and cross track velocities errors;
- $[b_u, \dot{b}_u]$ – denote the receiver's clock bias and drift errors;

In contrast to the ST receiver operation mode, the proposed VDFLL technique provides continuous and stable user's clock bias estimation during the overall course. As expected, the VDFLL-estimated clock bias convergence occurs in a longer time interval w.r.t the position estimation. This increased convergence latency is identified with the projection of the unestimated position errors to the clock bias, representing the least observable state in any KF configuration. While referring to the clock drift estimation performance, the same comments presented for the velocity terms are valid due to their relation embedded in the pseudorange rate measurement.

The detailed analysis of the navigation error performance statistics in the presence of multipath are provided in Table D-1.

Table D-1. *Navigation estimation error statistics in multipath condition*

	VDFLL				Scalar Tracking (ST) + KF			
	Mean	**RMS**	**95 %**	**99 %**	**Mean**	**RMS**	**95 %**	**99 %**
Position states								
Along track position error $[m]$	0.2	0.5	0.9	1.4	0.1	0.9	1.7	3.3
Cross track position error $[m]$	0.1	0.6	1.1	1.3	0.5	1.1	2.4	3.9
Velocity states								
Along track velocity error $[m/s]$	~0	0.2	0.4	0.6	~0	0.1	0.3	0.4
Cross track velocity error $[m/s]$	~0	0.1	0.3	0.5	~0	0.2	0.3	0.5
Clock states								
Clock bias error $[m]$	0.4	0.8	1.1	2.5	0.7	1.1	2	4.8
Clock drift error $[m/s]$	~0	0.1	0.2	0.4	~0	0.1	0.2	0.3

The position errors' RMS and $95\%/99\%$ confirm the nearly twice better VDFLL performance against the scalar tracking + KF positioning module in multipath signal reception condition. Whereas, nearly equivalent performance concerning the velocity, clock bias and drift estimations are noticed. Yet, the VDFLL superiority is not remarkably evident due to high number of measurements that are fed to the navigation filter. Indeed, the overdetermined number of observables induce lower navigation errors and tighter covariance bounds.

D.2.4.2. Channel Level Analysis

The performance analysis between the Scalar Tracking (ST) and VDFLL is now extended to the signal level, expressed by the code delay and carrier frequency estimation errors along the car trajectory. Recalling the LOS/NLOS satellites' categorization based on their PDP profiles, the tracking channel errors comparison will be performed for GPS and Galileo satellite pairs falling into the LOS, moderate LOS and NLOS satellite classes that are respectively shown in Figure D-8, Figure D-10 and Figure D-12, respectively. Each of these figures illustrate the code delay and carrier frequency error comparison in a) and b), along with the received signal power evolution in time in c) and the near echo PDP profile in d) for a GPS satellite (left plots) and a Galileo satellite (right plots).

D.2.4.2.1. Channel errors comparison for LOS satellites

In this subsection, the performance comparison in the channel level is performed for the LOS GPS PRN3 and Galileo PRN68 satellites, characterized by the red color in its PDP profile from Figure 7-7 and situated at a high elevation angles, referring to the skyplot in Figure 7-2.

For a better understanding of the channel errors comparison, the code delay and carrier frequency errors distributions concerning the GPS and Galileo LOS satellites pair for the two receiver architectures is illustrated in Figure D-9.

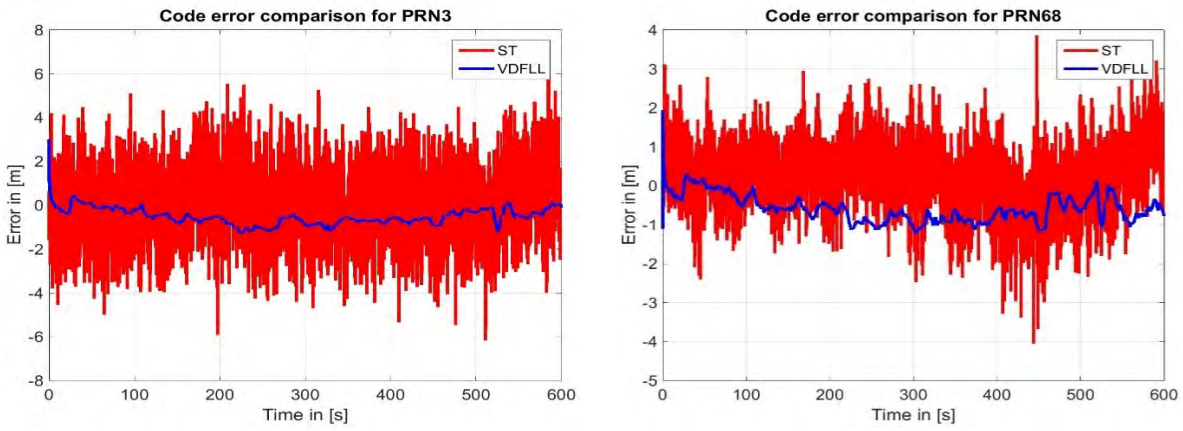

a)

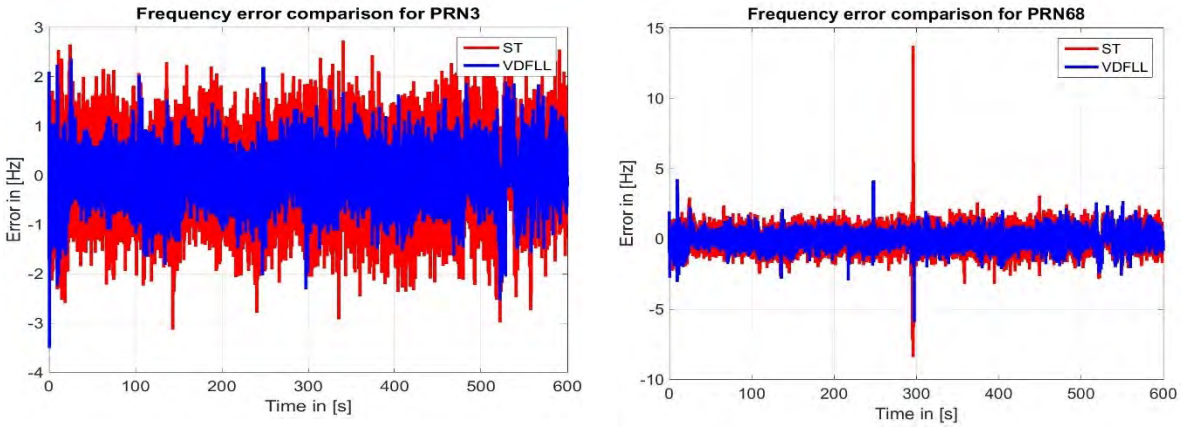

b)

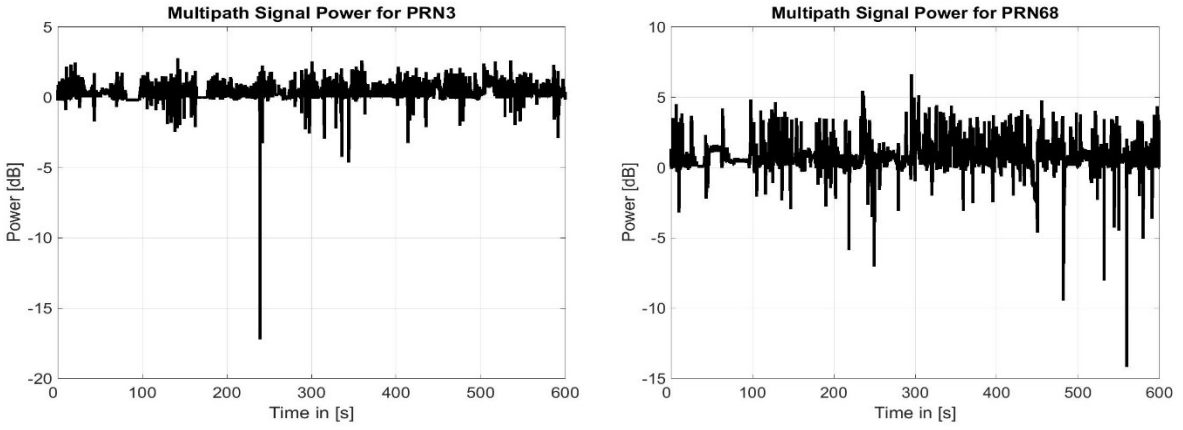

c)

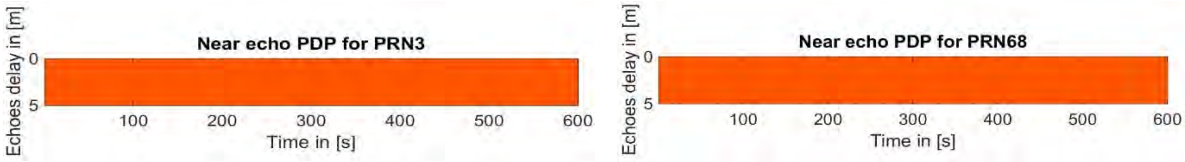

d)

Figure D-8. *Performance comparison in the tracking channel level for two LOS satellites in multipath condition.*

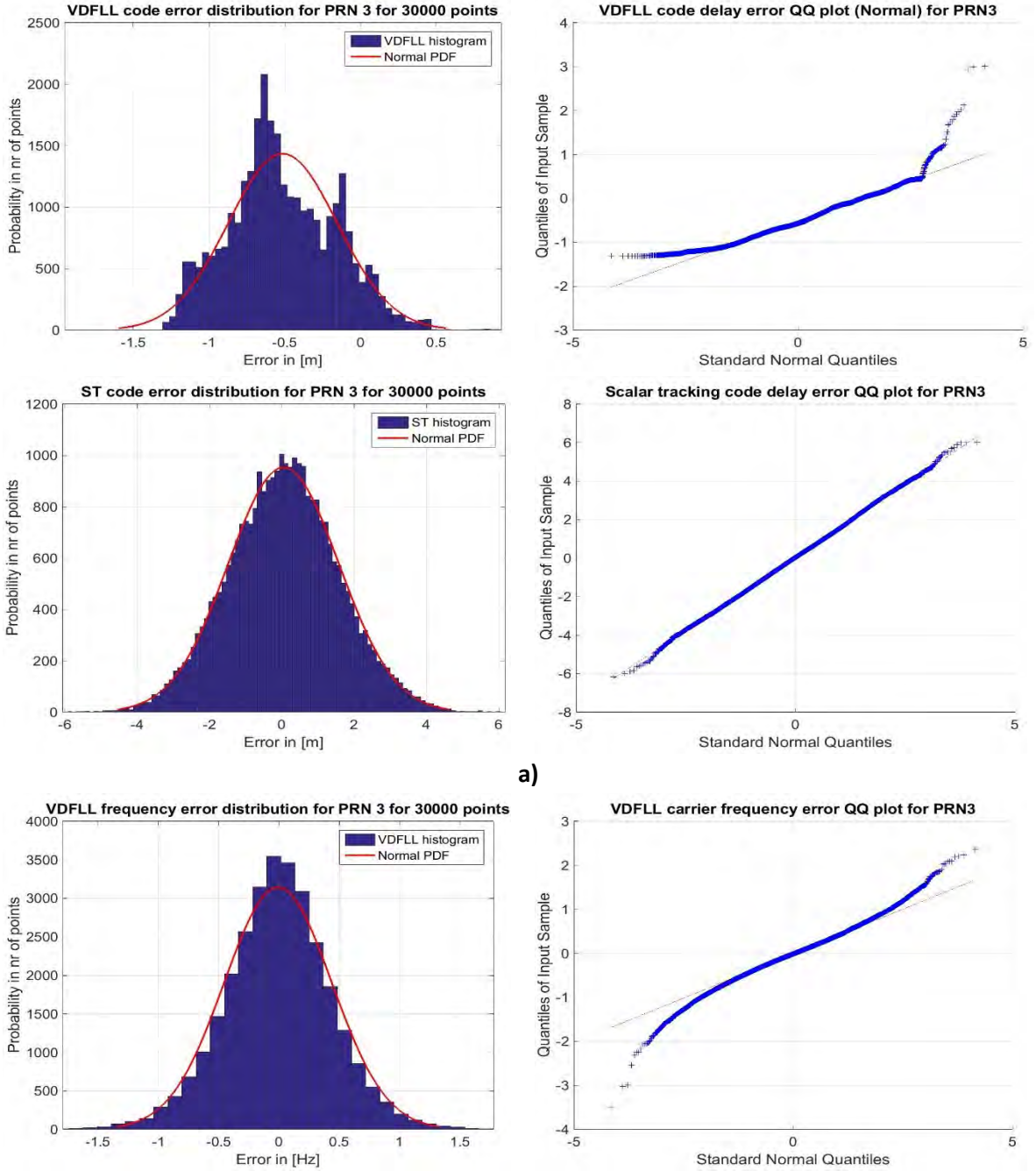

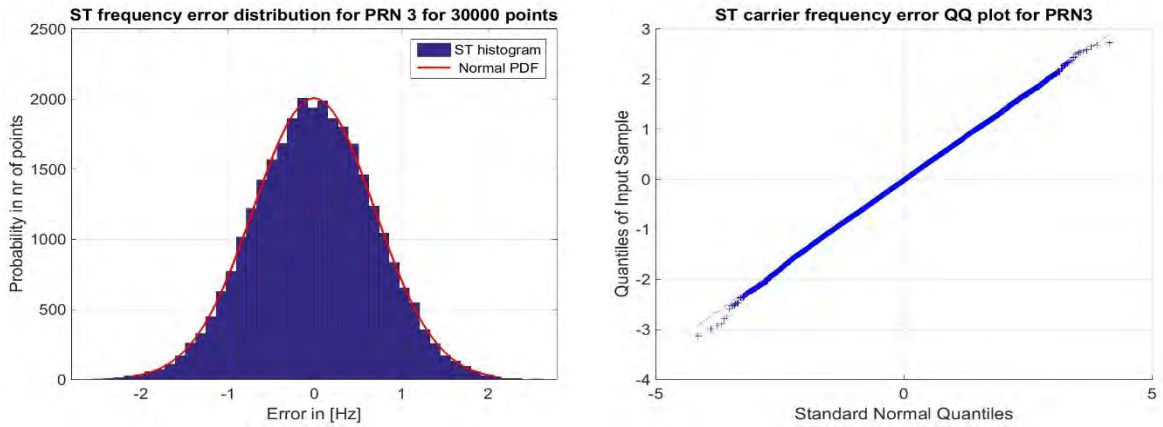

b)

Figure D-9. *Channel errors distribution for two LOS satellites (Scalar tracking VS VDFLL).*

The plots provided in Figure D-8 for the LOS GPS PRN3 and Galileo PRN 68 satellites, confirm the VDFLL better performance expectation w.r.t the ST loop that is especially manifested concerning the code delay estimation. This is purely related to VDFLL's principle of operation, for which the code delay correction is generated from the estimated user's position. Logically, a lower position error leads to a more accurate code delay estimation, which becomes even more evident for high-elevation LOS satellites. The sudden multipath power changes, seen around the 250^{th} epoch for GPS PRN 3 and after the 500^{th} epoch for Galileo PRN 68 are translated into strong code error oscillations concerning the ST loop. A total insensitivity regarding the code delay estimation is observed for the VDFLL algorithm due to the channels aiding property. The VDFLL/ST comparison in the tracking channel level is completed with the inclusion of the code- and carrier errors distributions, as shown in Figure D-9. Regarding the code delay error distribution, shown in Figure D-9 a), it may be noticed that the best distribution fit for the VDFLL- and ST- estimated code errors for a LOS satellite is the normal (Gaussian) distribution. However, the best graphical tool widely used in statistics to identify the probability distribution of the variable under study is the quantile-quantile (Q-Q) plot. As described in Chapter 7, the Q-Q plot is a probability plot capable of comparing two probability distributions by plotting their quantiles against each other. When the points of the Q-Q plot lie on the line $y = x$, this means that two distributions being compared are identical. The Q-Q plots, comparing the code delay- and carrier frequency errors distributions against the normal distribution, are illustrated in the right side of Figure D-9. Based on this description, it can be easily noted the Gaussian distribution characteristic of the ST-estimated code and carrier errors. This statement holds also for the major part of the VDFLL code- and carrier estimation errors of a LOS satellite but with minor deviations for the lower and higher quantiles. This is a proof-of-concept of the VDFLL error flow between the tracking channels due to the EKF-estimated code/carrier NCO update.

D.2.4.2.2. Channel errors comparison for moderate LOS satellites

Now, the channel level performance assessment is extended to two moderate LOS satellites (ex: GPS PRN4 and Galileo PRN 53), which provide the LOS ray during most of the car trajectory as depicted in the PDP profile from Figure 7-7 and situated at a mid-elevation, referring to the skyplot in Figure 7-2.

Similarly to the previous case, the code delay and carrier frequency error comparison for the two moderate LOS satellites in a) and b), along with the received signal power evolution in time in c) and the near echo PDP profile in d) for a GPS satellite (left plots) and a Galileo satellite (right plots) are

depicted in Figure D-10. Moreover, the code delay and carrier frequency errors distributions concerning the two moderate LOS satellites for the two receiver architectures are illustrated in Figure D-11.

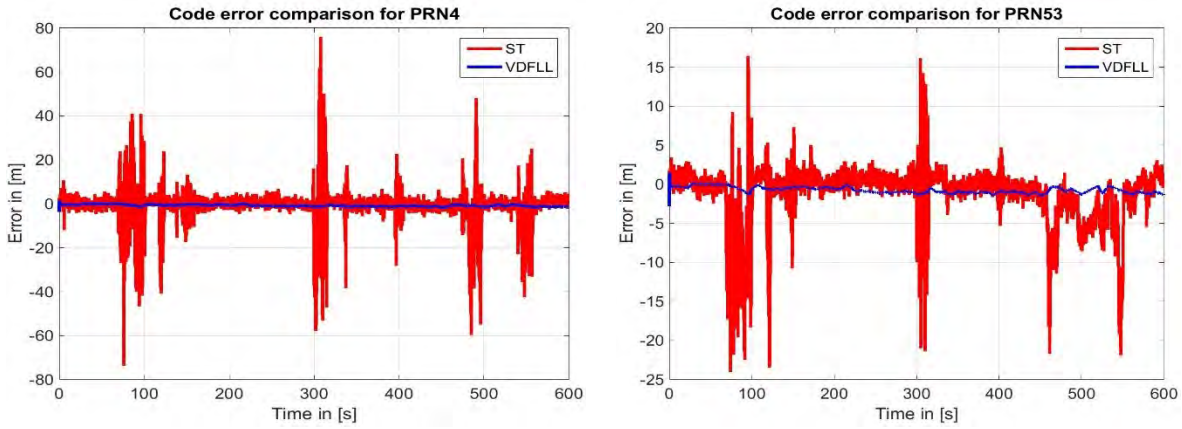

a)

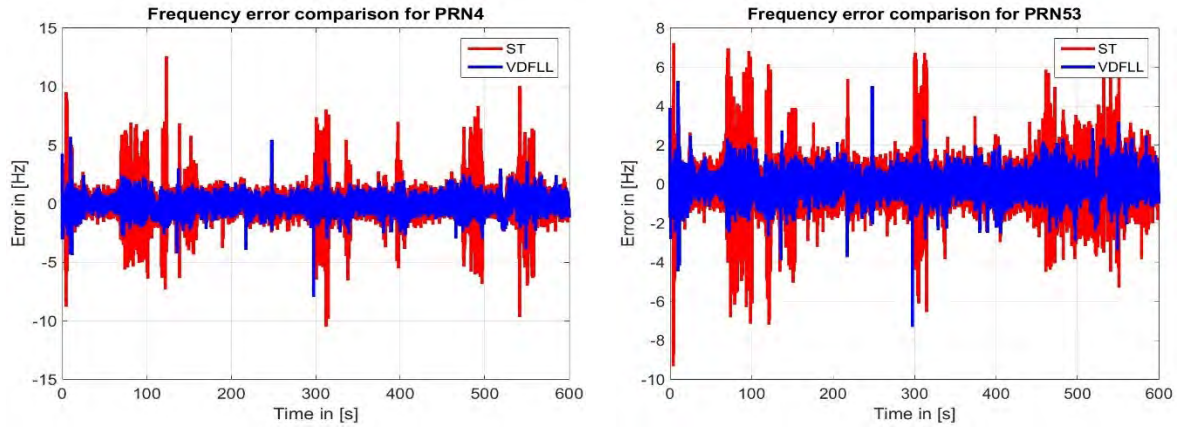

b)

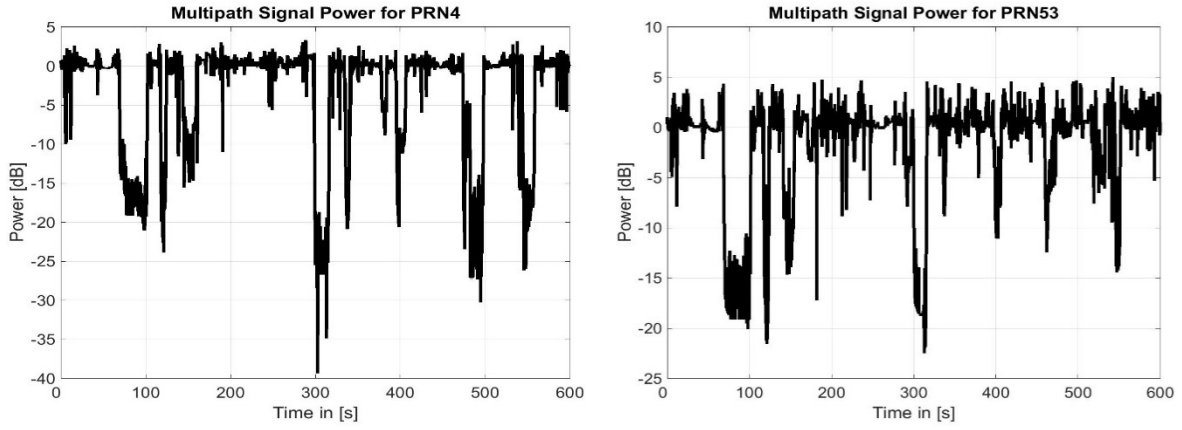

c)

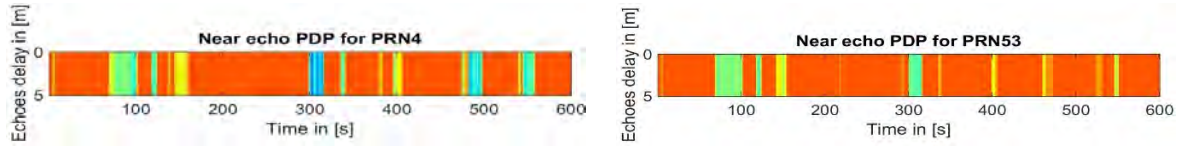

d)

Figure D-10. *Performance comparison in the tracking channel level for two moderate LOS satellites in multipath condition.*

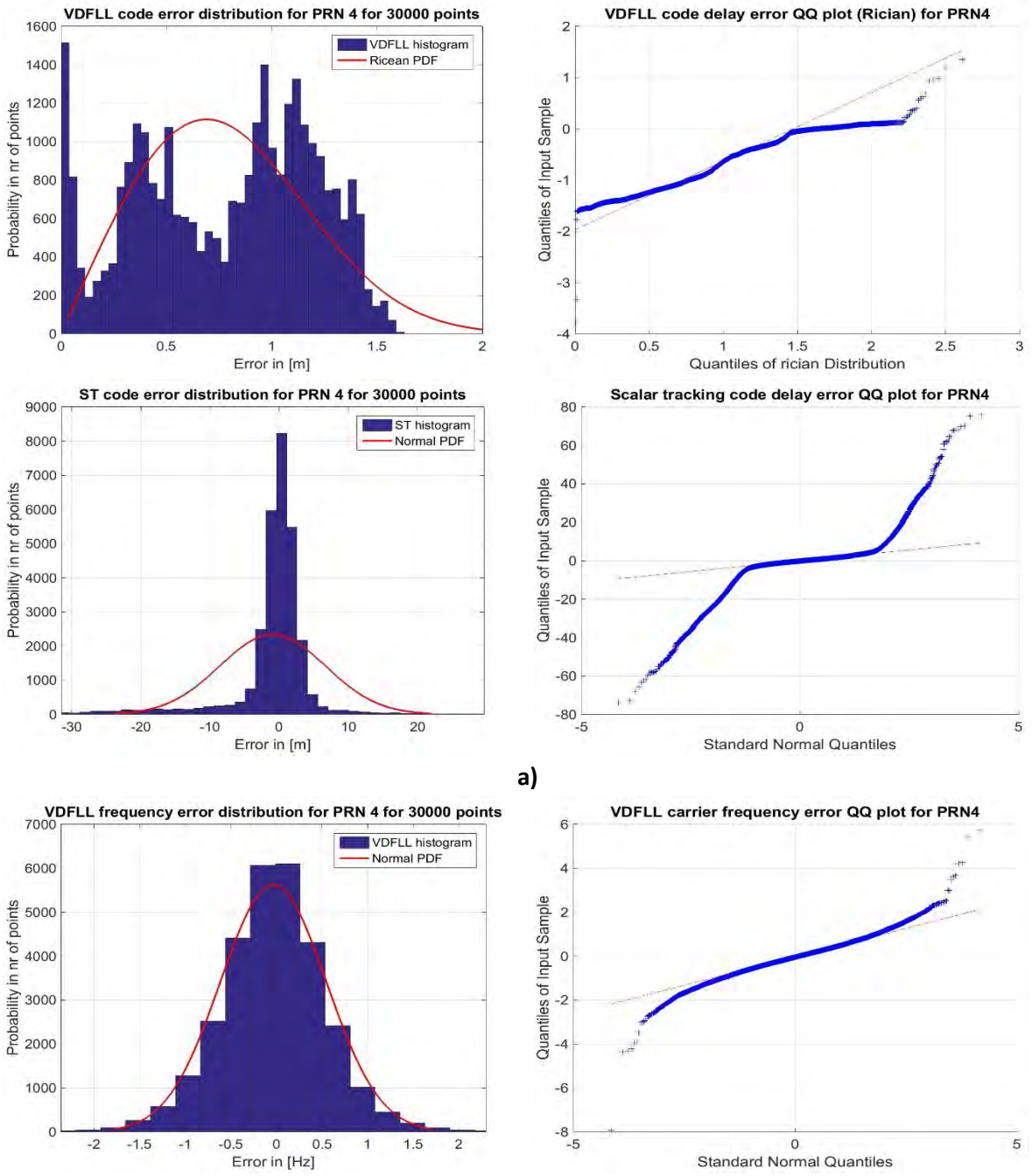

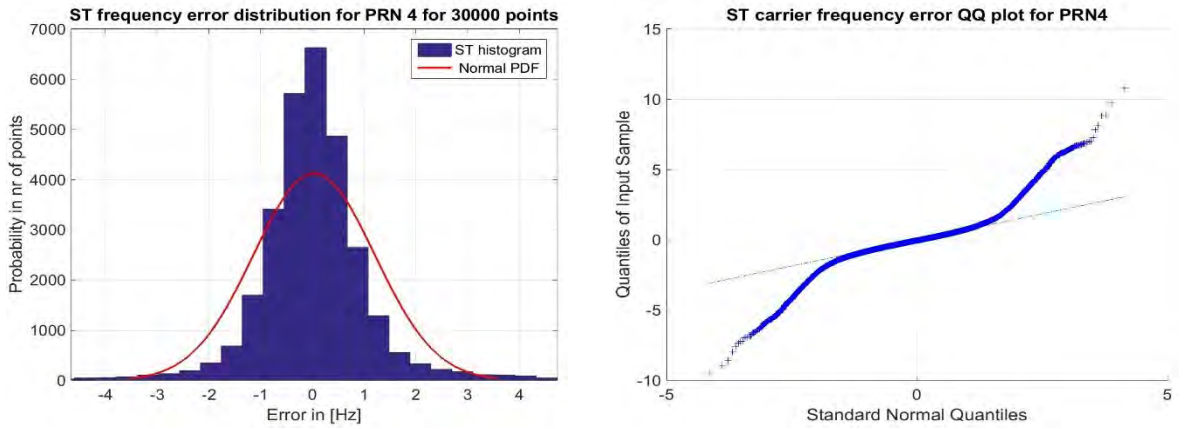

b)

Figure D-11. *Channel errors distribution for two moderate LOS satellites (Scalar tracking VS VDFLL).*

When observing the results in Figure D-10, once more the VDFLL algorithm outperforms the scalar tracking technique in the code delay and carrier frequency tracking accuracy for the moderate LOS satellites that experience several LOS blockages events. The LOS signal blockage, characterized by significant signal power drops and by the green/blue PDP regions at $100\ s$, $300\ s$ for Galileo PRN53 and at the middle of the trajectory after $300\ s$ for GPS PRN4 according to Figure D-10 c) and d), is reflected by a large code delay estimation error increase for the scalar tracking operation, as it can be seen in the left plot of Figure D-10 a). Contrary to the scalar tracking configuration, the VDFLL architecture assures an accurate and stable VDFLL code delay estimation even during these signal power drops. This is also confirmed for the Doppler frequency estimation but at a lower magnitude w.r.t the code delay estimation due to reduced impact of the multipath in the Doppler frequency. This VDFLL superiority is caused by the channel aiding characteristic of the VDFLL technique.

The comparison between the two tracking techniques is extended to the code and carrier errors distributions, as illustrated in Figure D-11. The LOS blockage occurrences introduce significant code delay and carrier frequency biases that affect the Gaussian-property of the distribution functions for the two architectures, as illustrated in Figure D-11. Indeed when observing the carrier frequency error Q-Q plots in Figure D-11 b), the Gaussian distribution is altered for both the architectures but is more obvious for the ST architecture due to the frequency biases during LOS signal blockages. This becomes even more evident for the scalar tracking architecture concerning the code delay estimation error distribution. As stated in results chapter, the definition of the best distribution fit to the VDFLL code errors is difficult due to the channel's coupling through the EKF-estimated position. However through several tests, the Rician bivariate distribution is the only known distribution that remotely fits the VDFLL code error distribution, as illustrated in the left plots from Figure D-11 a).

D.2.4.2.3. Channel errors comparison for NLOS satellites

Last but not least, the code and carrier estimation errors comparison for the two receiver architectures is performed for the NLOS GPS and Galileo satellite pair. Observing the multipath PDP profile from Figure 7-7, the GPS PRN14 and Galileo PRN 51 do represent the worst tracked satellites due to the frequent LOS blockage events and also these satellites are positioned at low elevation altitudes in the skyplot from Figure 7-2. The same figure representation for the previous LOS and moderate LOS satellites is conserved in this sub-section. Thus, the code delay and carrier frequency errors'

comparison between the scalar tracking and VDFLL techniques is shown in Figure D-12. Whereas, the code delay and carrier frequency error distributions and Q-Q plots are provided in Figure D-13.

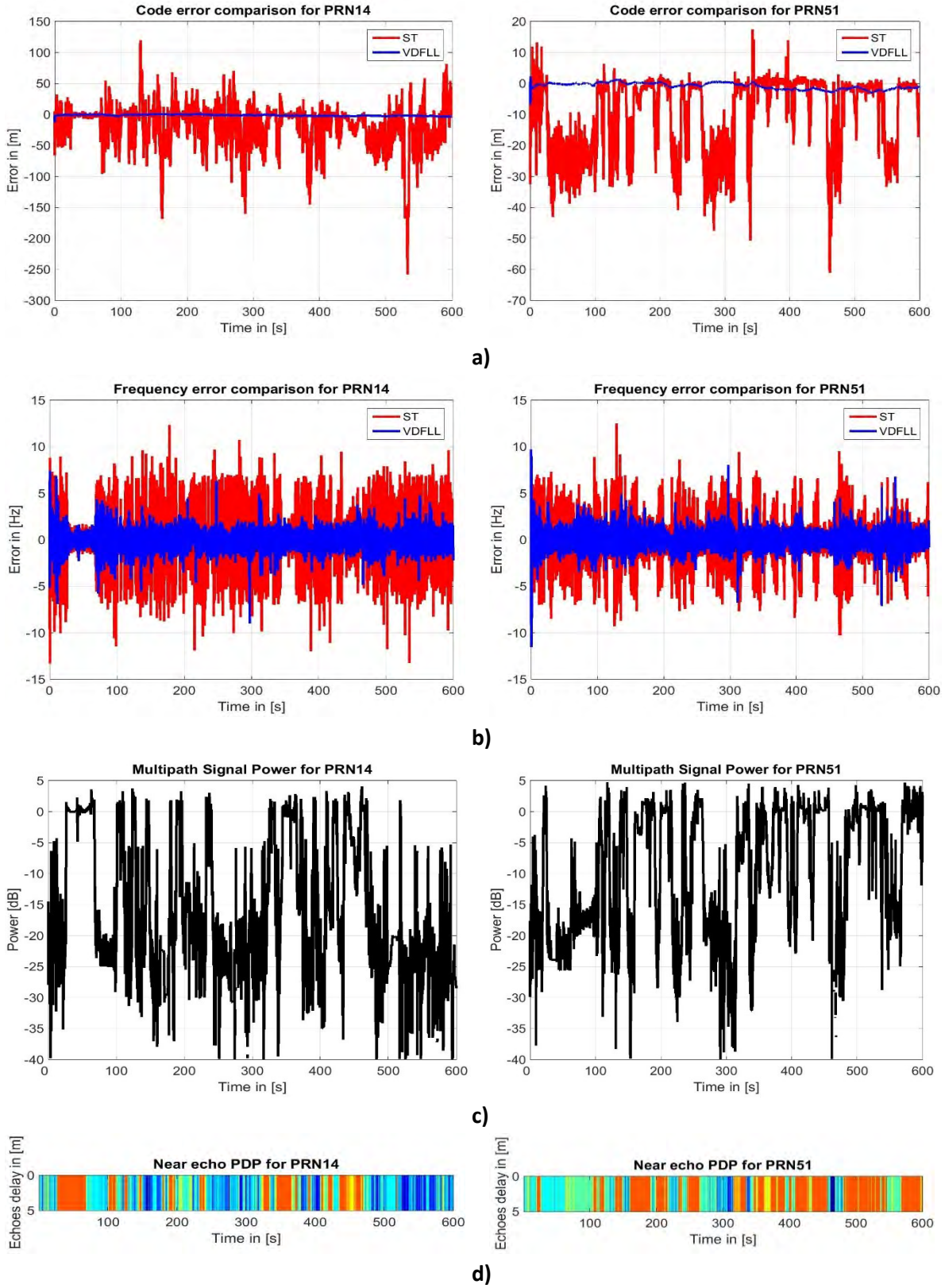

Figure D-12. *Performance comparison in the tracking channel level for two NLOS satellites in multipath condition.*

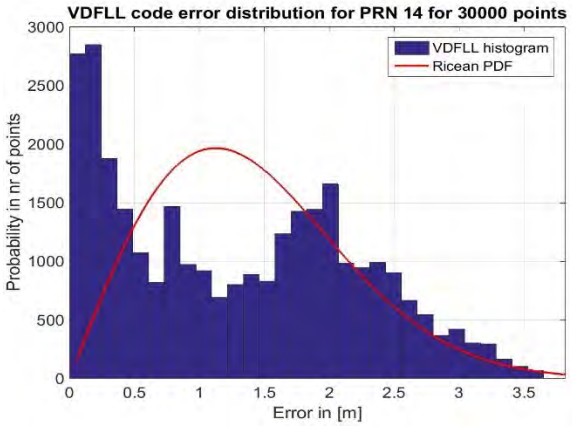
VDFLL code error distribution for PRN 14 for 30000 points
VDFLL histogram
Ricean PDF
Probability in nr of points
Error in [m]

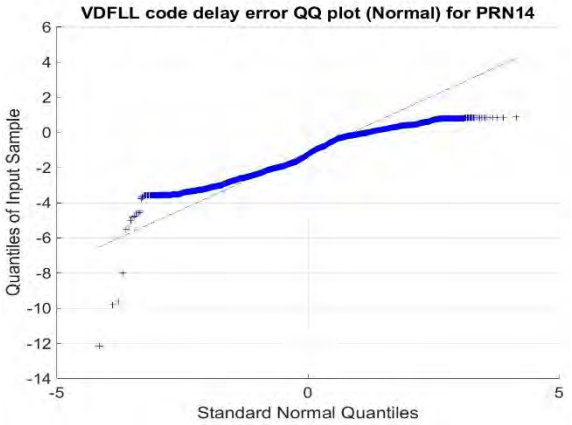
VDFLL code delay error QQ plot (Normal) for PRN14
Quantiles of Input Sample
Standard Normal Quantiles

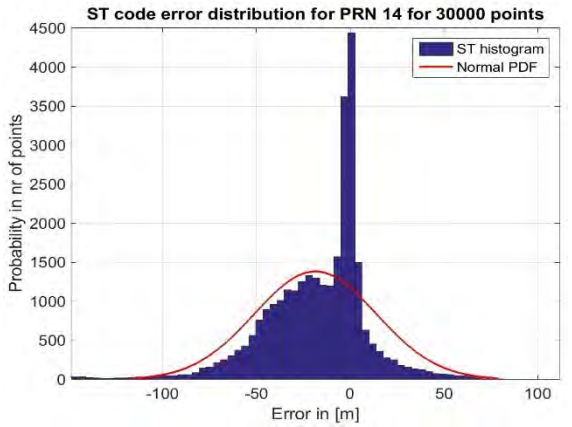
ST code error distribution for PRN 14 for 30000 points
ST histogram
Normal PDF
Probability in nr of points
Error in [m]

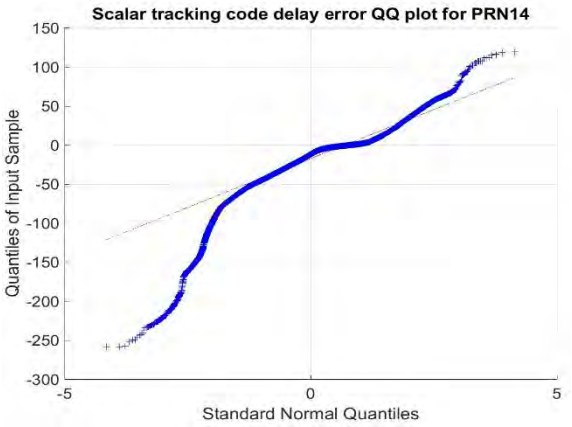
Scalar tracking code delay error QQ plot for PRN14
Quantiles of Input Sample
Standard Normal Quantiles

a)

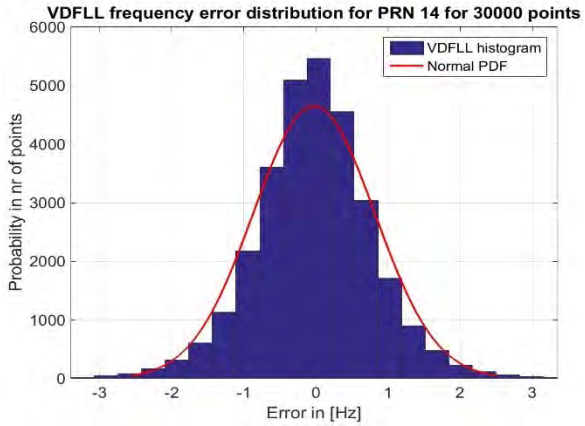
VDFLL frequency error distribution for PRN 14 for 30000 points
VDFLL histogram
Normal PDF
Probability in nr of points
Error in [Hz]

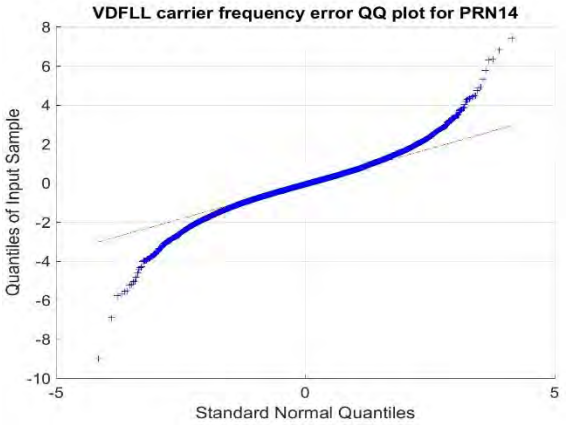
VDFLL carrier frequency error QQ plot for PRN14
Quantiles of Input Sample
Standard Normal Quantiles

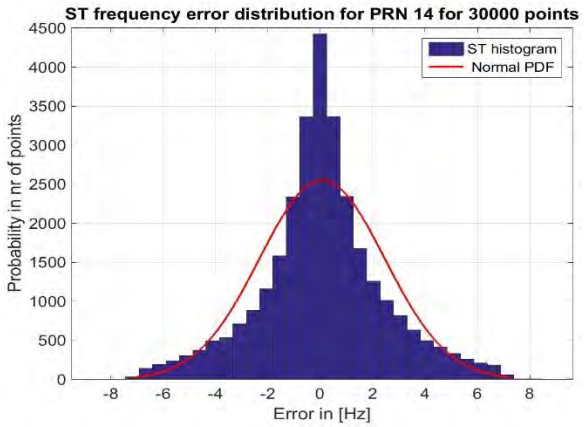
ST frequency error distribution for PRN 14 for 30000 points
ST histogram
Normal PDF
Probability in nr of points
Error in [Hz]

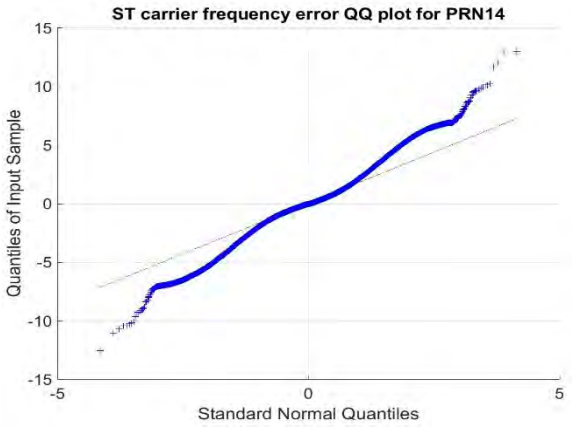
ST carrier frequency error QQ plot for PRN14
Quantiles of Input Sample
Standard Normal Quantiles

b)

Figure D-13. *Channel errors distribution for a NLOS satellite (Scalar tracking VS VDFLL).*

Based on the signal power graph in Figure D-13 c) and on the large duration of the NLOS signal presence in the last $100\ s$ of the trajectory as provided by the blue PDP region in Figure D-13 d), GPS PRN 14 is clearly the worst tracked satellite also with the highest probability of fault inclusion (in a integrity perspective) in the VDFLL filter.

It must be pointed out, that the code/carrier tracking estimation process is continuously carried on by the VDFLL architecture based on the mutual channel aiding. Whereas in the scalar tracking configuration, the NLOS satellite tracking process is interrupted after the lock detection test failure, which triggers the start of the $1\ s$ hot re-acquisition process. Indeed, the code loss-of-lock condition occurs when the code delay error exceeds the discriminator chip spacing, which is set to $0.5\ chips = 149\ m$ for GPS L1 and $0.2\ chips = 58\ m$ for the Galileo E1 signals as provided in Table 7-1. Returning to the code delay estimation error plot in Figure D-13 a), it can be seen that these loss-of-lock events take place three times for the GPS L1 channel and a single time for the Galileo PRN.

These loss-of-lock occurrences do also seriously affect the ST code and frequency errors histogram and therefore, transforming the ST Q-Q plots which are less Gaussian compared to the moderate LOS satellites, as illustrated in Figure D-14.

D.2.4.2.4. Channels' errors statistics

The performance comparison in terms of channel error statistics in the presence of multipath and LOS blockages, for the three LOS, moderate LOS and NLOS satellites presented above, are provided in Table D-2.

Table D-2. *Channel error statistics in multipath condition*

	VDFLL				Scalar Tracking (ST)			
	Mean	**RMS**	**95 %**	**99 %**	**Mean**	**RMS**	**95 %**	**99 %**
Category 1: LOS satellites (Ex: GPS PRN 3)								
Code error $[m]$	0.5	0.6	1.1	1.2	~0	1.5	2.7	3.2
Frequency error $[Hz]$	~0	0.4	0.9	1.1	~0	0.7	1.4	1.8
Category 2: Moderate LOS satellites (Ex: GPS PRN 4)								
Code error $[m]$	0.8	0.8	1.3	1.5	1	7.7	18.2	34.8
Frequency error $[Hz]$	~0	0.6	1.2	1.7	~0	1.2	2.4	4.8
Category 3: NLOS satellites (Ex: Galileo PRN 51)								
Code error $[m]$	0.9	1.3	2.5	2.8	9.9	15.3	30.2	36.6
Frequency error $[Hz]$	~0	0.8	1.6	2.4	~0	1.8	4.2	6.1

As it can be seen, the VDFLL technique assures nearly perfect code delay and carrier frequency synchronization even during LOS/NLOS transitions or when tracking pure NLOS satellites. Indeed, the VDFLL code delay estimations are nearly 20 times more precise w.r.t the scalar tracking operation mode.

D.2.4.2.5. Channel errors RMS description

In order to deduce whether there is a dependence of channel errors on the satellite elevation and bearing angle, the code and frequency errors RMSs due to the multipath contribution for the two architectures under comparison are illustrated in Figure D-14.

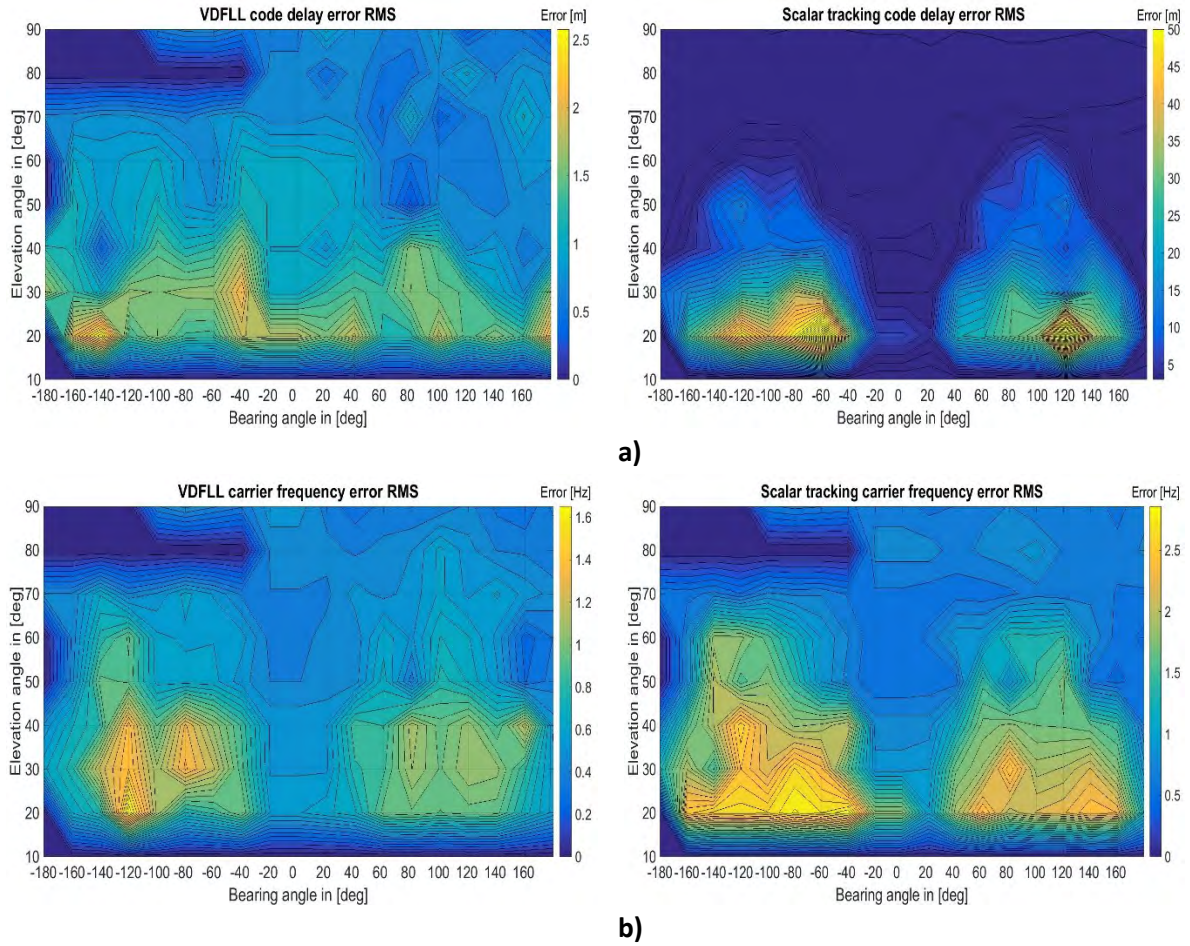

Figure D-14. ***a)*** *Code delay and* ***b)*** *Carrier frequency errors RMS in multipath presence.*

The contour plots for both the code and carrier frequency errors confirm our expectation, concerning their dependence to the satellite elevation angle only. In fact as illustrated by the bright yellow contour lines, the code delay- and carrier frequency errors are far more dominant in the low elevation region due to the increased possibility of the LOS shadowing caused by the urban obstacles. In other words, the low elevation satellites are highly probable to provide NLOS measurements to the receiver. As it can be observed in the first two plots in Figure D-14 a), the VDFLL code delay estimations for each tracking channels are far less erroneous w.r.t the scalar tracking estimations for the overall covered area. The VDFLL superiority for the code delay estimation, shown in the left upper plot, becomes more evident in low elevation region $(20^{\circ} - 40^{\circ})$ with large differences in the code delay error magnitudes. The large code delay errors for the scalar tracking technique are due to the DLL loss of lock occurrences for the NLOS satellites in view. Whereas, continuous tracking is performed by the VDFLL algorithm

through the feedback loop based on the EKF-estimated user position. Regarding, the carrier frequency error RMS in Figure D-14 b), a slightly better performance of the VDFLL technique is noticeable, which proves the low multipath effect on the pseudorange rate measurements. Furthermore, the Doppler frequency error RMSs concentration for both architectures in certain bearing angles is just related to the vehicle orientation during the trajectory that is translated into the heading angle.

D.2.4.2.6. Conclusions

This section provided the performance assessment in the navigation and channel level of the dual-constellation GPS/Galileo VDFLL and scalar tracking receiver architectures in urban environment representative, in the presence of multipath and LOS blockages. In this scenario, one simulation was conducted with the urban car trajectory shown in Figure 7-1 and by including the multipath data from the DLR urban channel model at the correlator output of the GNSS signal emulator as defined in section 6.2.

The results proved the VDFLL supremacy in the navigation domain, especially concerning the position and clock bias estimations since multipath majorly impacts the pseudorange measurements, which is later translated in the position domain. Approximately twice more accurate and stable position and clock bias estimations were observed for the VDFLL architecture and also verified by the lower RMS values in the table of statistics. Furthermore, the VDFLL reactivity was noted during LOS blockages intervals, for which an accurate navigation solution is assured by the VDFLL algorithm due to the position estimation-based code NCO update. Slightly better velocities and clock drift estimations are obtained from the vector tracking receiver, due to the low multipath impact on the Doppler measurements.

Regarding the channel estimations, the VDFLL tracking robustness was certified especially in the code delay tracking for moderate LOS and NLOS satellites that experience large signal power drops. During these epochs, the tracking process is performed without interruption by the VDFLL receiver based on the channel aiding. Whereas, a hot re-acquisition process is required after the loss-of-lock condition is reached for the scalar tracking architecture.

Abstract:

In the last decade, Global Navigation Satellites Systems (GNSS) have gained a significant position in the development of urban navigation applications and associated services. The urban environment presents several challenges to GNSS signal reception, such as multipath and GNSS Line-of-Sight (LOS) blockage, which are translated in the positioning domain in a decreased navigation solution accuracy up to the lack of an available position. For this matter, Vector Tracking (VT) constitutes a promising approach able to cope with the urban environment-induced effects including multipath, NLOS reception and signal outages. This thesis is particularly focused on the proposal and design of a dual constellation GPS + Galileo single frequency L1/E1 Vector Delay Frequency Lock Loop (VDFLL) architecture for the automotive usage in urban environment. From the navigation point of view, VDFLL represents a concrete application of information fusion, since all the satellite tracking channels are jointly tracked and controlled by the common navigation Extended Kalman filter (EKF). The choice of the dual-constellation single frequency vector tracking architecture ensures an increased number of observations and at the same time allowing the conservation of the low-cost feasibility criteria of the mobile user's receiver. Moreover, the use of single frequency L1 band signals implies the necessity of taking into account the ionospheric error effect. In fact, even after the application of the ionosphere error correction models, a resultant ionospheric residual error still remains in the received observations. The originality of this work relies on the implementation of a dual-constellation VDFLL architecture, capable of estimating the ionosphere residual error present in the received observations. This dissertation investigates the VDFLL superiority w.r.t the scalar tracking receiver in terms of positioning performance and tracking robustness for a real car trajectory in urban area in the presence of multipath and ionosphere residual error.

Abstract en Français:

Durant la dernière décennie, les systèmes de navigation par satellites ont obtenu une place majeure dans le développement d'application de navigation urbaine et les services associés. L'environnement urbain pose plusieurs défis à la réception des signaux GNSS, comprenant les multi-trajets et le phénomène de blocage des signaux directs, qui peuvent se traduire dans le domaine de la position, par une diminution de la précision de la solution de navigation voire par une indisponibilité de la position. Dans cette situation, la poursuite vectorielle constitue une approche intéressante capable de contrecarrer les effets propres à un environnement urbain tels que les multi-trajets, les réceptions de signaux non directs et les interruptions de signal. Cette thèse s'intéresse particulièrement à la proposition et au design d'une architecture double constellation GPS + Galileo, mono-fréquence L1/E1 VDFLL pour les véhicules routiers en milieu urbain. Concernant la navigation, le VDFLL représente une application concrète de la fusion d'information dû au fait que tous les canaux de poursuite sont contrôlés par le même filtre de navigation sous la forme d'un Filtre de Kalman Étendu (EKF). Le choix de l'architecture double constellation mono-fréquence a pour but d'augmenter le nombre de mesures et garantit une faisabilité bas coût du récepteur mobile. De plus, l'utilisation des signaux de mono-fréquence L1 implique la prise en compte des perturbations causées par la ionosphère. Malgré l'application des modèles de corrections ionosphérique, un résidu d'erreur ionosphérique reste toujours présent. L'originalité de ce travail repose sur l'implémentation d'une architecture VDFLL double constellation capable d'estimer le résidu d'erreurs ionosphériques présent sur les observations reçues. Ce doctorat analyse les avantages apportés par la solution proposée par rapport à la poursuite scalaire au regard de performances de positionnement et de robustesse de poursuite dans le cadre d'une trajectoire de véhicule en milieu urbain et en présence de multi-trajets et de résidus d'erreur ionosphérique.